

ABSTRACT

SEARCH FOR CHARGED HIGGS BOSONS IN THE $H^\pm \rightarrow \tau^\pm \nu_\tau$ FINAL STATE WITH 139 fb^{-1} OF pp COLLISION DATA AT $\sqrt{s} = 13 \text{ TeV}$ WITH THE ATLAS EXPERIMENT

Elliot Wesley Parrish, Ph.D.

Department of Physics

Northern Illinois University, 2022

Dhiman Chakraborty, Co-Director

Jahred Adelman, Co-Director

This dissertation uses 139 fb^{-1} of pp collision data collected at a center of mass energy of $\sqrt{s} = 13 \text{ TeV}$ by the ATLAS detector to search for charged Higgs bosons decaying to a tau lepton and a neutrino ($H^\pm \rightarrow \tau^\pm \nu_\tau$) in association with a top quark. Two subchannels are defined based on the leptonic decay ($\tau + \ell$) or hadronic decay ($\tau + \text{jets}$) of the associated top quark. Parameterized Neural Networks are investigated and optimized to improve signal separation from background in both subchannels across a wide m_{H^\pm} range of 80 GeV to 3000 GeV. Expected exclusion limits at 95% confidence on $\sigma(pp \rightarrow tbH^\pm) \times \mathcal{B}(H^\pm \rightarrow \tau\nu)$ are compared to previous observed limits.

NORTHERN ILLINOIS UNIVERSITY
DEKALB, ILLINOIS

DECEMBER 2022

**SEARCH FOR CHARGED HIGGS BOSONS IN THE $H^\pm \rightarrow \tau^\pm \nu_\tau$ FINAL
STATE WITH 139 fb^{-1} OF pp COLLISION DATA AT $\sqrt{s} = 13\text{ TeV}$ WITH
THE ATLAS EXPERIMENT**

BY

ELLIOT WESLEY PARRISH
© 2022 Elliot Wesley Parrish

A DISSERTATION SUBMITTED TO THE GRADUATE SCHOOL
IN PARTIAL FULFILLMENT OF THE REQUIREMENTS
FOR THE DEGREE
DOCTOR OF PHILOSOPHY

DEPARTMENT OF PHYSICS

Dissertation Doctoral Co-Directors:
Dhiman Chakraborty
Jahred Adelman

ACKNOWLEDGEMENTS

I would like to start by thanking Dhiman Chakraborty for the opportunity to be your student. Thank you for fighting for me from day one; I would not be here without your efforts. I would like to extend my gratitude to Jahred Adelman for taking me on as a student and ensuring I finish this program. I would also like to thank the rest of my committee for their mentorship.

Thank you to the incredible ATLAS and CERN communities, it was a pleasure to work with such dedicated people. Thank you to the Tile community for the unique opportunity to work on all aspects of the machine with experts from across the globe. To name a few, Oleg Solovyanov, Sanya Solodkov, Irakli Minashvili, Siarhei Harkusha, and all of the Charge Injection System experts. Thank you to the charged Higgs analysis group, it has been a truly incredible experience working with you. I'd like to especially thank Paweł Klimek for your guidance throughout this program. Thank you to Michalea Mlynarikova for your support as a friend and mentor over countless cups of coffee. Thank you to the University of Oregon ATLAS group for the many years of guidance. Thank you to the other NIU graduate students and the ATLAS group.

Thank you to all of the friends I have made along this journey. John Myers, Ian Snyder, and Jason Barkeloo for welcoming me with open arms all those years ago as an undergraduate who had no idea where he was going. Thank you Tyler Burch for helping guide me through the journey at NIU. Thank you to Jimmy Friedricks, Samantha Friedricks, Hayden Harris, and Kylie Harris for reminding me to enjoy life. Thank you to Rafael Oreamuno Madriz. To the numerous friends I made while living at CERN, thank you for the memories, I will

always look back fondly on our time together. Thank you to Christopher Heath Parent for your unconditional support and brotherhood.

Lastly, I would like to thank my family for their unwavering support. Thank you Amanda Steinhebel for the encouragement, patience, and support to see this to the end.

DEDICATION

To Dr. Dhiman Chakraborty. Thank you for everything.

TABLE OF CONTENTS

	Page
List of Tables	ix
List of Figures.	xii
List of Appendices.	xxix
Chapter	
1 Introduction.	1
2 Theory	3
2.1 The Standard Model	3
2.1.1 Particles	3
2.1.1.1 Fermions	4
2.1.1.2 Bosons	5
2.1.2 Interactions	6
2.1.2.1 Quantum Electrodynamics	6
2.1.2.2 Electroweak Interaction	6
2.1.2.3 Quantum Chromodynamics	7
2.1.3 The Higgs Mechanism	8
2.2 Supersymmetry.	11
2.2.1 Minimal Supersymmetric Standard Model Particles	12
2.2.2 2 Higgs Doublet Model	14
2.3 Charged Higgs Bosons	15
2.3.1 Previous Result	17

Chapter	Page
3 Experimental Apparatus	22
3.1 Particle Accelerators	22
3.1.1 Hadron Colliders.	22
3.1.2 The Large Hadron Collider	23
3.1.3 CERN Accelerator Complex	24
3.1.4 Luminosity.	26
3.2 The ATLAS Detector	30
3.2.1 Detector Coordinates	31
3.2.2 Magnet Systems	32
3.2.2.1 Solenoid System	33
3.2.2.2 Toroid System.	33
3.2.3 Inner Detector	34
3.2.3.1 Pixel	35
3.2.3.2 Semiconductor Tracker.	36
3.2.3.3 Transition Radiation Tracker	36
3.2.4 Calorimeters.	37
3.2.4.1 Liquid Argon Calorimeters.	38
3.2.4.2 Tile Calorimeter	41
3.2.5 Muon Spectrometer	42
3.2.6 Trigger System	43
4 Simulation	46
4.1 Event Generation and Hadronization	46
4.2 Detector Simulation	48

Chapter	Page
5 Event Reconstruction	50
5.1 Tracks	51
5.2 Topological Clusters	51
5.3 Muon Identification	52
5.4 e- γ Identification	54
5.5 Jets	56
5.5.1 b -jet Tagging	59
5.6 τ Identification	60
5.7 E_T^{miss}	61
6 Search for Charged Higgs Bosons	63
6.1 Signature and Event Selection	64
6.1.1 Object Definitions	64
6.1.2 Event Selections	67
6.2 Datasets	68
6.2.1 Signal Modeling	69
6.3 Background Modeling	70
6.4 Multivariate Analysis Techniques	83
6.4.1 Training	84
6.4.2 Input Variables Selection	86
6.4.3 Hyperparameter Optimization	87
6.5 Systematic Uncertainties	94
6.6 Expected Results	97
7 Conclusion	108
Appendices	109

Chapter	Page
Acronyms	207
Bibliography	221

LIST OF TABLES

Table	Page
2.1 Standard Model fermions and their properties [2].	5
2.2 Standard Model bosons and their properties [2]	6
2.3 Standard Model fermions and their Electroweak properties [2].	7
2.4 The Higgs boson's properties [2].	10
2.5 SM particles and their MSSM partners [2].	13
2.6 2HDM extended Higgs sector [8].	14
3.1 LHC parameters [17].	24
3.2 Accelerator final energies [16].	25
3.3 Design resolution of EM and hadronic calorimeters in the ATLAS Detector [32, 26].	38
4.1 MC generators for the main SM background samples at $\sqrt{s} = 13$ TeV used in this dissertation. Here, ℓ refers to the three lepton families e , μ and τ	48
6.1 H^\pm production mechanisms based on m_{H^\pm} , dominant H^\pm decay mode, and the main backgrounds associated with the diagram.	65
6.2 Definitions of physics objects used in this analysis.	67
6.3 $\tau + \text{jets}$ and $\tau + \ell$ signal region definitions.	68
6.4 For each H^\pm mass the generator xcross-section ($\sigma \times BR(H^\pm \rightarrow \tau^\pm \nu_\tau)$) is given, as well as the number of generated events for both $\tau + \ell$ and $\tau + \text{jets}$ subchannels.	70
6.5 Dominant backgrounds from prompt $\tau_{had-vis}$ and fake $\tau_{had-vis}$ candidates.	71

Table	Page
6.6 Cross sections for the main SM background samples at $\sqrt{s} = 13$ TeV . Here, ℓ refers to the three lepton families e , μ and τ . All background cross sections are normalized to NNLO predictions, except for diboson events, where the NLO prediction is used. A '*' indicates that the quoted cross section for the sample is neglecting leptonic/hadronic branching ratios.	71
6.7 Control region definitions for the $\tau+\text{jets}$ subchannel.	72
6.8 Control region definitions for the $\tau + \ell$ subchannel.	72
6.9 Expected event yields and efficiencies after cumulative selection cuts and comparison with 139 fb^{-1} of data for $\tau+\text{jets}$ sub-channel. The values shown for the signal correspond to $\sigma(pp \rightarrow [b]tH^\pm) \times Br(H^\pm \rightarrow \tau^\pm \nu_\tau) = 1\text{ pb}$. Statistical uncertainties are shown.	76
6.10 Expected event yields and efficiencies after cumulative selection cuts and comparison with 139 fb^{-1} of data for $\tau+e$ channel. The values shown for the signal correspond to $\sigma(pp \rightarrow [b]tH^\pm) \times Br(H^\pm \rightarrow \tau^\pm \nu_\tau) = 1\text{ pb}$. Statistical uncertainties are shown.	80
6.11 Expected event yields and efficiencies after cumulative selection cuts and comparison with 139 fb^{-1} of data for $\tau+\mu$ channel. The values shown for the signal correspond to $\sigma(pp \rightarrow [b]tH^\pm) \times Br(H^\pm \rightarrow \tau^\pm \nu_\tau) = 1\text{ pb}$. Statistical uncertainties are shown.	82
6.12 Two sets of kinematic variables used as input to the PNN in the $\tau + \ell$ subchannel. $\Delta\phi_{X,\text{miss}}$ denotes the difference in azimuthal angle between a reconstructed object X ($X = \tau$, b -jet, ℓ) and the direction of the missing transverse momentum. Distributions of all variables can be seen in Appendix C.	88
6.13 First grid, scanning over activation function and loss function. Binary cross-entropy was the chosen loss function, highlighted in red.	90
6.14 Second grid, scanning over width, depth, and dropout value. 0.1 was chosen for the dropout value, highlighted in red.	90
6.15 Third grid, scanning over activation function. LeakyReLU was chosen, highlighted in red.	90
6.16 Fourth grid, scanning over LeakyReLU α value. $\alpha = 0.05$ was chosen, highlighted in red.	91

Table	Page
6.17 Fifth grid, scanning over network width and depth. $width = 128$ and $depth = 3$ was chosen, highlighted in red.	91
6.18 AUCs of final HPO grid. An error of 0 corresponds to only one job k-fold finishing training due to computational limits. The LowMassAvg error takes into account difference between k-folds and the associated error from the averaging calculation.	92
6.19 Average AUCs of final HPO grid. An error of 0 corresponds to only one job k-fold finishing training due to computational limits.	92
6.20 Effect of the main systematic uncertainties on the expected event yield for $t\bar{t}$ and signal events ($m_{H^\pm} = 200$ GeV) passing the nominal event selection of the three SRs. The three components of the $\tau_{had-vis}$ energy scale uncertainty are shown in the table. Impacts are shown in percent change with respect to the nominal SR selections.	95
6.21 Effect on the shape variation and the yields of systematic uncertainties associated with the data-driven fake factor method, used to estimate the $j \rightarrow \tau$ background in the $\tau+jets$ and $\tau + \ell$ channel.	96
6.22 Effect of the combined main systematic uncertainties on the expected event yield for $t\bar{t}$ and signal events ($m_{H^\pm} = 200$ GeV) passing the nominal event selection of the three SRs. The three components of the $\tau_{had-vis}$ energy scale uncertainty are shown in the table. Impacts are shown in percent change with respect to the nominal SR selections.	96
6.23 Expected event yields for the backgrounds and a hypothetical H^\pm signal after applying all $\tau+jets$ selection criteria, and comparison with 139 fb^{-1} of data. The values shown for the signal assuming a charged Higgs boson mass of 170 GeV and 1000 GeV, with a cross-section times branching fraction $\sigma(pp \rightarrow tbH^\pm) \times \mathcal{B}(H^\pm \rightarrow \tau\nu)$ corresponding to $\tan\beta = 40$ in the hMSSM benchmark scenario. Statistical and systematic uncertainties are quoted, respectively.	97
6.24 Expected event yields for the backgrounds and a hypothetical H^\pm signal after applying all $\tau + \ell$ selection criteria, and comparison with 139 fb^{-1} of data. The values shown for the signal assuming a charged Higgs boson mass of 170 GeV and 1000 GeV, with a cross-section times branching fraction $\sigma(pp \rightarrow tbH^\pm) \times \mathcal{B}(H^\pm \rightarrow \tau\nu)$ corresponding to $\tan\beta = 40$ in the hMSSM benchmark scenario. Statistical and systematic uncertainties are quoted, respectively.	98

LIST OF FIGURES

Figure	Page
2.1 Quarks are fundamental particles that combine to create hadrons (protons, neutrons, $\pi^{0,\pm}$, etc.) [1]	4
2.2 The Higgs potential defined in Equation 2.2 with $\mu^2 < 0$ [5]	9
2.3 The distributions of the invariant mass of diphoton candidates after all selections for the combined 7 TeV and 8 TeV data sample. The result of a fit to the data of the sum of a signal component fixed to $m_H = 126.5$ GeV and a background component described by a fourth-order Bernstein polynomial is superimposed. Taken from [6].	11
2.4 Examples of leading-order Feynman diagrams contributing to the production of charged Higgs bosons in pp collisions: (a) non-resonant top-quark production prevalent in the intermediate-mass range, (b) single-resonant top-quark production that dominates at large H^\pm masses, (c) double-resonant top-quark production that dominates at low H^\pm masses. The interference between these three diagrams becomes most relevant in the intermediate-mass region.	15
2.5 Variation of $\sigma(pp \rightarrow tbH^\pm) \times B(H^\pm \rightarrow \tau^\pm \nu_\tau)$ with the charged Higgs boson mass in pp collisions at $\sqrt{s} = 13$ TeV , for $\tan\beta$ values of 7, 20, and 40 in the hMSSM scenario. Dashed lines correspond to $B(H^\pm \rightarrow \tau^\pm \nu_\tau)$ set to 1, hence they show the dependence of $\sigma(pp \rightarrow tbH^\pm)$ with m_{H^\pm} . Taken from Reference [10].	16
2.6 Branching fractions of H^\pm as a function of m_{H^\pm} for (a) $\tan\beta = 10$ and (b) $\tan\beta = 50$ in the m_h^{mod+} scenario of the MSSM [11].	17
2.7 Exclusion limits at 95% CL on $\sigma(pp \rightarrow tbH^\pm \times B(H^\pm \rightarrow \tau^\pm \nu))$ [pb]. Top left (a) shows the $\tau+jets$ subchannel, top right (b) corresponds to the $\tau + \ell$ subchannel and bottom (c) shows the combination of the two subchannels. Taken from Reference [10].	18
2.8 Exclusion limits at 95% CL on $\tan\beta$ as a function of m_{H^\pm} [10].	19
2.9 (a) Exclusion limits at 95% CL on $\sigma_{H^\pm} B(H^\pm \rightarrow \tau^\pm \nu_\tau)$ [pb] from the CMS collaboration [14]. (b) Exclusion limits at 95% CL on $\tan\beta$ and m_{H^\pm} [14].	20

Figure	Page
2.10 Exclusion limits at 95% CL on $\sigma(pp \rightarrow tbH^\pm) \times B(H^\pm \rightarrow tb)$ as a function of m_{H^\pm} [15].	20
2.11 Exclusion limits at 95% CL on $\tan\beta$ as a function of m_{H^\pm} in the (a) MSSM and (b) m_h^{mod+} scenario of the MSSM [15].	21
3.1 Cross-section of cryodipole (lengths in mm) [16].	25
3.2 Field of the LHC dipole magnets [18].	26
3.3 The CERN accelerator complex [19].	27
3.4 Cumulative luminosity versus time delivered to ATLAS (green), recorded by ATLAS (yellow), and certified to be good quality data (blue) during stable beams for pp collisions at 13 TeV center of mass energy in 2015-2018. The difference between the colored histograms reflects inefficiencies, especially those seen when restarting data taking [20].	28
3.5 The luminosity-weighted distribution of the mean number of interactions per bunch crossing for the 2015-2018 pp collision dataset at 13 TeV center of mass energy [20].	28
3.6 A display of a candidate Z boson event from proton-proton collisions recorded by ATLAS with LHC stable beams at a collision energy of 13 TeV. The Z boson candidate is reconstructed in a beam crossing with 28 additionally reconstructed primary vertices from the minimum bias interactions. The candidate event is reconstructed in the 2μ final state. In the left display, the red lines show the path of the two muons including the hits in the muon spectrometer and the orange tracks are the remaining charged particles from the 29 vertices, with transverse momentum above 0.5 GeV. The colored squares in the lower display correspond to the position of the reconstructed vertices. The invariant mass of the two muons is 92.3 GeV [21].	29
3.7 Cut-away view of the ATLAS detector with major subdetectors highlighted [23].	30
3.8 A diagram showing the pseudorapidity η and corresponding θ values [24]. . .	32
3.9 The ATLAS magnet systems [23].	32
3.10 (a) Cut-away view of the ATLAS Inner Detector. (b) Cross-sectional view of the ATLAS Inner Detector. Taken from Reference [23].	34

Figure	Page
3.11 Interaction lengths as a function of η in the ATLAS calorimeters. The unlabeled brown color is the material in front of the EM calorimeters and the unlabeled cyan is the amount of material in front of the first active layer of the muon spectrometer [33].	38
3.12 Cut-out view of the ATLAS detector's calorimeters [23].	39
3.13 An EMB module showing the accordion geometry and granularity [32].	40
3.14 (a) Diagram of an individual TileCal module. (b) Azimuthal view of two TileCal modules with the IP being to the right. Taken from Reference [26].	41
3.15 Cut-out view of the ATLAS detector Muon Spectrometer [23].	43
3.16 The ATLAS TDAQ system in Run-2 showing the components relevant for triggering as well as the detector read-out and data flow [36].	45
 4.1 A pictorial representation of the simulation chain used in the ATLAS experiment [37].	47
4.2 A pictorial representation of a parton shower of a $t\bar{t}H$ event [37].	49
 5.1 Cross section view of the ATLAS detector with subdetectors labeled. Various types of particles radial trajectories are shown [33].	50
5.2 Algorithm flow diagram for the electron and photon reconstruction [49].	55
5.3 A flow chart of how the particle flow algorithm proceeds, starting with track selection and continuing until the energy associated with the selected tracks has been removed from the calorimeter. At the end, charged particles, topoclusters which have not been modified by the algorithm, and remnants of topoclusters which have had part of their energy removed remain [50].	56
5.4 Idealized examples of how the algorithm is designed to deal with several different cases. The red cells are those which have energy from the π^+ , the green have cells energy from the photons in the π^0 decay, the dotted lines represent the original topocluster boundaries with those outlined in blue having been matched by the algorithm to the π^+ , while those in black are yet to be selected. The different layers in the EM calorimeter (Presampler, EMB1, EMB2, EMB3) are indicated. In this sketch only the first two layers of the Tile calorimeter are shown (TileBar0 and TileBar1) [50].	57
5.5 Comparison between several jet-finding algorithms [51].	59

Figure	Page
5.6 Stages of jet energy scale calibrations. Each one is applied to the four-momentum of the jet. Taken from Reference [53].	59
5.7 Schematic view of the tracks in a b -jet [54].	60
6.1 The electron identification efficiency in $Z \rightarrow ee$ events in data as a function of E_T for the Loose, Medium, and Tight operating points. The efficiencies are obtained by applying data-to-simulation efficiency ratios measured in $J/\Psi \rightarrow ee$ and $Z \rightarrow ee$ events to $Z \rightarrow ee$ simulation. The inner uncertainties are statistical and the total uncertainties are the statistical and systematic uncertainties in the data-to-simulation efficiency ratio added in quadrature. The bottom panel shows the data-to-simulation ratio. Taken from Reference [49].	66
6.2 Signal acceptance as a function of the charged Higgs boson mass for both the $\tau + \text{jets}$ (a) and $\tau + \ell$ subchannels (b). Statistical errors are shown but are negligible.	69
6.3 Mass of $\tau - e$ system in the Zee control region. All systematics except for $t\bar{t}$ theory uncertainties are included.	73
6.4 Combined FF for the $\tau + \text{jets}$ b-veto $m_T > 100$ control region, $\tau + \text{jets}$ signal region, $\tau + \text{electron(muon)}$ with same-sign control region and the $\tau + \ell$ signal region. Error bars represent systematic uncertainties of the method.	75
6.5 Comparison between the predicted and the measured E_T^{miss} distributions in various control regions defined for the $\tau + \text{jets}$ channel. The uncertainty band includes both statistical and systematic uncertainties on the background prediction.	77
6.6 Comparison between the predicted and the measured τp_T distributions in various control regions defined for the $\tau + \text{jets}$ channel. The uncertainty band includes both statistical and systematic uncertainties on the background prediction.	78
6.7 Comparison between the predicted and the measured E_T^{miss} distributions in various control regions defined for the $\tau + \ell$ channel. The uncertainty band includes both statistical and systematic uncertainties on the background prediction.	79

Figure	Page
6.8 Comparison between the predicted and the measured E_T^{miss} distributions in various control regions defined for the $\tau + \ell$ channel. The uncertainty band includes both statistical and systematic uncertainties on the background prediction	80
6.9 Comparison between the predicted and the measured τp_T distributions in various control regions defined for the $\tau + \ell$ channel. The uncertainty band includes both statistical and systematic uncertainties on the background prediction	81
6.10 Comparison between the predicted and the measured τp_T distributions in various control regions defined for the $\tau + \ell$ channel. The uncertainty band includes both statistical and systematic uncertainties on the background prediction	82
6.11 Comparison of performance of an optimized BDT and an unoptimized PNN on expected limits on $\sigma(pp \rightarrow tbH^\pm) \times \mathcal{B}(H^\pm \rightarrow \tau\nu)$ in the $\tau+\text{jets}$ (a) and $\tau + \ell$ (b) signal regions.	84
6.12 <i>Left</i> , individual networks with input variables (x_1, x_2) , each trained with examples with a single value of some parameter $\theta = \theta_a, \theta_b$. The individual networks are purely functions of the input variables. Performance for intermediate values of θ is not optimal nor does it necessarily vary smoothly between the networks. <i>Right</i> , a single network trained with input variables (x_1, x_2) as well as input parameter θ ; such a network is trained with examples at several values of the parameter θ [68].	85
6.13 The k-fold method for $k = 5$ [72].	85
6.14 Expected limits comparing input variables set A and B with various depths in the PNN architecture. X layers refers to the number of layers in the PNN.	89
6.15 Final model AUC for each mass point. Individual points correspond to the AUC average over 5 kfolds.	93
6.16 LeakyReLU activation function. The associated hyperparameter α is the slope of the negative portion of the function.	94
6.17 PNN score distributions in the signal region of the $\tau+\text{jets}$ channel, for chosen charged Higgs boson mass parameters. The lower panel of each plot shows the ratio of data to the SM background prediction. The uncertainty bands include all statistical and systematic uncertainties. The normalization of the signal (shown for illustration) corresponds to the integral of the background.	101

Figure	Page
6.18 PNN score distributions in the signal region of the $\tau+\text{jets}$ channel, for chosen charged Higgs boson mass parameters. The lower panel of each plot shows the ratio of data to the SM background prediction. The uncertainty bands include all statistical and systematic uncertainties. The normalization of the signal (shown for illustration) corresponds to the integral of the background.	102
6.19 PNN score distributions in the signal region of the $\tau+e$ sub-channel, for the chosen charged Higgs boson mass parameters. The lower panel of each plot shows the ratio of data to the SM background prediction. The uncertainty bands include all statistical and systematic uncertainties. The normalization of the signal (shown for illustration) corresponds to the integral of the background.	103
6.20 PNN score distributions in the signal region of the $\tau+e$ sub-channel, for the chosen charged Higgs boson mass parameters. The lower panel of each plot shows the ratio of data to the SM background prediction. The uncertainty bands include all statistical and systematic uncertainties. The normalization of the signal (shown for illustration) corresponds to the integral of the background.	104
6.21 PNN score distributions in the signal region of the $\tau+\mu$ sub-channel, for the chosen charged Higgs boson mass parameters. The lower panel of each plot shows the ratio of data to the SM background prediction. The uncertainty bands include all statistical and systematic uncertainties. The normalization of the signal (shown for illustration) corresponds to the integral of the background.	105
6.22 PNN score distributions in the signal region of the $\tau+\mu$ sub-channel, for the chosen charged Higgs boson mass parameters. The lower panel of each plot shows the ratio of data to the SM background prediction. The uncertainty bands include all statistical and systematic uncertainties. The normalization of the signal (shown for illustration) corresponds to the integral of the background.	106
6.23 Expected 95% CL exclusion limits on $\sigma(pp \rightarrow tbH^\pm) \times \mathcal{B}(H^\pm \rightarrow \tau\nu)$ as a function of the charged Higgs boson mass in 139 fb^{-1} of pp collision data at $\sqrt{s} = 13\text{ TeV}$ in the $\tau+e$ signal region (a), the $\tau+\mu$ signal region (b), and the $\tau+\text{jets}$ signal region (c). In the case of the expected limits, one- and two-standard-deviation uncertainty bands are also shown. As a comparison, the expected exclusion limits obtained with the dataset collected in 2015 and 2016 [10] are also shown.	107

Figure	Page
A.1 TileCal calibration checks within the readout chain [26]	112
A.2 Average response variation from the beginning of Run-2 of TileCal cell A13 is shown [78].	113
A.3 Schematic diagram illustrating the nominal Run-2 operations workflow for the data quality assessment of ATLAS data. Online histogram sources include the high-level trigger farm, the data acquisition system, and full reconstruction of a fraction of events accepted by the trigger [79].	114
A.4 Evolution of masked TileCal cells during Run-2 [78].	115
A.5 Cumulative integrated luminosity delivered to and recorded by ATLAS be- tween 2015 and 2018 during stable beam pp collision data-taking at $\sqrt{s} = 13$ TeV . This includes machine commissioning periods, special runs for detector calibration, and LHC fills with a low number of circulating bunches or bunch spacing greater than 25 ns. Also shown is the cumulative integrated luminos- ity certified for physics analysis usage for the ATLAS experiment between 2015 and 2018 during standard pp collision data-taking at $\sqrt{s} = 13$ TeV . The total integrated luminosity recorded for the standard $\sqrt{s} = 13$ TeV pp collision dataset corresponds to 145 fb^{-1} . It is this number that is used in the denominator when calculating the data quality efficiency of the standard $\sqrt{s} = 13$ TeV pp collision dataset [79].	116
A.6 Cumulative data quality efficiency versus total integrated luminosity delivered to the ATLAS experiment between 2015 and 2018 [79].	117
A.7 Luminosity-weighted data quality inefficiencies (in %) during stable beams in standard pp collision physics runs at $\sqrt{s} = 13$ TeV between 2015 and 2018. Taken from Reference [79].	117
B.1 Fake factors parameterized as a function of p_T^τ and the number of charged τ decay products (1-prong and 3-prong) obtained in the multi-jet and W+jets CRs. The errors shown represent the statistical uncertainty.	119
B.2 Corrected α_{MJ} values for the $\tau_{\text{had-vis}} + \text{jets}$ b-veto $m_T > 100$ control region, $\tau_{\text{had-vis}} + \text{jets}$ signal region, $\tau_{\text{had-vis}} + \text{electron(muon)}$ with same-sign con- trol region and the $\tau_{\text{had-vis}} + \text{lepton}$ signal region. Error bars represent uncertainties due to α_{MJ} fitting using template-fit method.	119

Figure	Page
B.3 Estimation of α_{MJ} in the $\tau_{had-vis} + \text{jets}$ signal region for $p_T \leq 60 \text{ GeV}$ 1-prong $\tau_{had-vis}$ candidates. Left: templates of discriminating variables for different $\tau_{had-vis} p_T$ and n-prong slices. Middle: shape of the discriminating variable obtained in the signal region and fitted shape using the templates measured in the control regions. Right: χ^2/ndf of the fit as a function of α_{MJ} , the error on α_{MJ} is defined by the band at $\chi^2_{\min}/\text{ndf} + \sqrt{\frac{2}{\text{ndf}}}$.	120
B.4 Estimation of α_{MJ} in the $\tau_{had-vis} + \text{jets}$ signal region for $p_T \geq 60 \text{ GeV}$ 1-prong $\tau_{had-vis}$ candidates. Left: templates of discriminating variables for different $\tau_{had-vis} p_T$ and n-prong slices. Middle: shape of the discriminating variable obtained in the signal region and fitted shape using the templates measured in the control regions. Right: χ^2/ndf of the fit as a function of α_{MJ} , the error on α_{MJ} is defined by the band at $\chi^2_{\min}/\text{ndf} + \sqrt{\frac{2}{\text{ndf}}}$.	121
B.5 Estimation of α_{MJ} in the $\tau_{had-vis} + \text{jets}$ signal region for 3-prong $\tau_{had-vis}$ candidates. Left: templates of discriminating variables for different $\tau_{had-vis} p_T$ and n-prong slices. Middle: shape of the discriminating variable obtained in the signal region and fitted shape using the templates measured in the control regions. Right: χ^2/ndf of the fit as a function of α_{MJ} , the error on α_{MJ} is defined by the band at $\chi^2_{\min}/\text{ndf} + \sqrt{\frac{2}{\text{ndf}}}$.	122
B.6 Estimation of α_{MJ} in the $\tau_{had-vis} + \text{lepton}$ signal region for $p_T \leq 50 \text{ GeV}$ 1-prong $\tau_{had-vis}$ candidates. Left: templates of discriminating variables for different $\tau_{had-vis} p_T$ and n-prong slices. Middle: shape of the discriminating variable obtained in the signal region and fitted shape using the templates measured in the control regions. Right: χ^2/ndf of the fit as a function of α_{MJ} , the error on α_{MJ} is defined by the band at $\chi^2_{\min}/\text{ndf} + \sqrt{\frac{2}{\text{ndf}}}$.	123
B.7 Estimation of α_{MJ} in the $\tau_{had-vis} + \text{lepton}$ signal region for $p_T \geq 50 \text{ GeV}$ 1-prong $\tau_{had-vis}$ candidates. Left: templates of discriminating variables for different $\tau_{had-vis} p_T$ and n-prong slices. Middle: shape of the discriminating variable obtained in the signal region and fitted shape using the templates measured in the control regions. Right: χ^2/ndf of the fit as a function of α_{MJ} , the error on α_{MJ} is defined by the band at $\chi^2_{\min}/\text{ndf} + \sqrt{\frac{2}{\text{ndf}}}$.	124

Figure	Page
B.8 Estimation of α_{MJ} in the $\tau_{\text{had-vis}} + \text{lepton}$ signal region for $p_T \leq 60\text{GeV}$ 3-prong $\tau_{\text{had-vis}}$ candidates. Left: templates of discriminating variables for different $\tau_{\text{had-vis}}$ p_T and n-prong slices. Middle: shape of the discriminating variable obtained in the signal region and fitted shape using the templates measured in the control regions. Right: χ^2/ndf of the fit as a function of α_{MJ} , the error on α_{MJ} is defined by the band at $\chi^2_{\min}/\text{ndf} + \sqrt{\frac{2}{\text{ndf}}}$	125
B.9 Estimation of α_{MJ} in the $\tau_{\text{had-vis}} + \text{lepton}$ signal region for $p_T \geq 60\text{GeV}$ 3-prong $\tau_{\text{had-vis}}$ candidates. Left: templates of discriminating variables for different $\tau_{\text{had-vis}}$ p_T and n-prong slices. Middle: shape of the discriminating variable obtained in the signal region and fitted shape using the templates measured in the control regions. Right: χ^2/ndf of the fit as a function of α_{MJ} , the error on α_{MJ} is defined by the band at $\chi^2_{\min}/\text{ndf} + \sqrt{\frac{2}{\text{ndf}}}$	126
C.1 Comparison between the predicted and the measured p_T^τ distributions in various control regions defined for the $\tau + \text{jets}$ channel. The uncertainty band includes both statistical and systematic uncertainties on the background prediction.	129
C.2 Comparison between the predicted and the measured p_T^{b-jet} distributions in various control regions defined for the $\tau + \text{jets}$ channel. The uncertainty band includes both statistical and systematic uncertainties on the background prediction.	130
C.3 Comparison between the predicted and the measured η^τ distributions in various control regions defined for the $\tau + \text{jets}$ channel. The uncertainty band includes both statistical and systematic uncertainties on the background prediction.	131
C.4 Comparison between the predicted and the measured η^{b-jet} distributions in various control regions defined for the $\tau + \text{jets}$ channel. The uncertainty band includes both statistical and systematic uncertainties on the background prediction.	132
C.5 Comparison between the predicted and the measured ϕ^τ distributions in various control regions defined for the $\tau + \text{jets}$ channel. The uncertainty band includes both statistical and systematic uncertainties on the background prediction.	133

Figure	Page
C.6 Comparison between the predicted and the measured ϕ^{b-jet} distributions in various control regions defined for the $\tau+jets$ channel. The uncertainty band includes both statistical and systematic uncertainties on the background prediction	134
C.7 Comparison between the predicted and the measured E_T^{miss} distributions in various control regions defined for the $\tau+jets$ channel. The uncertainty band includes both statistical and systematic uncertainties on the background prediction	135
C.8 Comparison between the predicted and the measured ϕ_T^{miss} distributions in various control regions defined for the $\tau+jets$ channel. The uncertainty band includes both statistical and systematic uncertainties on the background prediction	136
C.9 Comparison between the predicted and the measured Υ_τ distributions in various control regions defined for the $\tau+jets$ channel. The uncertainty band includes both statistical and systematic uncertainties on the background prediction	137
C.10 Comparison between the predicted and the measured p_T^τ distributions in various control regions defined for the $\tau + \ell$ channel. The uncertainty band includes both statistical and systematic uncertainties on the background prediction	139
C.11 Comparison between the predicted and the measured η^τ distributions in various control regions defined for the $\tau + \ell$ channel. The uncertainty band includes both statistical and systematic uncertainties on the background prediction	140
C.12 Comparison between the predicted and the measured ϕ^τ distributions in various control regions defined for the $\tau + \ell$ channel. The uncertainty band includes both statistical and systematic uncertainties on the background prediction	141
C.13 Comparison between the predicted and the measured p_T^ℓ distributions in various control regions defined for the $\tau + \ell$ channel. The uncertainty band includes both statistical and systematic uncertainties on the background prediction	142

Figure	Page
C.14 Comparison between the predicted and the measured η^ℓ distributions in various control regions defined for the $\tau + \ell$ channel. The uncertainty band includes both statistical and systematic uncertainties on the background prediction	143
C.15 Comparison between the predicted and the measured ϕ^ℓ distributions in various control regions defined for the $\tau + \ell$ channel. The uncertainty band includes both statistical and systematic uncertainties on the background prediction	144
C.16 Comparison between the predicted and the measured p_T^e distributions in various control regions defined for the $\tau + \ell$ channel. The uncertainty band includes both statistical and systematic uncertainties on the background prediction	145
C.17 Comparison between the predicted and the measured η^e distributions in various control regions defined for the $\tau + \ell$ channel. The uncertainty band includes both statistical and systematic uncertainties on the background prediction	146
C.18 Comparison between the predicted and the measured ϕ^e distributions in various control regions defined for the $\tau + \ell$ channel. The uncertainty band includes both statistical and systematic uncertainties on the background prediction	147
C.19 Comparison between the predicted and the measured p_T^μ distributions in various control regions defined for the $\tau + \ell$ channel. The uncertainty band includes both statistical and systematic uncertainties on the background prediction	148
C.20 Comparison between the predicted and the measured η^μ distributions in various control regions defined for the $\tau + \ell$ channel. The uncertainty band includes both statistical and systematic uncertainties on the background prediction	149
C.21 Comparison between the predicted and the measured ϕ^μ distributions in various control regions defined for the $\tau + \ell$ channel. The uncertainty band includes both statistical and systematic uncertainties on the background prediction	150

Figure	Page
C.22 Comparison between the predicted and the measured p_T^{b-jet} distributions in various control regions defined for the $\tau + \ell$ channel. The uncertainty band includes both statistical and systematic uncertainties on the background prediction	151
C.23 Comparison between the predicted and the measured η^{b-jet} distributions in various control regions defined for the $\tau + \ell$ channel. The uncertainty band includes both statistical and systematic uncertainties on the background prediction	152
C.24 Comparison between the predicted and the measured ϕ^{b-jet} distributions in various control regions defined for the $\tau + \ell$ channel. The uncertainty band includes both statistical and systematic uncertainties on the background prediction	153
C.25 Comparison between the predicted and the measured E_T^{miss} distributions in various control regions defined for the $\tau + \ell$ channel. The uncertainty band includes both statistical and systematic uncertainties on the background prediction	154
C.26 Comparison between the predicted and the measured $\phi_{E_T^{\text{miss}}}$ distributions in various control regions defined for the $\tau + \ell$ channel. The uncertainty band includes both statistical and systematic uncertainties on the background prediction	155
C.27 PNN input variable distributions in $\tau+\text{jets}$ signal region. The uncertainty band includes both statistical and systematic uncertainties on the background prediction	157
C.28 PNN input variable distributions in $\tau+\text{jets}$ signal region. The uncertainty band includes both statistical and systematic uncertainties on the background prediction	158
C.29 PNN input variable distributions in $\tau+\text{jets}$ signal region. The uncertainty band includes both statistical and systematic uncertainties on the background prediction	159
C.30 PNN input variable distributions in $\tau + \ell$ signal region. The uncertainty band includes both statistical and systematic uncertainties on the background prediction	161

Figure	Page
C.31 PNN input variable distributions in $\tau + \ell$ signal region. The uncertainty band includes both statistical and systematic uncertainties on the background prediction.	162
C.32 PNN input variable distributions in $\tau + \ell$ signal region. The uncertainty band includes both statistical and systematic uncertainties on the background prediction.	163
C.33 PNN input variable distributions in $\tau + \ell$ signal region. The uncertainty band includes both statistical and systematic uncertainties on the background prediction.	164
D.1 PNN score distributions in the signal region of the $\tau+\text{jets}$ channel, for the chosen charged Higgs boson mass parameters. The uncertainty bands include all statistical and systematic uncertainties. The normalization of the signal (shown for illustration) corresponds to the integral of the background.	167
D.2 PNN score distributions in the signal region of the $\tau+\text{jets}$ channel, for the chosen charged Higgs boson mass parameters. The uncertainty bands include all statistical and systematic uncertainties. The normalization of the signal (shown for illustration) corresponds to the integral of the background.	168
D.3 PNN score distributions in the signal region of the $\tau+\text{jets}$ channel, for the chosen charged Higgs boson mass parameters. The uncertainty bands include all statistical and systematic uncertainties. The normalization of the signal (shown for illustration) corresponds to the integral of the background.	169
D.4 PNN score distributions in the signal region of the $\tau+\text{jets}$ channel, for the chosen charged Higgs boson mass parameters. The uncertainty bands include all statistical and systematic uncertainties. The normalization of the signal (shown for illustration) corresponds to the integral of the background.	170
D.5 PNN score distributions in the signal region of the $\tau+\text{jets}$ channel, for the chosen charged Higgs boson mass parameters. The uncertainty bands include all statistical and systematic uncertainties. The normalization of the signal (shown for illustration) corresponds to the integral of the background.	171
D.6 PNN score distributions in the signal region of the $\tau+\text{jets}$ channel, for the chosen charged Higgs boson mass parameters. The uncertainty bands include all statistical and systematic uncertainties. The normalization of the signal (shown for illustration) corresponds to the integral of the background.	172

Figure	Page
D.7 PNN score distributions in the signal region of the $\tau + \text{jets}$ channel, for the chosen charged Higgs boson mass parameters. The uncertainty bands include all statistical and systematic uncertainties. The normalization of the signal (shown for illustration) corresponds to the integral of the background.	173
D.8 PNN score distributions in the signal region of the $\tau + \text{jets}$ channel, for the chosen charged Higgs boson mass parameters. The uncertainty bands include all statistical and systematic uncertainties. The normalization of the signal (shown for illustration) corresponds to the integral of the background.	174
D.9 PNN score distributions in the signal region of the $\tau + \text{jets}$ channel, for the chosen charged Higgs boson mass parameters. The uncertainty bands include all statistical and systematic uncertainties. The normalization of the signal (shown for illustration) corresponds to the integral of the background.	175
D.10 PNN score distributions in the signal region of the $\tau + \ell$ channel, for the chosen charged Higgs boson mass parameters. The uncertainty bands include all statistical and systematic uncertainties. The normalization of the signal (shown for illustration) corresponds to the integral of the background.	177
D.11 PNN score distributions in the signal region of the $\tau + \ell$ channel, for the chosen charged Higgs boson mass parameters. The uncertainty bands include all statistical and systematic uncertainties. The normalization of the signal (shown for illustration) corresponds to the integral of the background.	178
D.12 PNN score distributions in the signal region of the $\tau + \ell$ channel, for the chosen charged Higgs boson mass parameters. The uncertainty bands include all statistical and systematic uncertainties. The normalization of the signal (shown for illustration) corresponds to the integral of the background.	179
D.13 PNN score distributions in the signal region of the $\tau + \ell$ channel, for the chosen charged Higgs boson mass parameters. The uncertainty bands include all statistical and systematic uncertainties. The normalization of the signal (shown for illustration) corresponds to the integral of the background.	180
D.14 PNN score distributions in the signal region of the $\tau + \ell$ channel, for the chosen charged Higgs boson mass parameters. The uncertainty bands include all statistical and systematic uncertainties. The normalization of the signal (shown for illustration) corresponds to the integral of the background.	181

Figure	Page
D.15 PNN score distributions in the signal region of the $\tau + \ell$ channel, for the chosen charged Higgs boson mass parameters. The uncertainty bands include all statistical and systematic uncertainties. The normalization of the signal (shown for illustration) corresponds to the integral of the background.	182
D.16 PNN score distributions in the signal region of the $\tau + \ell$ channel, for the chosen charged Higgs boson mass parameters. The uncertainty bands include all statistical and systematic uncertainties. The normalization of the signal (shown for illustration) corresponds to the integral of the background.	183
D.17 PNN score distributions in the signal region of the $\tau + \ell$ channel, for the chosen charged Higgs boson mass parameters. The uncertainty bands include all statistical and systematic uncertainties. The normalization of the signal (shown for illustration) corresponds to the integral of the background.	184
D.18 PNN score distributions in the signal region of the $\tau + e$ channel, for the chosen charged Higgs boson mass parameters. The uncertainty bands include all statistical and systematic uncertainties. The normalization of the signal (shown for illustration) corresponds to the integral of the background.	186
D.19 PNN score distributions in the signal region of the $\tau + e$ channel, for the chosen charged Higgs boson mass parameters. The uncertainty bands include all statistical and systematic uncertainties. The normalization of the signal (shown for illustration) corresponds to the integral of the background.	187
D.20 PNN score distributions in the signal region of the $\tau + e$ channel, for the chosen charged Higgs boson mass parameters. The uncertainty bands include all statistical and systematic uncertainties. The normalization of the signal (shown for illustration) corresponds to the integral of the background.	188
D.21 PNN score distributions in the signal region of the $\tau + e$ channel, for the chosen charged Higgs boson mass parameters. The uncertainty bands include all statistical and systematic uncertainties. The normalization of the signal (shown for illustration) corresponds to the integral of the background.	189
D.22 PNN score distributions in the signal region of the $\tau + e$ channel, for the chosen charged Higgs boson mass parameters. The uncertainty bands include all statistical and systematic uncertainties. The normalization of the signal (shown for illustration) corresponds to the integral of the background.	190

Figure	Page
D.23 PNN score distributions in the signal region of the $\tau+e$ channel, for the chosen charged Higgs boson mass parameters. The uncertainty bands include all statistical and systematic uncertainties. The normalization of the signal (shown for illustration) corresponds to the integral of the background.	191
D.24 PNN score distributions in the signal region of the $\tau+e$ channel, for the chosen charged Higgs boson mass parameters. The uncertainty bands include all statistical and systematic uncertainties. The normalization of the signal (shown for illustration) corresponds to the integral of the background.	192
D.25 PNN score distributions in the signal region of the $\tau+e$ channel, for the chosen charged Higgs boson mass parameters. The uncertainty bands include all statistical and systematic uncertainties. The normalization of the signal (shown for illustration) corresponds to the integral of the background.	193
D.26 PNN score distributions in the signal region of the $\tau+\mu$ channel, for the chosen charged Higgs boson mass parameters. The uncertainty bands include all statistical and systematic uncertainties. The normalization of the signal (shown for illustration) corresponds to the integral of the background.	195
D.27 PNN score distributions in the signal region of the $\tau+\mu$ channel, for the chosen charged Higgs boson mass parameters. The uncertainty bands include all statistical and systematic uncertainties. The normalization of the signal (shown for illustration) corresponds to the integral of the background.	196
D.28 PNN score distributions in the signal region of the $\tau+\mu$ channel, for the chosen charged Higgs boson mass parameters. The uncertainty bands include all statistical and systematic uncertainties. The normalization of the signal (shown for illustration) corresponds to the integral of the background.	197
D.29 PNN score distributions in the signal region of the $\tau+\mu$ channel, for the chosen charged Higgs boson mass parameters. The uncertainty bands include all statistical and systematic uncertainties. The normalization of the signal (shown for illustration) corresponds to the integral of the background.	198
D.30 PNN score distributions in the signal region of the $\tau+\mu$ channel, for the chosen charged Higgs boson mass parameters. The uncertainty bands include all statistical and systematic uncertainties. The normalization of the signal (shown for illustration) corresponds to the integral of the background.	199

Figure	Page
D.31 PNN score distributions in the signal region of the $\tau+\mu$ channel, for the chosen charged Higgs boson mass parameters. The uncertainty bands include all statistical and systematic uncertainties. The normalization of the signal (shown for illustration) corresponds to the integral of the background.	200
D.32 PNN score distributions in the signal region of the $\tau+\mu$ channel, for the chosen charged Higgs boson mass parameters. The uncertainty bands include all statistical and systematic uncertainties. The normalization of the signal (shown for illustration) corresponds to the integral of the background.	201
D.33 PNN score distributions in the signal region of the $\tau+\mu$ channel, for the chosen charged Higgs boson mass parameters. The uncertainty bands include all statistical and systematic uncertainties. The normalization of the signal (shown for illustration) corresponds to the integral of the background.	202

LIST OF APPENDICES

Appendix	Page
A TileCal Data Quality	110
A.1 ATLAS Data Quality	111
A.2 Calibration Systems	111
A.3 TileCal Data Quality	113
B Fake Factors.	118
C Additional Validation Plots	127
C.1 τ +jets Background Validation Plots.	128
C.2 $\tau + \ell$ Background Validation Plots	138
C.3 τ +jets Signal Region Plots	156
C.4 $\tau + \ell$ Signal Region Plots	160
D Additional PNN Score Plots	165
D.1 τ +jets PNN Scores.	166
D.2 $\tau + \ell$ PNN Scores	176
D.3 τ +e PNN Scores	185
D.4 τ + μ PNN Scores.	194

CHAPTER 1

INTRODUCTION

Science has long sought to provide an explanation to the most fundamental questions. The field of particle physics tries to answer the question of “What are we made of?” The SM of particle physics is an attempt at combining all of the fundamental forces and particles into one mathematically based theory. The SM has been rigorously tested and for the most part, holds up except for a few key issues. To name a few of these issues: the absence of gravity in the theory, no candidate for dark matter, neutrino masses, and the matter-antimatter asymmetry of the universe.

There are many Beyond the Standard Model (BSM) theories that address these issues and more. A common theme of these models is an extended Higgs sector, meaning more Higgs boson-like particles. This dissertation focuses on a search for an additional Higgs boson that carries electromagnetic charge, H^\pm . The search is performed on data collected with the ATLAS detector on the Large Hadron Collider (LHC) at Conseil Européen pour la Recherche Nucléaire (CERN) in Geneva, Switzerland.

A theoretical motivation is given in Chapter 2 followed by a detailed explanation of the LHC and the ATLAS detector in Chapter 3. Simulation of particle collisions and the reconstruction of both simulated and actual data is detailed in Chapters 4 and 5 respectively. Chapter 6 provides a thorough description of the search for the H^\pm in the $\tau^\pm\nu_\tau$ final state. Lastly future works are discussed in Chapter 7.

A considerable amount of the author’s time in the Ph.D. program was dedicated towards the search described in this dissertation and acting as the Data Quality Co-Coordinator for the hadronic calorimeter within the ATLAS Collaboration. Some of these efforts are

described in Appendix A. In addition, the author assisted on various projects within the hadronic calorimeter group including two test beams and maintenance of the calorimeter within the larger ATLAS detector.

CHAPTER 2

THEORY

In this chapter, the theoretical motivation of a search for $H^\pm \rightarrow \tau^\pm \nu_\tau$ is described. A review of the Standard Model (SM) of particle physics is laid out, followed by a brief overview of Supersymmetry (SUSY) focusing on the Minimal Supersymmetric Standard Model (MSSM). Finally, the Type II 2-Higgs Doublet Model (2HDM) relation to the H^\pm production cross section and subsequent branching ratio into SM particles is described as motivation for the choice of studying $H^\pm \rightarrow \tau^\pm \nu_\tau$.

2.1 The Standard Model

The SM of particle physics is a Quantum Field Theory (QFT) that describes all known matter and forces¹. The SM describes forces as exchanges of particles called bosons and is described in detail in Section 2.1.2. These interactions occur between fundamental particles called fermions that comprise the known matter of the universe. Figure 2.1 shows how fermions called quarks are the building blocks of nucleons, and thus atoms.

2.1.1 Particles

The particles that make up the SM are defined by their properties, or quantum numbers. These quantum numbers are used to categorize particles into various types. Intrinsic angular

¹Notably, the SM does not describe gravity.

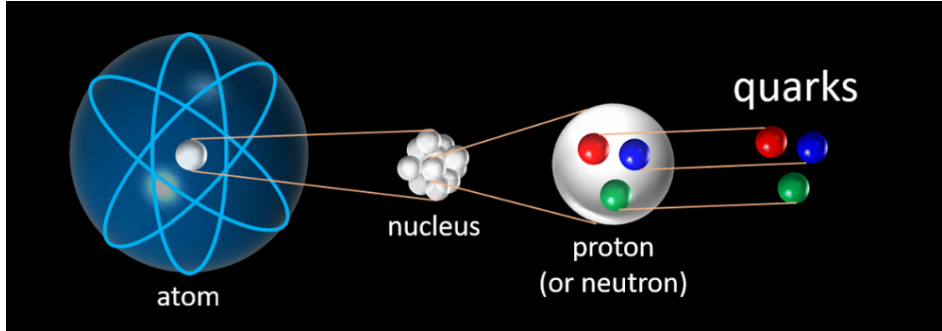


Figure 2.1: Quarks are fundamental particles that combine to create hadrons (protons, neutrons, $\pi^{0,\pm}$, etc.) [1].

momentum charge, or spin, is the first quantum number that separates particles into fermions or bosons. Fermions are those that carry half-integer spin, and thus obey Fermi-Dirac statistics, while bosons carry full integer spin values and obey Bose-Einstein statistics.

2.1.1.1 Fermions

The matter encountered in everyday life is comprised of fermions. Fermions are subdivided into two groups, quarks and leptons. The quarks participate in the strong interaction via their color charge. Quarks cannot exist as an isolated particle and thus combine into hadrons in a process called hadronization; the bound states they form are colorless. The proton and neutron are examples of hadrons. Hadrons, quarks, and their interaction with the strong force are detailed in Section 2.1.2.3. Leptons carry no color charge and therefore do not participate in strong force interactions. The fermions in the SM all participate in the electroweak interaction. However, the electromagnetic interaction is limited to those fermions that carry an electromagnetic charge. Section 2.1.2.2 describes the electroweak interaction in detail.

Fermions can then be further divided into three generations, each lepton has an electrically neutral weak force partner in the form of a neutrino. Table 2.1 lists all the SM fermions and

their properties. Every particle has a partner with identical properties except for an opposite Electromagnetism (EM) charge. These partners are called antimatter and are denoted with a bar above the particle symbol (u, \bar{u}).

Table 2.1: Standard Model fermions and their properties [2].

	1 st Generation	2 nd Generation	3 rd Generation	Spin	EM Charge	Color	Mass
Quarks	Up (u)	Charm (c)	Top (t)	$\frac{1}{2}$	$+\frac{2}{3}$	✓	$m_u = 2.16^{+0.49}_{-0.26} \text{ MeV}$ $m_c = 1.27 \pm 0.02 \text{ GeV}$ $m_t = 172.76 \pm 0.30 \text{ GeV}$
	Down (d)	Strange (s)	Bottom (b)	$\frac{1}{2}$	$-\frac{1}{3}$	✓	$m_d = 4.67^{+0.48}_{-0.17} \text{ MeV}$ $m_s = 93^{11}_{-5} \text{ MeV}$ $m_b = 4.18^{0.03}_{-0.02} \text{ GeV}$
Leptons	Electron (e^-)	Muon (μ^-)	Tau (τ^-)	$\frac{1}{2}$	-1	X	$m_{e^-} = 0.51 \text{ MeV}$ $m_{\mu^-} = 105.65 \text{ MeV}$ $m_{\tau^-} = 1776.86 \pm 0.12 \text{ MeV}$
	Electron Neutrino (ν_e)	Muon Neutrino (ν_μ)	Tau Neutrino (ν_τ)	$\frac{1}{2}$	0	X	$m_{\nu_e} < 1.1 \text{ eV}$ $m_{\nu_\mu} < 0.19 \text{ MeV}$ $m_{\nu_\tau} < 18.2 \text{ MeV}$

2.1.1.2 Bosons

Bosons are colloquially referred to as force-carriers in that the fundamental forces act via exchanging gauge bosons. This means that each force has associated boson(s) which is described by a field theory. The electroweak QFT is more complicated, and is described in detail in section 2.1.2.2. Table 2.2 lists the SM bosons², their associated field theory and properties.

²Excluding the Higgs boson.

Table 2.2: Standard Model bosons and their properties [2].

Field Theory	Boson	Spin	EM Charge	Color	Mass
Quantum Chromodynamics (QCD)	Gluon (g)	1	0	✓	0
Quantum Electrodynamics (QED)	Photon (γ)	1	0	X	0
Electroweak Theory	W^\pm	1	± 1	X	80.379 ± 0.012 GeV
	Z^0	1	0	X	91.1876 ± 0.0021 GeV

2.1.2 Interactions

The SM is based upon conservation laws. These conversation laws are what dictate the allowed interactions of matter. Lepton generation number³, electric charge, color charge, 4-momentum ($p = (E, \vec{p})$), and angular momentum are all conserved in the SM. In strong interactions baryon number⁴ ($B = \frac{1}{3}(n_q - n_{\bar{q}})$) is also conserved.

2.1.2.1 Quantum Electrodynamics

The electromagnetic force is governed by the QFT known as Quantum Electrodynamics (QED). This force is mediated by the photon, γ , a massless boson with EM charge 0. The EM force only interacts with electrically charged particles, including all quarks and the e , μ , and τ leptons.

2.1.2.2 Electroweak Interaction

The weak force is most often seen in nuclear decays and is mediated by the W^\pm and Z^0 bosons. Due to the relatively large mass of these bosons, the weak force has a very limited

³Ignoring neutrino oscillations.

⁴Here, n_q and $n_{\bar{q}}$ are the number of quarks and antiquarks that comprise the baryon.

range. The weak force interacts via the quantum number called weak isospin (T). The W^\pm affects the third component of weak isospin (T_3), thus only coupling to so-called left-handed fermions. In this way, T_3 defines the “handedness”, or chirality of a particle. At energies > 100 GeV the electromagnetic and weak forces combine into the electroweak force. Isospin and another quantum number hypercharge combine to give EM charge. $Q_{EM} = T_3 + \frac{1}{2}Y_W$. Table 2.3 contains the allowed values for weak isospin and hypercharge (Y_W).

Table 2.3: Standard Model fermions and their Electroweak properties [2].

	1^{st} Generation	2^{nd} Generation	3^{rd} Generation	EM Charge	Y_W		T		T_3	
Quarks	Up (u)	Charm (c)	Top (t)	$+\frac{2}{3}$	LH $+\frac{1}{3}$	RH $+\frac{4}{3}$	LH $\frac{1}{2}$	RH 0	LH $\pm\frac{1}{2}$	RH 0
	Down (d)	Strange (s)	Bottom (b)	$-\frac{1}{3}$	LH $+\frac{1}{3}$	RH $-\frac{2}{3}$	LH $\frac{1}{2}$	RH 0	LH $\pm\frac{1}{2}$	RH 0
Leptons	Electron (e^-)	Muon (μ^-)	Tau (τ^-)	-1	LH -1	RH 0	LH $\frac{1}{2}$	RH 0	LH $\pm\frac{1}{2}$	RH 0
	Electron Neutrino (ν_e)	Muon Neutrino (ν_μ)	Tau Neutrino (ν_τ)	0	LH -1	RH -2	LH $\frac{1}{2}$	RH 0	LH $\pm\frac{1}{2}$	RH 0

The W^\pm bosons have a T_3 component of weak isospin and act as raising or lowering operators on the T_3 component of left handed fermions. The Z boson does not have a T_3 component, and thus does not act on weak isospin of fermions. The Z boson instead transfers momentum, energy, and spin on all fermions regardless of their chirality.

2.1.2.3 Quantum Chromodynamics

Quantum Chromodynamics (QCD) is the QFT that describes the strong force which holds together atomic nuclei and other objects called hadrons. The strong force interacts via the color charge⁵ which can have values of either red, green, or blue. Particles that have a color charge cannot exist on their own, they must form colorless bound states called hadrons. Since the strong force grows with distance, if a quark is ejected out from a hadron, the stored

⁵This color does is not the visual color we are used to; merely a convenient analogous naming scheme.

energy is such that new particles with color charge will be spontaneously created from the vacuum, binding with the free quark in a process called hadronization. In a particle detector, the hadronization process cascades and creates showers of hadrons that are reconstructed as so called jets.

2.1.3 The Higgs Mechanism

The Higgs field is the mass generator of the SM and was first theorized by Peter Higgs [3], François Englert, and Robert Brout [4] in 1964. The SM itself has four massless bosons, B and \vec{W} ($W_{1,2,3}$), that do not correspond to the observed bosons. Instead, the Higgs mechanism couples to them via a complex scalar doublet (ϕ):

$$\phi = \begin{pmatrix} \phi^+ \\ \phi^0 \end{pmatrix} \quad (2.1)$$

The scalar potential that gives rise to this phenomena can be written as

$$V(\phi) = \mu^2 |\phi^\dagger \phi| + \lambda (|\phi^\dagger \phi|)^2 \quad (2.2)$$

When $\mu^2 > 0$ and $\lambda > 0$ the minimum of the potential $V(\phi)$ is 0. However, when $\mu^2 < 0$, the scalar potential $V(\phi)$ takes the shape shown in Figure 2.2. It follows that the Vacuum Expectation Value (VEV) of ϕ is then

$$\langle \phi \rangle = \sqrt{\frac{-\mu^2}{2\lambda}} = \frac{\nu}{\sqrt{2}} \quad (2.3)$$

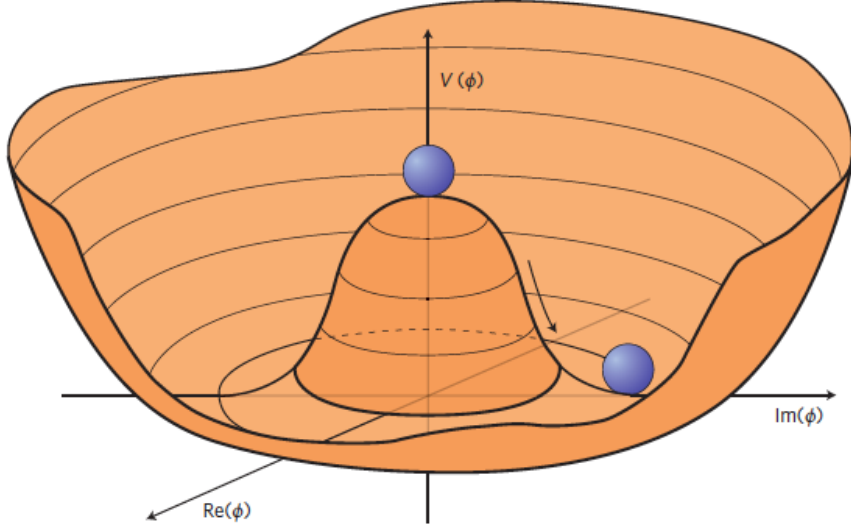


Figure 2.2: The Higgs potential defined in Equation 2.2 with $\mu^2 < 0$ [5].

where $\nu = \sqrt{\frac{-\mu^2}{\lambda}}$. From here, convention states to choose an arbitrary direction of the fluctuation as

$$\phi^0 = \frac{1}{\sqrt{2}} \begin{pmatrix} 0 \\ \nu \end{pmatrix} \quad (2.4)$$

By choosing these values three of the bosons are absorbed in giving mass to the W^\pm and Z^0 bosons leaving the final as the real scalar field $h(x)$

$$\phi(x) = \phi^0 + h(x) \quad (2.5)$$

Substituting the definition of ϕ^0 yields

$$\phi = \frac{1}{\sqrt{2}} \begin{pmatrix} 0 \\ \nu + h(x) \end{pmatrix} \quad (2.6)$$

which couples to the SM bosons via

$$\left(\frac{1}{2} g \vec{\sigma} \cdot \vec{W} + \frac{1}{2} g' B \right) \phi^0 \quad (2.7)$$

where $\vec{\sigma}$ are the Pauli matrices, g is the weak coupling constant, and g' is the hypercharge coupling constant. From this coupling, there are four eigenstates which correspond to the observed bosons

$$\begin{aligned} W^\pm &= \frac{1}{\sqrt{2}}(W_\mu^1 \mp iW_\mu^2) \\ Z^\mu &= \frac{-g'B_\mu + gW_\mu^3}{\sqrt{g^2 + g'^2}} \\ A^\mu &= \frac{gB_\mu + g'W_\mu^3}{\sqrt{g^2 + g'^2}} \end{aligned} \tag{2.8}$$

These eigenstates have corresponding mass values of

$$\begin{aligned} M_W^2 &= \frac{1}{4}g^2\nu^2 \\ M_Z^2 &= \frac{1}{4}(g^2 + g'^2)\nu \\ M_A^2 &= 0 \end{aligned} \tag{2.9}$$

The eigenstate labeled here as A is the photon. The Higgs boson was discovered in 2012 by the ATLAS and Compact Muon Solenoid (CMS) collaborations at CERN with a mass of 125 GeV [6, 7]. The ATLAS result in the $H \rightarrow \gamma\gamma$ can be seen in Figure 2.3. The scalar boson that was found appears to be the SM Higgs Boson with the properties shown in Table 2.4.

Table 2.4: The Higgs boson's properties [2].

Field Theory	Boson	Spin	EM Charge	Color	Mass	Y_W	T_3
Higgs Mechanism	Higgs (H)	0	0	X	125.25 ± 0.17 GeV	$\pm\frac{1}{2}$	∓ 1

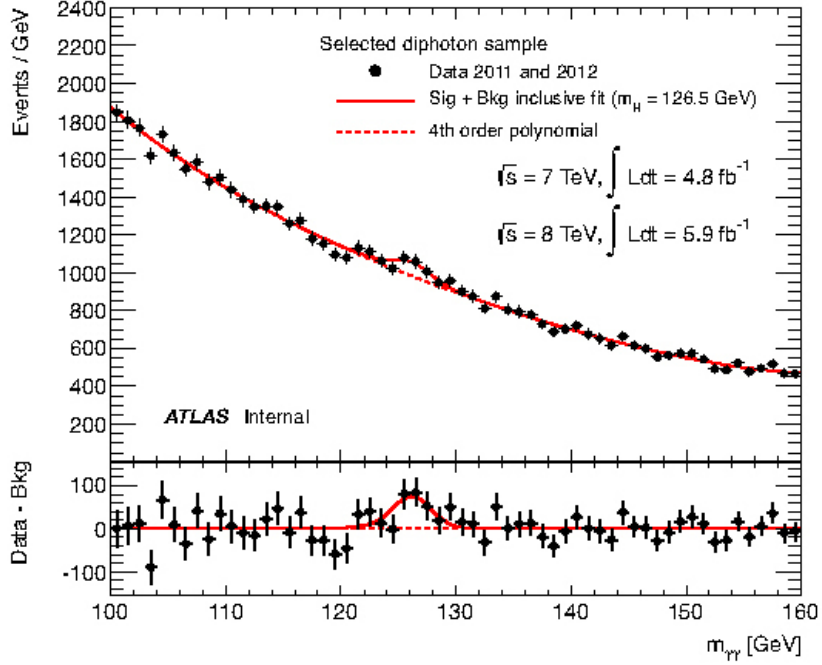


Figure 2.3: The distributions of the invariant mass of diphoton candidates after all selections for the combined 7 TeV and 8 TeV data sample. The result of a fit to the data of the sum of a signal component fixed to $m_H = 126.5$ GeV and a background component described by a fourth-order Bernstein polynomial is superimposed. Taken from [6].

2.2 Supersymmetry

While the SM describes a wide range of physics to a high degree of accuracy, it is not without issues. For instance, the SM does not offer an explanation for gravity, dark matter, or the observed matter-antimatter asymmetry of the universe. In addition, the SM predicts the mass of neutrinos to be 0. Observed neutrino mixing, where $\nu_e \rightarrow \nu_\mu$, $\nu_\tau \rightarrow \nu_\mu$, etc., contradicts this; neutrinos must have mass [2].

One promising model that offers solutions to many of these issues is SUSY. As discussed previously, the SM is built upon symmetries, and the breaking of these symmetries gives us

electroweak unification. SUSY proposes another symmetry, this time between fermions and bosons.

$$\begin{aligned} Q|Fermion\rangle &= |Boson\rangle, \\ Q|Boson\rangle &= |Fermion\rangle \end{aligned} \tag{2.10}$$

Equation 2.10 shows how the SUSY operator Q acts on particles. Here, Q provides a bosonic supersymmetric partner to every fermion and vice versa. SUSY naturally offers solutions to the “hierarchy problem” with the SM.

The hierarchy problem arises from the difference in electroweak ($M_W \sim 100$ GeV) and Planck ($M_P \sim 2.4 \times 10^{18}$ GeV) mass scales. For the Higgs mass to be on the scale of $M_H \sim 125$ GeV incredibly large and small mass terms must cancel perfectly, leading to a feeling of “unnaturalness”. SUSY brings many new particles into the picture, theorized to occupy the intermediate mass range leading to a more natural theory.

2.2.1 Minimal Supersymmetric Standard Model Particles

SUSY is a large group of theories that include theories with various numbers of additional superpartner particles. The MSSM is the smallest extension of the SM that introduces SUSY. In the MSSM⁶, each SM particle is part of a supermultiplet with its superpartner where both particles have the same quantum numbers, except spin. If this supersymmetry is unbroken, then the superpartner and the SM particle would have the same mass as well. However, SUSY has not been observed, so the supersymmetry must be broken putting the mass scale on the TeV scale. Table 2.5 lists the MSSM supermultiplets and the associated naming conventions.

⁶As well as all other SUSY models.

Table 2.5: SM particles and their MSSM partners [2].

SM	MSSM
Spin- $\frac{1}{2}$ quarks and spin-0 squarks ($\times 3$ generations)	
$(u_L d_L)$	$(\tilde{u}_L \tilde{d}_L)$
u_R^\dagger	\bar{u}_R^*
d_R^\dagger	\bar{d}_R^*
Spin- $\frac{1}{2}$ leptons and spin-0 sleptons ($\times 3$ generations)	
$\nu_L e_L$	$(\tilde{\nu}_L \tilde{e}_L)$
e_R^\dagger	\bar{e}_R^*
Spin-0 Higgs and spin- $\frac{1}{2}$ Higgsinos	
$(H_u^\dagger H_u^0)$	$(\tilde{H}_u^+ \tilde{H}_u^0)$
$(H_d^0 H_d^-)$	$(\tilde{H}_d^0 \tilde{H}_d^-)$
Spin-1 gauge bosons and spin- $\frac{1}{2}$ gauginos	
g	\tilde{g}
$(W^\pm W^0)$	$(\tilde{W}^\pm \tilde{W}^0)$
B^0	\tilde{B}^0

2.2.2 2 Higgs Doublet Model

Having only one Higgs chiral supermultiplet with hypercharge $Y_W = \pm \frac{1}{2}$ leads to a gauge anomaly [8]. This can be resolved by introducing two Higgs doublets with hypercharge $Y_W = \frac{1}{2}$ and $Y_W = -\frac{1}{2}$. Such is the case in the MSSM which requires two complex doublet scalar fields where one couples to the up-type quarks and the other couples to down-type quarks and charged leptons. The MSSM Higgs sector has 8 degrees of freedom. Following the same type of mechanism described in Section 2.1.3 three of these degrees of freedom give the observed W^\pm and Z^0 bosons. This leaves the extended Higgs sector shown in Table 2.6, where

Table 2.6: 2HDM extended Higgs sector [8]

light neutral scalar	h^0
heavy neutral scalar	H^0
neutral pseudoscalar	A^0
two charged scalars	H^\pm

the h^0 is a SM-like Higgs. The boson discovered by the ATLAS and CMS collaborations in 2012 is consistent with the h^0 . When referring to the charged Higgs bosons, we often refer to them using one symbol H^\pm . In the 2HDM there are two free parameters⁷, the masses of the H^\pm and the ratio of their vacuum expectation values which is defined as $\tan \beta$. At the time of writing, the extended Higgs sector is an active area of research with many new searches actively being performed [2]. The most recent results from ATLAS can be seen in Reference [9].

⁷There are more free parameters with regards to the full 2HDM. These are the two regarding the charged Higgs bosons that are relevant for the rest of this dissertation.

2.3 Charged Higgs Bosons

Since the H^\pm couplings are proportional to the fermion masses, the main production modes at the LHC are through $t\bar{t}$ and Wt diagrams where the W^\pm boson is replaced by a H^\pm . The production diagrams considered in this dissertation can be seen in Figure 2.4. The

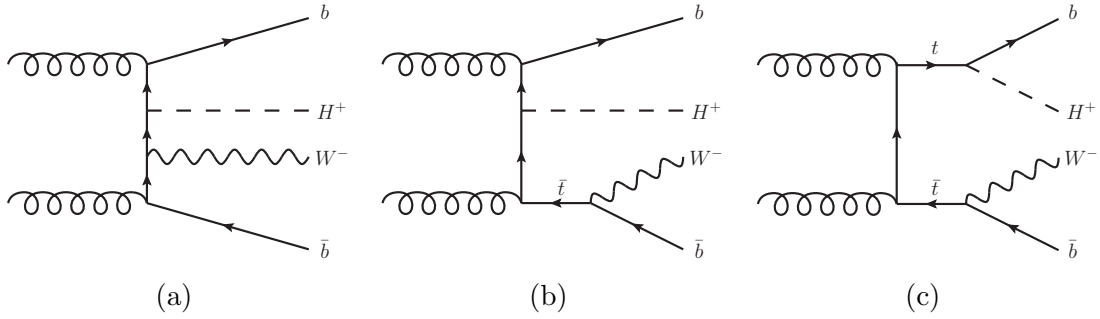


Figure 2.4: Examples of leading-order Feynman diagrams contributing to the production of charged Higgs bosons in pp collisions: (a) non-resonant top-quark production prevalent in the intermediate-mass range, (b) single-resonant top-quark production that dominates at large H^\pm masses, (c) double-resonant top-quark production that dominates at low H^\pm masses. The interference between these three diagrams becomes most relevant in the intermediate-mass region.

cross section at various $\tan \beta$ values can be seen as a function of m_{H^\pm} in Figure 2.5. The cross section scales with $\tan \beta$ and at very small values the top Yukawa couplings become non-perturbative, meaning they are very difficult to predict and very unlikely to occur. In this dissertation the decay channel considered is $H^\pm \rightarrow \tau^\pm \nu_\tau$. As can be seen in Figure 2.6, the $H^\pm \rightarrow \tau^\pm \nu_\tau$ decay channel is especially relevant at low m_{H^\pm} and high $\tan \beta$. This dissertation describes a search for charged Higgs bosons produced in association with a top quark, where only the $H^\pm \rightarrow \tau^\pm \nu_\tau$ decay channel is considered. Other decay modes of the H^\pm to SM particles are covered in other searches [12]. Decay channels of H^\pm to other MSSM are not considered in this dissertation. The search consists of two sub-channels, $\tau + \text{jets}$ and $\tau + \ell$, where the associated top quark decays either hadronically or leptonically respectively.

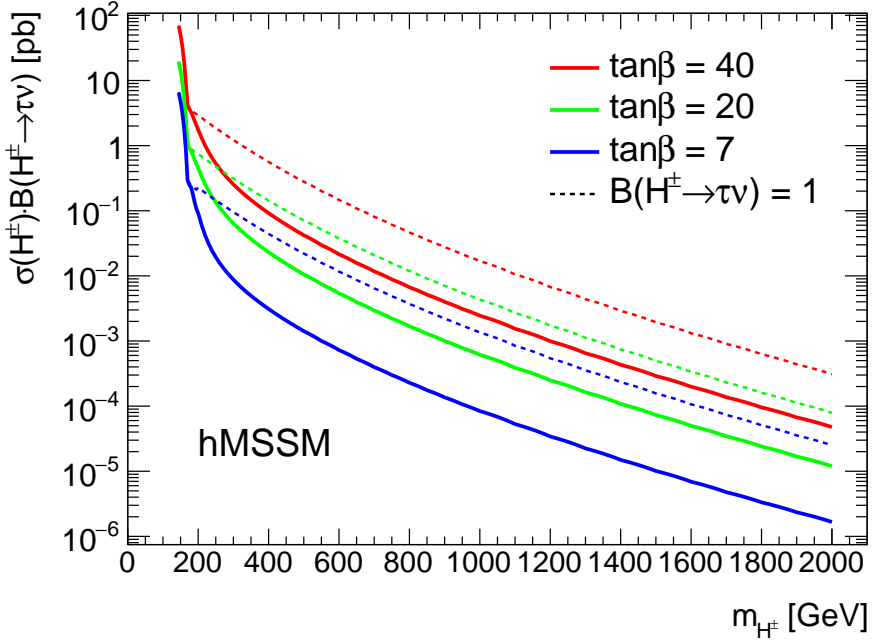


Figure 2.5: Variation of $\sigma(pp \rightarrow tbH^\pm) \times B(H^\pm \rightarrow \tau^\pm \nu_\tau)$ with the charged Higgs boson mass in pp collisions at $\sqrt{s} = 13$ TeV, for $\tan\beta$ values of 7, 20, and 40 in the hMSSM scenario. Dashed lines correspond to $B(H^\pm \rightarrow \tau^\pm \nu_\tau)$ set to 1, hence they show the dependence of $\sigma(pp \rightarrow tbH^\pm)$ with m_{H^\pm} . Taken from Reference [10].

Within the MSSM, several benchmarks are defined taking into account higher-order corrections and keeping the number of free parameters in the model small [12]. Figure 2.5 is made assuming the hMSSM model, where h^0 is taken as the observed 125 GeV Higgs and the absence of observed SUSY at the LHC is taken into account by setting the SUSY scale to $M_{SUSY} > 1$ TeV [13]. Figure 2.6 shows the branching ratios of H^\pm for various $\tan\beta$ values in the m_h^{mod+} model where the benchmark scenario m_h^{max} has been modified to interpret h as the observed boson⁸ [12].

⁸The m_h^{max} scenario is constructed to yield the highest possible mass for h at any given $\tan\beta$.

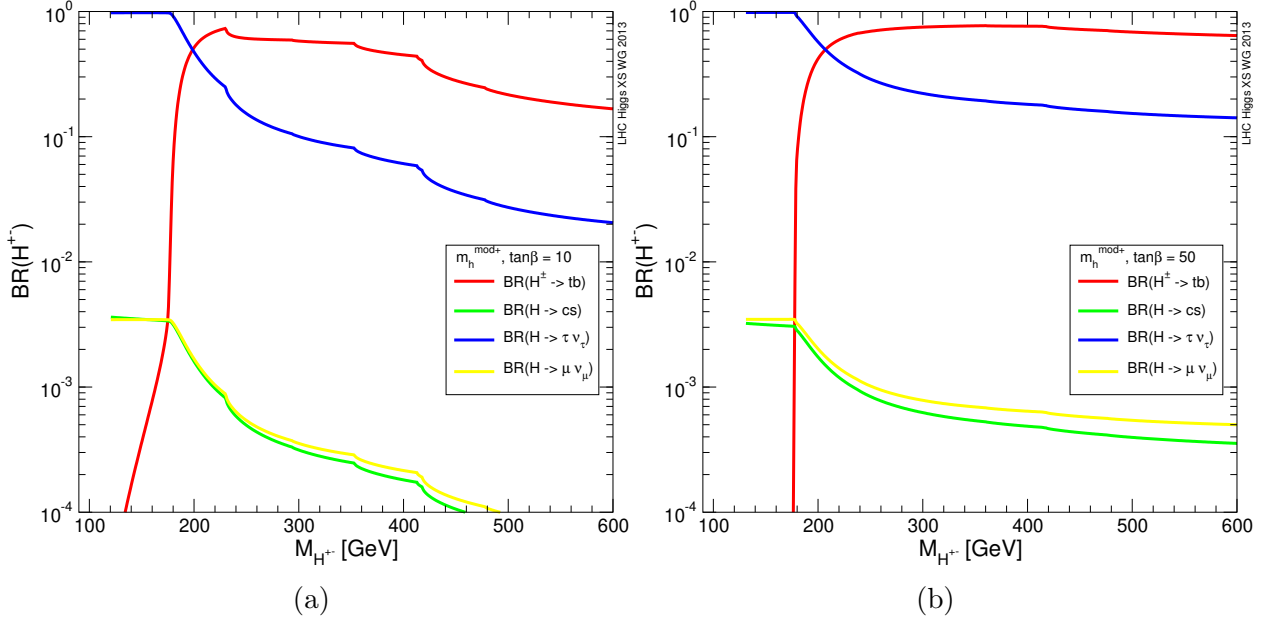


Figure 2.6: Branching fractions of H^\pm as a function of m_{H^\pm} for (a) $\tan\beta = 10$ and (b) $\tan\beta = 50$ in the $m_h^{\text{mod}+}$ scenario of the MSSM [11].

2.3.1 Previous Result

To add context to this dissertation, it is important to reference the results of the previous iteration of the search discussed in this dissertation⁹. The ATLAS collaboration published a paper in 2018 covering the data taking years of 2015 and 2016 [10], whereas this dissertation covers the full Run-2 (2015-2018) dataset. Figure 2.7 shows the limits on the cross section and Figure 2.8 shows the limits on $\tan\beta$ as a function of m_{H^\pm} .

There are many other searches for charged Higgs bosons that have been performed by several experiments in many different decay channels. Figure 2.9 shows the results from CMS in the same $H^\pm \rightarrow \tau^\pm \nu_\tau$ decay channel [14]. Figure 2.10 shows the ATLAS results for a charged Higgs search in the $H^\pm \rightarrow tb$ decay channel and Figure 2.11 shows the previous $H^\pm \rightarrow \tau^\pm \nu_\tau$ search results overlayed on the $H^\pm \rightarrow tb$ results in two theoretical models [15].

⁹The author joined the analysis team towards the end of this iteration and performed validation studies.

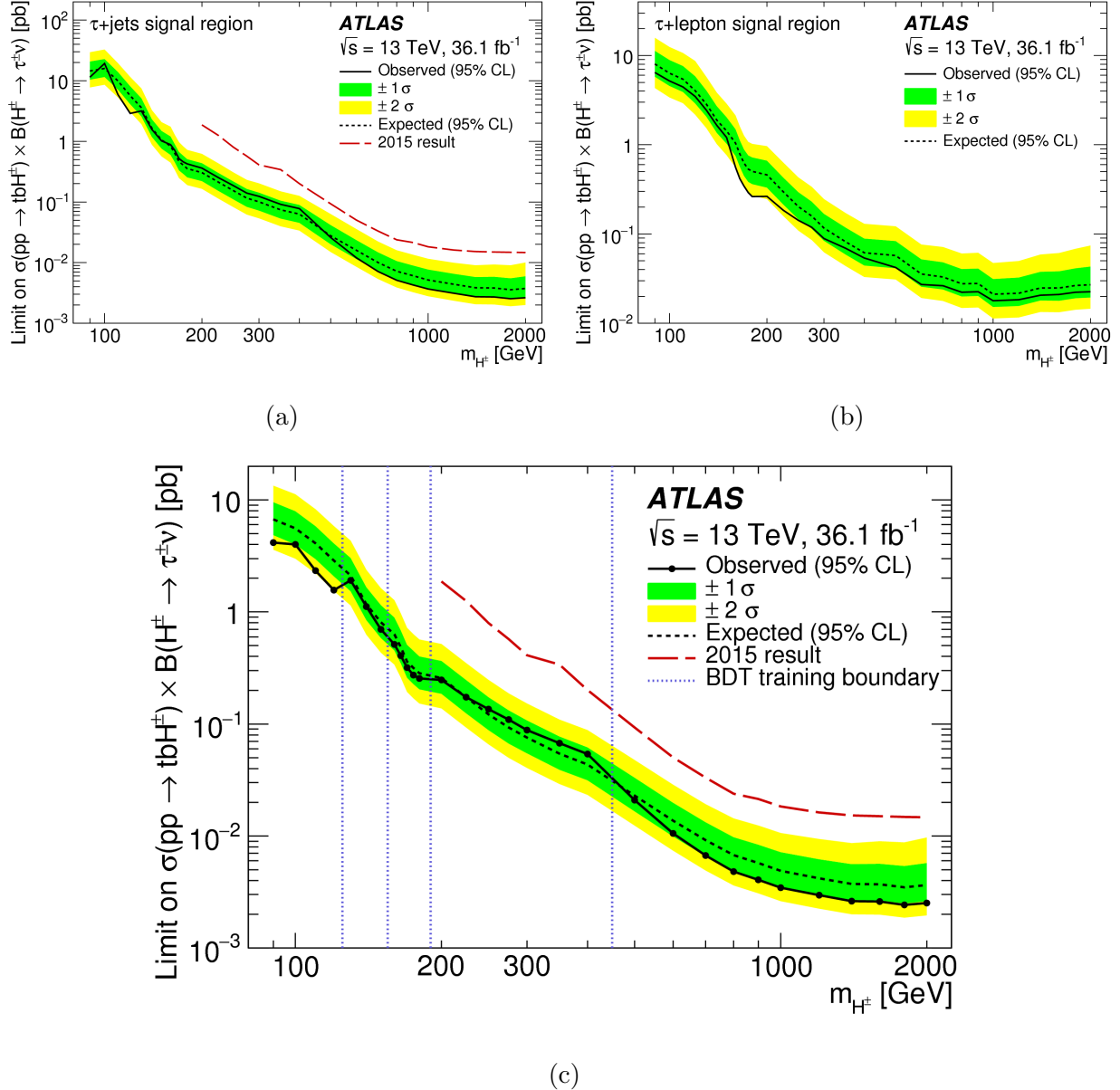


Figure 2.7: Exclusion limits at 95% CL on $\sigma(pp \rightarrow tbH^\pm \times B(H^\pm \rightarrow \tau^\pm \nu))$ [pb]. Top left (a) shows the $\tau + \text{jets}$ subchannel, top right (b) corresponds to the $\tau + \ell$ subchannel and bottom (c) shows the combination of the two subchannels. Taken from Reference [10].

The previous iteration of this analysis relied on boosted decision trees (BDT) binned in m_{H^\pm} , using five separate classifiers to cover the mass range of 90 – 2000 GeV. The mass bins can be seen as the blue dotted lines in Figure 2.7c. It is important to note the inclusion of

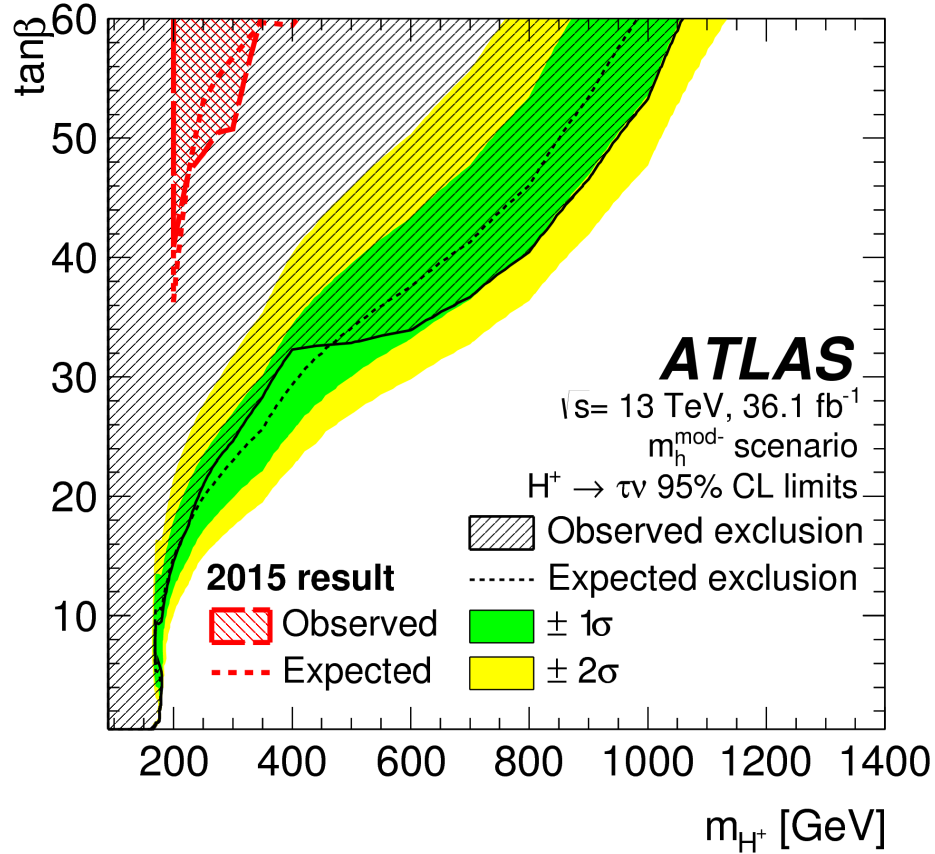


Figure 2.8: Exclusion limits at 95% CL on $\tan\beta$ as a function of m_{H^\pm} [10].

the mass range $90 - 200$ GeV, as Reference [10] was the first search to include this mass region below the top quark mass.

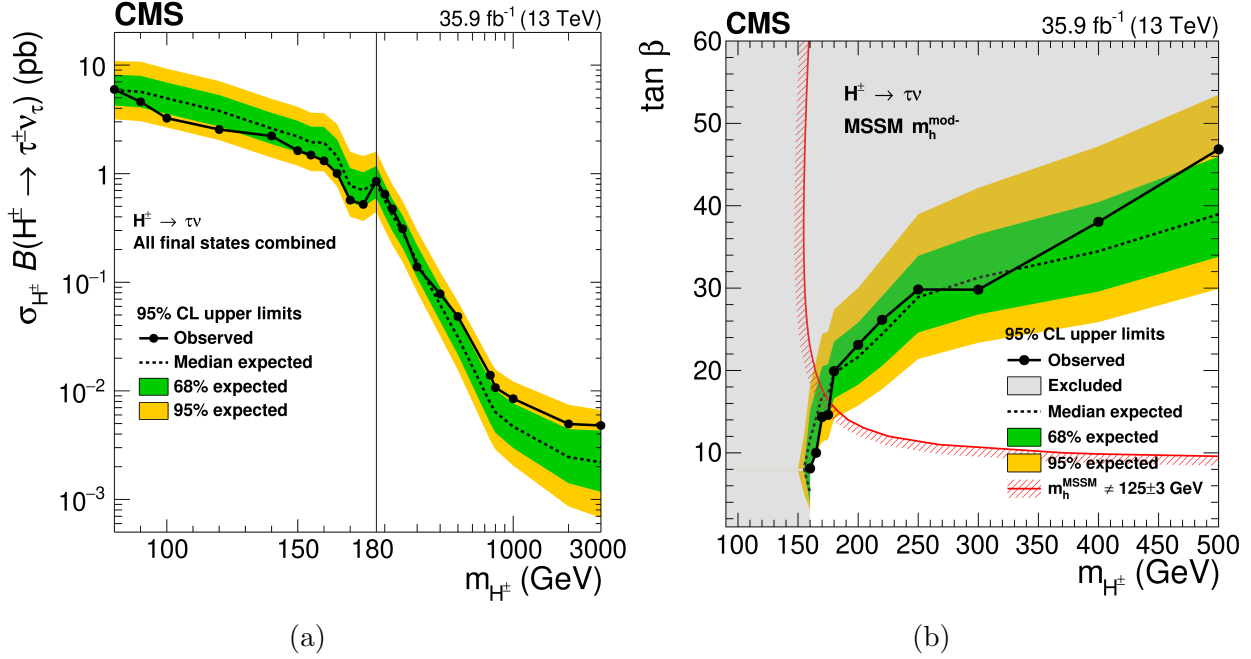


Figure 2.9: (a) Exclusion limits at 95% CL on $\sigma_{H^\pm} B(H^\pm \rightarrow \tau^\pm \nu_\tau)$ [pb] from the CMS collaboration [14]. (b) Exclusion limits at 95% CL on $\tan \beta$ and m_{H^\pm} [14].

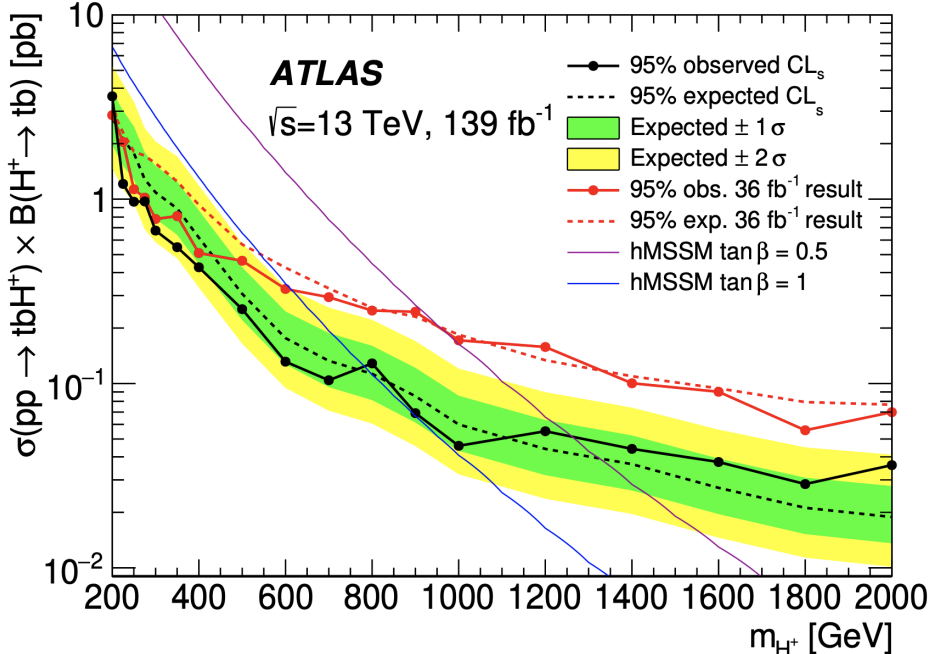


Figure 2.10: Exclusion limits at 95% CL on $\sigma(pp \rightarrow tbH^\pm) \times B(H^\pm \rightarrow tb)$ as a function of m_{H^\pm} [15].

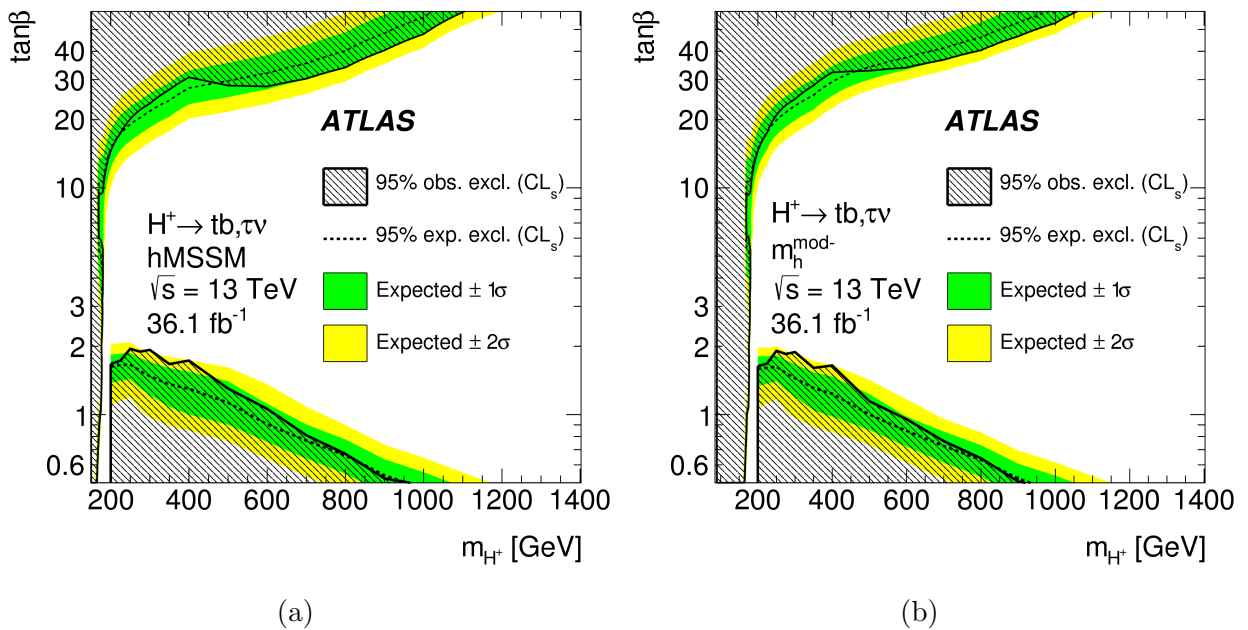


Figure 2.11: Exclusion limits at 95% CL on $\tan\beta$ as a function of m_{H^\pm} in the (a) MSSM and (b) $m_h^{\text{mod}+}$ scenario of the MSSM [15].

CHAPTER 3

EXPERIMENTAL APPARATUS

3.1 Particle Accelerators

To study the SM, the Higgs boson, and search for hints of new physics, particle accelerators are used. Particle accelerators can be categorized as either fixed target or colliders. As the naming suggests, in a fixed target accelerator the beam hits a target that then produces the desired particle collisions. A collider uses two beams, often in a circle, that are brought to collide inside a detector. For colliders with two beams of equal energy, the center of mass energy (E_{CM}) of a fixed target accelerator energy scales as the square root of the beam energy (E_{beam}), $E_{CM} = \sqrt{E_{beam}}$, whereas a collider scales as $E_{CM} = 2 E_{beam}$. Colliders are the preferred accelerator for maximizing the center of mass energy. The analyses discussed in this dissertation use a particle collider.

3.1.1 Hadron Colliders

Collider beams consist of either leptons or hadrons. Lepton colliders are often considered as precision machines, as the longitudinal momentum is known and backgrounds are clean. The center of mass energy is well controlled in a lepton collider, meaning particles can be produced on resonance, increasing the desired particle yield. On the other hand, due to the nature of hadrons not being fundamental particles a hadron collider produces a wide variety of collisions, making them well suited for discovery but also making for messier backgrounds.

The constituents of a hadron participate in the collisions, meaning it is impossible to know the exact longitudinal momentum of the initial state; instead momentum in the transverse plane is used (p_T). The synchrotron radiation produced from a hadron collider is typically much lower than that of a lepton collider, meaning the beams are easier to control and can be pushed to higher energies without extra losses. The analyses discussed in this dissertation use a hadron collider, the Large Hadron Collider.

3.1.2 The Large Hadron Collider

The Large Hadron Collider (LHC) is a 27 km circumference circular collider built outside of Geneva, Switzerland at Conseil Européen pour la Recherche Nucléaire (CERN). At a center of mass energy 13 TeV (6.5 TeV in each beam), the LHC is the largest and highest energy particle accelerator ever built [16]. There are four main collision points along the LHC: the ATLAS, CMS, ALICE, and LHCb experiments. ATLAS and CMS are general purpose particle detectors while ALICE and LHCb focus on more specialized physics. The numbers stated in the following sections are in reference to proton-proton collisions.

The LHC consists of 1104 NbTi superconducting dipole magnets, each being 15 m long, weighing 35 tonnes, cooled to 2 K, operating at 11,000 Amps, and produce a magnetic field of 8.3 T. A cross-section of a dipole magnet and the surrounding cryogenic system can be seen in Figure 3.1. The dipole magnets are used to bend the beam around the ring with another 128 used in the beam dump system to remove the beam safely from the LHC. A 2-in-1 configuration is used within the dipole magnets to create the required magnetic fields to bend two equally charged beams in opposite directions. A diagram of the magnetic fields in this configuration produced can be seen in Figure 3.2. To focus the beam in the horizontal and vertical planes two quadrupole magnets are used; one magnet focuses in one plane while

defocusing in the other. The end result is a horizontally and vertically focused beam. While in the LHC, the hadrons are accelerated using radiofrequency cavities. Each oppositely circulating beam is not a solid column of protons but instead consists of 2808 bunches of protons with 1.2×10^{11} protons per bunch. Collisions occur when bunches are brought to collide in a bunch crossing. Table 3.1 lists some information on the LHC.

Table 3.1: LHC parameters [17].

Circumference	26,659 m
Dipole operating temperature	1.9 K
Dipole magnets	1232
Quadrupole magnets	392
Radiofrequency cavities	16 (8 per beam)
Beam energy	6.5 TeV (13 CM TeV)
Protons per bunch	1.2×10^{11}
Bunches per beam	2808
Revolutions per second	11245
Collisions per second	1,000,000,000

3.1.3 CERN Accelerator Complex

There are a series of accelerators used to get each beam up to its final energy of 6.5 TeV. The protons used in collisions are sourced from hydrogen atoms. The hydrogen is ionized, leaving the nucleus consisting of one proton, these protons are then accelerated in radiofrequency (RF) cavities. Figure 3.3 shows in detail the full accelerator complex at CERN¹. The protons used in the LHC start the accelerating process in the linear accelerator LINAC 2. They then are accelerated in the booster, PS, SPS, and are finally injected at the LHC where they are accelerated to the final 6.5 TeV beam energy. The final energies of protons from each accelerator can be seen in Table 3.2. Once the beams are at final collision

¹Figure 3.3 shows the newer LINAC 4 at the start of Run-3. This work is concerning data taken with LINAC 2.

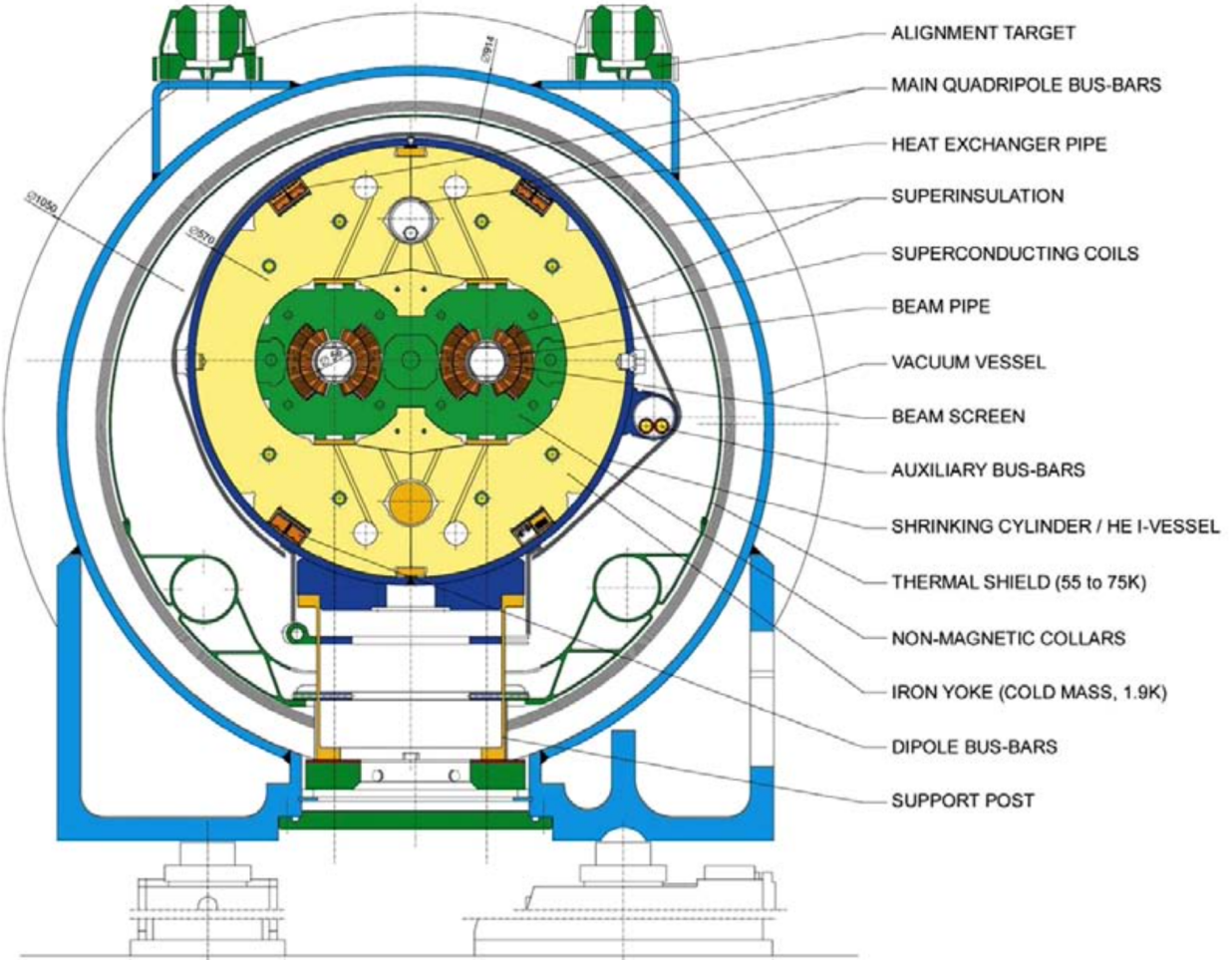


Figure 3.1: Cross-section of cryodipole (lengths in mm) [16].

Table 3.2: Accelerator final energies [16].

Accelerator	Final Energy
LINAC 2	50 MeV
Booster	1.4 GeV
Proton Synchrotron (PS)	26 GeV
Super Proton Synchrotron (SPS)	450 GeV
Large Hadron Collider (LHC)	6.5 TeV

energy they are then focused, aligned, and squeezed using the series of magnets discussed above. The term stable beams is used to refer to the status of the beams within the LHC when they have reached optimal conditions for data taking.

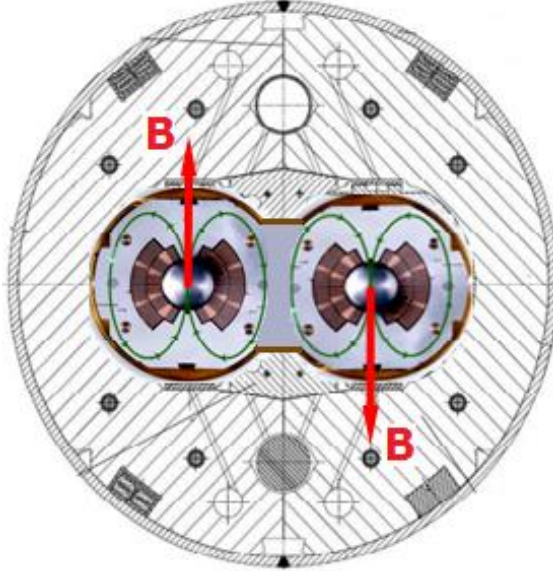


Figure 3.2: Field of the LHC dipole magnets [18].

3.1.4 Luminosity

The amount of data collected from colliders is often referred to in terms of luminosity. Luminosity is measured in terms of inverse barns, where $1 b = 10^{-28} m^2$. The instantaneous luminosity of one bunch crossing can be written as

$$\mathcal{L}_{bunch} = \frac{\mu f}{\sigma} \quad (3.1)$$

where σ is the cross section and can be thought of as the probability of a collision occurring, μ is the number of inelastic interactions per bunch crossing, and f is the revolution frequency of the LHC $f = 11246$ Hz. Therefore, the total instantaneous luminosity is

$$\mathcal{L} = N_b \frac{\langle \mu \rangle f}{\sigma} \quad (3.2)$$

where $\langle \mu \rangle$ is the average number of inelastic interactions per bunch crossing.

The CERN accelerator complex

Complexe des accélérateurs du CERN

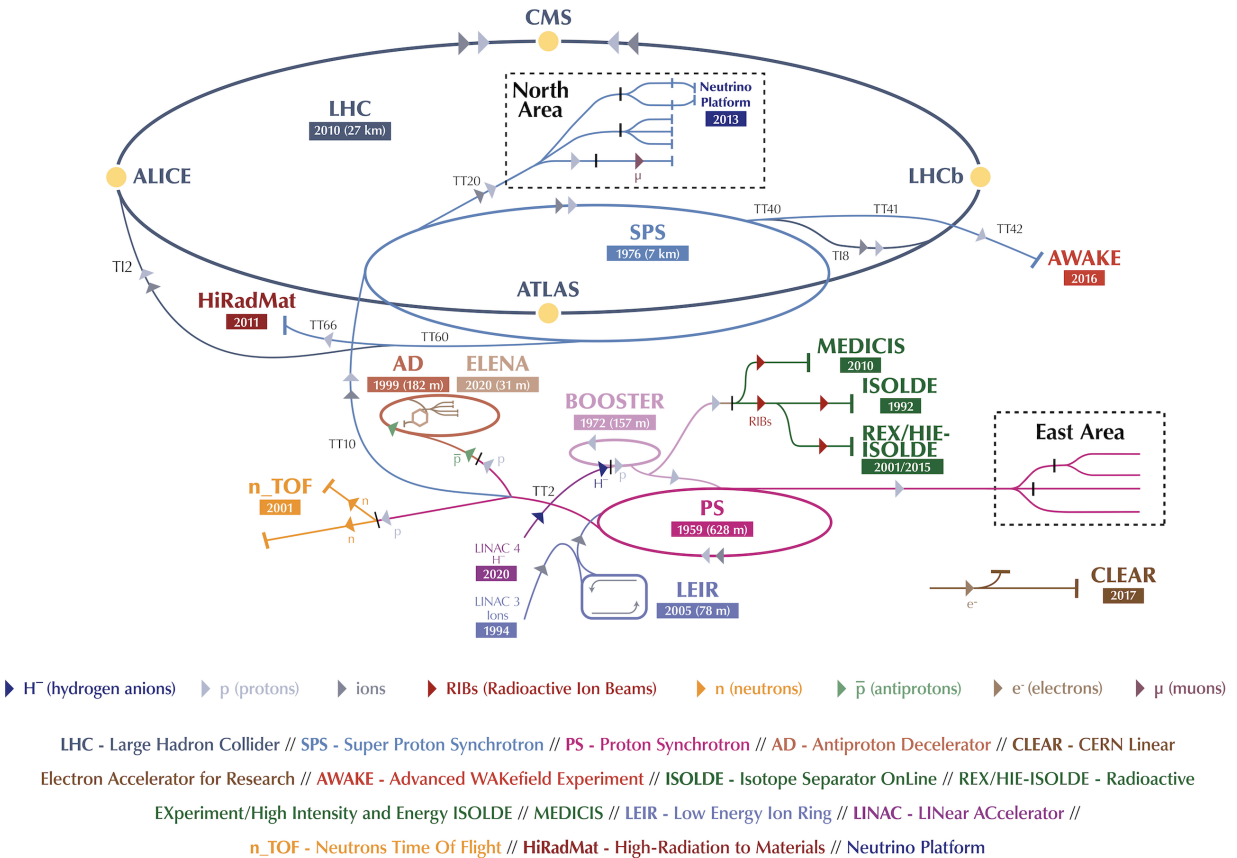


Figure 3.3: The CERN accelerator complex [19].

The integrated luminosity then corresponds to the total amount of data that was taken during a time period and can be seen for the LHC Run-2 in Reference 3.4. The value of $\langle \mu \rangle$ changed throughout data taking and can be seen in Figure 3.5. It is referred to as pileup because the higher the $\langle \mu \rangle$ value, the more messy a collision becomes. The effect of high pileup can be seen in the bottom right insert of Figure 3.6, a collision event taken in 2018 with 29 reconstructed vertices shown on the bottom right as colored circles. High pileup leads to many tracks being reconstructed from several vertices. This makes finding the primary interaction in the event difficult.

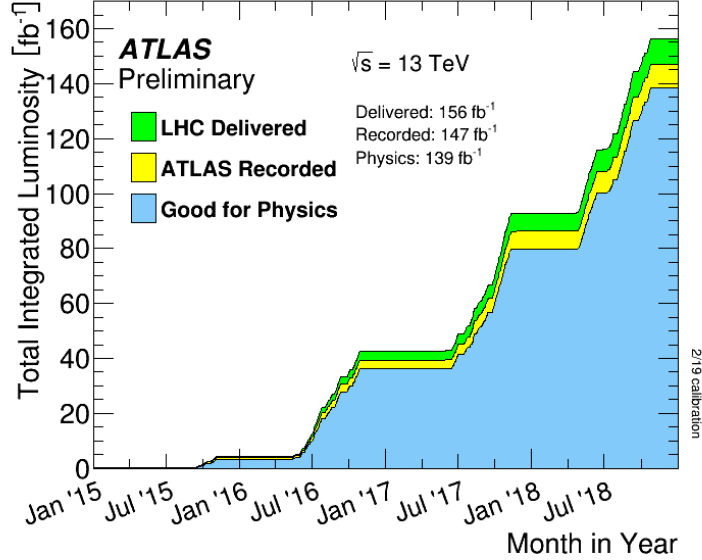


Figure 3.4: Cumulative luminosity versus time delivered to ATLAS (green), recorded by ATLAS (yellow), and certified to be good quality data (blue) during stable beams for pp collisions at 13 TeV center of mass energy in 2015-2018. The difference between the colored histograms reflects inefficiencies, especially those seen when restarting data taking [20].

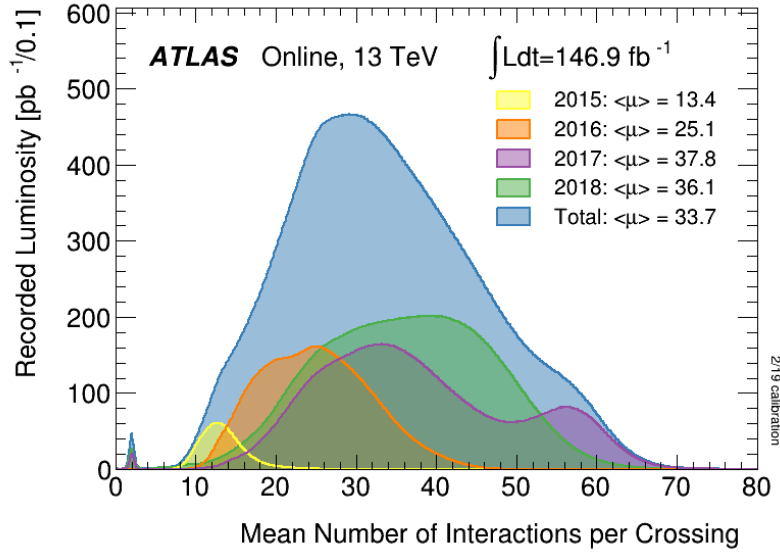


Figure 3.5: The luminosity-weighted distribution of the mean number of interactions per bunch crossing for the 2015-2018 pp collision dataset at 13 TeV center of mass energy [20].

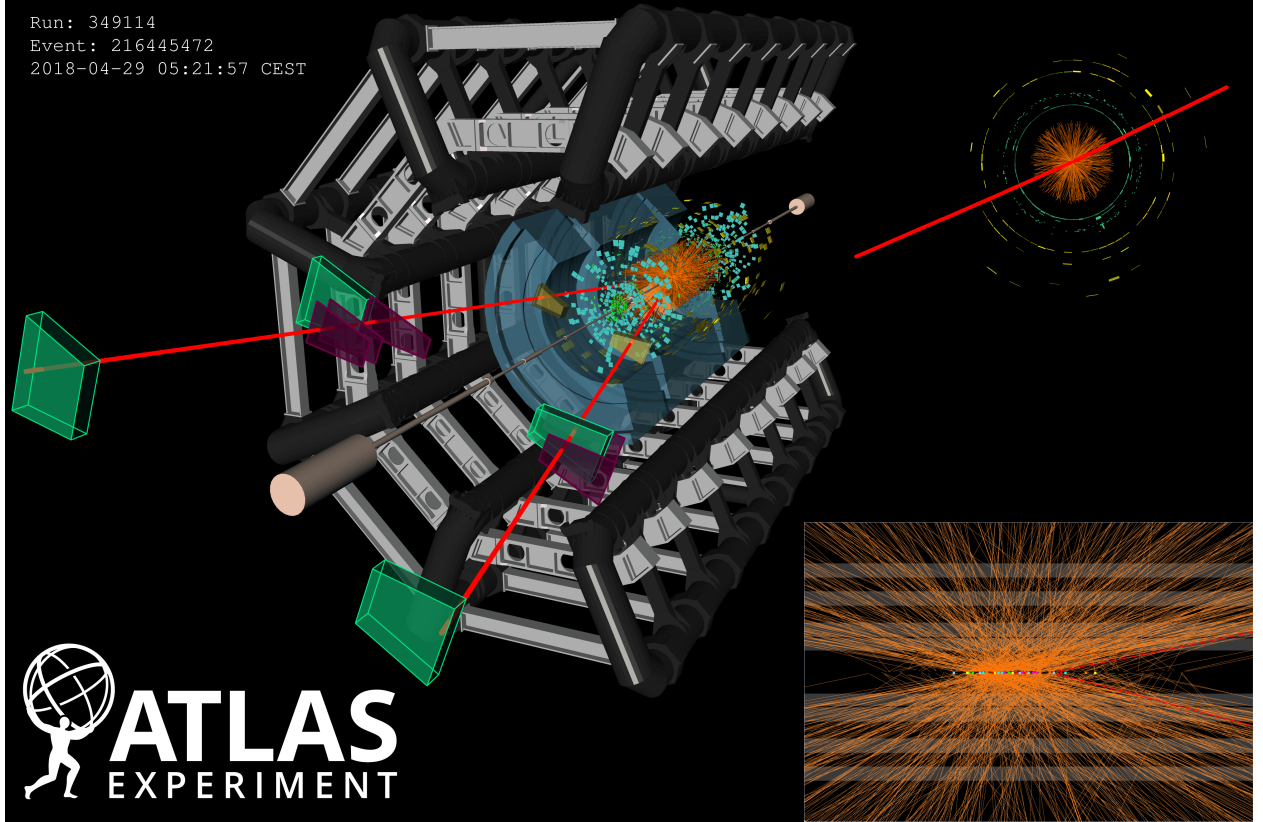


Figure 3.6: A display of a candidate Z boson event from proton-proton collisions recorded by ATLAS with LHC stable beams at a collision energy of 13 TeV. The Z boson candidate is reconstructed in a beam crossing with 28 additionally reconstructed primary vertices from the minimum bias interactions. The candidate event is reconstructed in the 2μ final state. In the left display, the red lines show the path of the two muons including the hits in the muon spectrometer and the orange tracks are the remaining charged particles from the 29 vertices, with transverse momentum above 0.5 GeV. The colored squares in the lower display correspond to the position of the reconstructed vertices. The invariant mass of the two muons is 92.3 GeV [21].

A common calculation using the total integrated luminosity is shown in Equation 3.3; the number of times a particular process was produced N_x is calculated as:

$$N_x = \mathcal{L}\sigma_x \quad (3.3)$$

where again, σ_x is the cross section for the process x to occur.

3.2 The ATLAS Detector

The A Toroidal LHC Apparatus (ATLAS) detector is one of two general purpose particle detectors on the LHC; the other being the Compact Muon Solenoid (CMS). ATLAS is comprised of four main components: the inner detector, calorimeters, muon system, and the magnet system. Each component has several types of technology in order to measure the energy and trajectory of the original particle². The full ATLAS detector measures 44 m in length, 25 m in diameter, and weighs over 7000 tonnes [22]. Figure 3.7 shows a 3D model of the ATLAS detector³. All of the subdetectors output data to the TDAQ system that selects collisions with interesting physics using a complex mix of hardware and software algorithms detailed in Section 3.2.6.

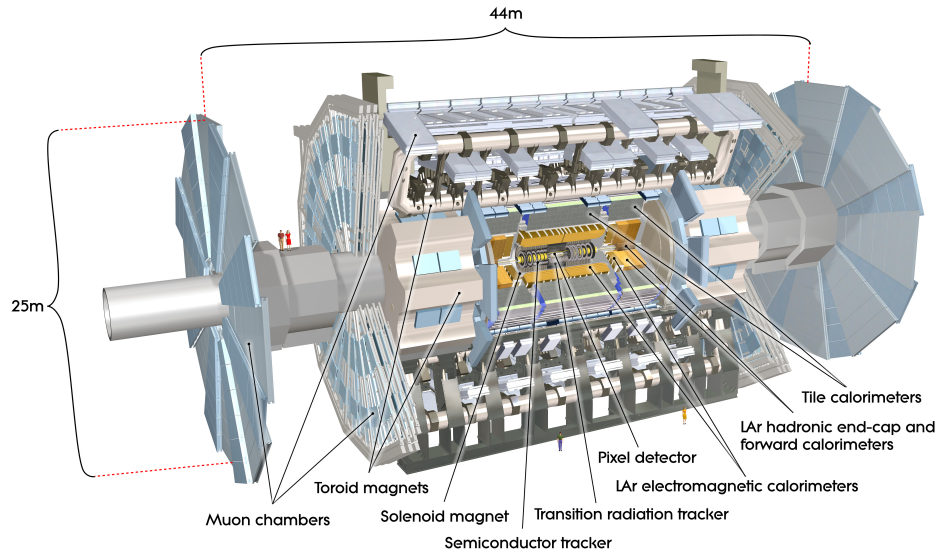


Figure 3.7: Cut-away view of the ATLAS detector with major subdetectors highlighted [23].

²Neutrinos are not directly detected, but inferred via a missing transverse energy calculation described in Section 5.7.

³Figure 3.7 shows the New Small Wheel muon-chambers. This dissertation concerns data collected with the old Small Wheel muon-chambers.

3.2.1 Detector Coordinates

Since ATLAS is a cylinder⁴, it is convenient to start with polar cylindrical coordinates. For ATLAS, the z-axis is in line with the beam line, the x-axis points towards the center of the LHC ring, and the y-axis points vertically. However, since particle collisions are relativistic by nature, a set of Lorentz invariant coordinates is much more useful. The radial coordinate r defines the radial distance from the Interaction Point (IP) at the center of ATLAS, ϕ is the azimuthal angle describing the angle from the x axis and η , the pseudorapidity, is defined as

$$\eta \equiv -\ln \left(\tan \left(\frac{\theta}{2} \right) \right) \quad (3.4)$$

where θ is the angle from the y-axis. The differences in η between particles is Lorentz invariant in the coordinate system of (r, ϕ, η) . Due to the large collision energies of the LHC, the pseudorapidity is a close estimate to the true rapidity (y)⁵ of the particles:

$$y \equiv \frac{1}{2} \ln \left(\frac{E + p_Z}{E - p_Z} \right) \approx \eta \quad (3.5)$$

A useful metric to define the distance between objects in the detector is ΔR :

$$\Delta R \equiv \sqrt{(\Delta\eta)^2 + (\Delta\phi)^2} \quad (3.6)$$

Figure 3.8 shows visually how η relates to θ . In the ATLAS detector, the central barrel section⁶ generally corresponds to a range of $|\eta| < 1$.

⁴The ATLAS detector is not a perfect cylinder but can be closely approximated as one.

⁵In this sense, y is now the rapidity, not the y-axis coordinate.

⁶The exact $|\eta|$ range differs between each subdetector.

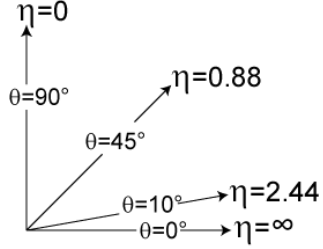


Figure 3.8: A diagram showing the pseudorapidity η and corresponding θ values [24].

3.2.2 Magnet Systems

The ATLAS detector makes use of two superconducting magnet systems; a central solenoid and a toroid system. Both systems provide large magnetic fields to curve charged particles. The curvature can be used to measure the electromagnetic charge and charge-to-mass ratio, effectively measuring the momentum of charged particles. Figure 3.9 shows the magnets in ATLAS.

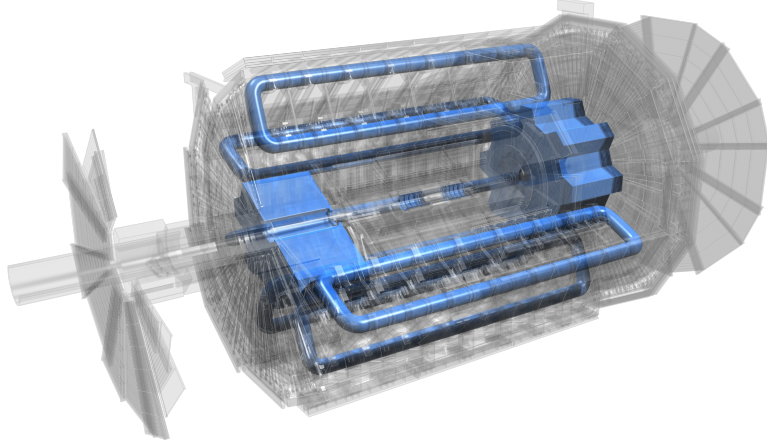


Figure 3.9: The ATLAS magnet systems [23].

3.2.2.1 Solenoid System

The central solenoid encases the Inner Detector (ID), creating an axially symmetric 2 T magnetic field. This magnetic field bends charged particles in the transverse plane throughout the ID. The solenoid magnet itself measures 5.3 m in length and 2.63 m in diameter. In an effort to decrease the amount of material in front of the calorimeters the solenoid magnet was made to be thin. It is a single-layer coil with approximately 1200 turns of NbTi superconducting wires encased in Al-Cu to structurally stabilize the magnet material [25]. The steel structure within the Tile calorimeter acts as the magnetic flux return for the solenoid magnet system. 70% of this flux passes through the supporting girder structure, 25% through the active calorimeter material, and roughly 2% through the front-plates of the Tile calorimeter [26].

3.2.2.2 Toroid System

The ATLAS detector gets its name from the toroidal magnetic system that is critical in the measurements of muon properties. The toroid system bends any charged particles that make it past the calorimeters along the beam axis. This is achieved through a radially symmetric magnetic field of 3.9 T in the barrel and 4.1 in the end-caps. The barrel toroid system is comprised of 8 air core superconducting toroid magnets that each measure 25 m in length, 10 m in diameter, and weigh 750 tonnes. The superconducting wires are the same used in the solenoid, NbTi encased in Al-Cu [27]. Each magnet is encased in a stainless steel cryogenic chamber, or cryostat. The toroid magnet system has two end-cap toroids that are very similar in construction to the barrel toroids. The end-cap toroids also have 8 coils measuring 5 m in length and 10 m in diameter. Instead of individual cryostats for each coil,

the end-caps are encased in large cryostats that hold all 8 coils. This allows the end-caps to be pulled out and offers easy access to the rest of the detector. Just like with the central solenoid system, the design of the toroid system was chosen to limit the amount of material between detector components. A solenoid magnet of similar size to the toroid system would not only add more material, but would be cost prohibitive as well.

3.2.3 Inner Detector

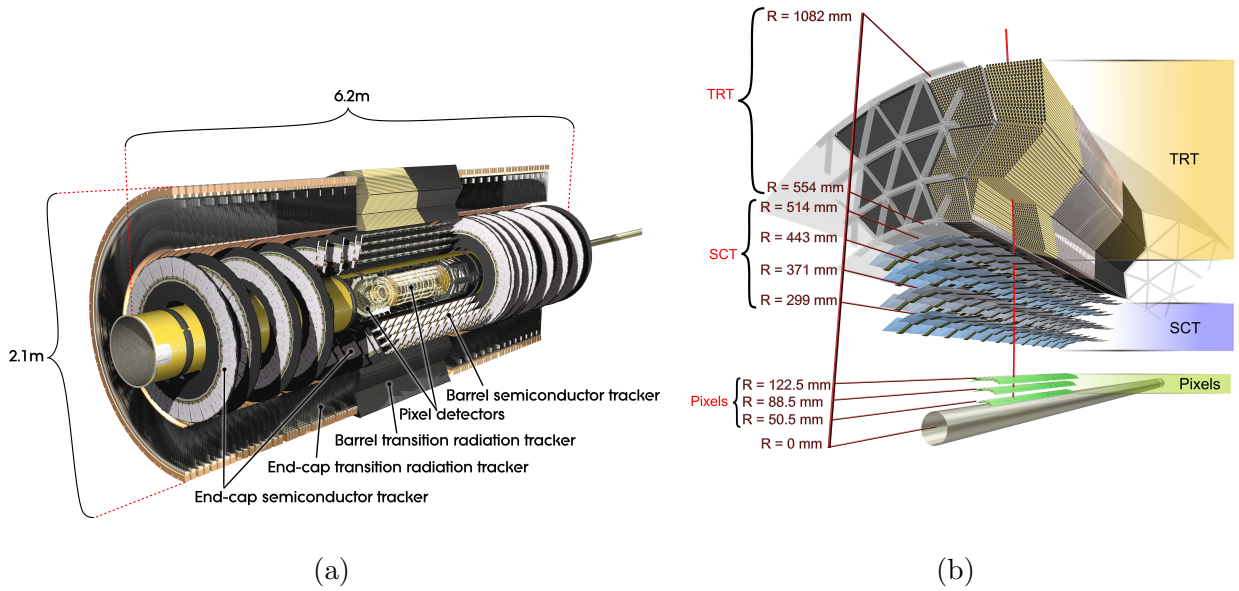


Figure 3.10: (a) Cut-away view of the ATLAS Inner Detector. (b) Cross-sectional view of the ATLAS Inner Detector. Taken from Reference [23].

The Inner Detector (ID) is the inner-most detector, closest to the IP and is used to track the trajectory of charged particles leading to the measurement of electromagnetic charge and momentum. The ID is immersed in the 2 T magnetic field provided by the central solenoid described in Section 3.2.2.1 and covers a pseudorapidity range of $|\eta| < 2.5$ [28]. The three subdetectors within the ID can be seen in Figure 3.10, the Pixel, Semiconductor Tracker

(SCT), and the Transition Radiation Tracker (TRT). Like the toroid system, and many of the other subdetectors, the ID is comprised of barrel and end-cap segments. The ID barrel section is 1.6 m in length and covers $|\eta| < 1$ while the end-caps measure over 7 m in length and cover $1 < |\eta| < 2.5$.

A track is considered good if there are hits in at least 3 pixel layers and 8 strips [29]. The ID tracking system was designed with a resolution of

$$\frac{\sigma_{p_T}}{p_T} = 0.05\% p_T \oplus 1\% \quad (3.7)$$

3.2.3.1 Pixel

The detector closest to the beam and IP is the Pixel Detector. The Pixel Detector is designed to measure particle hits with high-precision and high-granularity. The barrel Pixel detector consists of three layers of n-type silicon substrate with n-type implants. The closest layer to the IP sits at 50.5 mm and the outermost layer extends out to 12 cm. This combination gives the Pixel Detector the ability to determine the impact parameters of collisions with incredible precision. Due to the high radiation dose this close to the IP, the Pixel Detector was designed to be operated only in partial depletion. Each pixel cell measures $200\mu m \times 400\mu m \times 250\mu m$. There are five Pixel disks on each end-cap of the ID. In total there are 1,744 modules, with 46,080 readout channels per module, giving over 80 million channels with a spatial resolution of $10\mu m(R - \phi) \times 115\mu m(z)$ [30].

In order to keep up with the increased demand of Run-2 data taking conditions, an additional layer of pixels was installed in the Long Shutdown 1 (LS1) between 2013 and 2015. This Insertable B Layer (IBL) provides even finer granularity tracking with pixel cells measuring $50\mu m \times 250\mu m$ installed at a radial distance of $R = 33.25$ mm from the IP and a

spatial resolution of $8\,\mu m(R - \phi) \times 40\,\mu m(z)$ [31]. The IBL has proved incredibly useful in the reconstruction of displaced vertices from processes like b -jet hadronization and $\gamma \rightarrow e^+e^-$.

3.2.3.2 Semiconductor Tracker

Moving radially outward, at a radial distance of $299\,mm \leq R \leq 544\,mm$, the next subdetector is the SCT that provides tracking in the intermediate radial range from the IP and covers a range of $|\eta| < 2.5$. Similar to the Pixel Detector, the SCT has 4 barrel layers and 9 end-cap wheels on each side. The SCT provides four measurements per track via silicon microstrip detectors. Each microstrip is made of two $6.36 \times 6.40\,cm^2$ detectors glued end to end so each microstrip is $12.8\,cm$ long. Two microstrips are then glued back to back with a $40\,\mu rad$ angle. In total there are 768 strips, giving 6.2 million readout channels. The SCT has a spatial resolution of $17\,\mu m(R - \phi) \times 580\,\mu m(z)$ and can distinguish tracks with as small as a $200\,\mu m$ separation [28].

3.2.3.3 Transition Radiation Tracker

The final subdetector of the ID is the TRT ($R = 554\,mm - 1082\,mm$) . Instead of silicon detectors the TRT uses 4 mm diameter straw tubes; a hollow tube with a sense wire that is held at high voltage in the middle. The maximum length of a straw is 150 cm. The straws are filled with a gaseous mixture⁷ of 70% Xe, 27% CO₂, 3% O₂. Charged particles ionize the gas mixture, thereby releasing an electron and an ion. The ion drifts to the straw surface and the electron drifts to the wire; this charge drift is then measured as a signal. The TRT checks the signals against two thresholds, a lower threshold for measuring the drift time to

⁷During Run-2 the Xe was replaced with Ar as a cost saving measure. Ar provides similar performance as Xe in tracking, but is less efficient in absorbing X-rays from transition radiation.

derive a position and a higher threshold that is used to identify transition radiation X-rays. Transition radiation occurs when a charged particle hits the boundary of two media with differing dielectric constants. The higher threshold provides discriminating power between charged pions and electrons.

The TRT consists of a barrel section and 18 wheels in each end-cap. In the barrel, there are 50,000 straws divided in two at the center to allow for two separate readouts. The end-caps have 320,000 straws. In total, there are 420,000 readout channels. Each straw provides a spatial resolution of $170\mu\text{m}$ [28].

3.2.4 Calorimeters

The ATLAS detector makes use of two types of sampling calorimeters, one that uses liquid argon as the active medium and another that uses scintillating plastic tiles. Both types of calorimeters are designed to fully absorb particles via showering. Incoming particles interact with an absorber material and generate secondary particles. Those secondary particles interact with the absorber and create another set of particles. This cascading effect creates showers of particles inside the calorimeters. The shape and depth of these particles is important in the design choices for the calorimeters as well as particle identification. Two helpful variables when talking about shower depth are radiation length χ_0 and nuclear interaction length λ . χ_0 is defined as the distance where a particle has lost energy via bremsstrahlung⁸ equal to $\frac{1}{e}$, whereas λ is the mean free path of a hadron before undergoing a inelastic nuclear interaction. In order to fully absorb a wide energy range of incident particles the calorimeters are designed such that any path through them is at least $25 \chi_0$ or 10λ [32, 26]. Figure 3.11 shows the calorimeter layers and their nuclear interaction lengths as a function of η .

⁸ χ_0 can also be defined as $\frac{7}{9}$ of the mean free path of a high energy photon.

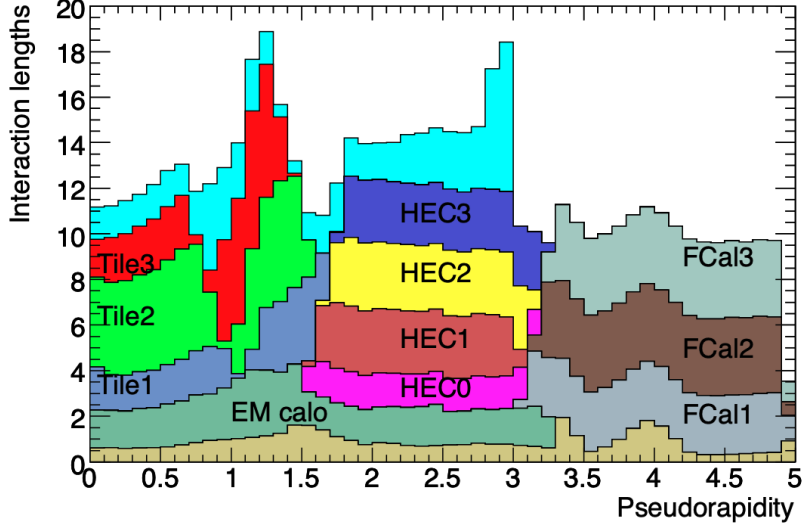


Figure 3.11: Interaction lengths as a function of η in the ATLAS calorimeters. The unlabeled brown color is the material in front of the EM calorimeters and the unlabeled cyan is the amount of material in front of the first active layer of the muon spectrometer [33].

The design resolution of the calorimeters can be seen in Table 3.3.

Table 3.3: Design resolution of EM and hadronic calorimeters in the ATLAS Detector [32, 26].

Calorimeter	Pseudorapidity range	Resolution
Electromagnetic	$ \eta < 3.2$	$\frac{\sigma}{E} = \frac{10\%}{\sqrt{E}} \oplus 0.7\%$
	$ \eta < 3.2$	$\frac{\sigma}{E} = \frac{50\%}{\sqrt{E}} \oplus 3\%$
Hadronic	$3.1 < \eta < 4.9$	$\frac{\sigma}{E} = \frac{100\%}{\sqrt{E}} \oplus 10\%$

The layout of calorimeters in the ATLAS detector can be seen in Figure 3.12.

3.2.4.1 Liquid Argon Calorimeters

The Liquid Argon (LAr) calorimeters are based on a similar principle to the straw tubes of the TRT described in Section 3.2.3.3. In this case, the LAr is the active medium that is ionized by the incoming particle. The free electron then drifts to an electrode, copper-tungsten in the

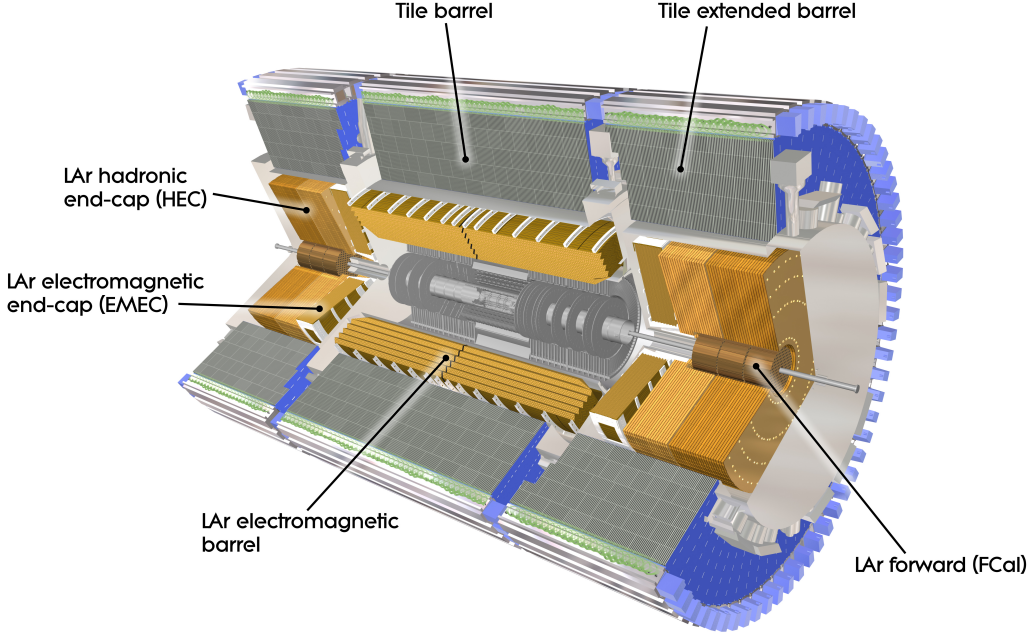


Figure 3.12: Cut-out view of the ATLAS detector’s calorimeters [23].

case of the barrel LAr calorimeter. The drifting electrons are then readout as an electrical signal; there are approximately 180,000 LAr readout channels in the ATLAS detector. LAr was chosen as the active medium due to its intrinsic radiation hardness, stability over time, and linear response. The LAr must be kept at very cold temperatures, around 85 K. To achieve this, the LAr calorimeters are kept in cryostats, the barrel calorimeter shares the cryostat and vacuum with the central solenoid.

There are four LAr calorimeters within the ATLAS detector. The EMB is designed for electromagnetic calorimetry with a lead-stainless steel absorber and covers a pseudorapidity range of $|\eta| < 2.5$. Extending to larger η is the LAr Electromagnetic End-Cap (EMEC) that also uses lead-stainless steel absorber and the LAr Hadronic End-Cap (HEC) which has a copper plate absorber; both EMEC and LAr Hadronic End-Cap (HEC) cover $1.5 < |\eta| < 3.2$. The final LAr calorimeter is the aptly named LAr Forward Calorimeter (FCAL) that covers $|\eta| < 4.9$ and has three modules. The first is optimized for EM calorimetry and uses a copper

absorber. The other two FCAL modules are used to measure hadronic showers and use tungsten absorbers.

The EMB and EMEC both utilize an accordion geometry pictured in Figure 3.13 to ensure a full ϕ coverage. The EMB consists of four layers, the first being a LAr presampler of 1.1 cm

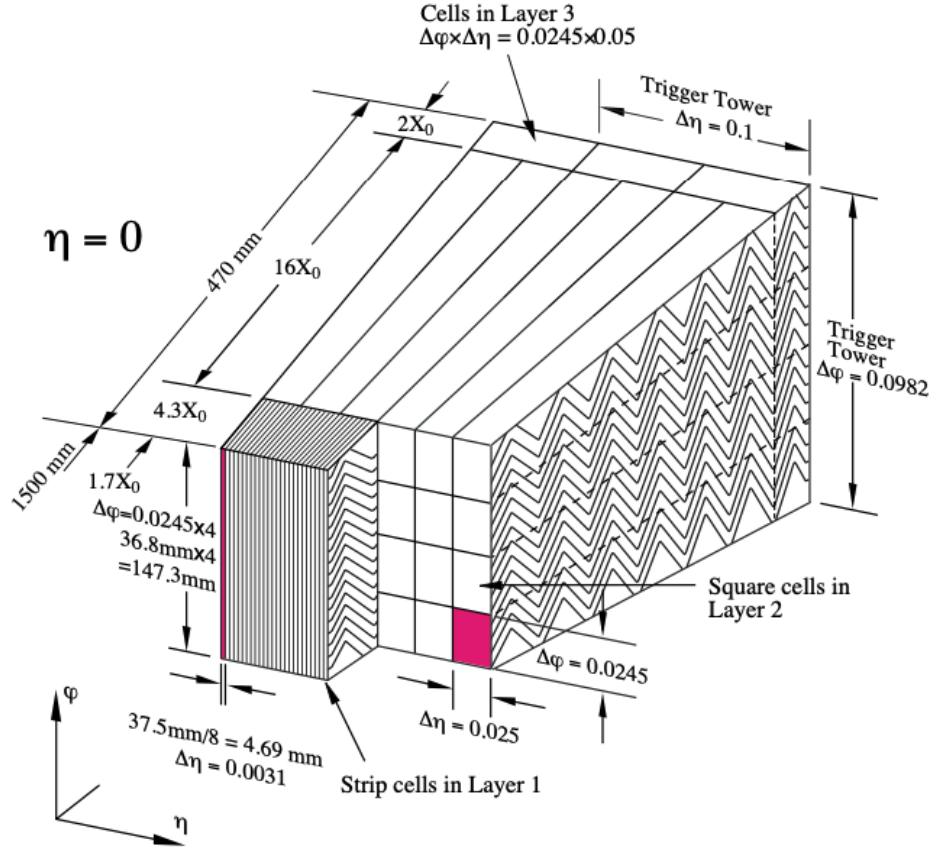
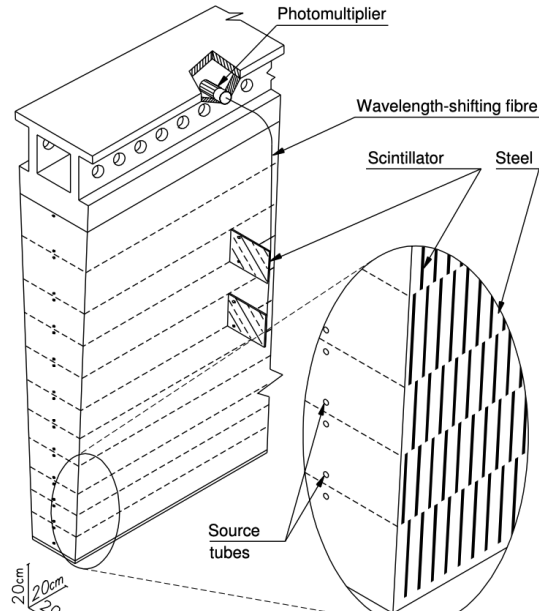


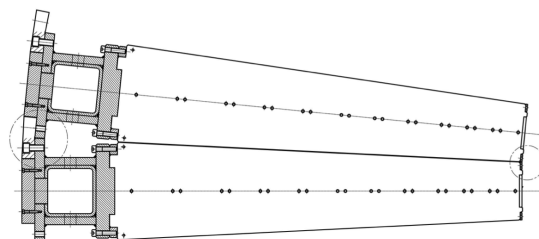
Figure 3.13: An EMB module showing the accordion geometry and granularity [32].

thickness. The presampler is used to correct for energy losses due to material in front of the calorimeter. The first layer after the presampler is finely segmented to ensure good position measurements. The second layer is $16 \chi_0$ thick and collects most of the electromagnetic showers. Typically, only the tails of EM showers make it to the third and final layer, so a coarser granularity is used. Detailed information on the design of the LAr calorimeters can be found in Reference [32].

3.2.4.2 Tile Calorimeter



(a)



(b)

Figure 3.14: (a) Diagram of an individual TileCal module. (b) Azimuthal view of two TileCal modules with the IP being to the right. Taken from Reference [26].

The hadronic TileCal is a sampling calorimeter that is designed to fully absorb hadronic showers covering a range of $|\eta| < 1.7$ at a radial distance of $2.28 \text{ m} \leq R \leq 4.25 \text{ m}$ from the IP. This radial distance translates to approximately 7.4λ . A similar design of absorber and electrode is used in TileCal to capture the full energy of hadronic showers. TileCal uses a steel absorber. However, instead of a liquid or gas being ionized and the free electrons

being collected as a signal, TileCal takes advantage of a special material called scintillating plastic. When an ionizing particle interacts with the scintillating plastic, light is created; this light is absorbed in wavelength shifting fibers. It is then re-emitted and transmitted to Photomultiplier Tubes (PMTs). The PMT signal is then shaped, amplified at two gains with a ratio of 64:1, then digitized at 40 MHz with 10-bit analogue-to-digital converters. Each cell within TileCal has 2 PMTs, giving over 10,000 readout channels. There are 256 modules within TileCal. A diagram of an individual module and the layout of two modules side-by-side can be seen in Figure 3.14.

A significant fraction of the author’s time and effort during their PhD went to data quality monitoring and maintenance of TileCal. These works are detailed in Appendix A.

3.2.5 Muon Spectrometer

High momentum muons provide a vital signature at the LHC. Muons are minimally ionizing particles, meaning they leave a small amount of energy inside detectors and travel to the edge and beyond the volume of the ATLAS detector. Instead of attempting to fully absorb muons, high precision position measurements are taken to track their trajectories. The toroid magnet system described in Section 3.2.2.2 is an integral part of the Muon Spectrometer (MS); it provides the bending force, changing the trajectories to the direction of the beamline. The barrel section of the MS consists of three concentric cylindrical shells at $R = 5\text{ m}, 7.5\text{ m}, 10\text{ m}$ made of Monitored Drift Tubes (MDTs) ($|\eta| < 1$) [34]. These cylindrical shells sit in-between and on the air core toroid magnets. On the 2nd and 3rd shells are Resistive Plate Chambers (RPCs) that provide quick triggering. Complimenting the barrel section are the end-caps, referred to as wheels for the MS. The wheels are placed at $|z| \approx 7.4\text{ m}, 10.8\text{ m}, 14\text{ m}, \text{ and } 21.5\text{ m}$ ($2.0 < |\eta| < 2.7$). The innermost layer of these wheels experience the highest rates of incident

particles. To cope with this, Cathode Strip Chambers (CSCs) with a finer granularity than the MDTs that are used in the barrel. Similarly, Thin Gap Chambers (TGCs) are used for triggering instead of RPCs. These wheels provide spatial coordinates orthogonal to those of the precision-tracking MDTs in the barrel. Figure 3.15 shows the positioning of the various MS components. Detailed information on the design of the MS can be found in Reference [34].

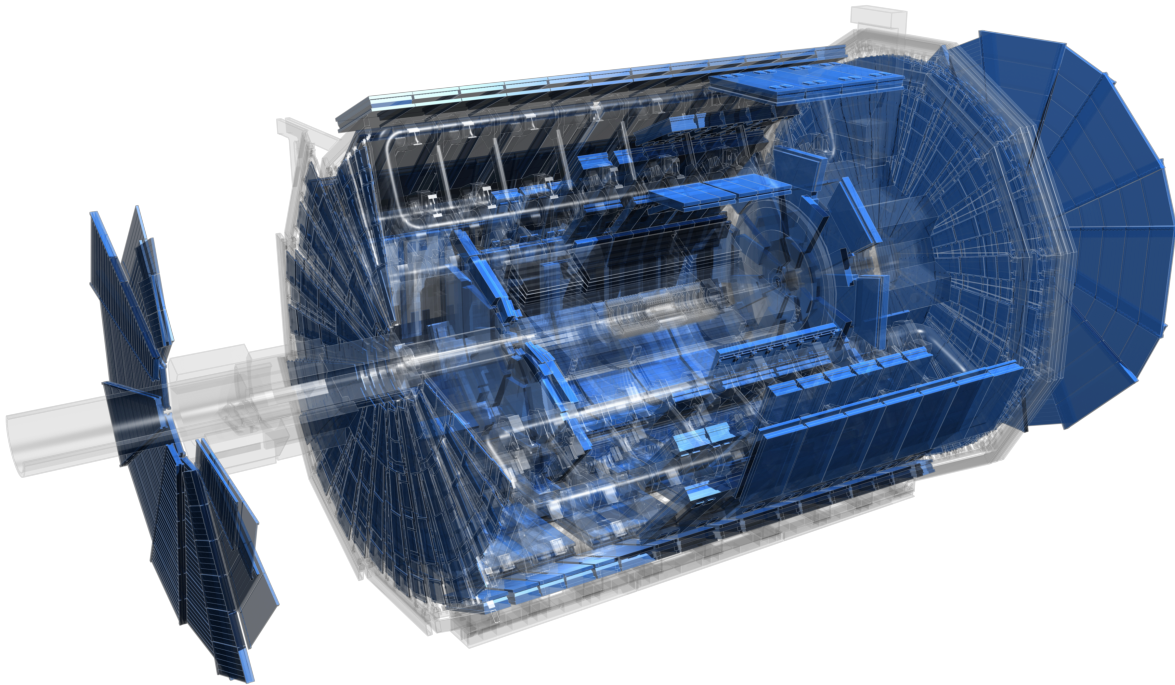


Figure 3.15: Cut-out view of the ATLAS detector Muon Spectrometer [23].

3.2.6 Trigger System

The large luminosity provided by the LHC is critical in collecting enough data to make detailed physics analyses. However, it also means that there is an incredibly large amount of data to sort through. So much that it is not possible to write out the data from every bunch

crossing. As shown in the bottom inlay of Figure 3.6, even one single event can contain a very large amount of data. Another issue arises due to the nature of hadron collisions; not all bunch crossing provide hard scatter inelastic collisions that are interesting enough to save data on.

To solve this issue, the data coming out of ATLAS is combed through in real time at a variable rate of 1 kHz to 40 MHz. This is done with a TDAQ system. The TDAQ system used in Run-2 is described in detail in Reference [35]. The TDAQ system reads in data from the ATLAS detector, calculates relevant quantities, and makes a decision on if there was an event worth storing. A diagram showing the data flow into the TDAQ system⁹ is shown in Figure 3.16. The ATLAS TDAQ system consists of two main components, Level-1 Trigger (L1 Trigger) and High Level Trigger (HLT). The L1 Trigger is a hardware based trigger system that reads in data from the calorimeters and muon spectrometer. The L1 Trigger has a latency of $2.5\ \mu\text{s}$ and can read-out accepted events up to 100 kHz, the detector maximum readout rate. The HLT is a software based trigger system based on the offline reconstruction software. During Run-2 the HLT operated with an average output rate of 1.2 kHz, which translates to about 1.2 GB/s of data sent to permanent storage.

After the TDAQ system accepts an event, the data is set to be stored on magnetic tape for long term storage. It is also processed at the local computing farm named Tier-0 with the full reconstruction software suite described in Chapter 5.

⁹Figure 3.16 shows the Fast TracKer (FTK). During Run 2 FTK was undergoing commissioning and was not used in the active TDAQ system.

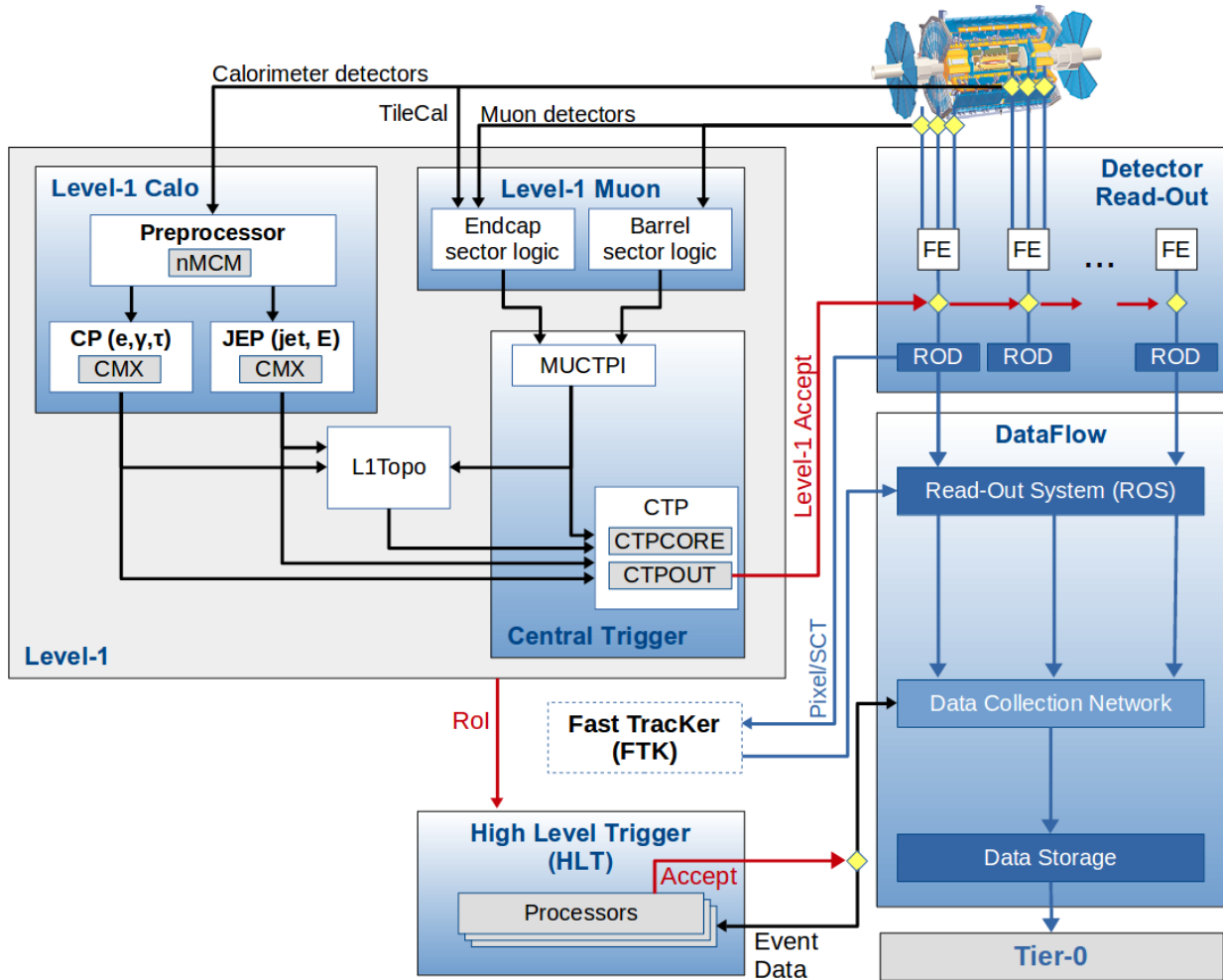


Figure 3.16: The ATLAS TDAQ system in Run-2 showing the components relevant for triggering as well as the detector read-out and data flow [36].

CHAPTER 4

SIMULATION

The data collected by the ATLAS experiment must be compared to a well understood dataset. This dataset is most often a dataset of simulation particle collisions that aim to mimic physics processes and particle interaction with detector material, as well as the detector's response. Figure 4.1 shows the chain of simulations by which these datasets are produced.

Many particle physics experiments, ATLAS included, use MC simulation techniques to produce these datasets. Monte Carlo simulation techniques use repeated random sampling of underlying probability density functions to closely model various processes.

4.1 Event Generation and Hadronization

Since protons and other hadrons are not fundamental particles, it is impossible to know the exact constituents (partons) that interacted during a collision. To mimic this intrinsic probabilistic nature, Parton Distribution Functions (PDFs) are used. A Parton Distribution Function (PDF) models the probability of any parton within a proton (or hadron) to carry a fraction of the beam energy at a given hadron momentum. The PDF and subsequent inelastic hard scattering of the interacting partons are modeled via a Matrix Element (ME) calculation, which can be depicted through Feynman diagrams. This ME calculation is done to fixed order in perturbation theory, Leading Order (LO), Next-to-Leading Order (NLO), Leading-Logarithmic Order (LL), etc. This first level event generation can be done by a

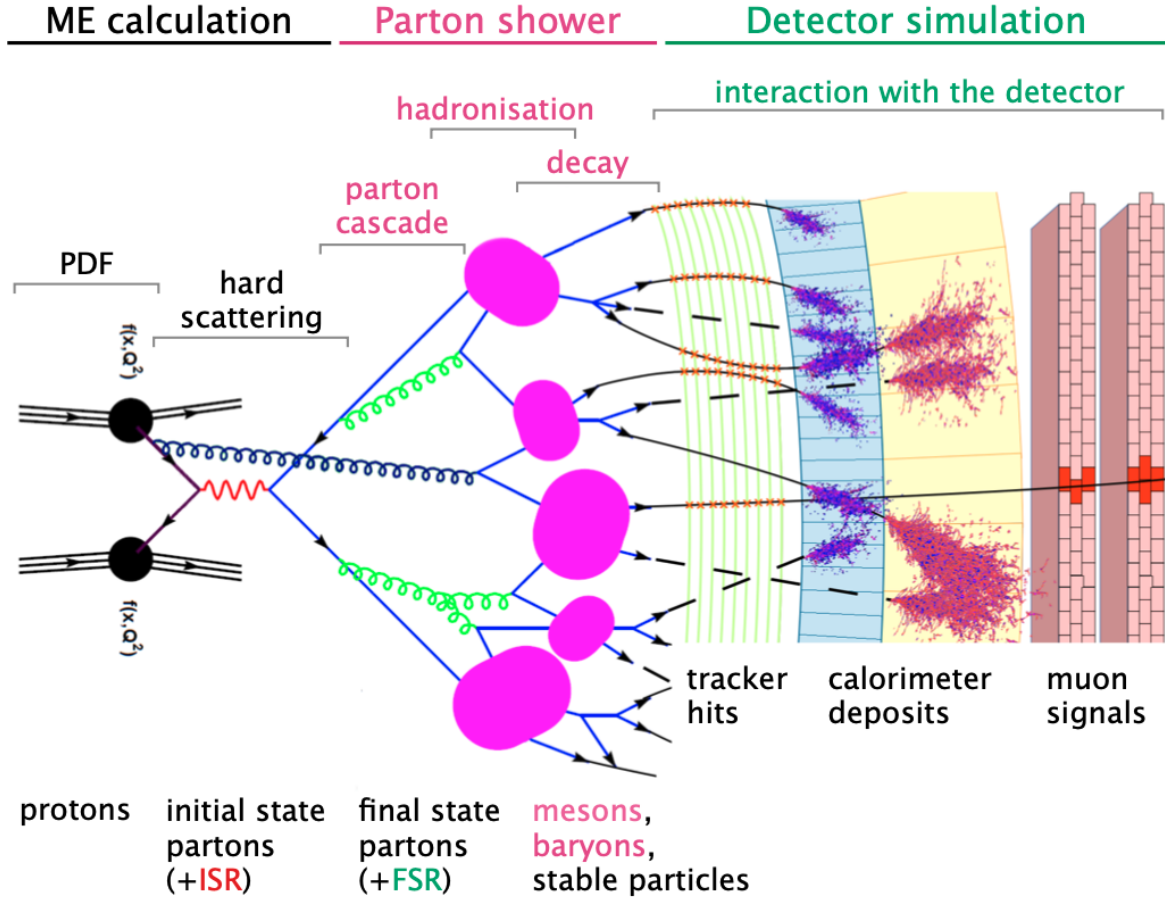


Figure 4.1: A pictorial representation of the simulation chain used in the ATLAS experiment [37].

myriad of MC event generators. Often specific choices are made based on individual generator performance for a given physics process.

The next step in the simulation chain is the parton showering and hadronization. This can be done with a different set of MC simulations. Parton showering and hadronization are complex, computationally expensive steps to simulate and are done iteratively. An example of a parton shower generator output can be seen in Figure 4.2.

The MC generators used in this dissertation for background simulations are Pythia [38], Powheg-Box [39, 40], and Sherpa [41]. For signal, MadGraph is used [42]. For all processes,

Pythia8 is used to simulate the parton shower, fragmentation, and underlying event. Table 4.1 shows which MC generator is used for each background process.

Table 4.1: MC generators for the main SM background samples at $\sqrt{s} = 13$ TeV used in this dissertation. Here, ℓ refers to the three lepton families e , μ and τ .

Background process	Generator & parton shower
$t\bar{t}$ with at least one lepton ℓ	Powheg & Pythia8
Single top-quark	Powheg & Pythia8
$W(\ell\nu) + \text{jets}$	Sherpa
$Z/\gamma^*(\ell\ell, \nu\nu) + \text{jets}$	Sherpa
WW	Powheg & Pythia8
WZ	Powheg & Pythia8
ZZ	Powheg & Pythia8

4.2 Detector Simulation

The final step in the simulation chain is simulating the particle's interaction with the detector material and the detector's response. Up until this point, the MC generators used are generic non-experiment dependent simulations. The ATLAS collaboration uses a GEANT4 based generator suite to simulate these interactions [43]. These detailed simulations include all support structure, material densities, readout electronics, and digitization in order to fully simulate the path of a real particle through the ATLAS detector. These simulations are often too slow to produce enough statistics for physics analyses. In the full simulation, around 80% of the simulation time is spent on particles traversing the calorimeters and 75% is spent on electromagnetic particles alone [44]. Instead, several methods were developed to speed up the simulation known as FAST simulations. A detailed description of the ATLAS simulation chain and options can be seen in Reference [44]. The final simulated dataset is output into a raw data format identical to real data coming off of the ATLAS detector.

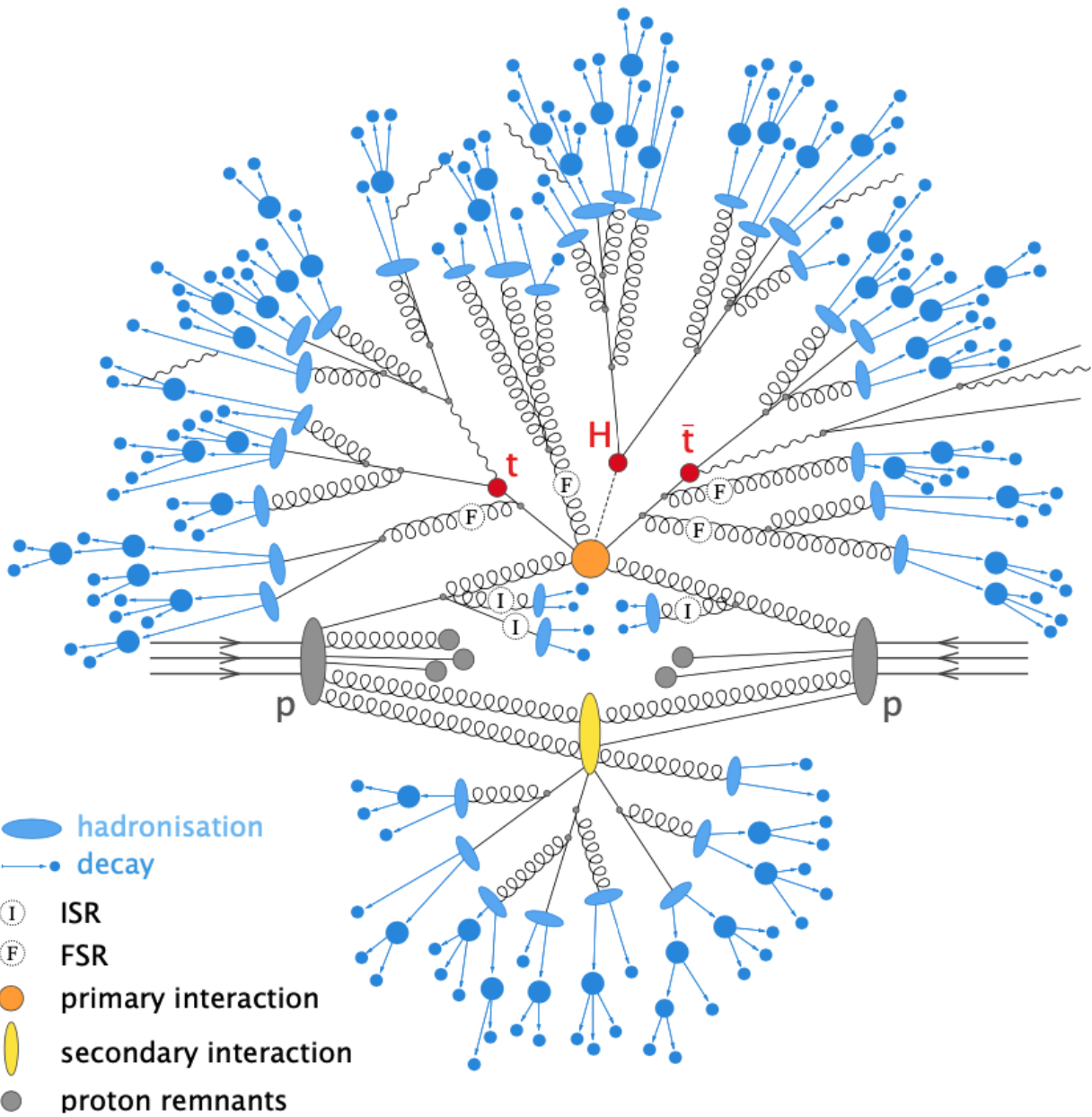


Figure 4.2: A pictorial representation of a parton shower of a $t\bar{t}H$ event [37].

CHAPTER 5

EVENT RECONSTRUCTION

Before any physics analysis can be performed on the raw data from the ATLAS detector or MC simulations the raw datasets go through a reconstruction software suite called Athena [45]. Various algorithms are employed to identify energy deposits as particles based on shower shapes, tracker hits, calculated charge to mass ratios, etc. Figure 5.1 shows the signatures of various particles within the ATLAS detector.

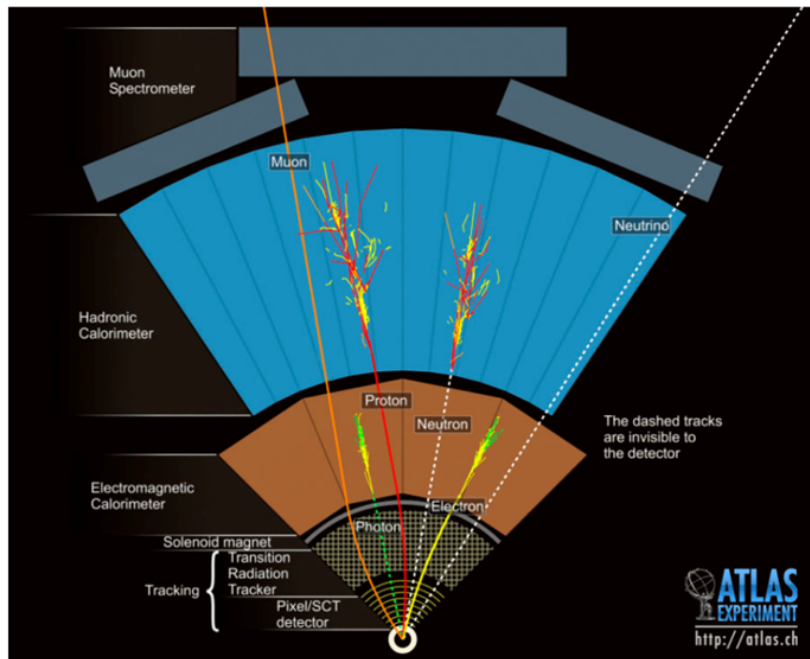


Figure 5.1: Cross section view of the ATLAS detector with subdetectors labeled. Various types of particles radial trajectories are shown [33].

The following sections detail the identification processes of muons, electrons, photons, jets, τ leptons, and a calculated quantity called missing transverse energy (E_T^{miss}). These reconstructed physics objects are the inputs to the majority of physics analyses.

5.1 Tracks

Tracks are made from fit-connecting three-dimensional space-points in the ID. These space-points are created from clusters of hits in the ID. A set of three space-points are combined into one track seed, then fed into three methods in the ATLAS detector: inside-out, outside-in, and TRT-standalone. The inside-out method creates tracks by starting with a seed hit in the pixel detector, then SCT hits are added, finally the track is extrapolated out into the TRT. This method creates tracks of particles that are mostly produced in the hard pp interaction and has a requirement of $p_T > 400$ MeV. On the other-hand the outside-in method starts with track segments in the TRT and extrapolates towards the beamline using silicon that were not used in the inside-out method. Outside-in tracking typically reconstructs secondary vertices from particles that have long enough lifetimes to decay while inside the ID, including b quarks and τ leptons. Lastly, TRT-standalone tracks are made only from seeds within the TRT and are not extrapolated to the silicon subdetectors [46]. The reconstructed tracks are used in the identification of various types of particles.

5.2 Topological Clusters

A topocluster is defined as a cluster of topologically connected calorimeter cell signals. Topological clusters in the ATLAS detector’s calorimeters are vital to the identification of hadronic final states, meaning jets (Section 5.5), isolated hadrons, and hadronically decaying τ leptons (Section 5.6). Topoclusters are also included in the calculation of missing transverse energy discussed in Section 5.7, as they represent the direction and energy of softer particles in a collision event.

A topocluster is created via a growing volume algorithm that operates based on a set of three thresholds. These thresholds are defined using the calorimeter cell significance ξ_{cell} [47]:

$$\xi_{cell} = \frac{E_{cell}}{\sigma_{noise,cell}} \quad (5.1)$$

where E_{cell} is the energy in the calorimeter cell and $\sigma_{noise,cell}$ is the average expected noise of a given calorimeter cell. An in-depth review of how the $\sigma_{noise,cell}$ value is calculated for TileCal is given in Appendix A. A topocluster starts with a seed cell that has a significance greater than the seed threshold S . From the seed cell, all three-dimensionally neighboring cells with a significance greater than the growth threshold N are added to the topocluster. This is done repeatedly until there are no more neighboring cells that pass the requirement $|\xi_{cell}| > N$. If a neighboring cell also passes the $|\xi_{cell}| > S$ threshold, then the topocluster corresponding to the neighbor cell is merged into the original topocluster. Finally, a last layer of the topocluster is added from all neighboring cells passing a threshold of $|\xi_{cell}| > P$. In the ATLAS experiment, the threshold values are set at $(S, N, P) = (4, 2, 0)$.

5.3 Muon Identification

Muons are identified using a combination of information from the ID and the MS. Within the ID, muons leave tracks identical to any other charged particle; however, in the MS tracks are identified within the MDTs through a straight-line fit in a single layer and by doing a combinatorial search of CSC hits in the $\eta - \phi$ plane [48]. Muons are identified through five strategies, each using the information from the ID, MS, and calorimeter (in one case).

- Combined (CB): Match ID and MS tracks. Perform a combined track fit on ID and MS hits. Takes into account energy loss in calorimeters

- Inside-Out (IO): Extrapolate ID tracks, look for at least three loosely aligned MS hits. Calorimeter energy loss is accounted for.
- Muon Spectrometer Extrapolated (ME): Extrapolate MS tracks back to the beamline. No ID hits are taken into account.
- Segmented-Tagged (ST): Extrapolate ID tracks and match to MS segments with tight angular requirements. Muon parameters are taken directly from the ID.
- Calorimeter-Tagged (CT): Extrapolate ID tracks into the calorimeters. Look for energy deposits consistent with minimum ionizing particles. Tag as muon, take parameters from ID.

All muon identification strategies have a transverse momentum cut on ID tracks of $p_T^{track} > 2$ GeV, except for CT, which has a cut on the transverse momentum of the tracks of $p_T^{track} > 5$ GeV.

Reconstructed muons are divided into three Working Points (WPs) to allow analyzers a choice of purity, efficiency, and background rejection [48]:

- Loose: Optimized for reconstruction of $H \rightarrow 4\mu$. Lowest purity and highest efficiency.
- Medium: Efficiency and purity are suitable for a wide range of analyses with small systematic uncertainties.
- Tight: High purity, slightly lower efficiency than medium WP. Significantly higher background rejection.

More details on the requirements on muon objects can be found in Reference [34]. The analysis discussed in this dissertation uses the Loose WP for muons to allow for larger statistics in the signal region.

To ensure muons originated at a hard-scatter and discriminate them from muons in hadronic decays an isolation requirement is applied. The isolation is defined as the transverse energy (momentum) inside a reconstructed cone around the muon divided by the muon p_T [34]. This isolation can be calculated either using calorimeter information (energy) or ID information (momentum). As with identification, several isolation WPs are defined. This dissertation uses a tight isolation requirement.

5.4 e- γ Identification

Electrons and photons deposit the majority of their energy in the EM calorimeters in similar fashion. Electrons produce Bremsstrahlung photons as they interact with the EM calorimeter, the produced photons then convert into an electron-positron pair. This process repeats and produces a shower. A photon that is produced in the ID and travels to the EM calorimeters creates a very similar shower by converting into an electron-antielectron (positron) pair. The discerning difference between an electron's signature and that of a photon is the presence of tracks that match to spatial coordinates of the showers in the EM calorimeters. An electron carries an EM charge, thus leaving a track in the ID; whereas a photon does not carry an EM charge, therefore does not leave a track. The process of identifying an EM shower as either electron initiated or photon initiated is detailed in Ref [49]. A brief algorithm flow chart of this process can be seen in Figure 5.2. If tracks in the ID are found to match a topocluster in the EM calorimeter, then it is identified as an electron, re-clustered into so called superclusters to ensure the full shower is captured, calibrated, then lastly made into an analysis object for use in physics analyses. The same algorithm is used to identify photons with the exception of matching tracks to the ID. Instead, photons are matched to conversion vertices where the initial photon first converted into an electron-positron pair.

Both electrons and photons are reconstructed at three WPs. As with muons, there are three WPs, Loose, Medium, and Tight; the stricter WPs being subsets of the looser WPs. The analysis discussed in this dissertation uses the Loose WP for electrons.

To ensure that an electron or photon is indeed an initial particle and not part of another shower, whether it be from a converted photon in a hadron decay, electrons from heavy flavor hadrons or a light hadron mis-identified as an electron, an isolation variable is calculated. The isolation variable is based on track isolation and defined as the sum of transverse momenta of all tracks within a cone around the electron candidate of $\Delta R = 0.2$ or in the case of high energy photons, $10 \text{ GeV}/E_T$, where E_T is the transverse energy of the electron.

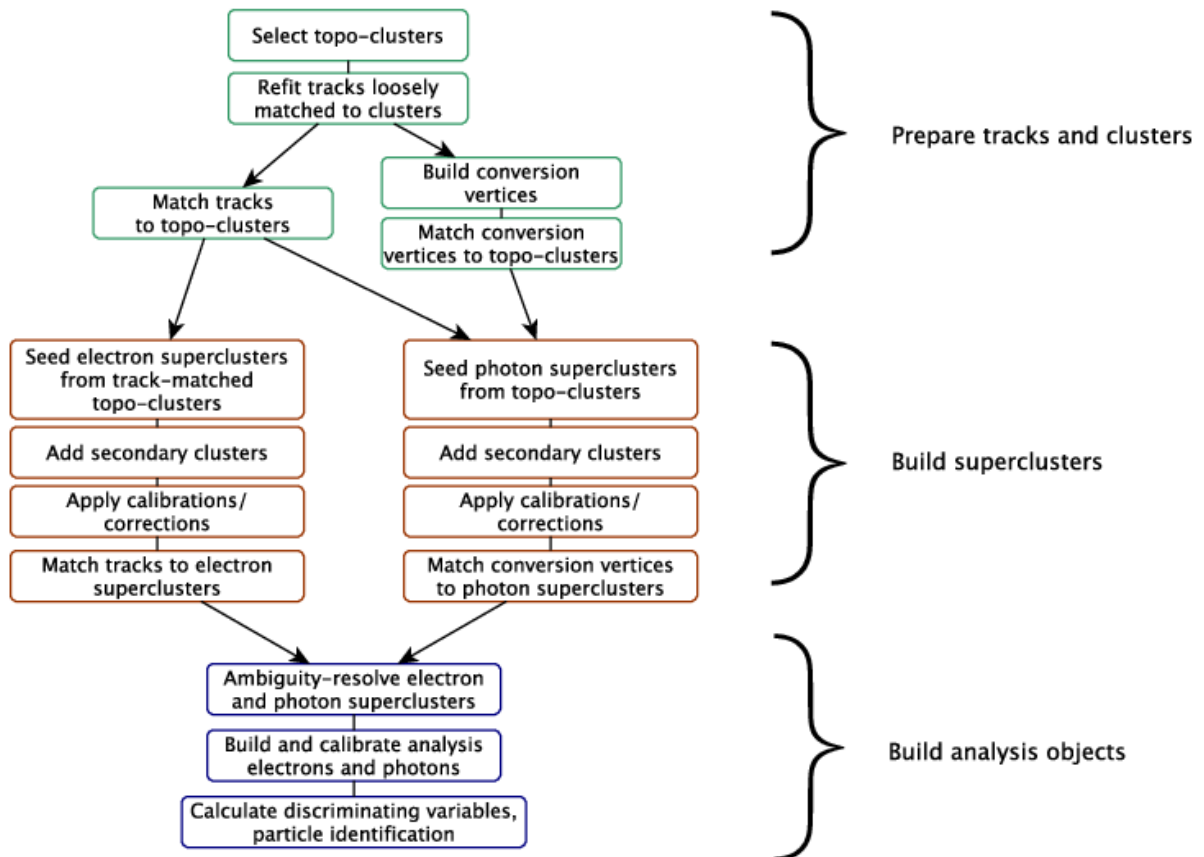


Figure 5.2: Algorithm flow diagram for the electron and photon reconstruction [49].

5.5 Jets

A jet is a reconstructed object that is meant to capture the energy¹ and direction of a hadronic shower, typically initiated from hard scatter quarks, hadrons, or gluons. There are several algorithms available to perform a clustering of calorimeter topoclusters to form jets. This dissertation uses jets created from particle flow objects. The particle flow algorithm is described in detail in Reference [50]. A flow chart of the algorithm is shown in Figure 5.3 and an idealized example of the particle flow algorithm performing the reconstruction of hadrons is shown in Figure 5.4.

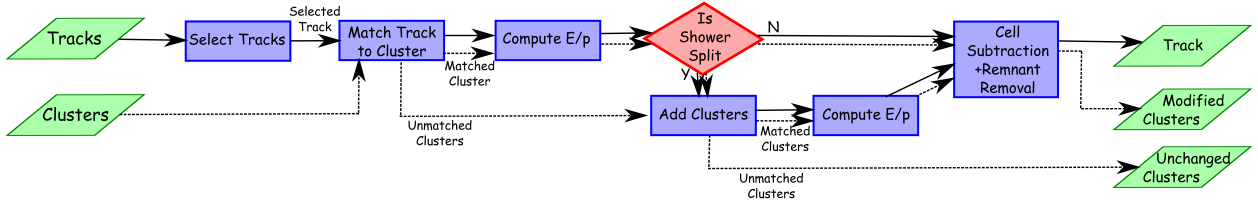


Figure 5.3: A flow chart of how the particle flow algorithm proceeds, starting with track selection and continuing until the energy associated with the selected tracks has been removed from the calorimeter. At the end, charged particles, topoclusters which have not been modified by the algorithm, and remnants of topoclusters which have had part of their energy removed remain [50].

The particle flow algorithm starts by matching selected tracks to a single topocluster. The expected energy of the initial particle in the calorimeter is calculated from the track momentum and the topocluster position. The probability of the track-topocluster system being deposited in multiple topoclusters is then calculated. The algorithm then adds in more topoclusters to the output object based on this probability. The expected energy of the initial particle is subtracted from the energy of the matched topoclusters cell by cell. If the energy of the output object is consistent with a single particle signal, then the remaining

¹The jet objects in this dissertation use the particle flow algorithm that includes track objects in the full jet energy calculation.

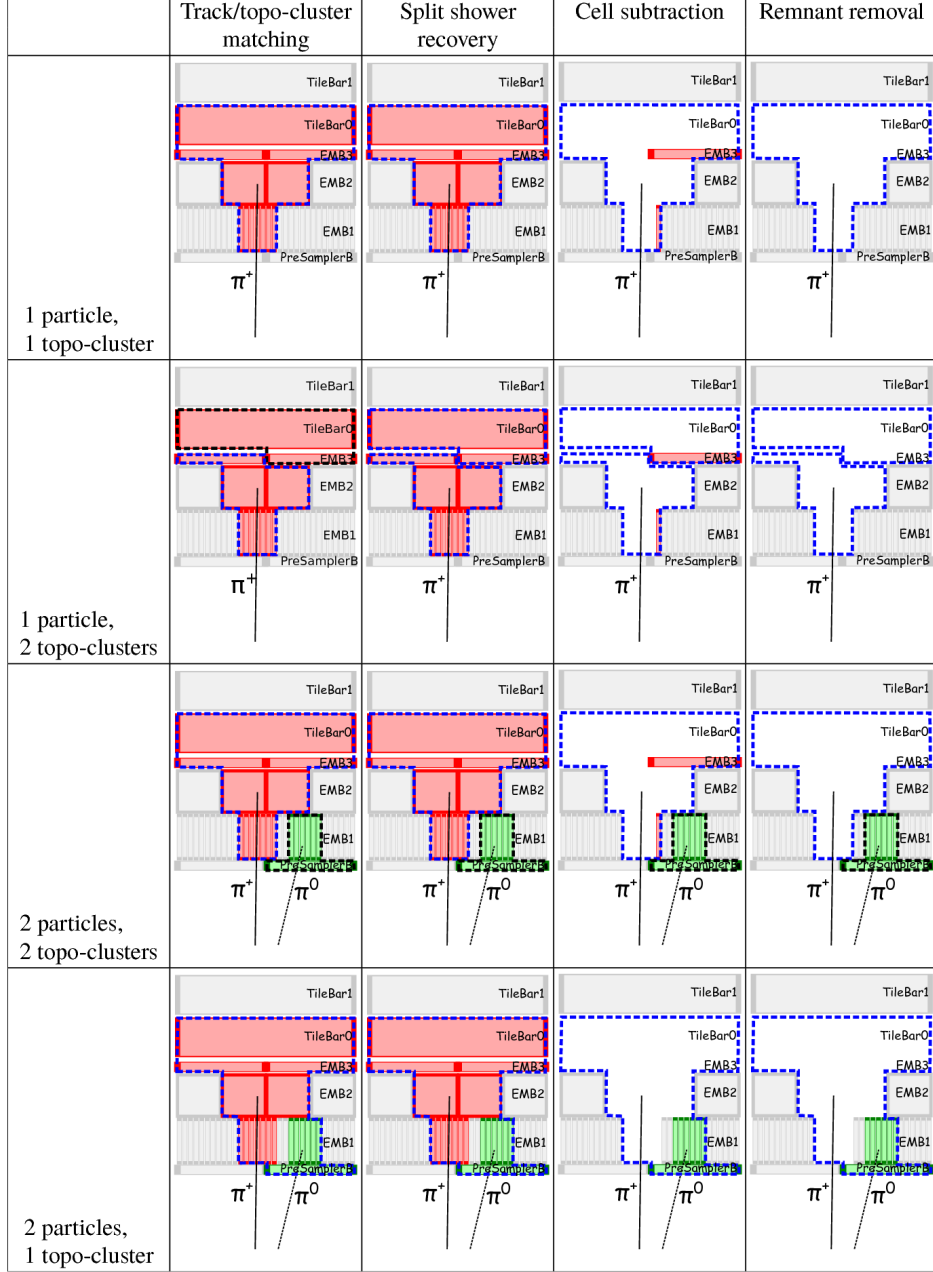


Figure 5.4: Idealized examples of how the algorithm is designed to deal with several different cases. The red cells are those which have energy from the π^+ , the green have cells energy from the photons in the π^0 decay, the dotted lines represent the original topocluster boundaries with those outlined in blue having been matched by the algorithm to the π^+ , while those in black are yet to be selected. The different layers in the EM calorimeter (Presampler, EMB1, EMB2, EMB3) are indicated. In this sketch only the first two layers of the Tile calorimeter are shown (TileBar0 and TileBar1) [50].

topocluster remnants are removed. The outputs of the particle flow algorithm are then fed into the anti- k_t algorithm [51] with a radius value of $R = 0.4$.

The anti- k_t algorithm is a jet-finding algorithm that is collinear and infrared safe, meaning the number of identified jets does not change due to splitting or merging of high transverse momentum particles, nor the presence of soft gluon emission between jets [52]. A jet is constructed in the anti- k_t algorithm through an iterative process using a the distance parameter defined as

$$d_{ij} = \min(k_{t,i}^{-2}, k_{t,j}^{-2}) \frac{\Delta_{ij}^2}{R^2} \quad (5.2)$$

where k_t is the transverse momentum, R is an input parameter defining the radius of the jet cone, and Δ_{ij} is the distance between objects i and j defined as

$$\Delta_{ij} = (y_i - y_j)^2 + (\phi_i - \phi_j)^2 \quad (5.3)$$

The anti-kt algorithm first identifies the smallest d_{ij} and clusters the particle flow objects if $d_{ij} > k_{t,i}^{-2}$. If $d_{ij} > k_{t,i}^{-2}$ then the particle flow object is discarded. This process continues iteratively until there are no more objects to consider. Objects with $\Delta > R$ are still considered, making the R input parameter an energy cut-off for clustering and not a direct radius value. Figure 5.5 shows the anti- k_t algorithm's performance compared to other jet-finding algorithms. The anti- k_t algorithm results in a more conical shape than other jet-finding algorithms; better encapsulating the shower profile of jets.

After jets are reconstructed, they must be calibrated at the jet energy scale. This process is detailed in Ref [53]. A flow chart showing the process of calibrating a jet is shown in Figure 5.6.

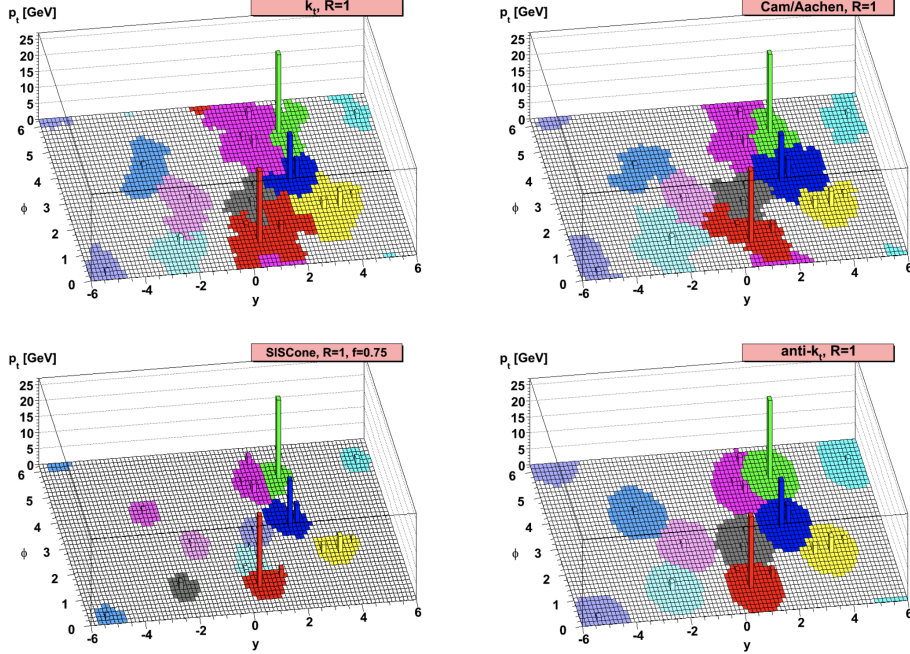


Figure 5.5: Comparison between several jet-finding algorithms [51].

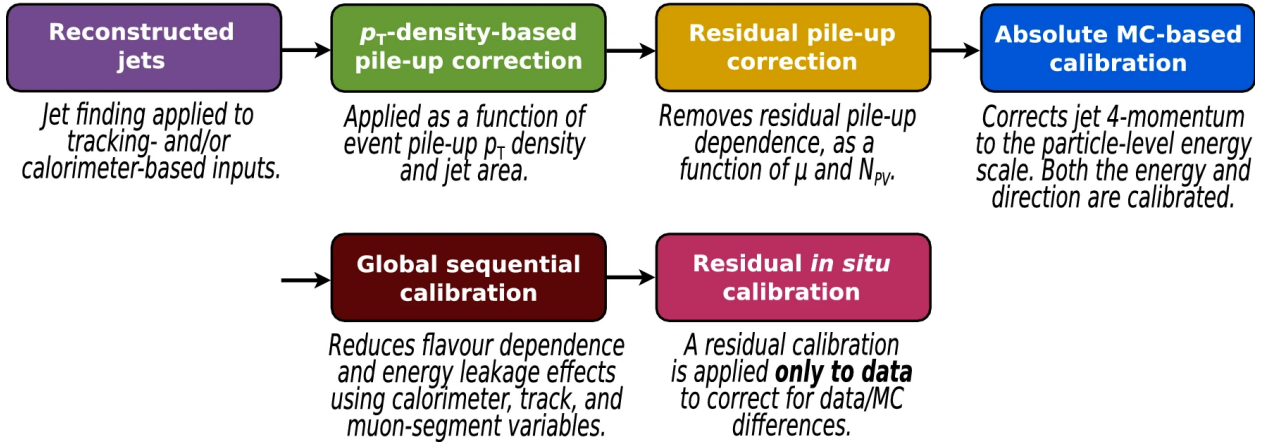


Figure 5.6: Stages of jet energy scale calibrations. Each one is applied to the four-momentum of the jet. Taken from Reference [53].

5.5.1 b-jet Tagging

Jets originating from hard scatter b quarks are an important signature in high energy physics colliders, especially so in the analysis discussed in this dissertation. An initial state b

quark hadronizes into B-hadrons which have a relatively long lifetime. Due to the relativistic speeds and long lifetime of the B-hadrons they travel a distance away from the IP before decaying and creating a hadronic shower. This leads to a secondary vertex that can be measured. A pictorial representation is shown in Figure 5.7. The impact parameter d_0 shown is the minimum distance between the tracks from the secondary vertex and IP.

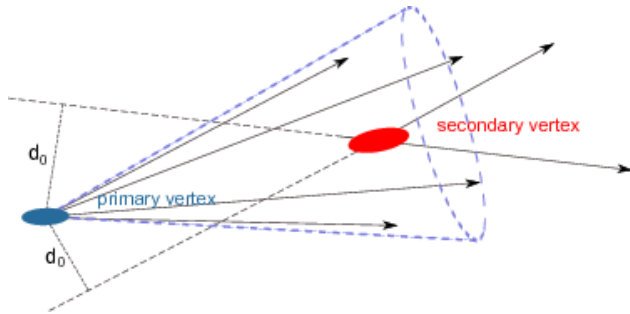


Figure 5.7: Schematic view of the tracks in a b -jet [54].

There are several methods used to tag a jet as coming from a b quark; this analysis uses the DL1 high level tagger [55] that is based on an artificial deep neural network. Neural networks are discussed in detail in Section 6.4. DL1 not only tags b -jets, but also outputs the probability for a jet to be initiated from a charm or light flavor quark. The DL1 tagger has over 20 input variables, including the p_T and η of jets [56]. The analysis discussed in this dissertation uses a fixed cut working point that corresponds to an average efficiency of 70% for b -jets in $t\bar{t}$ events.

5.6 τ Identification

One of the most important particles in the final state of the search discussed in this dissertation is the τ lepton. The decay channels of τ leptons make them difficult to reconstruct. A τ lepton can decay to hadrons, an electron, or a muon; in each decay mode, at least one neutrino is also present. Due to the great difficulty in discerning lepton τ decays from

true leptons, the analysis discussed in this dissertation only considers τ leptons that have decayed hadronically. The hadronic decay mode consists charged hadrons (π^\pm), a neutrino, and possible neutral hadrons (π^0). A τ lepton decaying in this manner within the ATLAS detector leaves tracks in the ID and collimated showers of energy in the calorimeters; the neutrino does not interact with the ATLAS detector, therefore no direct signature is left behind. Reconstruction is done on the visible part of the hadronically decaying τ lepton, further referred to as $\tau_{had-vis}$ in the rest of this dissertation.

The $\tau_{had-vis}$ candidates start with an anti- k_t jet seed with $E_T > 10$ GeV in the calorimeter; tracks and topoclusters within $\Delta R = 0.2$ are added to the $\tau_{had-vis}$ candidate. The axis of the original jet seed is redefined in the direction of the $\tau_{had-vis}$ candidate and calibration is done at the $\tau_{had-vis}$ scale [57]. An overlap removal is done to ensure the $\tau_{had-vis}$ candidate is isolated from electrons and muons. Tracks are required to have $E_T > 30$ GeV, $|\eta| < 2.3$ and strictly either 1 or 3 tracks. A $\tau_{had-vis}$ candidate is referred to as 1-prong or 3-prong based on the associated number of tracks. To discern $\tau_{had-vis}$ objects from quark-initiated and gluon-initiated jets a Recurrent Neural Network (RNN) is used [58]. The search described in this analysis uses a medium WP that corresponds to 75% identification efficiency for 1-prong and 60% for 3-prong in $\gamma \rightarrow \tau\tau$ collision events with a rejection factor of $\sim 35 - 240$ for jets [58].

5.7 E_T^{miss}

The final SM particle in the reconstruction scheme is the neutrino². The presence of a neutrino, or another minimally interacting particle, can be inferred through the calculation³

²The W, Z and gluon do not have long enough lifetimes to leave signatures within the ATLAS detector volume. Instead, their presence is inferred through their decay products.

³The choice of E_T^{miss} to represent missing transverse momentum is a common nomenclature. Other choices include p_T^{miss} , MET, and E T miss.

of E_T^{miss} ; which takes advantage of the initial collision having a small momentum in the transverse plane ($p_T \simeq 0$). The initial momentum in the z direction (along the beamline) cannot be known due to the composite nature of the colliding protons and the associated PDFs of their components.

The calculation of E_T^{miss} in the ATLAS detector is defined as

$$E_T^{\text{miss}} = -\sum E_T = \sum p_T^\mu + \sum p_T^e + \sum p_T^\gamma + \sum p_T^\tau + \sum p_T^{\text{jets}} + \sum p_T^{\text{soft}} \quad (5.4)$$

where the p_T^{soft} term comes from soft tracks that are not associated with any physics objects [59]. The analysis discussed in this dissertation uses E_T^{miss} triggers in one of the subchannels to select events and is described in Chapter 6.

CHAPTER 6

SEARCH FOR CHARGED HIGGS BOSONS

This chapter details a search for a charged Higgs boson decaying to a hadronically decaying tau lepton and a neutrino; the phenomenology is discussed in Section 2.3. The search contains two subchannels, $\tau + \text{jets}$ and $\tau + \ell$ based on the decay of the associated top quark in the collision event. The $\tau + \text{jets}$ subchannel ($t \rightarrow Wb$, $W \rightarrow q\bar{q}$) has a higher branching fraction, leading to higher sensitivity at larger m_{H^\pm} values. The $\tau + \ell$ subchannel ($t \rightarrow Wb$, $W \rightarrow \ell\nu$) has a much lower branching fraction, but takes advantage of single-lepton triggers which enhance background suppression of QCD jet $\rightarrow \tau$ fakes. This leads to an increased sensitivity at lower m_{H^\pm} values. The extra neutrino in the $\tau + \ell$ decay mode creates extra difficulties in separating signal from background in this subchannel by adding a significant contribution to the E_T^{miss} calculation for the event.

The search described by this dissertation uses a profile likelihood ratio as the test statistic in a simultaneous fit in two Control Regions (CRs) and three SRs. The discriminating variable is chosen to be the output score distribution of a Multivariate Analysis Technique (MVA). In the previous publication described in Section 2.3.1 several BDT were used, binned in m_{H^\pm} ; this analysis uses a PNN to classify events as signal-like or background-like.

This chapter discusses in detail the entire analysis, including the signal signatures, event selections, analyzed datasets, modeling of backgrounds, training and evaluation of classifiers, studies of systematic uncertainties, and results.

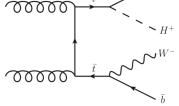
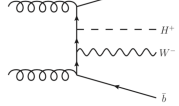
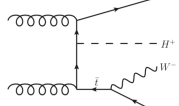
6.1 Signature and Event Selection

As shown in Figure 2.4, the production of the H^\pm is dependent on its mass m_{H^\pm} . Table 6.1 shows the production mechanisms for m_{H^\pm} values in bins of the top quark mass m_t as well as the main decay mode (and theoretical constraints), and the main source of background. Three mass ranges are defined, low mass $80 \leq m_{H^\pm} \leq 130$ GeV, intermediate mass $140 \leq m_{H^\pm} \leq 190$, and high mass $200 \leq m_{H^\pm} \leq 3000$ GeV. In the low mass bin the H^\pm takes the place of the W^\pm in the top quark decay. Results of searches for other non-standard decays of top quarks limits on the branching ratio can be seen in Reference [2]. The two subchannels of this analysis have similar signal signatures with a hard-scatter source of E_T^{miss} , one $\tau_{\text{had-vis}}$, and at least 1 b -jet from the associated top decay. In the $\tau + \ell$ subchannel there is an extra requirement of a lepton (e or μ). Due to the variable amount of energy available to the final state products based on m_{H^\pm} the event topology changes as a function of m_{H^\pm} . As described in Section 6.4, classifiers are trained and evaluated in m_{H^\pm} bins to account for the varying event topology.

6.1.1 Object Definitions

After physics objects are reconstructed additional kinematic and identification cuts are applied to allow for high identification efficiency while keeping significant statistics [58, 53, 55, 49, 48]. Table 6.2 shows the identification requirements on all objects used in the analysis. In both subchannels $\tau_{\text{had-vis}}$ candidates are required to fit the medium working point described in Section 5.6 that corresponds to a 75% efficiency for 1-prong and 60% efficiency for 3-prong $\tau_{\text{had-vis}}$ identification, an $|\eta|$ cut of < 2.3 that also excludes the gap and crack region of the ATLAS calorimeters at $1.37 < |\eta| < 1.52$, and an overlap removal with electrons. For

Table 6.1: H^\pm production mechanisms based on m_{H^\pm} , dominant H^\pm decay mode, and the main backgrounds associated with the diagram.

H^\pm Mass	Production Mechanism	Decay	Main Backgrounds
$m_{H^\pm} < m_t$	double-resonant $t \rightarrow H^\pm b$ (LO) 	$H^\pm \rightarrow \tau^\pm \nu_\tau$ (low $\tan \beta \implies H^\pm \rightarrow cs$ or $H^\pm \rightarrow cb$)	$t\bar{t}$, single-top
$m_{H^\pm} \simeq m_t$	non-resonant $t \rightarrow H^\pm b$ (LO) 	$H^\pm \rightarrow \tau\nu$	$t\bar{t}$, single-top
$m_{H^\pm} > m_t$	interferences taken into account single-resonant $gg \rightarrow tbH^\pm$ (NLO) 	$H^\pm \rightarrow tb$ ($\cos(\beta - \alpha) \simeq 0$ and large $\tan(\beta) \implies H^\pm \rightarrow \tau\nu$ $BR(H^\pm \rightarrow \tau^\pm \nu_\tau) \simeq 10 - 15\%$)	multi-jet

the $\tau + \text{jets}$ subchannel, the $\tau_{had-vis}$ p_T is required to be greater than 40 GeV and greater than 30 GeV for the $\tau + \ell$ subchannel. Although muons and electrons are not part of the $\tau + \text{jets}$ signal final state, a loose identification and isolation requirement is used to veto events; while the $\tau + \ell$ subchannel requires there to be either an electron or a muon that passes the tight identification and isolation requirements as well as a p_T above 30 GeV. The jets in candidate events are required to have greater than 25 GeV in p_T and are made with the anti- k_t algorithm with $R=0.4$. Any event that contains a jet with $p_T > 25$ GeV and fails quality cuts is discarded. This ensures that no jet is consistent with having originated from instrumental effects or non-collision backgrounds. Jets tagged as b -jets are done so at a 70% efficient working point using the DL1r tagger described in Section 5.5.1. The p_T requirements listed above for each physics object were chosen to maximize identification efficiency of each object. An example of identification efficiency can be seen for electrons in Figure 6.1. The chosen cut of $p_T^e > 30$ GeV corresponds to an identification efficiency of $\approx 70\%$. Similar choices for τ leptons [58], jets [53], b -jets [55], E_T^{miss} [59], and muons [60] were made.

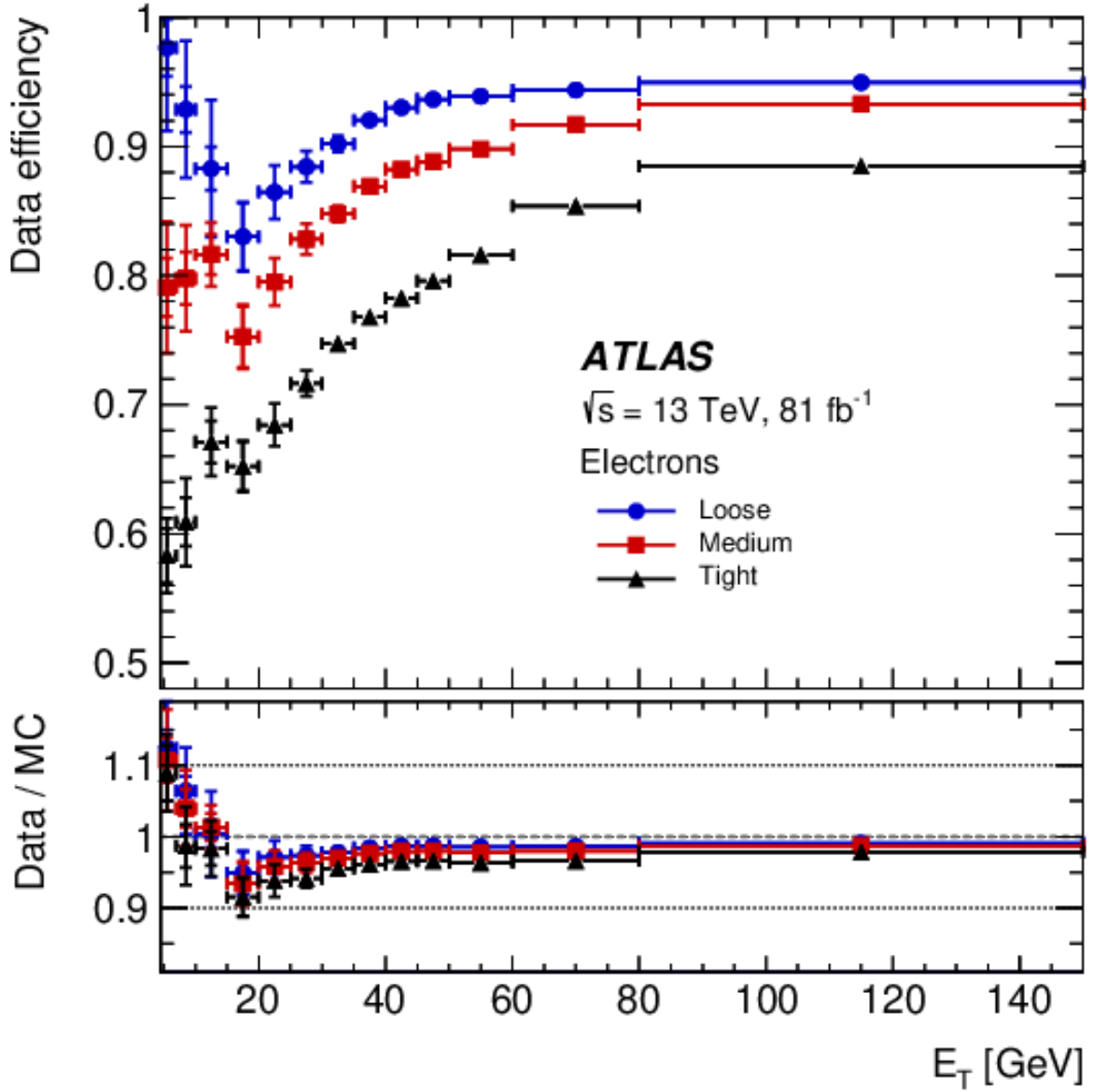


Figure 6.1: The electron identification efficiency in $Z \rightarrow ee$ events in data as a function of E_T for the Loose, Medium, and Tight operating points. The efficiencies are obtained by applying data-to-simulation efficiency ratios measured in $J/\Psi \rightarrow ee$ and $Z \rightarrow ee$ events to $Z \rightarrow ee$ simulation. The inner uncertainties are statistical and the total uncertainties are the statistical and systematic uncertainties in the data-to-simulation efficiency ratio added in quadrature. The bottom panel shows the data-to-simulation ratio. Taken from Reference [49].

Table 6.2: Definitions of physics objects used in this analysis.

Object	$\tau + \text{jets}$	$\tau + \ell$
$\tau_{\text{had-vis}}$	Leading reconstructed τ (regardless of its ID), mediumID*, $p_T > 40$ GeV, $ \eta ^{***} < 2.3$, e OLR	Leading reconstructed τ (regardless of its ID), mediumID*, $p_T > 30$ GeV, $ \eta ^{***} < 2.3$, e OLR
e	LoseLLH, $p_T > 20$ GeV, $ \eta ^{***} < 2.47$, Loose isolation, IP cuts	TightLLH, $p_T > 30$ GeV, $ \eta ^{***} < 2.47$, Tight isolation, IP cuts
μ	LooseID, $p_T > 20$ GeV, $ \eta < 2.5$, Loose isolation, IP cuts	TightID, $p_T > 30$ GeV, $ \eta < 2.5$, Tight isolation, IP cuts
jet	AntiKt4EMPFlow, $p_T > 25$ GeV $ \eta < 2.5$, JVT** > 0.59, Btag=70%, DL1r	AntiKt4EMPFlow, $p_T > 25$ GeV, $ \eta < 2.5$, JVT** > 0.59, Btag=70%, DL1r

6.1.2 Event Selections

Each subchannel signal region has stricter requirements than the object definitions described in Section 6.1.1. Table 6.3 details these selections. The channels differ in the triggers used; the $\tau + \text{jets}$ subchannel relies on E_T^{miss} triggers while the $\tau + \ell$ subchannel relies on single lepton triggers. Detailed information on the triggers and the efficiencies of the trigger options can be found in References [61] (E_T^{miss}), [62] (e), and [63] (μ). Due to the difficulty of separating signal from background and the large amount of background, the $\tau + \text{jets}$ subchannel has a higher p_T cut on the $\tau_{\text{had-vis}}$ of 40 GeV as opposed to the $\tau + \ell$ value of 30 GeV. In addition, a higher value of E_T^{miss} of 150 GeV is required for the $\tau + \text{jets}$ subchannel compared to 50 GeV in the $\tau + \ell$ subchannel. In the $\tau + \text{jets}$ subchannel a value of 50 GeV is also required of the transverse mass m_T defined as

$$m_T = \sqrt{2p_T^\tau E_T^{\text{miss}}(1 - \cos\Delta\phi_{\tau, E_T^{\text{miss}}})} \quad (6.1)$$

The $\tau + \ell$ has no such requirement, but does require the $\tau_{\text{had-vis}}$ and lepton to have opposite electromagnetic charge. A set of orthogonal CRs are defined for each subchannel to verify

proper background modelling and are described in Section 6.3. The acceptance of signal in the signal regions defined in Table 6.3 is shown in Figure 6.2. The instability of the data points is due to the boundaries of the H^\pm production diagrams. Due to the larger branching fraction of $t \rightarrow W + b; W \rightarrow q\bar{q}$ as opposed to $t \rightarrow W + b; W \rightarrow \ell + \nu$ the $\tau + \text{jets}$ subchannel has a factor of 10 larger signal acceptance than the $\tau + \ell$ subchannel. In both channels, the signal acceptance decreases for m_{H^\pm} values > 1000 GeV. This is an artifact of objects becoming boosted, meaning their decay products are extremely collimated, resulting in lower efficiencies for object identification.

Table 6.3: $\tau + \text{jets}$ and $\tau + \ell$ signal region definitions.

$\tau + \text{jets SR}$	$\tau + \ell \text{ SR}$
E_T^{miss} Trigger	Single lepton triggers (e or μ)
1 $\tau_{\text{had-vis}}$; $p_T^\tau > 40$ GeV	1 $\tau_{\text{had-vis}}$; $p_T^\tau > 30$ GeV
0 ℓ (e or μ) ; $p_T^\ell > 20$ GeV	1 ℓ (e or μ) ; $p_T^\ell > 30$ GeV
≥ 3 jets ; $p_T^j > 25$ GeV	≥ 1 jet ; $p_T^j > 25$ GeV
≥ 1 b -jets; $p_T^{b-jet} > 25$ GeV	≥ 1 b -jets; $p_T^{b-jet} > 25$ GeV
$E_T^{\text{miss}} > 150$ GeV	$E_T^{\text{miss}} > 50$ GeV
$m_T(\tau, E_T^{\text{miss}}) > 50$ GeV	Opposite sign τ and ℓ

6.2 Datasets

This analysis uses the full Run-2 ATLAS dataset collected between 2015 and 2018 corresponding to $139.0 \pm 2.4 \text{ fb}^{-1}$ [64]. The datasets used are required to be included in the ATLAS ‘‘Good Run Lists’’ (GRLs), meaning they have passed nominal data quality checks with all detector subsystems operating within normal conditions. Further event cleaning is applied that removes events in which a reconstructed jet originated from detector noise or

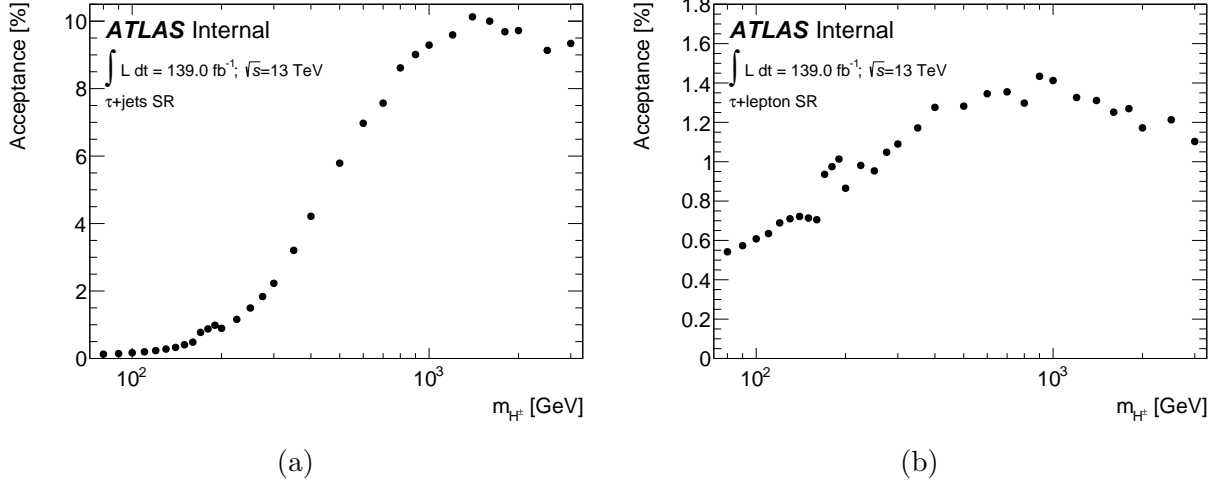


Figure 6.2: Signal acceptance as a function of the charged Higgs boson mass for both the $\tau + \text{jets}$ (a) and $\tau + \ell$ subchannels (b). Statistical errors are shown but are negligible.

non-collision backgrounds. The collection of data throughout Run-2 can be seen in Figure 3.4.

6.2.1 Signal Modeling

MC simulations of H^\pm signal events are generated at varying orders dependent on m_{H^\pm} . In all cases, the 2HDM Type II model described in Section 2.2.2 is assumed and the generator MadGraph is used. The lower mass range corresponding to $m_{H^\pm} < 140$ GeV where a H^\pm takes the place of a W^\pm in a top decay is generated at LO. The intermediate mass range of $140 \leq m_{H^\pm} < 200$ GeV is generated at LO, taking into account the non-resonant, single-top resonant and double-resonant diagrams and their interferences. In this mass range, the final state contains one H^\pm , one W^\pm , and two b quark. For charged Higgs masses of 200 GeV and above, the H^\pm is produced in association with a top quark and is generated at NLO. The Powheg-box v2 [39, 40] generator is used with the NNPDF3.0 NLO PDF [65] set in the matrix element calculations to generate $t\bar{t}$ and single top-quarks in the W t- and s-channels.

In all cases, the parton generator is interfaced with Pythia v8.230 [38] with the NNPDF2.3 LO PDF [66] using the A14 underlying event tuning parameters [67]. Table 6.4 shows the cross section and raw number of events generated for each m_{H^\pm} point for both subchannels.

Table 6.4: For each H^\pm mass the generator xcross-section ($\sigma \times BR(H^\pm \rightarrow \tau^\pm \nu_\tau)$) is given, as well as the number of generated events for both $\tau + \ell$ and $\tau + \text{jets}$ subchannels.

m_{H^\pm} [GeV]	σ [pb]	$\tau + \ell$ Generated Events	$\tau + \text{jets}$ Generated Events
80	61.639	220k	110k
90	52.823	220k	110k
100	43.777	220k	110k
110	34.770	220k	110k
120	26.092	220k	110k
130	18.069	220k	110k
140	15.023	220k	220k
150	7.681	220k	220k
160	2.665	220k	220k
170	0.63748	220k	220k
180	0.52979	220k	220k
190	0.47201	220k	220k
200	0.55632	110k	220k
225	0.44081	110k	220k
250	0.3573	110k	220k
275	0.28592	110k	220k
300	0.23373	110k	220k
350	0.15774	110k	220k
400	0.10818	110k	220k
500	0.054139	110k	220k
600	0.02847	110k	220k
700	0.015764	110k	220k
800	0.009067	110k	220k
900	0.005324	110k	220k
1000	0.003271	110k	220k
1200	0.001311	110k	220k
1400	0.000558	110k	220k
1600	0.000252	110k	220k
1800	0.000120	110k	220k
2000	0.0000587	110k	220k
2500	0.0000111	110k	220k
3000	0.00000234	110k	220k

6.3 Background Modeling

The main sources of backgrounds are shown in Table 6.5, separated between backgrounds with a prompt $\tau_{had-vis}$ in the hard scatter process and those that arise from the misidentifi-

cation of other physics objects as a $\tau_{had-vis}$. The cross section of all simulated background samples and the relevant generators can be seen in Table 6.6. Control regions that are designed to be orthogonal to the signal region are created for both subchannels in order to study the modeling of the backgrounds. These control regions are defined by the cuts in Table 6.7 ($\tau+jets$) and Table 6.8 ($\tau + \ell$). For the $\tau + \ell$ subchannel the Same Sign and b-veto control regions are further split into two control regions, one that requires a μ in the event and another that requires an electron.

Table 6.5: Dominant backgrounds from prompt $\tau_{had-vis}$ and fake $\tau_{had-vis}$ candidates.

Backgrounds w/ prompt $\tau_{had-vis}$	Backgrounds w/ fake τ
$t\bar{t}$ estimated with MC	Fake $j \rightarrow \tau$ estimated with data driven fake factor method
$W(Z) + jets$ estimated with MC	Fake $\ell \rightarrow \tau$ estimated with MC, validated on $Z \rightarrow ee$
Diboson estimated with MC	

Table 6.6: Cross sections for the main SM background samples at $\sqrt{s} = 13$ TeV . Here, ℓ refers to the three lepton families e , μ and τ . All background cross sections are normalized to NNLO predictions, except for diboson events, where the NLO prediction is used. A '*' indicates that the quoted cross section for the sample is neglecting leptonic/hadronic branching ratios.

Background process	Generator & parton shower	Cross section number(s) [pb]
$t\bar{t}$ with at least one lepton ℓ	Powheg & Pythia8	729.77*
Single top-quark t -channel		59.17*
Single top-quark s -channel		3.29*
Single top-quark Wt -channel		83.83
$W(\ell\nu) + jets$	Sherpa 2.2.1	2.0×10^4 2.0×10^4 2.0×10^4
$Z/\gamma^*(\ell\ell, \nu\nu) + jets$	Sherpa 2.2.1	2.1×10^3 2.1×10^3 2.1×10^3
WW		54.81
WZ	Powheg & Pythia8	16.34
ZZ		8.94

Table 6.7: Control region definitions for the $\tau + \text{jets}$ subchannel.

	$t\bar{t}$ CR	W+Jets CR	b-veto CR	b-veto $m_T > 100$ CR
Number of $\tau_{had-vis}$	1	1	0	0
p_T^τ	> 40 GeV	> 40 GeV	> 40 GeV	> 40 GeV
Number of jets	≥ 3	≥ 3	≥ 3	≥ 3
p_T^{jet}	≥ 25 GeV	≥ 25 GeV	≥ 25 GeV	≥ 25 GeV
Number of b -jets	≥ 2	0	0	0
Number of ℓ	0	0	0	0
E_T^{miss}	> 150 GeV	> 150 GeV	> 150 GeV	> 150 GeV
$m_T(\tau, E_T^{\text{miss}})$	< 100 GeV	< 100 GeV	> 50 GeV	> 100 GeV
Type of modeling	$t\bar{t}$	W+Jets	Close to SR	Fake $j \rightarrow \tau$ enriched

Table 6.8: Control region definitions for the $\tau + \ell$ subchannel.

	Dilepton-btag CR	Zee CR	b-veto CR	Same Sign (τ, ℓ) CR
Number of $\tau_{had-vis}$	0	1	0	0
p_T^τ	> 30 GeV	> 30 GeV	> 30 GeV	> 30 GeV
Number of jets	≥ 1	≥ 1	≥ 1	≥ 1
p_T^{jet}	≥ 25 GeV	≥ 25 GeV	≥ 25 GeV	≥ 25 GeV
Number of b -jets	≥ 1	0	0	≥ 1
Number of ℓ	2 (1 e , 1 μ)	1 e	1 tight e (μ)	1 tight e (μ)
E_T^{miss}	> 50 GeV	> 50 GeV	> 50 GeV	> 50 GeV
mass(τ, e)	N/A	$> 40; < 140$ GeV	N/A	N/A
Type of modeling	$t\bar{t}$ and single-top	Fake $\ell \rightarrow \tau$ enriched	Close to SR	Fake $j \rightarrow \tau$ enriched

As seen in Table 6.5 misidentified objects appearing as $\tau_{had-vis}$ candidates comprise a significant portion of the total background. Fakes arising from $\ell \rightarrow \tau$ misidentification are well modeled in MC simulations and are reweighted with scale factors provided by the ATLAS τ combined performance group. The mass of the $\tau_{had-vis}$ electron system can be seen in Figure 6.3 as verification of fake $\ell \rightarrow \tau$ modeling. Fakes due to $j \rightarrow \tau$ misidentification have poorly understood systematic uncertainties associated with the fake $\tau_{had-vis}$ object and limited statistics of simulated events. To combat this, a data driven method is used to extract a scaling constant referred to as a fake factor.

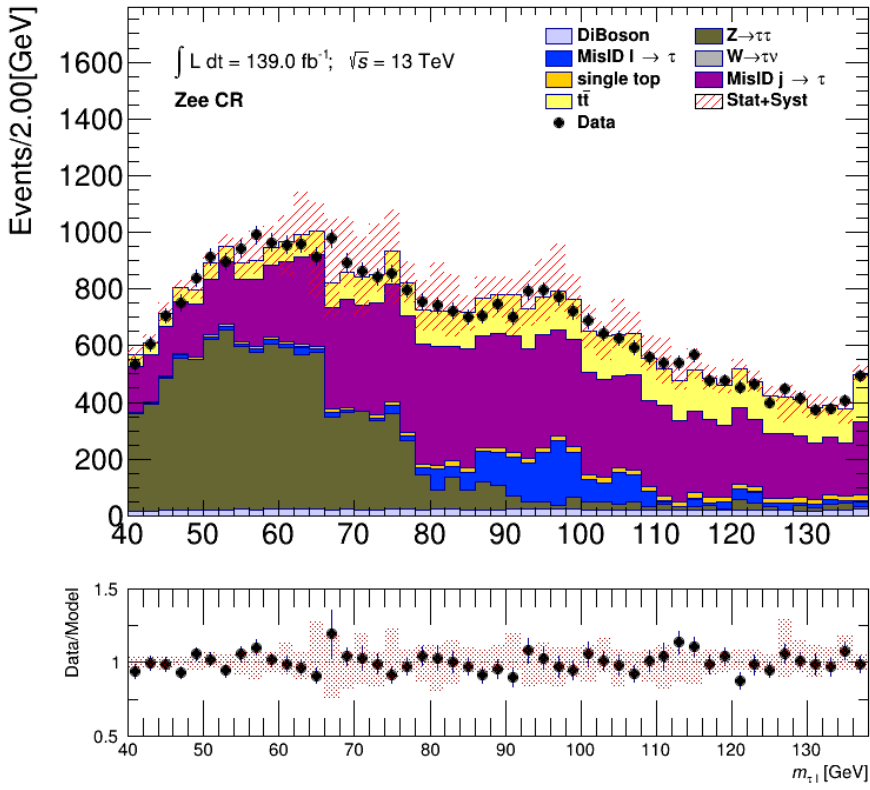


Figure 6.3: Mass of τ - e system in the Zee control region. All systematics except for $t\bar{t}$ theory uncertainties are included.

In the $\tau + \ell$ final state a significant portion of $j \rightarrow \tau$ fakes come from misidentifying $\tau_{had-vis}$ candidates in W+jets events that contain a true ℓ in the W decay and have a misidentified jet as a $\tau_{had-vis}$. Fakes of this manner also arise from QCD-like multi-jet interactions. The FF method used to estimate the amount of expected fake $\tau_{had-vis}$ objects that pass the $\tau_{had-vis}$ identification procedure is described in Section 5.6. This method applies weights, or fake factors, to a subset of “anti- $\tau_{had-vis}$ ” objects that have failed the selection and identification criteria in the signal region. A control region is defined to be rich in anti- $\tau_{had-vis}$ objects, where the $\tau_{had-vis}$ candidates fail the loose τ working point but have a small, non-zero τ identification RNN score. The FF and number of events with misidentified $\tau_{had-vis}$ objects (N_{fakes}^τ) are defined as:

$$FF = \frac{N^{\tau-id}}{N^{anti-\tau-id}} \quad (6.2)$$

$$N_{fakes}^\tau = N_{fakes}^{anti-\tau} \times FF$$

Both of these values are then corrected for $\tau_{had-vis}$ candidates matching a true hadronic τ at generator level:

$$N^{\tau-id} = N^{\tau-id}(Data) - N^{\tau-id}(MC) \quad (6.3)$$

$$N_{fakes}^{anti-\tau} = N^{anti-\tau}(Data) - N_{true}^{anti-\tau}(MC)$$

Two CRs are created, one to capture the multi-jet (MJ) fakes and the other to study the W+jets fakes. The MJ CR uses the $\tau + \text{jets}$ signal region definition with an additional b-veto and an $E_T^{\text{miss}} < 80$ GeV cut. The W+jets CR¹ uses the $\tau + \ell$ signal region definition

¹This W+jets CR is not the one defined in Table 6.7. This is a new region used to extract the fake factors.

with a b-veto, no E_T^{miss} cut, and a cut on the transverse mass of the $\ell-E_T^{\text{miss}}$ system of $60 < m_T(\ell, E_T^{\text{miss}}) < 160$ GeV. The FF in the signal region is defined as

$$FF_{\text{sig}} = \alpha_{MJ} \times FF_{MJ} + (1 - \alpha_{MJ}) \times FF_{W+jets} \quad (6.4)$$

where α is taken from a template fit of the τ -ID score distributions of the anti- τ s using template shapes from the anti- τ distributions in the MJ and W+jets control regions. In the signal regions, the number of events containing fake- $\tau_{\text{had-vis}}$ candidates is defined as

$$N_{\text{fake-}\tau} = FF_{\text{sig}} \times N_{\text{anti-}\tau} \quad (6.5)$$

Figure 6.4 shows FF plotted in each control region for 1-prong and 3-prong $\tau_{\text{had-vis}}$ binned in $p_T\tau$; extracted α values and their fits can be seen in Appendix B.

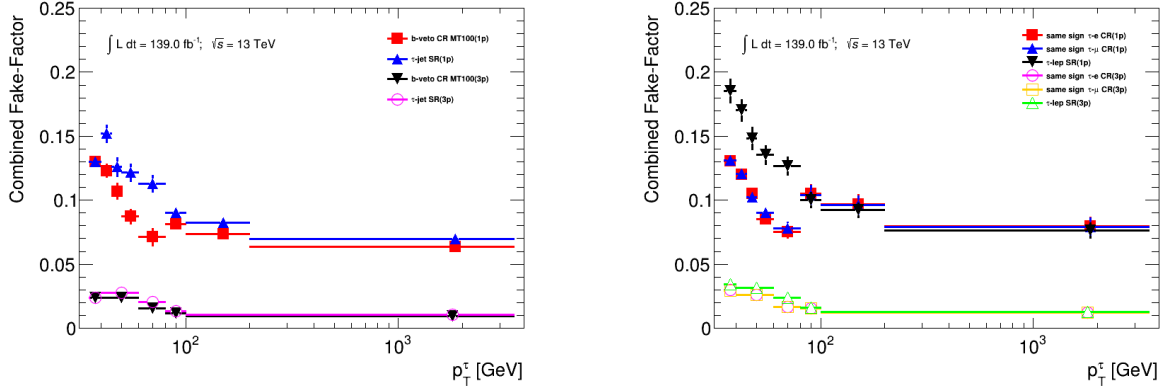


Figure 6.4: Combined FF for the τ +jets b-veto $m_T > 100$ control region, τ +jets signal region, τ +electron(muon) with same-sign control region and the $\tau + \ell$ signal region. Error bars represent systematic uncertainties of the method.

To verify background modeling, the E_T^{miss} distributions in each of the control regions are plotted with final scale factors including fake factors in Figure C.7 (τ +jets) and Figures 6.7 - 6.8 ($\tau + \ell$). Similar distributions of the τ p_T can be seen in Figure C.1 (τ +jets) and Figures

6.9 - 6.10. These plots include a ratio of reconstructed data events and simulated MC events bin by bin to ensure proper modeling across variable shapes. More background modeling plots can be seen in Appendix C. Tables 6.9, 6.10 and 6.11 show the expected event yields and the effect of each selection cut on the background sources as well as selected m_{H^\pm} values of 110, 170, and 1000 GeV. At the time of writing, the analysis is still blinded so data yields are not known.

Table 6.9: Expected event yields and efficiencies after cumulative selection cuts and comparison with 139 fb^{-1} of data for $\tau + \text{jets}$ sub-channel. The values shown for the signal correspond to $\sigma(pp \rightarrow [b]tH^\pm) \times Br(H^\pm \rightarrow \tau^\pm \nu_\tau) = 1 \text{ pb}$. Statistical uncertainties are shown.

Selection	$t\bar{t}$	Single-top-quark	$W \rightarrow \tau\nu$	$Z \rightarrow \tau\tau$
Trigger and skim	342315.32 ± 205.10	38154.55 ± 66.40	296087.10 ± 539.63	52976.26 ± 148.89
Loose tau, $p_T^\tau > 40 \text{ GeV}$	231610.69 ± 169.16 (68%)	26454.25 ± 55.97 (69%)	197122.72 ± 436.12 (67%)	37617.08 ± 119.38 (71%)
Medium tau	133237.32 ± 127.99 (58%)	16879.04 ± 44.91 (64%)	142441.76 ± 319.72 (72%)	27017.86 ± 101.54 (72%)
Lepton veto	114888.70 ± 118.99 (86%)	15450.09 ± 42.79 (92%)	142390.47 ± 319.70 (100%)	23911.34 ± 97.78 (89%)
≥ 1 b-jet	93242.48 ± 106.97 (81%)	11711.18 ± 37.03 (76%)	11788.34 ± 62.30 (8%)	2923.99 ± 23.68 (12%)
$E_T^{\text{miss}} > 150 \text{ GeV}$	48457.24 ± 78.37 (52%)	7129.31 ± 29.82 (61%)	7160.34 ± 43.20 (61%)	1194.29 ± 11.05 (41%)
$m_T > 50 \text{ GeV}$ (SR)	18369.33 ± 48.16 (38%)	2276.08 ± 16.69 (32%)	1972.76 ± 23.54 (28%)	241.05 ± 5.47 (20%)
Selection	Diboson (WW, WZ, ZZ)	Misidentified $e, \mu \rightarrow \tau_{\text{had-vis}}$	Misidentified jet $\rightarrow \tau_{\text{had-vis}}$	All backgrounds
Trigger and skim	13094.19 ± 53.23	708734.11 ± 890.75	3195982.69 ± 560.82	4647344.22 ± 1212.70
Loose tau, $p_T^\tau > 40 \text{ GeV}$	9387.33 ± 45.05 (72%)	375566.87 ± 328.44 (53%)	1645126.81 ± 354.50 (51%)	2522885.75 ± 686.86 (54%)
Medium tau	6591.35 ± 37.96 (70%)	2924.49 ± 84.42 (1%)	198869.55 ± 137.33 (12%)	527961.36 ± 397.94 (21%)
Lepton veto	5976.46 ± 37.70 (91%)	2247.49 ± 83.45 (77%)	191880.62 ± 134.54 (96%)	496745.16 ± 392.74 (94%)
≥ 1 b-jet	625.84 ± 10.33 (10%)	1194.29 ± 40.93 (53%)	38868.36 ± 61.73 (20%)	160354.47 ± 151.16 (32%)
$E_T^{\text{miss}} > 150 \text{ GeV}$	414.89 ± 8.66 (66%)	428.96 ± 7.80 (36%)	3009.41 ± 21.14 (8%)	67794.44 ± 97.99 (42%)
$m_T > 50 \text{ GeV}$ (SR)	133.30 ± 4.67 (32%)	327.51 ± 6.82 (76%)	2490.58 ± 17.35 (83%)	25810.61 ± 59.60 (38%)
Selection	H^\pm (110 GeV)	H^\pm (170 GeV)	H^\pm (1000 GeV)	Data (139 fb^{-1})
Trigger and skim	1951.47 ± 11.05	4992.07 ± 19.02	34812.84 ± 94.47	XXX \pm XXX
Loose tau, $p_T^\tau > 40 \text{ GeV}$	1554.18 ± 9.87 (80%)	4047.73 ± 17.14 (81%)	27900.09 ± 84.24 (80%)	XXX \pm XXX
Medium tau	1016.12 ± 7.99 (65%)	2890.75 ± 14.52 (71%)	19994.71 ± 72.07 (72%)	XXX \pm XXX
Lepton veto	901.33 ± 7.53 (89%)	2694.19 ± 14.02 (93%)	18343.94 ± 68.93 (92%)	XXX \pm XXX
≥ 1 b-jet	729.40 ± 6.76 (81%)	2075.45 ± 12.29 (77%)	13611.31 ± 60.35 (74%)	XXX \pm XXX
$E_T^{\text{miss}} > 150 \text{ GeV}$	425.52 ± 5.25 (58%)	1333.74 ± 10.03 (64%)	12797.45 ± 58.63 (94%)	XXX \pm XXX
$m_T > 50 \text{ GeV}$ (SR)	264.68 ± 4.13 (62%)	1044.07 ± 8.86 (78%)	12728.36 ± 58.47 (99%)	XXX \pm XXX

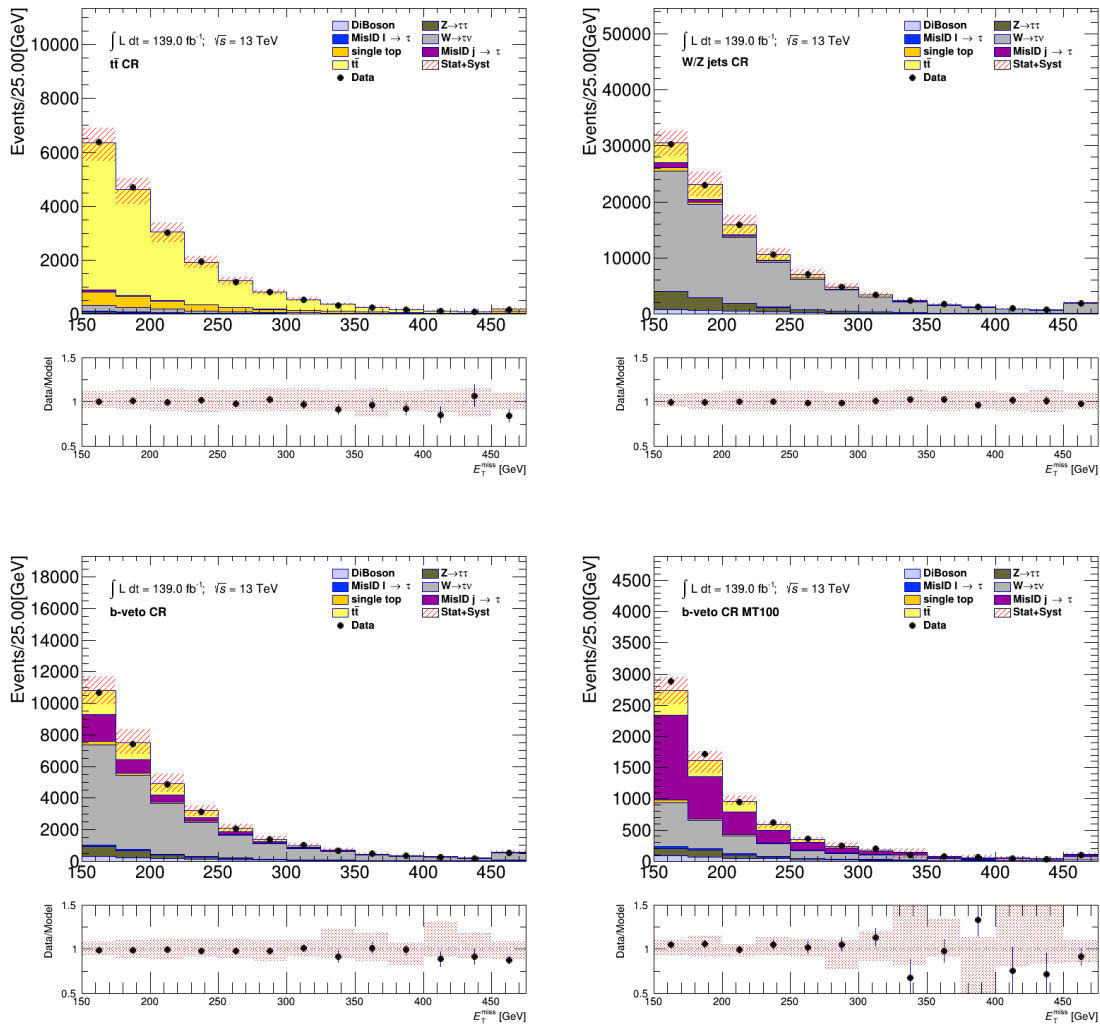


Figure 6.5: Comparison between the predicted and the measured E_T^{miss} distributions in various control regions defined for the $\tau + \text{jets}$ channel. The uncertainty band includes both statistical and systematic uncertainties on the background prediction.

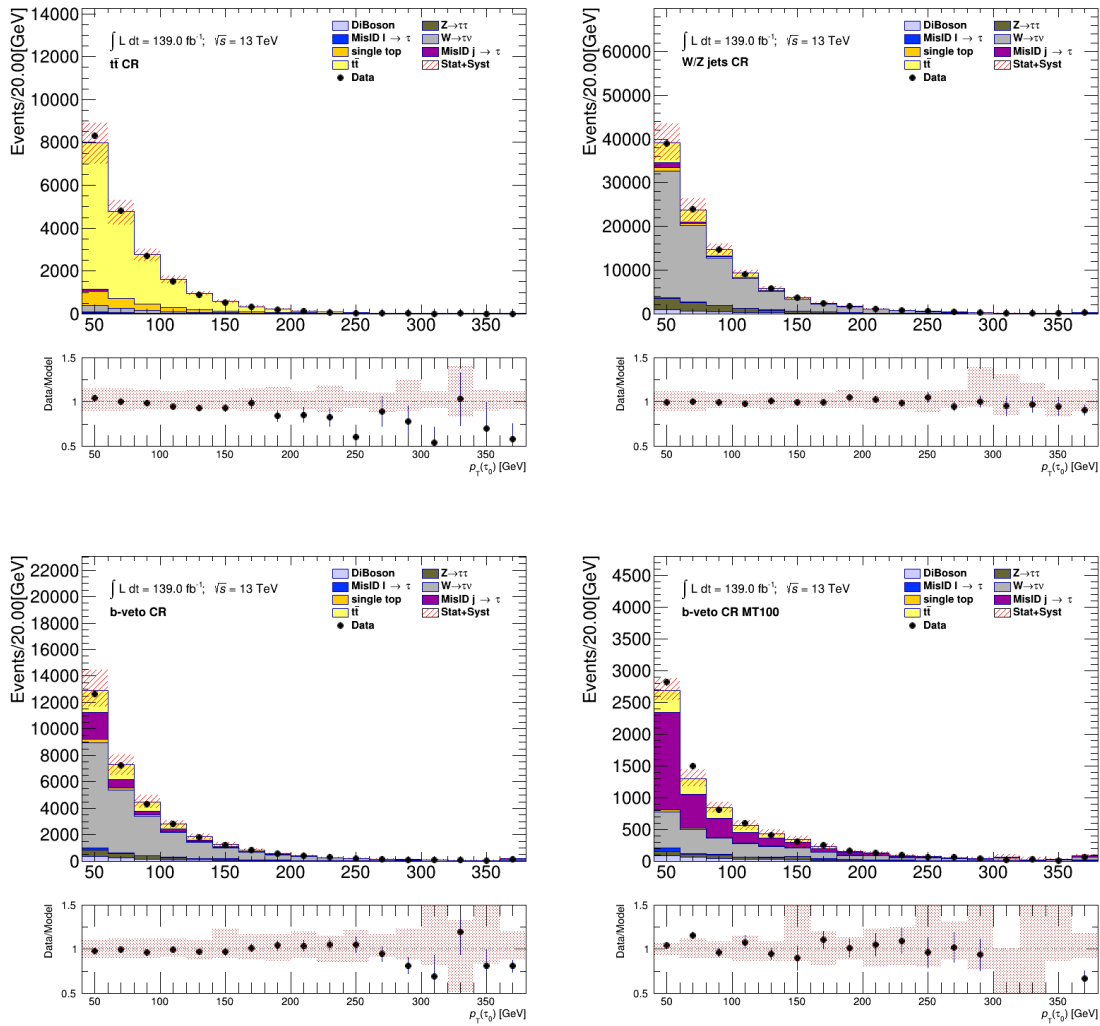


Figure 6.6: Comparison between the predicted and the measured τ p_T distributions in various control regions defined for the $\tau + \text{jets}$ channel. The uncertainty band includes both statistical and systematic uncertainties on the background prediction.

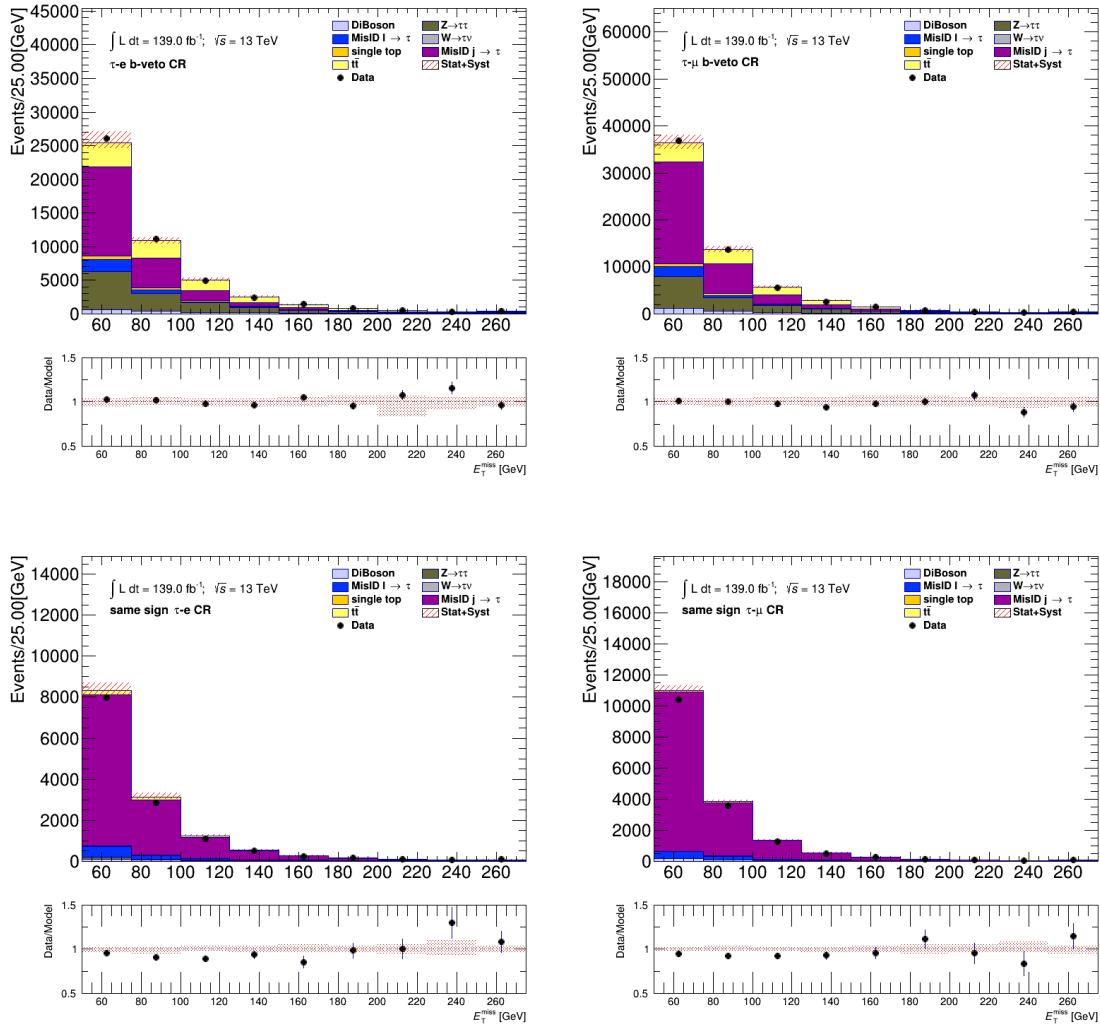


Figure 6.7: Comparison between the predicted and the measured E_T^{miss} distributions in various control regions defined for the $\tau + \ell$ channel. The uncertainty band includes both statistical and systematic uncertainties on the background prediction.

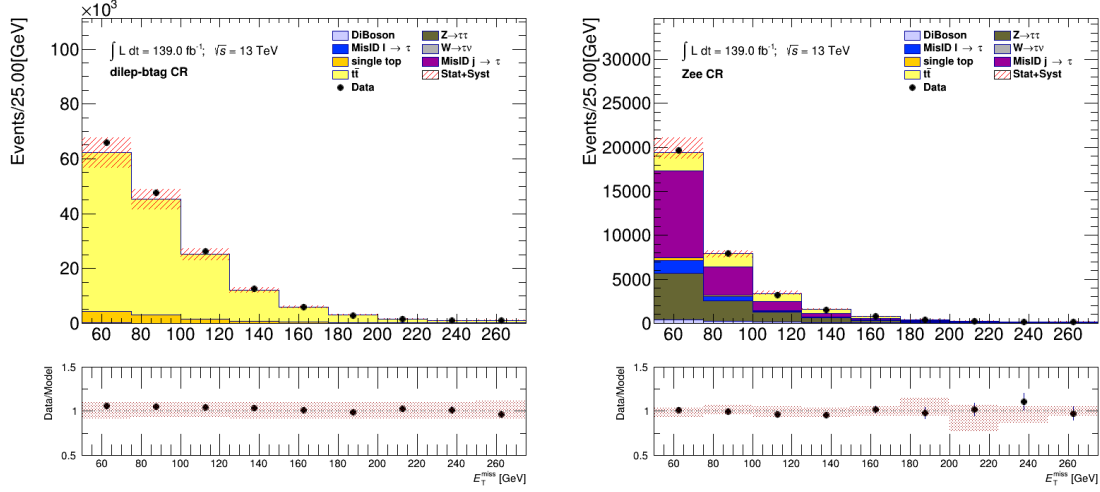


Figure 6.8: Comparison between the predicted and the measured E_T^{miss} distributions in various control regions defined for the $\tau + \ell$ channel. The uncertainty band includes both statistical and systematic uncertainties on the background prediction.

Table 6.10: Expected event yields and efficiencies after cumulative selection cuts and comparison with 139 fb^{-1} of data for $\tau + e$ channel. The values shown for the signal correspond to $\sigma(pp \rightarrow [b]tH^\pm) \times Br(H^\pm \rightarrow \tau^\pm \nu_\tau) = 1 \text{ pb}$. Statistical uncertainties are shown.

Selection	$t\bar{t}$	Single-top-quark	$W \rightarrow \tau\nu$	$Z \rightarrow \tau\tau$
Trigger and skim	410886.20 ± 232.60	40098.96 ± 68.91	1504.99 ± 67.50	214323.27 ± 1518.06
Loose tau, $p_T^\tau > 30 \text{ GeV}$	355267.50 ± 216.28 (86%)	34634.86 ± 64.10 (86%)	1280.89 ± 61.15 (85%)	184446.15 ± 1411.31 (86%)
Medium tau	179348.02 ± 154.01 (50%)	17098.32 ± 46.93 (49%)	426.20 ± 44.28 (33%)	128420.09 ± 1199.81 (70%)
Tight electron, $p_T^e > 30 \text{ GeV}$	80461.17 ± 104.31 (45%)	6920.81 ± 30.31 (40%)	112.68 ± 16.71 (26%)	39581.52 ± 621.39 (31%)
Electron and tau with OS	79604.45 ± 103.76 (99%)	6837.95 ± 30.14 (99%)	83.19 ± 15.00 (74%)	39164.25 ± 618.78 (99%)
$E_T^{\text{miss}} > 50 \text{ GeV}$	53813.81 ± 85.27 (68%)	4547.93 ± 24.61 (67%)	38.97 ± 6.28 (47%)	12448.80 ± 218.27 (32%)
≥ 1 b-jet (SR)	43814.66 ± 76.84 (81%)	3260.70 ± 20.81 (72%)	2.41 ± 0.56 (6%)	913.61 ± 20.42 (7%)
Selection	Diboson (WW, WZ, ZZ)	Misidentified $e, \mu \rightarrow \tau_{\text{had-vis}}$	Misidentified jet $\rightarrow \tau_{\text{had-vis}}$	All backgrounds
Trigger and skim	18533.34 ± 23.85	3537419.24 ± 4942.14	2403411.34 ± 714.76	6626177.34 ± 5225.34
Loose tau, $p_T^\tau > 30 \text{ GeV}$	16060.23 ± 22.20 (87%)	1939418.21 ± 2933.87 (55%)	2027356.60 ± 588.57 (84%)	4558464.44 ± 3316.76 (69%)
Medium tau	10957.22 ± 17.56 (68%)	56819.79 ± 851.44 (3%)	443714.51 ± 304.58 (22%)	836784.15 ± 1511.77 (18%)
Tight electron, $p_T^e > 30 \text{ GeV}$	3619.35 ± 10.40 (33%)	20011.76 ± 495.63 (35%)	152485.84 ± 182.97 (34%)	303193.13 ± 823.07 (36%)
Electron and tau with OS	3122.54 ± 9.91 (86%)	17202.16 ± 452.06 (86%)	95723.92 ± 147.37 (63%)	241738.46 ± 788.01 (80%)
$E_T^{\text{miss}} > 50 \text{ GeV}$	1903.40 ± 7.70 (71%)	3616.05 ± 157.27 (21%)	31529.78 ± 79.00 (33%)	107898.73 ± 294.27 (45%)
≥ 1 b-jet (SR)	73.21 ± 1.53 (4%)	1096.64 ± 24.36 (30%)	8773.81 ± 37.64 (28%)	57935.04 ± 93.63 (54%)
Selection	$H^\pm (110 \text{ GeV})$	$H^\pm (170 \text{ GeV})$	$H^\pm (1000 \text{ GeV})$	Data (139 fb^{-1})
Trigger and skim	3202.25 ± 13.97	4116.46 ± 17.10	5268.21 ± 30.05	XXX \pm XXX
Loose tau, $p_T^\tau > 30 \text{ GeV}$	2793.23 ± 13.05 (87%)	3600.92 ± 15.99 (87%)	4313.45 ± 27.22 (82%)	XXX \pm XXX
Medium tau	1915.08 ± 10.81 (69%)	2592.01 ± 13.58 (72%)	3132.37 ± 23.23 (73%)	XXX \pm XXX
Tight electron, $p_T^e > 30 \text{ GeV}$	852.54 ± 7.40 (45%)	1107.30 ± 9.12 (43%)	1356.64 ± 15.63 (43%)	XXX \pm XXX
Electron and tau with OS	845.17 ± 7.37 (99%)	1094.53 ± 9.06 (99%)	1330.08 ± 15.48 (98%)	XXX \pm XXX
$E_T^{\text{miss}} > 50 \text{ GeV}$	547.00 ± 5.94 (65%)	837.08 ± 7.93 (76%)	1302.14 ± 15.29 (98%)	XXX \pm XXX
≥ 1 b-jet (SR)	440.11 ± 5.33 (80%)	613.35 ± 6.78 (73%)	956.26 ± 13.50 (73%)	XXX \pm XXX

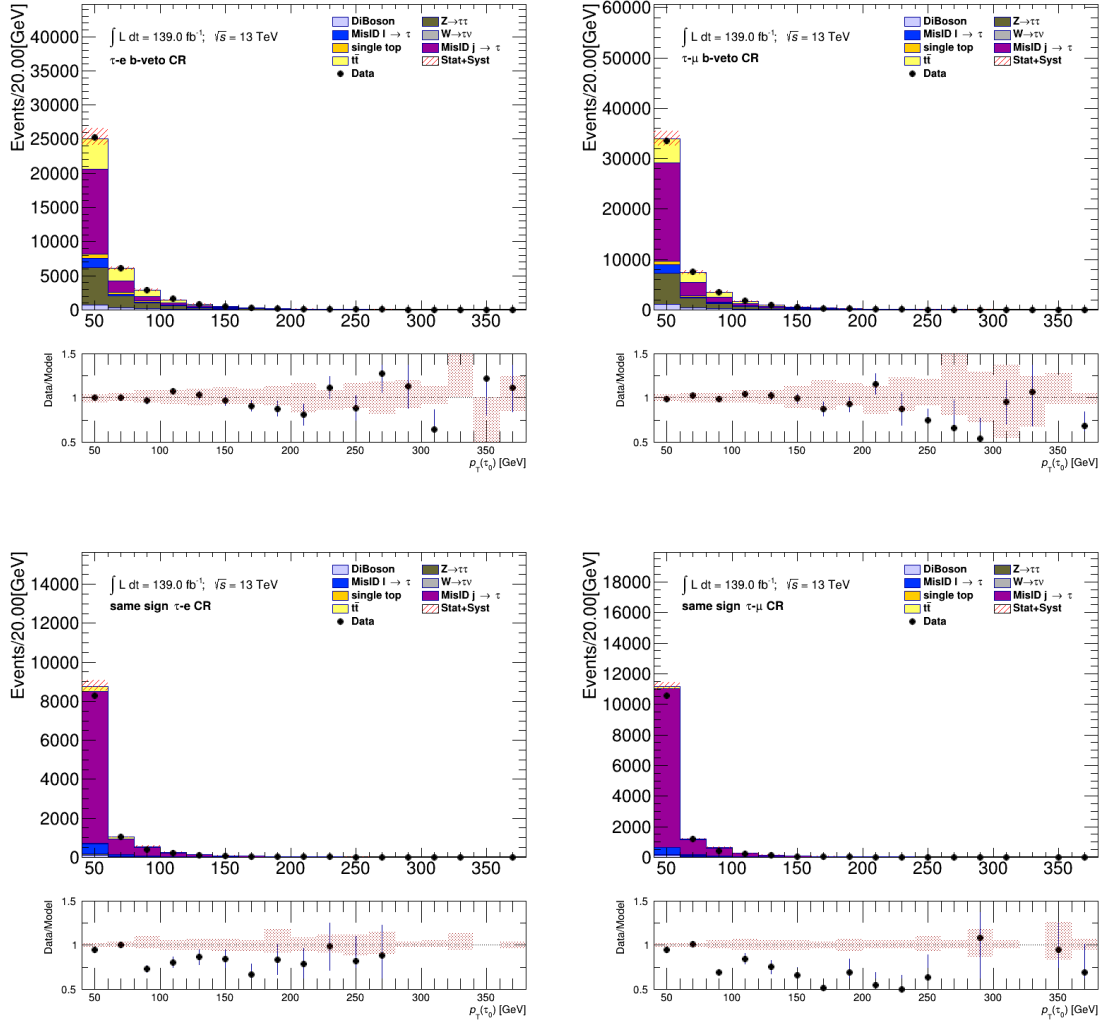


Figure 6.9: Comparison between the predicted and the measured τp_T distributions in various control regions defined for the $\tau + \ell$ channel. The uncertainty band includes both statistical and systematic uncertainties on the background prediction.

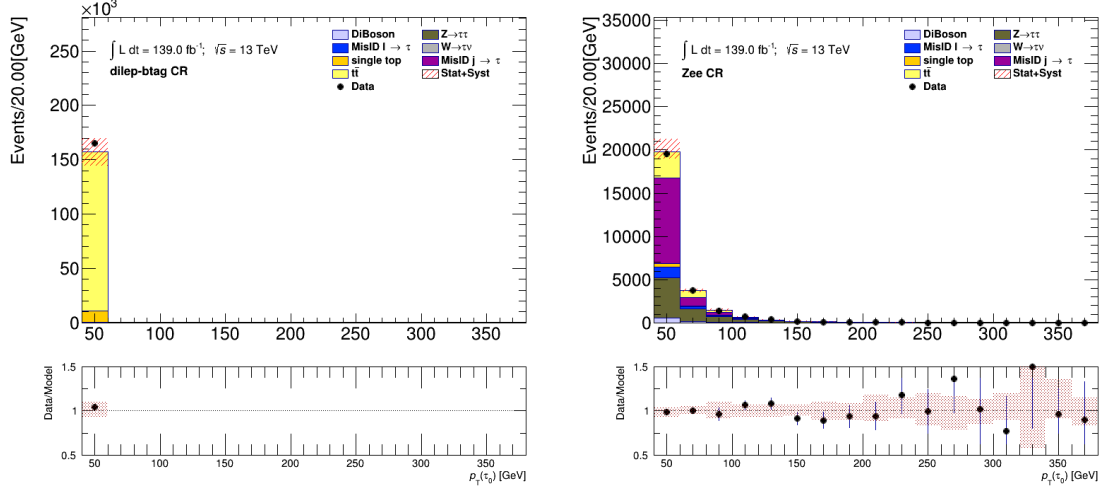


Figure 6.10: Comparison between the predicted and the measured τ p_T distributions in various control regions defined for the $\tau + \ell$ channel. The uncertainty band includes both statistical and systematic uncertainties on the background prediction.

Table 6.11: Expected event yields and efficiencies after cumulative selection cuts and comparison with 139 fb^{-1} of data for $\tau + \mu$ channel. The values shown for the signal correspond to $\sigma(pp \rightarrow [b]tH^\pm) \times Br(H^\pm \rightarrow \tau^\pm \nu_\tau) = 1 \text{ pb}$. Statistical uncertainties are shown.

Selection	$t\bar{t}$	Single-top-quark	$W \rightarrow \tau\nu$	$Z \rightarrow \tau\tau$
Trigger and skim	410886.20 ± 232.60	40098.96 ± 68.91	1504.99 ± 67.50	214323.26 ± 1518.06
Loose tau, $p_T^\tau > 30 \text{ GeV}$	355267.50 ± 216.28 (86%)	34634.86 ± 64.10 (86%)	1280.89 ± 61.15 (85%)	184446.15 ± 1411.31 (86%)
Medium tau	179348.02 ± 154.01 (50%)	17098.32 ± 46.93 (49%)	426.20 ± 44.28 (33%)	128420.09 ± 1199.81 (70%)
Tight muon, $p_T^e > 30 \text{ GeV}$	83293.59 ± 103.84 (46%)	8704.78 ± 33.09 (51%)	44.56 ± 12.50 (10%)	57089.24 ± 811.41 (44%)
Muon and tau with OS	82852.63 ± 103.57 (99%)	8653.92 ± 33.01 (99%)	42.72 ± 12.17 (96%)	56860.99 ± 810.34 (100%)
$E_T^{\text{miss}} > 50 \text{ GeV}$	55250.05 ± 84.70 (67%)	5516.70 ± 26.38 (64%)	7.66 ± 2.72 (18%)	13803.33 ± 220.41 (24%)
≥ 1 b-jet (SR)	44490.69 ± 75.96 (81%)	3874.57 ± 22.06 (70%)	0.07 ± 0.12 (1%)	845.89 ± 22.07 (6%)
Selection	Diboson (WW, WZ, ZZ)	Misidentified $e, \mu \rightarrow \tau_{\text{had-vis}}$	Misidentified jet $\rightarrow \tau_{\text{had-vis}}$	All backgrounds
Trigger and skim	18533.34 ± 23.85	3537419.44 ± 4942.14	2403411.34 ± 714.76	6626177.54 ± 5225.34
Loose tau, $p_T^\tau > 30 \text{ GeV}$	16060.23 ± 22.20 (87%)	1939418.20 ± 2933.87 (55%)	2027356.60 ± 588.57 (84%)	4558464.43 ± 3316.76 (69%)
Medium tau	10957.22 ± 17.56 (68%)	56819.79 ± 851.44 (3%)	443714.51 ± 304.58 (22%)	836784.15 ± 1511.77 (18%)
Tight muon, $p_T^e > 30 \text{ GeV}$	5709.54 ± 12.47 (52%)	30268.99 ± 623.62 (53%)	199706.03 ± 205.19 (45%)	384816.73 ± 1049.56 (46%)
Muon and tau with OS	4960.17 ± 11.89 (87%)	27996.60 ± 611.93 (92%)	131414.33 ± 171.52 (66%)	312781.35 ± 1035.68 (81%)
$E_T^{\text{miss}} > 50 \text{ GeV}$	2799.13 ± 8.89 (56%)	3766.50 ± 161.20 (13%)	42513.90 ± 90.25 (32%)	123657.27 ± 301.10 (40%)
≥ 1 b-jet (SR)	81.32 ± 1.53 (3%)	1074.28 ± 15.90 (29%)	8558.21 ± 37.23 (20%)	58925.03 ± 91.57 (48%)
Selection	H^\pm (110 GeV)	H^\pm (170 GeV)	H^\pm (1000 GeV)	Data (139 fb^{-1})
Trigger and skim	3202.25 ± 13.97	4116.46 ± 17.10	5268.21 ± 30.05	XXX \pm XXX
Loose tau, $p_T^\tau > 30 \text{ GeV}$	2793.23 ± 13.05 (87%)	3600.92 ± 15.99 (87%)	4313.45 ± 27.22 (82%)	XXX \pm XXX
Medium tau	1915.08 ± 10.81 (69%)	2592.01 ± 13.58 (72%)	3132.37 ± 23.23 (73%)	XXX \pm XXX
Tight muon, $p_T^e > 30 \text{ GeV}$	889.27 ± 7.17 (46%)	1264.26 ± 9.25 (49%)	1499.58 ± 15.93 (48%)	XXX \pm XXX
Muon and tau with OS	884.48 ± 7.15 (99%)	1258.52 ± 9.22 (100%)	1485.25 ± 15.88 (99%)	XXX \pm XXX
$E_T^{\text{miss}} > 50 \text{ GeV}$	563.90 ± 5.71 (64%)	946.69 ± 8.01 (75%)	1447.52 ± 15.62 (97%)	XXX \pm XXX
≥ 1 b-jet (SR)	447.73 ± 5.07 (79%)	693.80 ± 6.85 (73%)	1004.35 ± 12.95 (69%)	XXX \pm XXX

6.4 Multivariate Analysis Techniques

Once variables distributions are properly scaled and data/MC agreement is verified, multivariate analysis techniques are employed to separate signal-like events from background-like events in the signal regions. In the previous publication (described in Section 2.3.1), BDTs binned in m_{H^\pm} were used as the classifier, whereas this publication uses one PNN for the entire m_{H^\pm} spectrum. BDTs excel at separating linear correlations, whereas neural networks take advantage of nonlinear correlations. In the case of a PNN the parameterized variable, here m_{H^\pm} , is taken as an input to the network in addition with other input variables. PNNs offer the advantage of having one classifier model that can evaluate at any m_{H^\pm} value by learning how the signal event topology changes as m_{H^\pm} varies [68]. For illustrative purposes, expected limits on $\sigma(pp \rightarrow tbH^\pm) \times \mathcal{B}(H^\pm \rightarrow \tau\nu)$ in both subchannels is shown comparing an optimized BDT and an unoptimized PNN in Figure 6.11. It is seen that the PNN performs similarly to the BDTs used in the previous analysis. A PNN was chosen as the discriminator.

A Neural Network (NN) is a computing system loosely inspired by the human brain. NNs combine adaptive nonlinear basis functions in an attempt to perform a task; classification in the context of this dissertation. A NN contains layers of nodes connected to each other with an associated weight and threshold. As long as a node has output greater than the given threshold value, data will flow through that node². Otherwise, that node is not activated and data are not sent to the next layer. The NN as a whole relies on a process called training where the node weights are varied, an accuracy is calculated based on a given loss function, the weights are then varied again and the process repeats. This is done until a preferred accuracy is reached; the final node weights are saved and new data can be evaluated. A

²This is true of basic NNs. In some cases, this dissertation included, nodes are allowed small non-zero weights (negative or positive) to retain a so-called “leaky” node.

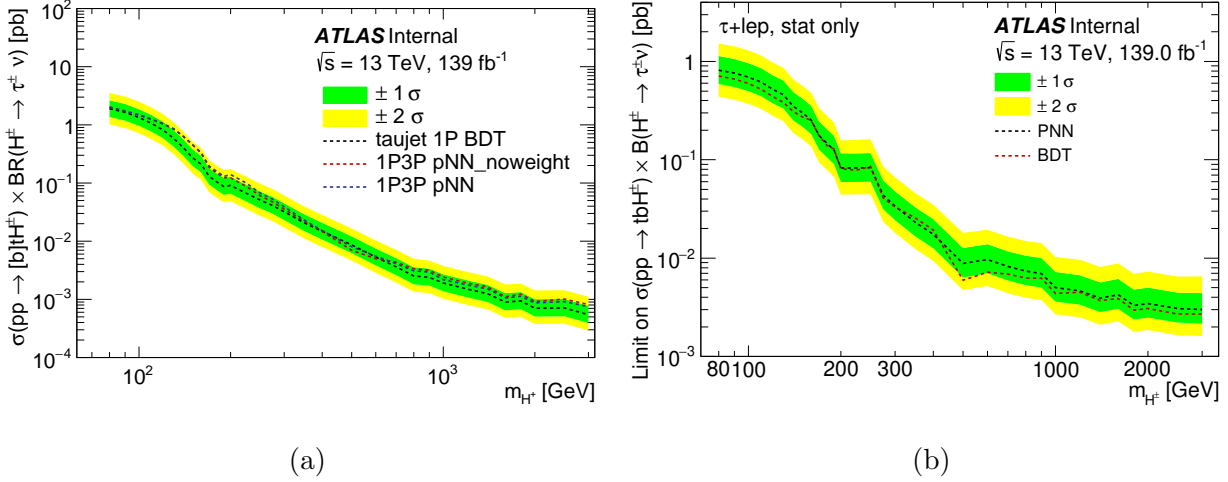


Figure 6.11: Comparison of performance of an optimized BDT and an unoptimized PNN on expected limits on $\sigma(pp \rightarrow tbH^\pm) \times B(H^\pm \rightarrow \tau^\pm \nu)$ in the $\tau + \text{jets}$ (a) and $\tau + \ell$ (b) signal regions.

diagram of a PNN can be seen in Figure 6.12, where the parameterized input is labeled as θ . The learned function of a NN can be written as:

$$y(x) = w_0^2 + \sum_{m=1}^M [w_m^2 \cdot h(w_{0m}^1 + \sum_{k=1}^D w_{km}^1 x_k)] \quad (6.6)$$

where w is the neuron weights, M is the number of basis functions being combined, D is the number of inputs and h is the activation function.

This analysis uses four PNNs; the two subchannels each have separate networks for 1-prong τ and 3-prong τ events.

6.4.1 Training

The training of the PNNs used in this dissertation are done with the Keras [69] library using the TensorFlow [70] library as backend. In order to increase the significance of training statistics and protect from overtraining, the k -fold method is used. Overtraining occurs

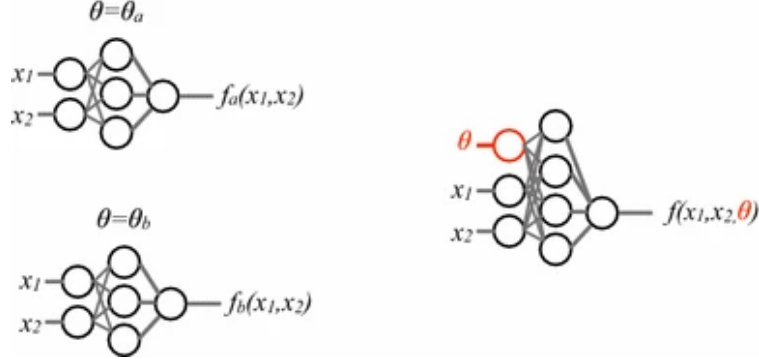


Figure 6.12: *Left*, individual networks with input variables (x_1, x_2) , each trained with examples with a single value of some parameter $\theta = \theta_a, \theta_b$. The individual networks are purely functions of the input variables. Performance for intermediate values of θ is not optimal nor does it necessarily vary smoothly between the networks. *Right*, a single network trained with input variables (x_1, x_2) as well as input parameter θ ; such a network is trained with examples at several values of the parameter θ [68].

	Fold 1	Fold 2	Fold 3	Fold 4	Fold 5	Background
Partition 1	Evaluation	Train	Train	Train	Train	Fold 1
Partition 2	Train	Evaluation	Train	Train	Train	Fold 2
Partition 3	Train	Train	Evaluation	Train	Train	Fold 3
Partition 4	Train	Train	Train	Evaluation	Train	Fold 4
Partition 5	Train	Train	Train	Train	Evaluation	Fold 5

Figure 6.13: The k -fold method for $k = 5$ [72].

when a NN has been fine tuned to have a high accuracy with a specific dataset and does not generalize to other datasets. To protect against this, dropout is used [71]. The k -fold method divides input training samples into k equally populated subsets. The k -th subset is trained on the other $k - 1$ subsets and evaluated on the k -th subset. Figure 6.13 shows a pictorial representation of the k -fold method. The standard choice of $k = 5$ is used in this analysis; this ensures statistical independence of training and evaluation of the PNNs and retaining a reasonable computational demand.

A single PNN training is performed on all m_{H^\pm} values at once, with the m_{H^\pm} value being taken as an input variable. For signal events, the m_{H^\pm} value from the MC generator is given; background events are replicated 32 times (the number of simulated m_{H^\pm} points is 32) and

each m_{H^\pm} value is given for each set. To avoid biasing the training due to varying statistics at each m_{H^\pm} value, the background events are weighted by a factor of $w = N_S^i/N_B^i$ where i corresponds to a given m_{H^\pm} value and N_S^i and N_B^i are the number of signal and background events, respectively. When the PNN is evaluated, the m_{H^\pm} value is assumed and the output is used as the discriminant at that m_{H^\pm} .

6.4.2 Input Variables Selection

The choice of input variables to the PNNs is critical to the performance of the analysis. Several sets of variables were compared using expected limits as the figure of merit. All studies were performed in the $\tau + \ell$ signal region, as this region proves the most difficult challenge to separate signal-like events from background-like events. One such study investigated the discriminating power of two sets of input variables. Input variables set A, consisting of the four vector components of the main physics objects in each event, were compared against another set of input variables B. Tables of the two sets of input variables are shown in Table 6.12. These two sets of variables were chosen to investigate the difference in signal-background separation between a PNN trained with engineered variables (Set B) and lower level kinematic information (Set A). Plots of all variables used in this study can be seen in Appendix C.

The variable $m_{H^\pm}^{Truth}$ corresponds to the m_{H^\pm} value the training and evaluation is performed at. In both cases, the variable Υ is used. Υ is a measure of the $\tau_{had-vis}$ polarization, computed by taking the asymmetry of energies carried by the charged and neutron pions from the 1-prong τ decay measured in the laboratory frame. Υ is defined as

$$\Upsilon = \frac{E_T^{\pi^\pm} - E_T^{\pi^0}}{E_T^\tau} \approx 2 \frac{p_T^{\tau-track}}{p_T^\tau} - 1 \quad (6.7)$$

where $p_T^{\tau-\text{track}}$ is the transverse momentum of the track associated with the 1-prong $\tau_{\text{had-vis}}$ candidate. As such, Υ is only defined for 1-prong $\tau_{\text{had-vis}}$ candidates. As demonstrated in the previous analysis, Υ provides a large contribution to signal-backgrounds separation at charged Higgs masses below 400 GeV [10]. This is due to W^- bosons coupling exclusively to left-handed τ^- leptons in $W \rightarrow \tau\nu$ decays and W^+ bosons coupling exclusively to τ^+ leptons. In such a case, Υ is expected to have a value of -1 . Whereas in the MSSM, a charged scalar Higgs boson would lead to an Υ value of $+1$ [73]. A detailed explanation and dedicated measurement of τ polarization can be seen in Reference [73].

An estimate of the impact of two sets of input variables on the expected limits on $\sigma(pp \rightarrow tbH^\pm) \times \mathcal{B}(H^\pm \rightarrow \tau\nu)$ is shown in 6.14. Input variables set A was chosen as performance was similar at low m_{H^\pm} and greater at high m_{H^\pm} . An optimization of the number of layers in the PNN and several other parameters of the PNN is discussed in detail in Section 6.4.3.

6.4.3 Hyperparameter Optimization

In order to optimize the PNN, a scan of hyperparameters and network architecture was done, referred to as HPO. A calculated Area Under the Curve (AUC) was used as the figure of merit. As in the normal training scheme, the k -fold method with $k = 5$ was used to keep background modelling and classifier training statistically independent. To prevent overtraining, the early stopping method was used and the best weights kept to calculate the AUC. The early stopping method has two parameters, Δ_{\min} and patience. Δ_{\min} is the minimum allowed difference in AUC between training epochs. Once the Δ_{\min} value is lower than the user defined threshold several more epochs are trained to ensure a global minima is found. The patience is this number of extra training epochs. For this dissertation

Table 6.12: Two sets of kinematic variables used as input to the PNN in the $\tau + \ell$ subchannel. $\Delta\phi_{X, \text{miss}}$ denotes the difference in azimuthal angle between a reconstructed object X ($X = \tau, b - \text{jet}, \ell$) and the direction of the missing transverse momentum. Distributions of all variables can be seen in Appendix C.

Set A Input Variables

p_T^τ	η^τ	ϕ^τ
p_T^ℓ	η^ℓ	ϕ^ℓ
p_T^{b-jet}	η^{b-jet}	ϕ^{b-jet}
p_T^{jet}	η^{jet}	ϕ^{jet}
E_T^{miss}	$\phi^{E_T^{\text{miss}}}$	$p_T^{j_1}$
Υ	$m_{H^\pm}^{\text{Truth}}$	

(a) Set A of input variables

Set B Input Variables

E_T^{miss}
p_T^τ
p_T^{b-jet}
p_T^ℓ
p_T
$\Delta\phi_{\tau, \text{miss}}$
$\Delta\phi_{b-jet, \text{miss}}$
$\Delta\phi_{\ell, \text{miss}}$
$\Delta R_{\tau, \ell}$
$\Delta R_{b-jet, \ell}$
$\Delta R_{b-jet, \tau}$
$\Delta\phi_{\tau, \text{miss}}/\Delta\phi_{\text{jet,miss}}$
Υ
$m_{H^\pm}^{\text{Truth}}$

(b) Set B of input variables

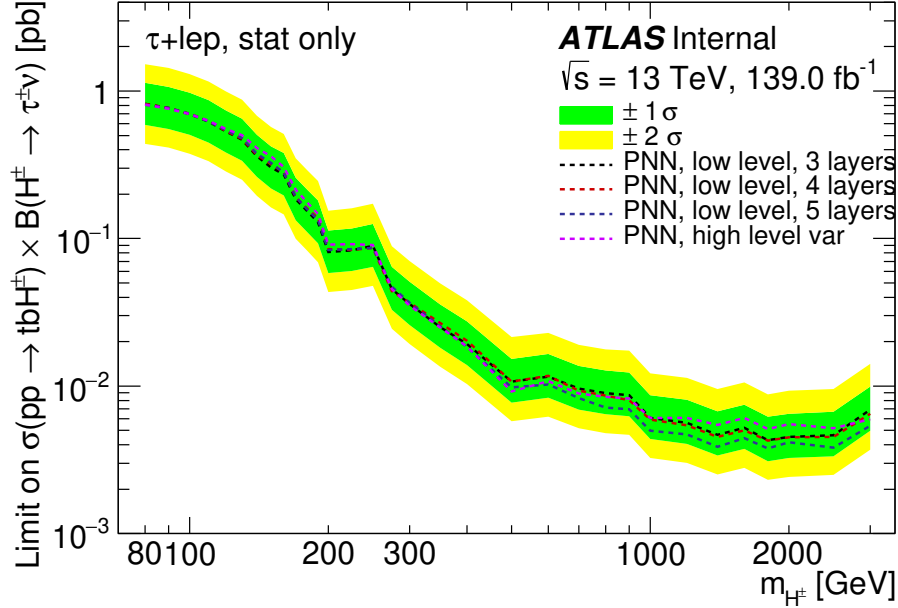


Figure 6.14: Expected limits comparing input variables set A and B with various depths in the PNN architecture. X layers refers to the number of layers in the PNN.

$\Delta_{min} = 0.00001$ and a patience of 10 were used. Due to the low signal acceptance and the increased difficulty of separating signal from background at lower m_{H^\pm} values, the PNN was optimized for low m_{H^\pm} values. To optimize for PNN performance in low H^\pm mass points, a separate average taking into account only H^\pm mass values between 80 and 500 GeV was used as the final figure of merit. In an effort to keep the computational needs low, several small grids of hyperparameters and architecture structures were scanned. Tables 6.13 - 6.17 show the hyperparameter grids that were searched. Here, width refers to the number of neurons per layer and depth is the number of layers. The final hyperparameter from each grid search is highlighted in red. The results of the final grid search can be seen in Tables 6.18 and 6.19; the quoted errors are taken from the standard deviation across all k -folds. The AUC values for each m_{H^\pm} point for the final chosen model are shown in Figure 6.15.

Table 6.13: First grid, scanning over activation function and loss function. Binary cross-entropy was the chosen loss function, highlighted in red.

Parameter			
activation function	softsign	relu	LeakyReLU
loss function	binary cross-entropy	mean squared error	mean absolute error
width		32	
depth		10	
batch size		1025	

Table 6.14: Second grid, scanning over width, depth, and dropout value. 0.1 was chosen for the dropout value, highlighted in red.

Parameter			
width	8	16	32
depth	3	5	10
dropout	0.1	0.3	
activation function		softsign	
loss function	binary cross-entropy		
batch size		1024	

Table 6.15: Third grid, scanning over activation function. LeakyReLU was chosen, highlighted in red.

Parameter			
width	32	64	128
depth	2	3	4
activation function	softsign	relu	LeakyReLU
dropout		0.1	
batch size		1024	
loss function	binary cross-entropy		

Table 6.16: Fourth grid, scanning over LeakyReLU α value. $\alpha = 0.05$ was chosen, highlighted in red.

Parameter				
width	32	64	128	
depth	2	3	4	
α	0.01	0.05	0.001	0.005
batch size			1024	
dropout			0.1	
activation function			LeakyReLU	
loss function			binary cross-entropy	

Table 6.17: Fifth grid, scanning over network width and depth. $width = 128$ and $depth = 3$ was chosen, highlighted in red.

Parameter				
width	32	64	128	256
depth	2	3	4	5
batch size			1024	
dropout			0.1	
activation function			LeakyReLU	
batch size			1024	
α			0.05	
loss function			binary cross-entropy	

Table 6.18: AUCs of final HPO grid. An error of 0 corresponds to only one job k-fold finishing training due to computational limits. The LowMassAvg error takes into account difference between k-folds and the associated error from the averaging calculation.

width	depth	80	150	250	500	Avg	LowMassAvg
128	3	0.6661 ± 0.0000	0.8145 ± 0.0000	0.9031 ± 0.0000	0.9633 ± 0.0000	0.8876 ± 0.0000	0.8261 ± 0.0968
128	5	0.6492 ± 0.0000	0.8043 ± 0.0000	0.9078 ± 0.0000	0.9628 ± 0.0000	0.8861 ± 0.0000	0.8235 ± 0.1000
128	4	0.6593 ± 0.0000	0.8117 ± 0.0000	0.9012 ± 0.0000	0.9638 ± 0.0000	0.8858 ± 0.0000	0.8232 ± 0.0994
128	2	0.6444 ± 0.0000	0.8070 ± 0.0000	0.9075 ± 0.0000	0.9631 ± 0.0000	0.8857 ± 0.0000	0.8231 ± 0.1006
64	4	0.6576 ± 0.0050	0.8080 ± 0.0013	0.9052 ± 0.0045	0.9656 ± 0.0016	0.8857 ± 0.0002	0.8230 ± 0.0994
64	2	0.6528 ± 0.0066	0.8052 ± 0.0023	0.9057 ± 0.0032	0.9651 ± 0.0007	0.8855 ± 0.0004	0.8228 ± 0.0996
64	5	0.6538 ± 0.0050	0.8044 ± 0.0019	0.9058 ± 0.0037	0.9653 ± 0.0014	0.8853 ± 0.0005	0.8224 ± 0.0997
64	3	0.6520 ± 0.0067	0.8051 ± 0.0018	0.9042 ± 0.0044	0.9649 ± 0.0019	0.8853 ± 0.0011	0.8223 ± 0.0994
256	5	0.6536 ± 0.0010	0.8044 ± 0.0033	0.9036 ± 0.0042	0.9644 ± 0.0022	0.8844 ± 0.0002	0.8213 ± 0.1003
256	4	0.6434 ± 0.0000	0.8018 ± 0.0000	0.9017 ± 0.0000	0.9619 ± 0.0000	0.8823 ± 0.0000	0.8181 ± 0.1013
32	3	0.6369 ± 0.0094	0.7950 ± 0.0041	0.8977 ± 0.0032	0.9635 ± 0.0022	0.8798 ± 0.0012	0.8139 ± 0.1031
32	4	0.6384 ± 0.0037	0.7935 ± 0.0033	0.8986 ± 0.0037	0.9636 ± 0.0016	0.8799 ± 0.0009	0.8139 ± 0.1031
32	2	0.6399 ± 0.0058	0.7924 ± 0.0024	0.8983 ± 0.0033	0.9629 ± 0.0023	0.8796 ± 0.0004	0.8135 ± 0.1023
32	5	0.6350 ± 0.0077	0.7931 ± 0.0056	0.8981 ± 0.0022	0.9625 ± 0.0005	0.8792 ± 0.0011	0.8128 ± 0.1035
256	2	0.6320 ± 0.0044	0.7971 ± 0.0000	0.8939 ± 0.0034	0.9587 ± 0.0018	0.8781 ± 0.0002	0.8120 ± 0.1023

Table 6.19: Average AUCs of final HPO grid. An error of 0 corresponds to only one job k-fold finishing training due to computational limits.

width	depth	Avg	LowMassAvg
128	3	0.8876 ± 0.0000	0.8261 ± 0.0968
128	5	0.8861 ± 0.0000	0.8235 ± 0.1000
128	4	0.8858 ± 0.0000	0.8232 ± 0.0994
128	2	0.8857 ± 0.0000	0.8231 ± 0.1006
64	4	0.8857 ± 0.0002	0.8230 ± 0.0994
64	2	0.8855 ± 0.0004	0.8228 ± 0.0996
64	5	0.8853 ± 0.0005	0.8224 ± 0.0997
64	3	0.8853 ± 0.0011	0.8223 ± 0.0994
256	5	0.8844 ± 0.0002	0.8213 ± 0.1003
256	4	0.8823 ± 0.0000	0.8181 ± 0.1013
32	3	0.8798 ± 0.0012	0.8139 ± 0.1031
32	4	0.8799 ± 0.0009	0.8139 ± 0.1031
32	2	0.8796 ± 0.0004	0.8135 ± 0.1023
32	5	0.8792 ± 0.0011	0.8128 ± 0.1035
256	2	0.8781 ± 0.0002	0.8120 ± 0.1023

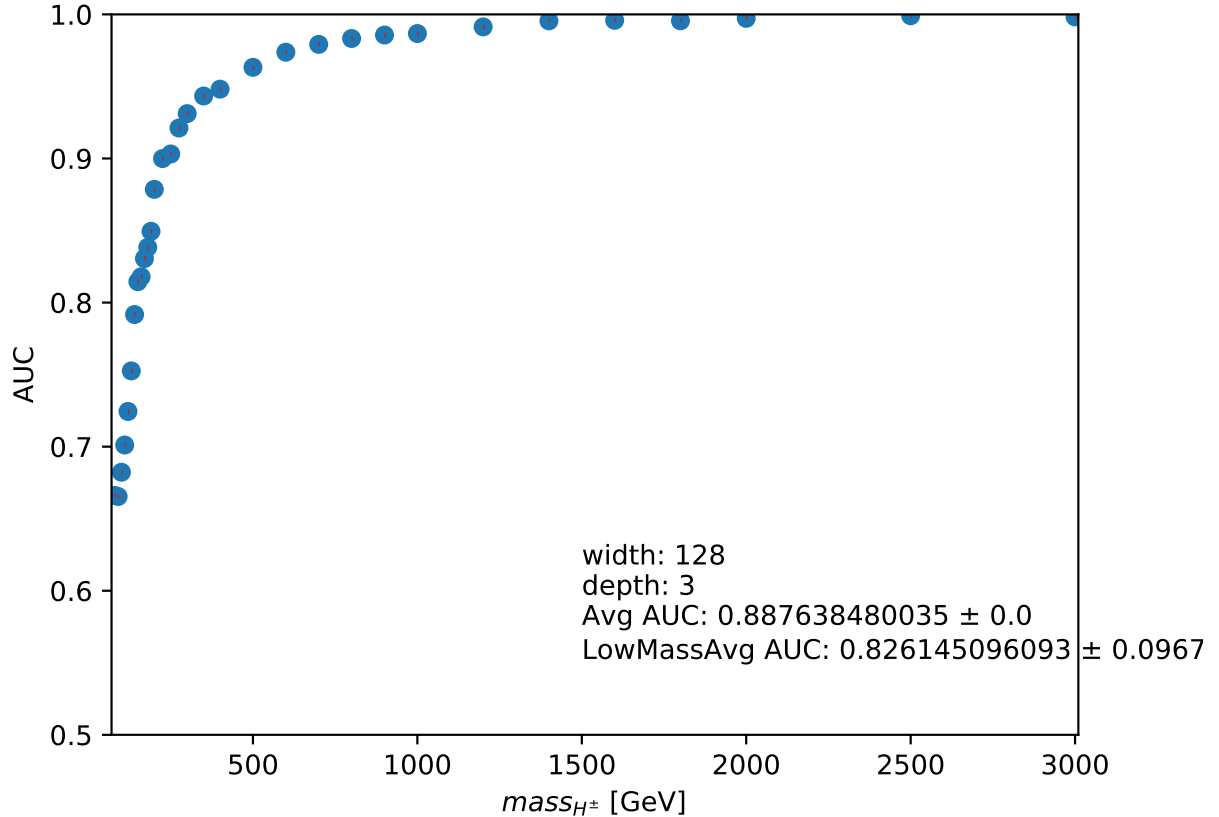


Figure 6.15: Final model AUC for each mass point. Individual points correspond to the AUC average over 5 kfolds.

The final model was chosen to have 128 neurons per layer with three layers, with the binary cross-entropy chosen as the loss function, a dropout of 0.1, LeakyReLU as the activation function with $\alpha = 0.05$. The LeakyReLU activation function is depicted in Figure 6.16, where the α value is the slope of the negative portion. Allowing negative weight values prevents neurons from becoming deactivated prematurely.

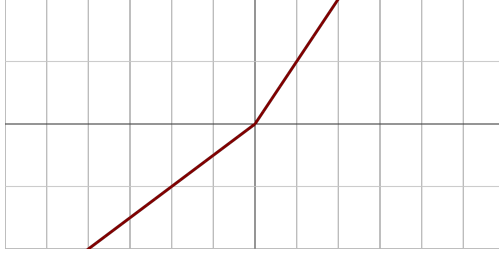


Figure 6.16: LeakyReLU activation function. The associated hyperparameter α is the slope of the negative portion of the function.

6.5 Systematic Uncertainties

Systematic uncertainties have a variety of sources and are discussed here. Detector-related systematic uncertainties from the reconstruction and identification of leptons and $\tau_{had-vis}$ objects [74], simulation of the electron and muon triggers, reconstruction of E_T^{miss} , and energy/momentum scale and resolution of all physics objects such as τ leptons [74], jets [53], electrons [75], E_T^{miss} [59], and muons [60] are studied by varying selection cuts by ± 1 standard deviation. The difference in event yields is then taken as a systematic error and summed in quadrature with all other sources of error to give the final quoted errors. Systematic errors resulting in an upward fluctuation are kept separate from downward fluctuations. The effect of the main sources of uncertainties on the event yield for $t\bar{t}$ and an arbitrary mass point of $m_{H^\pm} = 200$ GeV are shown in Table 6.20 for all SRs. Jet systematic uncertainties arising from reconstruction, identification, flavor composition, resolution account for the largest contribution. Systematic uncertainties arising from the data-driven fake factor method are shown in Table 6.21. The uncertainty listed as “Fake factors: True $\tau_{had-vis}$ in the anti- $\tau_{had-vis}$ CR” is a conservative uncertainty of 50% applied to account for amount of $\tau_{had-vis}$ candidates that are subtracted when computing $N_{fakes}^{anti-\tau}$. Table 6.22 shows systematic uncertainties combined by their source. The combined fake factor systematic uncertainty is the largest contributor, followed by the jet systematics listed above. Theoretical uncertainties

Table 6.20: Effect of the main systematic uncertainties on the expected event yield for $t\bar{t}$ and signal events ($m_{H^\pm} = 200$ GeV) passing the nominal event selection of the three SRs. The three components of the $\tau_{had-vis}$ energy scale uncertainty are shown in the table. Impacts are shown in percent change with respect to the nominal SR selections.

Source	Impact on the expected event yield (%)					
	$\tau + \text{jets}$		$\tau + e$		$\tau + \mu$	
	$t\bar{t}$	H^\pm 200 GeV	$t\bar{t}$	H^\pm 200 GeV	$t\bar{t}$	H^\pm 200 GeV
$\tau_{had-vis}$ reconstruction efficiency	± 1.24	± 1.22	± 1.23	$+1.22$ -1.23	± 1.23	± 1.22
$\tau_{had-vis}$ -id	± 1.79	± 0.52	± 1.40	± 0.50	± 1.40	± 0.48
$\tau_{had-vis}$ energy scale	$+2.53$ -2.80	$+2.00$ -1.66	$+1.60$ -1.44	$+1.28$ -1.66	$+1.53$ -1.39	$+1.72$ -1.46
$\tau_{had-vis}$ energy scale (detector)	$+1.96$ -1.55	$+1.64$ -1.49	$+0.23$ -0.21	$+1.15$ -1.08	$+0.16$ -0.55	$+0.49$ -1.5
$\tau_{had-vis}$ energy scale (in-situ)	$+1.44$ -1.43	$+0.22$ -0.74	$+1.17$ -1.20	$+0.74$ -0.63	$+1.14$ -1.15	$+0.54$ -0.37
$\tau_{had-vis}$ energy scale (model)	$+0.56$ -0.61	-0.06	$+0.23$ -0.21	$+1.15$ -1.08	$+0.16$ -0.55	$+0.49$ -1.50
$\tau_{had-vis}$ energy scale (physics list)	$+1.27$ -1.26	-0.72	$+0.74$ -0.65	$+0.67$ -0.25	$+0.72$ -0.63	$+0.83$ -0.60
jet uncertainties	$+7.38$ -8.39	$+6.51$ -9.06	$+3.41$ -3.31	$+4.49$ -2.78	$+3.18$ -3.24	$+3.67$ -2.96
E_T^{miss} soft term scale/resolution	$+1.31$ -1.12	$+1.15$ -1.49	$+0.29$ -0.24	$+0.88$ -0.34	$+0.30$ -0.23	$+0.21$ -0.11
trigger	$+1.23$ -1.61	0	± 0.03	0	$+0.55$ -0.56	± 0.56
e -id	0	0	± 0.71	± 0.73	0	0
μ -id/reconstruction/isolation	0	0	0 -0.01	0 -0.11	$+0.97$ -1.40	$+1.00$ -2.94
μ MS	0	0	0	0	$+0.09$ -0.12	$+0.40$ -0.34

for signal and $t\bar{t}$ background were considered in the last publication; at the time of writing this dissertation the simulations are being produced and therefore are not included. In the previous result, H^\pm signal modelling systematic errors were found to have an impact on expected limits of 2.5% for $m_{H^\pm} = 170$ GeV and 6.4% for $m_{H^\pm} = 1000$ GeV [10].

Table 6.21: Effect on the shape variation and the yields of systematic uncertainties associated with the data-driven fake factor method, used to estimate the $j \rightarrow \tau$ background in the $\tau + \text{jets}$ and $\tau + \ell$ channel.

Source of uncertainty	$\tau + \text{jets}$		$\tau + \ell$	
	Effect on yield	Shape	Effect on yield	Shape
Fake factors: statistical uncertainties	3.9%	✗	3.2%	✗
Fake factors: True $\tau_{\text{had-vis}}$ in the anti- $\tau_{\text{had-vis}}$ CR	+3.4% -3.2%	✗	+4% -4.3%	✗
Fake factors: tau RNN Identification SF	2.7%	✓	2.7%	✓
Fake factors: α_{MJ} uncertainty	3.6%	✗	1.9%	✗
Fake factors: heavy flavor jet fraction	6%	✓	5.53%	✓

Table 6.22: Effect of the combined main systematic uncertainties on the expected event yield for $t\bar{t}$ and signal events ($m_{H^\pm} = 200$ GeV) passing the nominal event selection of the three SRs. The three components of the $\tau_{\text{had-vis}}$ energy scale uncertainty are shown in the table. Impacts are shown in percent change with respect to the nominal SR selections.

Source	Impact on the expected event yield (%)					
	$\tau + \text{jets}$		$\tau + e$		$\tau + \mu$	
	$t\bar{t}$	H^\pm 200 GeV	$t\bar{t}$	H^\pm 200 GeV	$t\bar{t}$	H^\pm 200 GeV
Fake factor uncertainties	+9.11 -9.04	+9.11 -9.04	+8.23 -8.34	+8.23 -8.34	+8.23 -8.34	+8.23 -8.34
jet uncertainties	+7.38 -8.39	+6.51 -9.06	+3.41 -3.31	+4.49 -2.78	+3.18 -3.24	+3.67 -2.96
τ uncertainties	± 4.36	+2.91 -2.80	+2.84 -2.74	+2.65 -2.70	+2.77 -2.78	+2.58 -2.97
E_T^{miss} uncertainties	+1.31 -1.12	+1.15 -1.49	+0.29 -0.24	+0.88 -0.34	+0.30 -0.23	+0.21 -0.11
trigger uncertainties	+1.23 -1.61	0	± 0.03	0	+0.55 -0.56	± 0.56
e uncertainties	0	0	± 0.71	± 0.73	0	0
μ uncertainties	0	0	-0.01	-0.11	+0.97 -1.41	+1.08 -2.96

Table 6.23: Expected event yields for the backgrounds and a hypothetical H^\pm signal after applying all $\tau+\text{jets}$ selection criteria, and comparison with 139 fb^{-1} of data. The values shown for the signal assuming a charged Higgs boson mass of 170 GeV and 1000 GeV, with a cross-section times branching fraction $\sigma(pp \rightarrow tbH^\pm) \times \mathcal{B}(H^\pm \rightarrow \tau\nu)$ corresponding to $\tan\beta = 40$ in the hMSSM benchmark scenario. Statistical and systematic uncertainties are quoted, respectively.

Sample	Event yields $\tau_{had-vis} + \text{jets}$		
$t\bar{t}$	18443	\pm 48	+1545 -1697
Single-top-quark	2284	\pm 17	+184 -207
$W \rightarrow \tau\nu$	1979	\pm 23	+179 -229
$Z \rightarrow \tau\tau$	242	\pm 5	+24 -32
Diboson (WW, WZ, ZZ)	133	\pm 4	+9 -12
Misidentified $e, \mu \rightarrow \tau_{had-vis}$	328	\pm 6	+25 -34
Misidentified jet $\rightarrow \tau_{had-vis}$	2506	\pm 17	+130 -133
All backgrounds	25917	\pm 59	+1572 -1730
H^\pm (170 GeV), hMSSM $\tan\beta = 40$	1075	\pm 9	+82 -79
H^\pm (1000 GeV), hMSSM $\tan\beta = 40$	12910	\pm 59	+784 -720

6.6 Expected Results

The expected event yields for backgrounds and signal³ are summarized in Table 6.23 ($\tau+\text{jets}$) and Table 6.24 ($\tau + \ell$).

The test statistic \tilde{q}_μ [76] is used to test the agreement of the data with the background-only and signal+background hypotheses. The test statistic is based on a profile likelihood

³At the time of writing, the analysis is still blinded so data is not included.

Table 6.24: Expected event yields for the backgrounds and a hypothetical H^\pm signal after applying all $\tau + \ell$ selection criteria, and comparison with 139 fb^{-1} of data. The values shown for the signal assuming a charged Higgs boson mass of 170 GeV and 1000 GeV, with a cross-section times branching fraction $\sigma(pp \rightarrow tbH^\pm) \times \mathcal{B}(H^\pm \rightarrow \tau\nu)$ corresponding to $\tan\beta = 40$ in the hMSSM benchmark scenario. Statistical and systematic uncertainties are quoted, respectively.

Sample	Event yields $\tau+e$			Event yields $\tau+\mu$				
$t\bar{t}$	43813	\pm	76	+1749 -1833	44486	\pm	75	+1811 -1907
Single-top-quark	3260	\pm	20	+124 -134	3873	\pm	22	+158 -165
$W \rightarrow \tau\nu$	2.41	\pm	0.56	+0.22 -2.15	0.07	\pm	0.12	+0.08 -0.16
$Z \rightarrow \tau\tau$	913	\pm	20	+64 -149	845	\pm	22	+88 -111
Diboson (WW, WZ, ZZ)	72.64	\pm	1.52	+5.25 -3.91	80.81	\pm	1.53	+5.40 -6.45
Misidentified $e, \mu \rightarrow \tau_{had-vis}$	1083	\pm	24	+41 -73	1060	\pm	15	+43 -70
Misidentified jet $\rightarrow \tau_{had-vis}$	8662	\pm	37	+450 -470	8426	\pm	37	+440 -459
All backgrounds	57809	\pm	93	+1812 -1846	58773	\pm	90	+1873 -1970
H^\pm (170 GeV), hMSSM $\tan\beta = 40$	598	\pm	6	+20 -22	702	\pm	6	+22 -16
H^\pm (1000 GeV), hMSSM $\tan\beta = 40$	938	\pm	13	+48 -37	1024	\pm	13	+48 -57

ratio where the binned likelihood function $\mathcal{L}(\mu, \theta)$ is constructed as the product of Poisson probability terms over all bins and regions. The likelihood ratio is the ratio between the conditional maximum-likelihood estimator of the nuisance parameters, θ , for a given signal hypothesis μ and the unconditional maximum-likelihood estimator for μ and the nuisance parameters. \tilde{q}_μ is defined as:

$$\tilde{q}_\mu = \begin{cases} -2 \ln \frac{\mathcal{L}(\mu, \hat{\theta}(\mu))}{\mathcal{L}(0, \hat{\theta}(0))}, & \hat{\mu} < 0 \\ -2 \ln \frac{\mathcal{L}(\mu, \hat{\theta}(\mu))}{\mathcal{L}(\hat{\mu}, \hat{\theta})}, & 0 \leq \hat{\mu} \leq \mu \\ 0 & \hat{\mu} > \mu \end{cases} \quad (6.8)$$

Here, $\hat{\mu}$ and $\hat{\theta}$ are the values of the parameters that maximize the likelihood function. $\hat{\theta}(\mu)$ corresponds to the values of the nuisance parameters that maximize the likelihood function for a given signal strength μ .

The fit is performed on the PNN score distributions in the three SRs, $\tau+\text{jets}$, $\tau+\text{e}$, $\tau+\mu$, and the dilepton-btag CR which is enriched in the dominant $t\bar{t}$ background. Pre-fit PNN score distributions are shown in Figures 6.17 - 6.22. At the time of writing this dissertation, the analysis is still blinded. Assuming the fit agrees with the background-only hypothesis expected limits of $\sigma(pp \rightarrow tbH^\pm) \times \mathcal{B}(H^\pm \rightarrow \tau\nu)$ are calculated. Exclusion limits are set at the 95% confidence level (CL) using the CL_s procedure [77]. The expected exclusion limits on $\sigma(pp \rightarrow tbH^\pm) \times \mathcal{B}(H^\pm \rightarrow \tau\nu)$ can be seen in Figure 6.23 compared to the previous 36.1 fb^{-1} result. In all three subchannels an improvement across the entire m_{H^\pm} range can be seen. The result of this search is expected to improve the limits by a factor of $\gtrsim 3\times$ depending on the m_{H^\pm} value. The $\tau+\text{e}$ and $\tau+\mu$ SRs outperform the $\tau+\text{jets}$ SR at low m_{H^\pm} while the $\tau+\text{jets}$ SR excels at high mass values. In all three SRs the limits turn upwards between 2500 GeV and 3000 GeV; this is due to the decreased signal acceptance shown in Figure 6.2. At

the time of writing the combination of the $\tau + \ell$ and $\tau + \text{jets}$ subchannels is underway. As in the previous result [10] the combined limit will be extrapolated to set limits on $\tan \beta$.

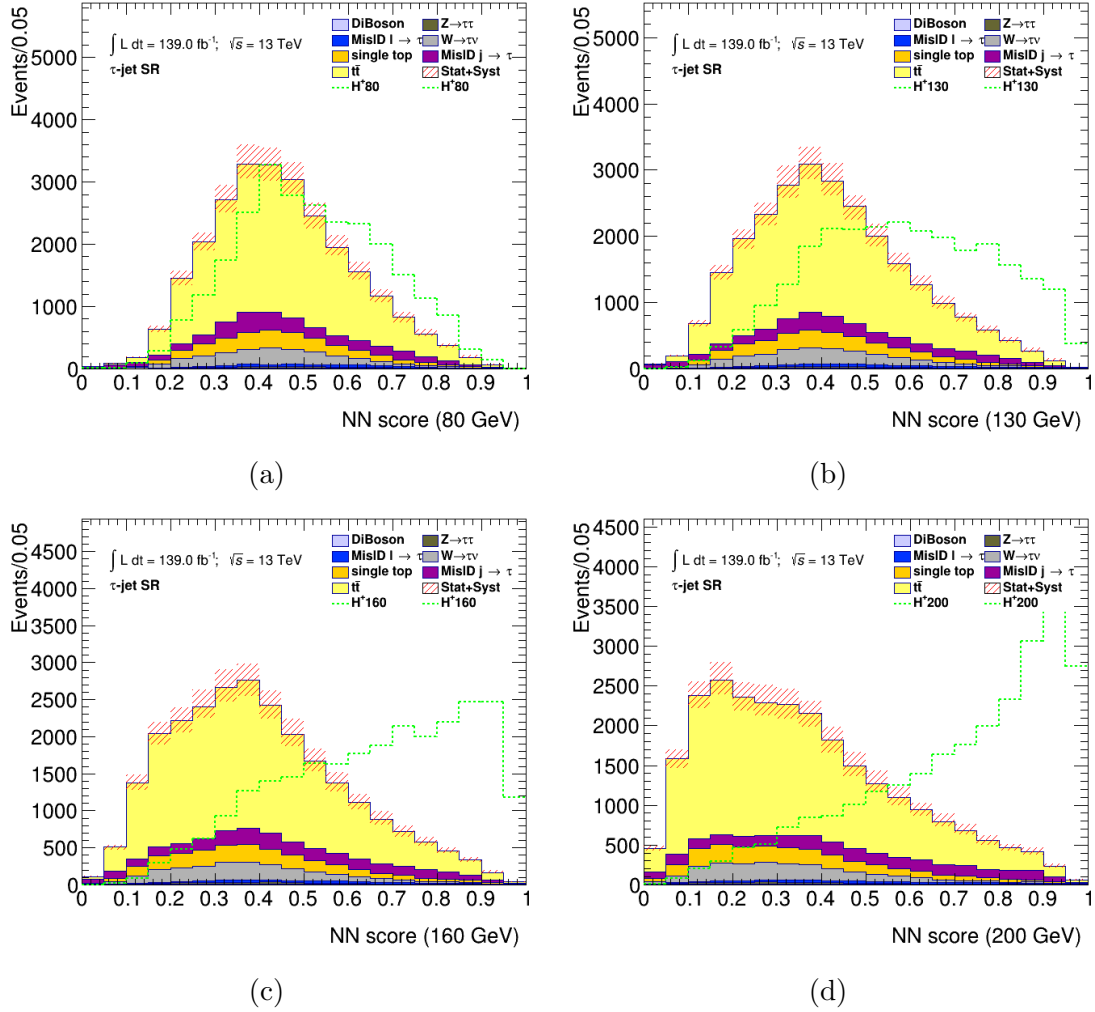


Figure 6.17: PNN score distributions in the signal region of the $\tau + \text{jets}$ channel, for chosen charged Higgs boson mass parameters. The lower panel of each plot shows the ratio of data to the SM background prediction. The uncertainty bands include all statistical and systematic uncertainties. The normalization of the signal (shown for illustration) corresponds to the integral of the background.

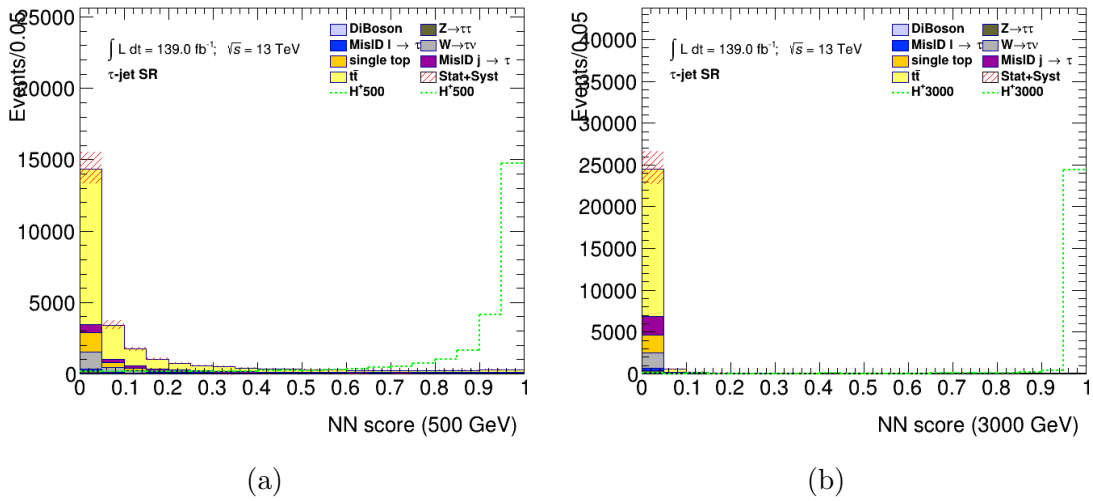


Figure 6.18: PNN score distributions in the signal region of the τ +jets channel, for chosen charged Higgs boson mass parameters. The lower panel of each plot shows the ratio of data to the SM background prediction. The uncertainty bands include all statistical and systematic uncertainties. The normalization of the signal (shown for illustration) corresponds to the integral of the background.

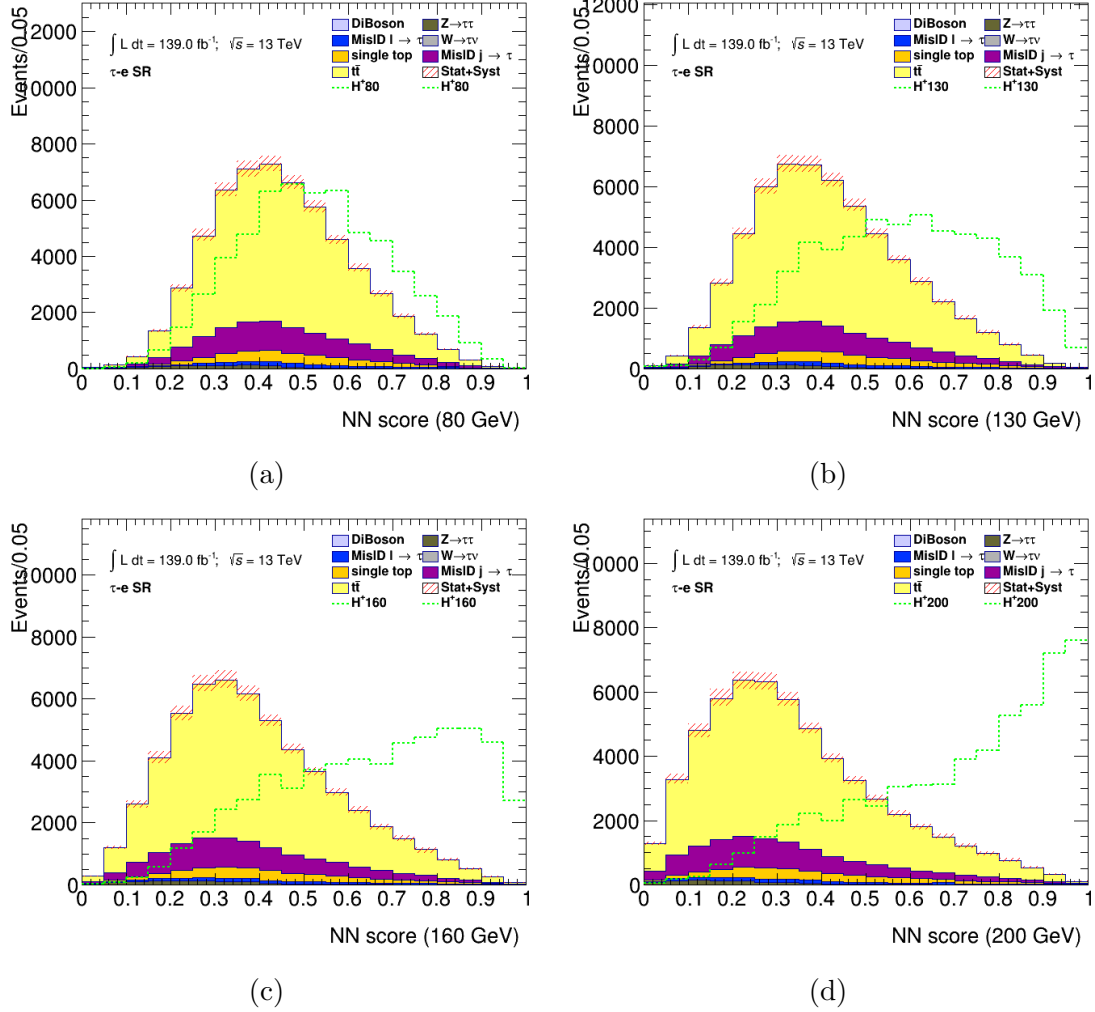


Figure 6.19: PNN score distributions in the signal region of the $\tau + e$ sub-channel, for the chosen charged Higgs boson mass parameters. The lower panel of each plot shows the ratio of data to the SM background prediction. The uncertainty bands include all statistical and systematic uncertainties. The normalization of the signal (shown for illustration) corresponds to the integral of the background.

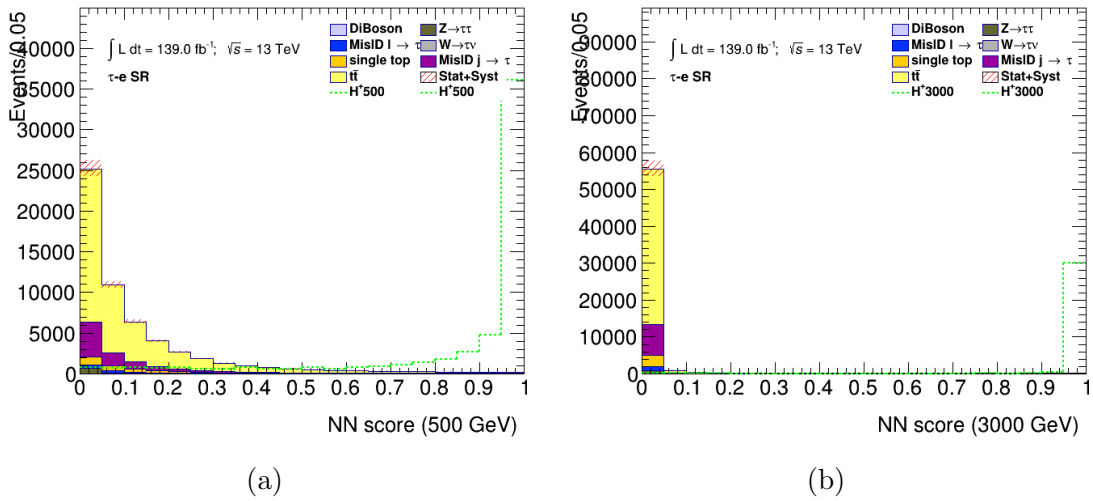


Figure 6.20: PNN score distributions in the signal region of the $\tau+e$ sub-channel, for the chosen charged Higgs boson mass parameters. The lower panel of each plot shows the ratio of data to the SM background prediction. The uncertainty bands include all statistical and systematic uncertainties. The normalization of the signal (shown for illustration) corresponds to the integral of the background.

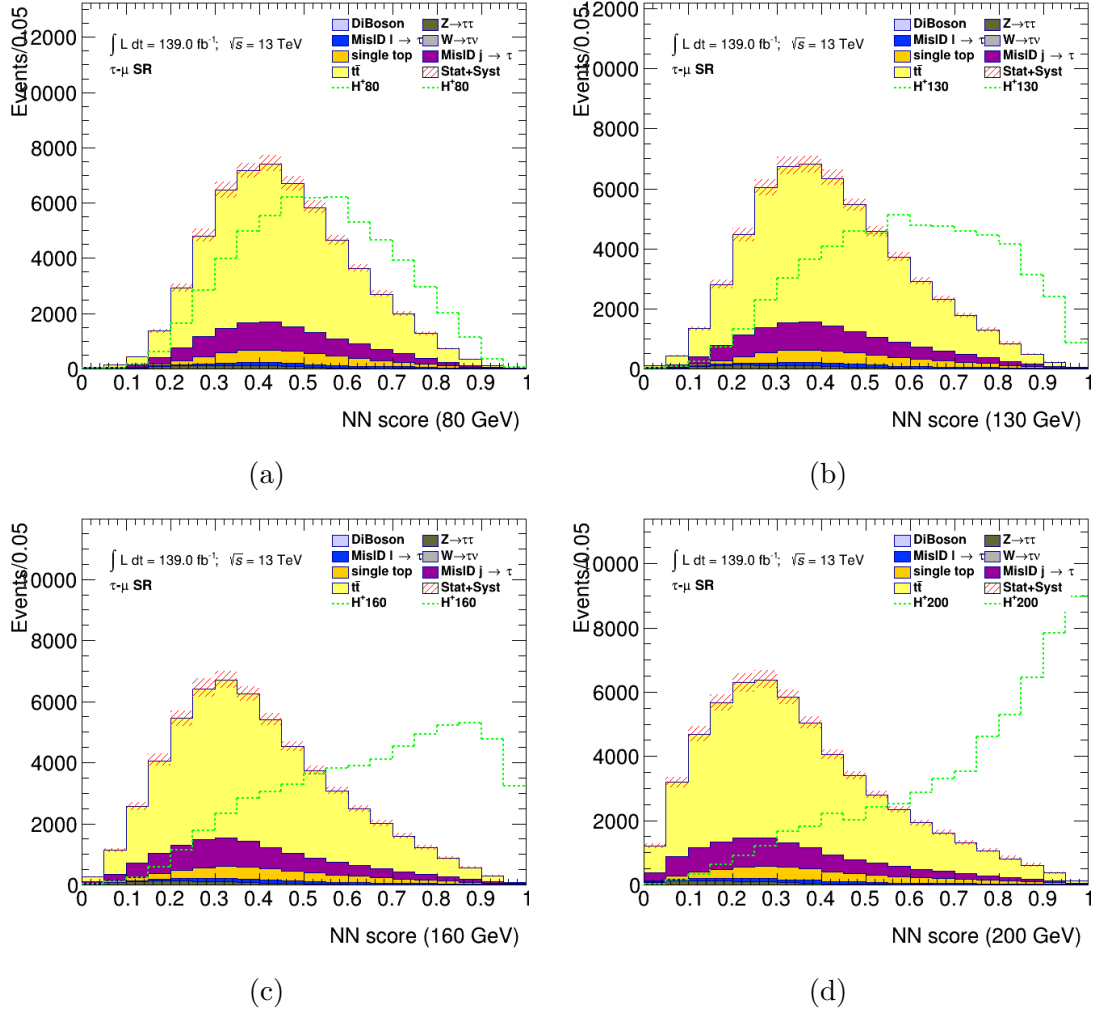


Figure 6.21: PNN score distributions in the signal region of the $\tau+\mu$ sub-channel, for the chosen charged Higgs boson mass parameters. The lower panel of each plot shows the ratio of data to the SM background prediction. The uncertainty bands include all statistical and systematic uncertainties. The normalization of the signal (shown for illustration) corresponds to the integral of the background.

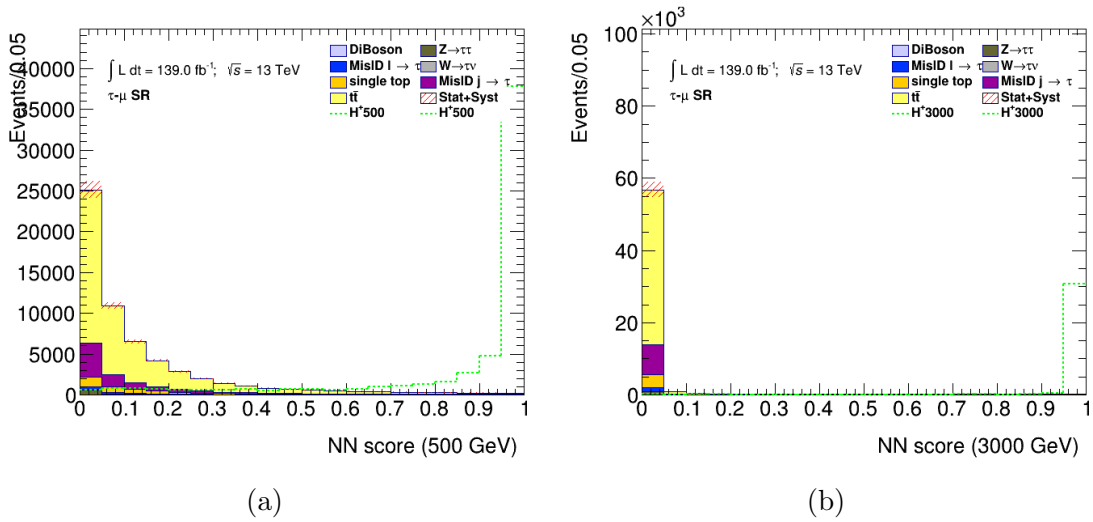


Figure 6.22: PNN score distributions in the signal region of the $\tau + \mu$ sub-channel, for the chosen charged Higgs boson mass parameters. The lower panel of each plot shows the ratio of data to the SM background prediction. The uncertainty bands include all statistical and systematic uncertainties. The normalization of the signal (shown for illustration) corresponds to the integral of the background.

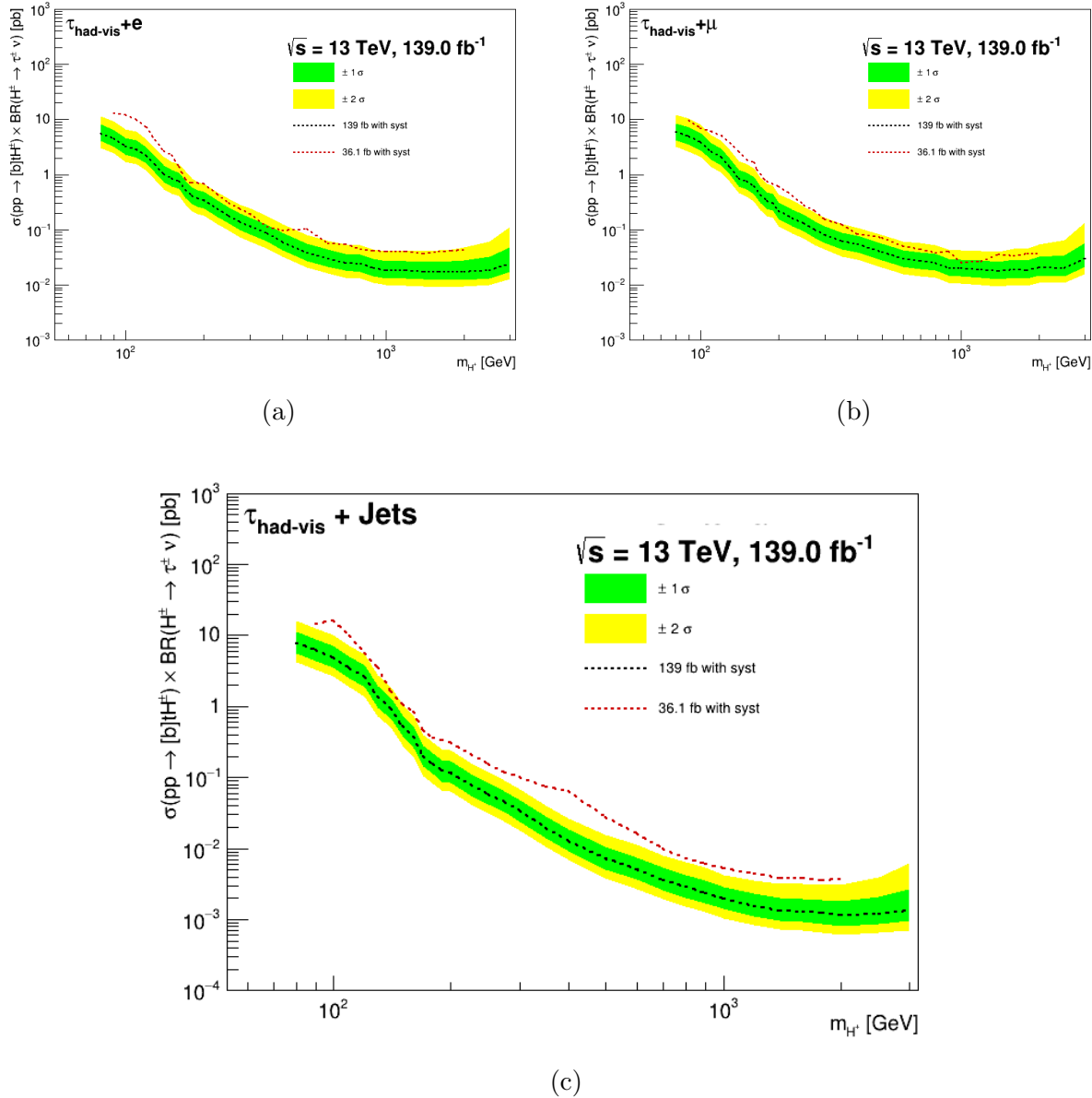


Figure 6.23: Expected 95% CL exclusion limits on $\sigma(pp \rightarrow tbH^\pm) \times \mathcal{B}(H^\pm \rightarrow \tau\nu)$ as a function of the charged Higgs boson mass in 139 fb^{-1} of pp collision data at $\sqrt{s} = 13 \text{ TeV}$ in the $\tau+e$ signal region (a), the $\tau+\mu$ signal region (b), and the $\tau+\text{jets}$ signal region (c). In the case of the expected limits, one- and two-standard-deviation uncertainty bands are also shown. As a comparison, the expected exclusion limits obtained with the dataset collected in 2015 and 2016 [10] are also shown.

CHAPTER 7

CONCLUSION

The Standard Model is an incredibly accurate model of fundamental particle physics, but is ultimately incomplete. There are many possible extensions to the Standard Model; this dissertation covers a search for a charged Higgs boson in the $H^\pm \rightarrow \tau^\pm \nu_\tau$ final state within the 2-Higgs Doublet Model (2HDM) theory.

The search consists of two subchannels based on the decay of the associated top quark; $\tau + \ell$ for the leptonic decay channel and $\tau + \text{jets}$ for the hadronic decay channel. Parameterized Neural Networks were investigated and optimized to separate signal from background in the Signal Regions. Assuming a result consistent with the SM expected results are shown compared to previously observed results showing an improvement of $\gtrsim 3\times$. At the time of writing, the final unblinding procedure within the ATLAS collaboration is underway.

Appendices

APPENDIX A

TILECAL DATA QUALITY

This appendix gives an overview of the TileCal and ATLAS Data Quality Monitoring (DQM) systems. The author served as Data Quality (DQ) Co-Coordinator for a significant portion of their time in the Ph.D. program. During their tenure, it was their responsibility to verify the integrity and sign off on all physics data coming out of TileCal.

A.1 ATLAS Data Quality

The process of data collection with the ATLAS detector begins with an LHC fill. Each fill corresponds to injections of protons into the LHC in preparation for data taking. When the beams are collimated and focused, the LHC team declares a period of “stable beams”. At this point, the ATLAS team begins to ramp up the high voltage in the tracker and muon systems. Once the pixel preamplifiers are turned on, ATLAS declares “ready for physics”. Data collected by ATLAS is recorded against a six digit number referred to as a run number. Each run is subdivided into Luminosity Blocks (LBs), with each LB corresponding to 60 seconds of data taking. LBs provide a granularity for checking quality of data and sorting of data based on its quality.

A.2 Calibration Systems

To ensure the data being collected by TileCal is accurate and meets the required standards a series of calibration checks are performed with varying frequency. The systems used for calibration were designed to be built into the full detector; allowing calibration between physics data taking runs without requiring physical access to the detector. A diagram of the various calibration systems and where in the readout chain each calibration is done can be seen in Figure A.1.

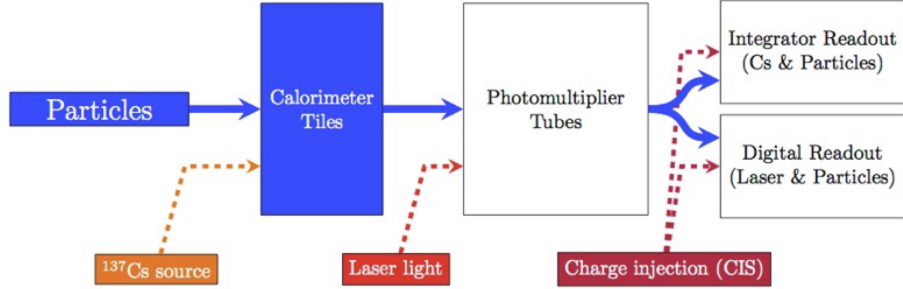


Figure A.1: TileCal calibration checks within the readout chain [26].

The cesium calibration system within TileCal is meant to calibrate the entire readout chain from scintillator to final digital signal readout. Several sources of Cs^{137} are hydraulically moved throughout the detector. The cesium calibration was designed to be run once a month¹. The laser calibration system measures the response of the PMTs with respect to the last cesium scan. Laser calibration can be done during empty bunches within the LHC fill and with dedicated calibration runs as well. The Charge Injection System (CIS) measures the response of digitizers and readout electronics by injecting controlled charges into the electronics. CIS calibration is done with dedicated calibration runs. The last calibration system is the minimum bias system, where physics signal is integrated over $\sim 10 - 20$ ms. Minimum bias calibration is used to fill in the gaps between cesium calibration scans. The average response variation for one cell from the laser, cesium, and minimum bias systems can be seen in Figure A.2.

Calibration constants are extracted from each calibration system and stored in a central ATLAS conditions database. Bookkeeping is done with an Interval of Validity (IOV) that corresponds to specific LBs within a run. The energy reconstructed at the EM scale is

$$E = \frac{A[\text{ADC Counts}]}{C_{Cs} \cdot C_{Las} \cdot C_{CIS}[\text{ADC counts}/\mu\text{C}] \cdot C_{TB}[\mu\text{C}/\text{GeV}]} \quad (\text{A.1})$$

¹Due to historical issues with leaking hydraulic fluid, the frequency of cesium scans was drastically reduced during Run-2.

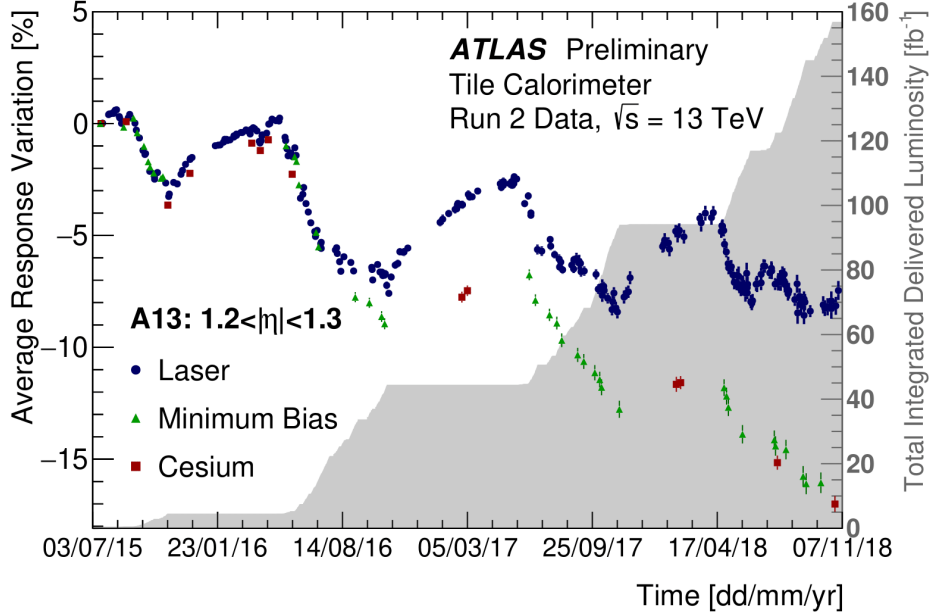


Figure A.2: Average response variation from the beginning of Run-2 of TileCal cell A13 is shown [78].

where A is the amplitude of the PMT signal after it has been shaped, amplified, and digitized at 40 MHz with 10-bit Analog to Digital Converters (ADCs) and C_{TB} is a calibration constant that was determined at dedicated test beams.

A.3 TileCal Data Quality

Quality of data is monitored both online and offline; a schematic of the path of data can be seen in Figure A.3. Online monitoring offers real time feedback on the data being collected, whereas offline monitoring is delayed but more detailed. Approximately 10% of collision events are quickly reconstructed in an express data stream. The data in this express stream is reviewed within 48 hours to allow subsystems an opportunity to change calibration constants and/or mask channels deemed bad. Figure A.4 shows the evolution of TileCal

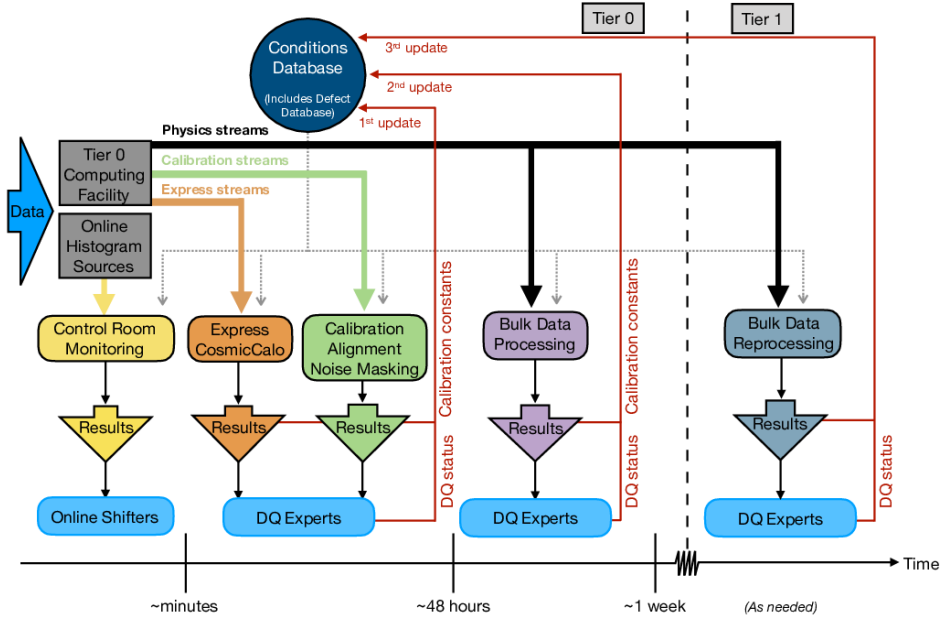


Figure A.3: Schematic diagram illustrating the nominal Run-2 operations workflow for the data quality assessment of ATLAS data. Online histogram sources include the high-level trigger farm, the data acquisition system, and full reconstruction of a fraction of events accepted by the trigger [79].

masked channels and cells throughout Run-2. After the 48 hour window, the full run is reconstructed using the updated conditions and once again reviewed by subsystem experts. The subsystem experts then approve the data or reject it based on a combination of automated test and human judgement. Figure A.5 shows the amount of collected luminosity throughout Run-2 and how much of it passes the “good for physics” requirements and Figure A.6 shows the overall efficiency of the whole ATLAS detector. Figure A.7 shows the inefficiencies by subsystem. For the whole of Run-2 TileCal was 99.65% efficient in terms of data quality.

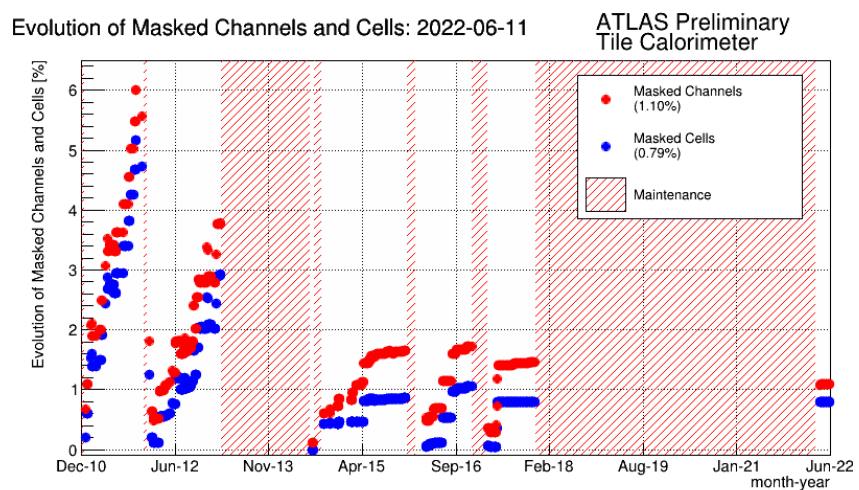


Figure A.4: Evolution of masked TileCal cells during Run-2 [78].

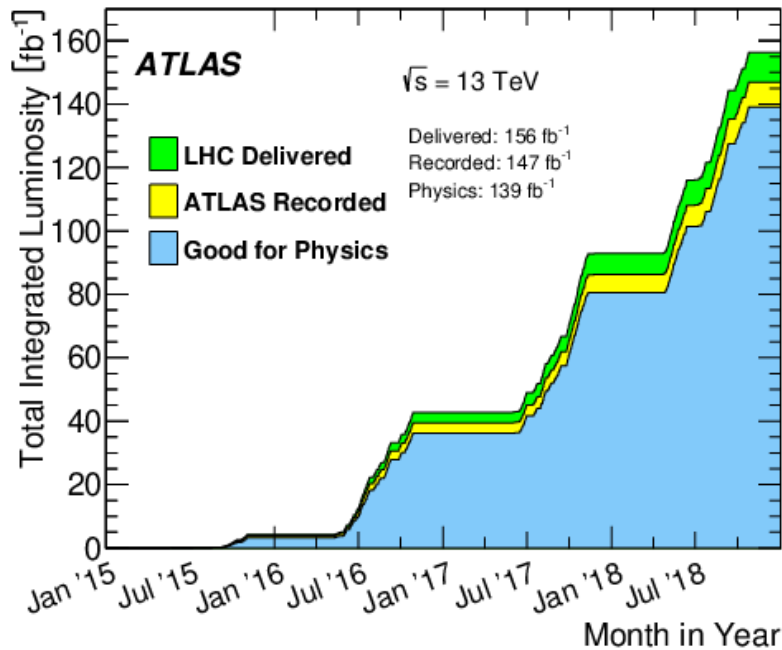


Figure A.5: Cumulative integrated luminosity delivered to and recorded by ATLAS between 2015 and 2018 during stable beam pp collision data-taking at $\sqrt{s} = 13$ TeV . This includes machine commissioning periods, special runs for detector calibration, and LHC fills with a low number of circulating bunches or bunch spacing greater than 25 ns. Also shown is the cumulative integrated luminosity certified for physics analysis usage for the ATLAS experiment between 2015 and 2018 during standard pp collision data-taking at $\sqrt{s} = 13$ TeV . The total integrated luminosity recorded for the standard $\sqrt{s} = 13$ TeV pp collision dataset corresponds to 145 fb^{-1} . It is this number that is used in the denominator when calculating the data quality efficiency of the standard $\sqrt{s} = 13$ TeV pp collision dataset [79].

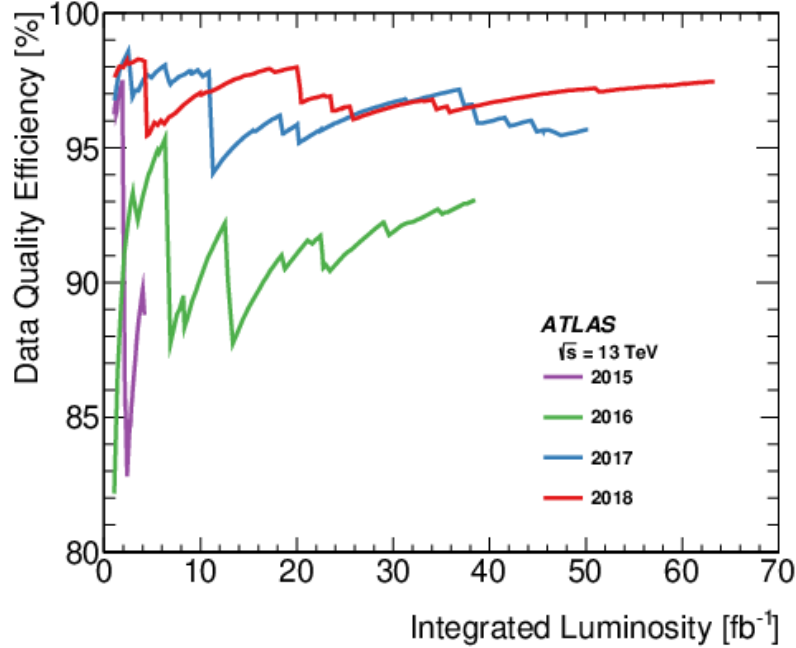


Figure A.6: Cumulative data quality efficiency versus total integrated luminosity delivered to the ATLAS experiment between 2015 and 2018 [79].

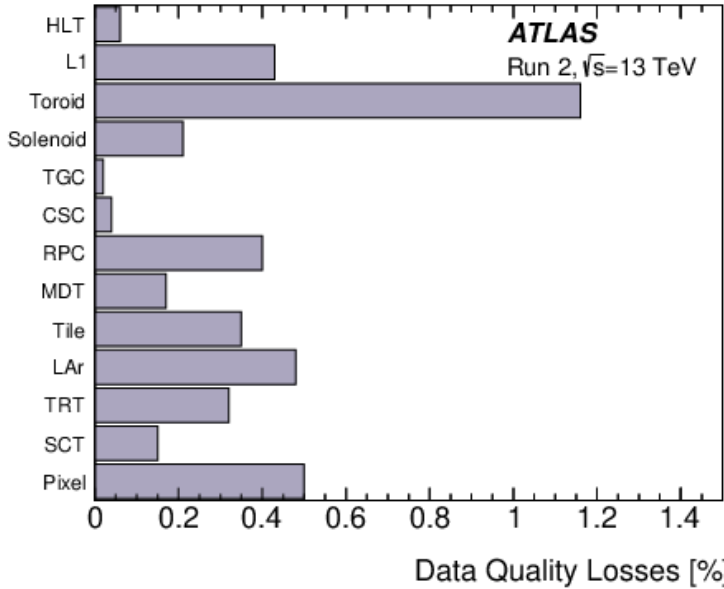


Figure A.7: Luminosity-weighted data quality inefficiencies (in %) during stable beams in standard pp collision physics runs at $\sqrt{s} = 13$ TeV between 2015 and 2018. Taken from Reference [79].

APPENDIX B

FAKE FACTORS

This appendix contains supplementary material for the fake factor extraction procedure outlined in 6.3. Figures B.1 shows the fake factors for both multijet and W+jets CRs. Figure B.2 shows the extracted and corrected α values in the SRs and CRs. Figures B.3 through B.9 show the process of extracting the α values, including the fits.

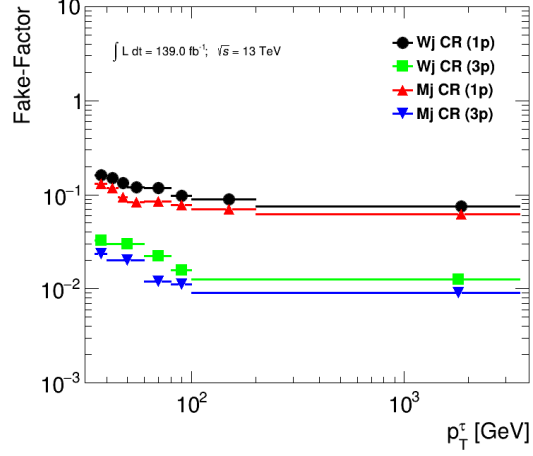


Figure B.1: Fake factors parameterized as a function of p_T^τ and the number of charged τ decay products (1-prong and 3-prong) obtained in the multi-jet and W+jets CRs. The errors shown represent the statistical uncertainty.

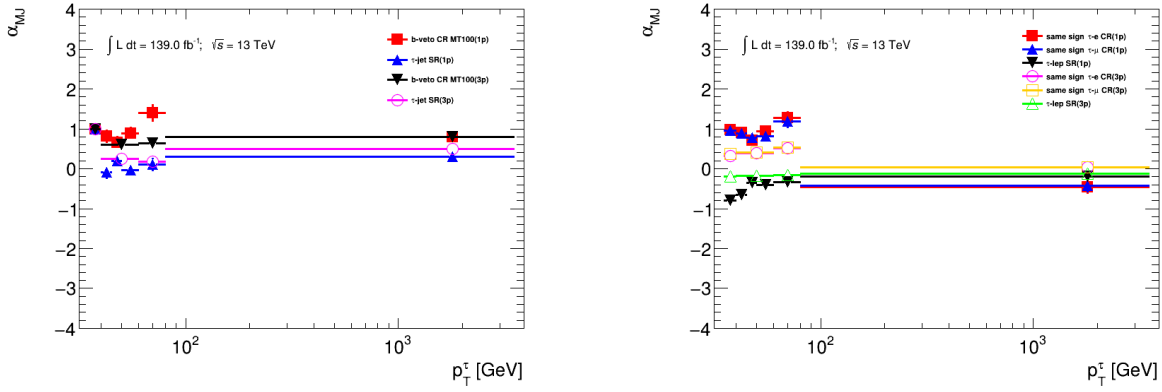


Figure B.2: Corrected α_{MJ} values for the $\tau_{had-vis} + \text{jets}$ b-veto $m_T > 100$ control region, $\tau_{had-vis} + \text{jets}$ signal region, $\tau_{had-vis} + \text{electron(muon)}$ with same-sign control region and the $\tau_{had-vis} + \text{lepton}$ signal region. Error bars represent uncertainties due to α_{MJ} fitting using template-fit method.

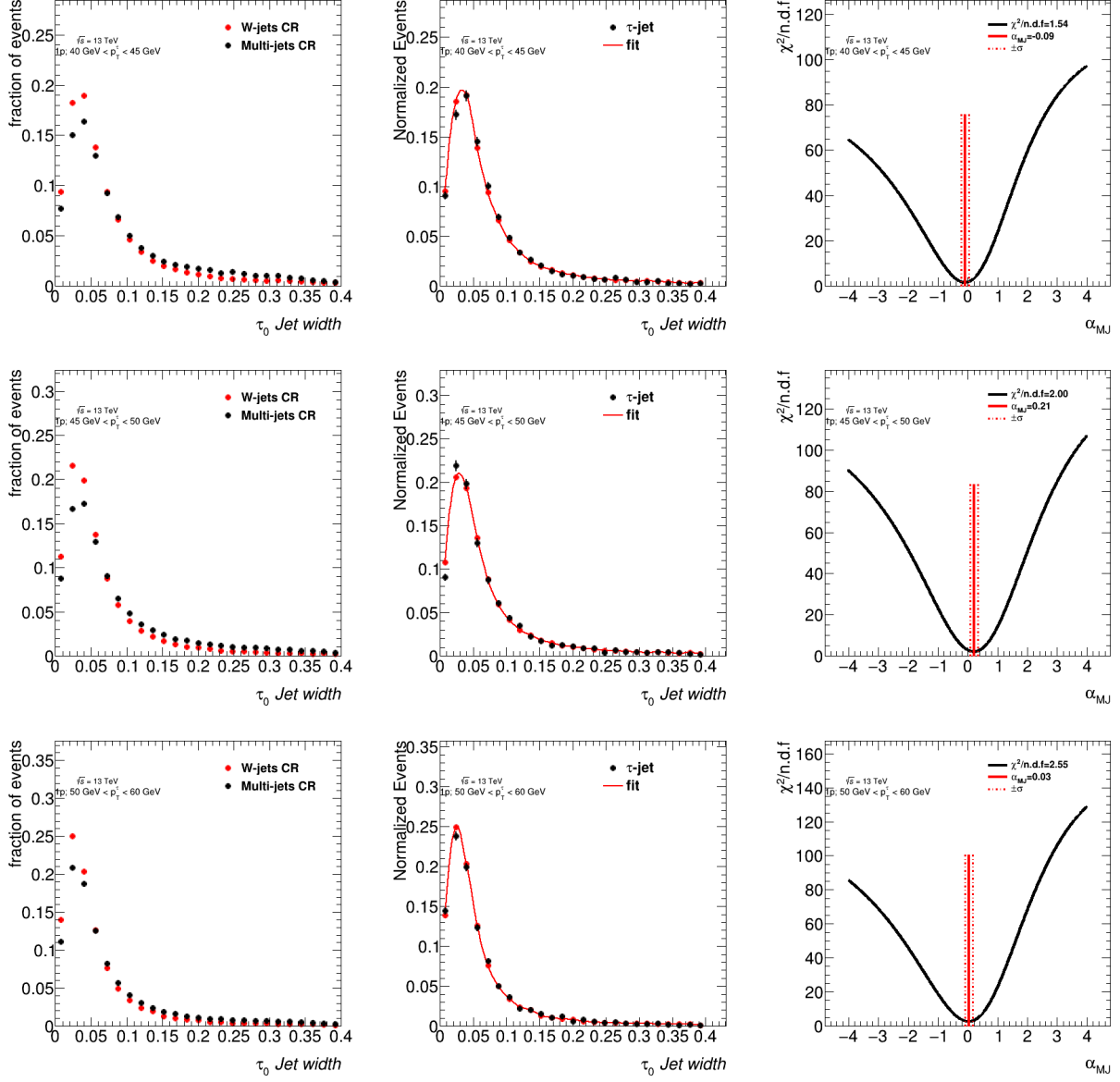


Figure B.3: Estimation of α_{MJ} in the $\tau_{\text{had-vis}} + \text{jets}$ signal region for $p_T \leq 60 \text{ GeV}$ 1-prong $\tau_{\text{had-vis}}$ candidates. Left: templates of discriminating variables for different $\tau_{\text{had-vis}}$ p_T and n-prong slices. Middle: shape of the discriminating variable obtained in the signal region and fitted shape using the templates measured in the control regions. Right: χ^2/ndf of the fit as a function of α_{MJ} , the error on α_{MJ} is defined by the band at $\chi^2_{\min}/\text{ndf} + \sqrt{\frac{2}{\text{ndf}}}$.

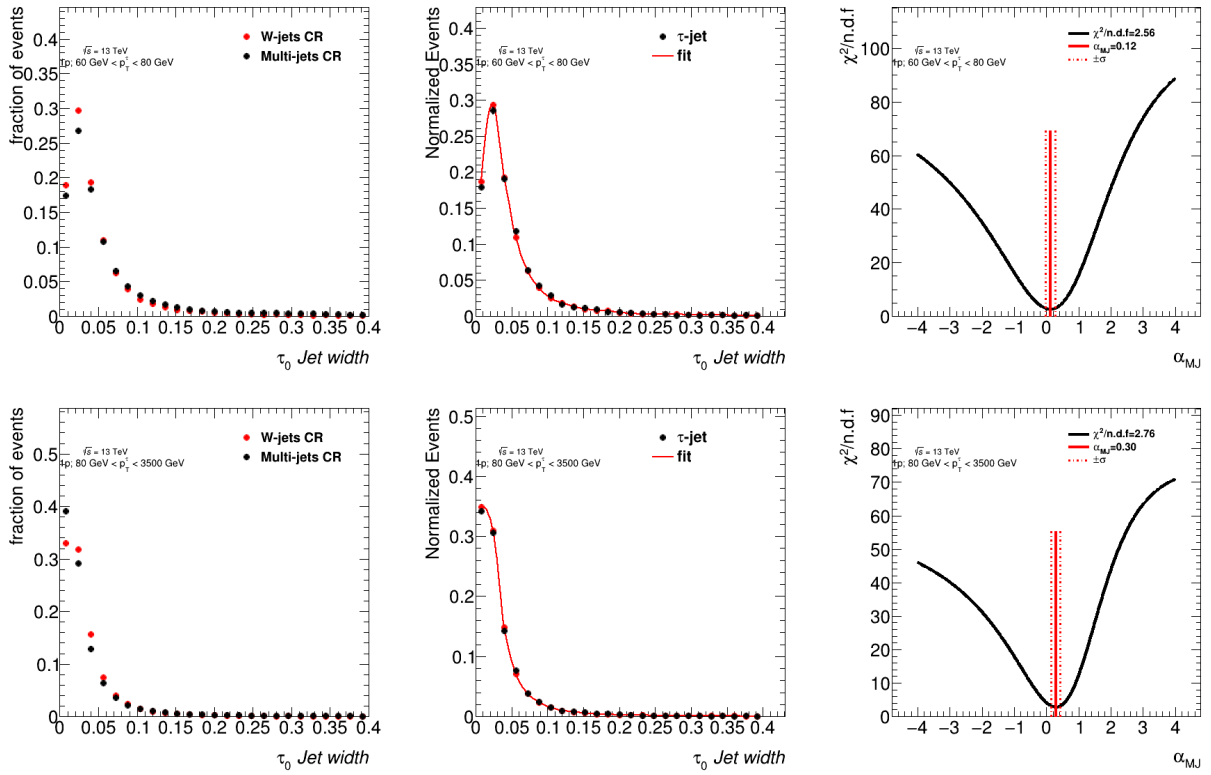


Figure B.4: Estimation of α_{MJ} in the $\tau_{\text{had-vis}} + \text{jets}$ signal region for $p_T \geq 60 \text{ GeV}$ 1-prong $\tau_{\text{had-vis}}$ candidates. Left: templates of discriminating variables for different $\tau_{\text{had-vis}}$ p_T and n-prong slices. Middle: shape of the discriminating variable obtained in the signal region and fitted shape using the templates measured in the control regions. Right: χ^2/ndf of the fit as a function of α_{MJ} , the error on α_{MJ} is defined by the band at $\chi^2_{\min}/\text{ndf} + \sqrt{\frac{2}{\text{ndf}}}$.

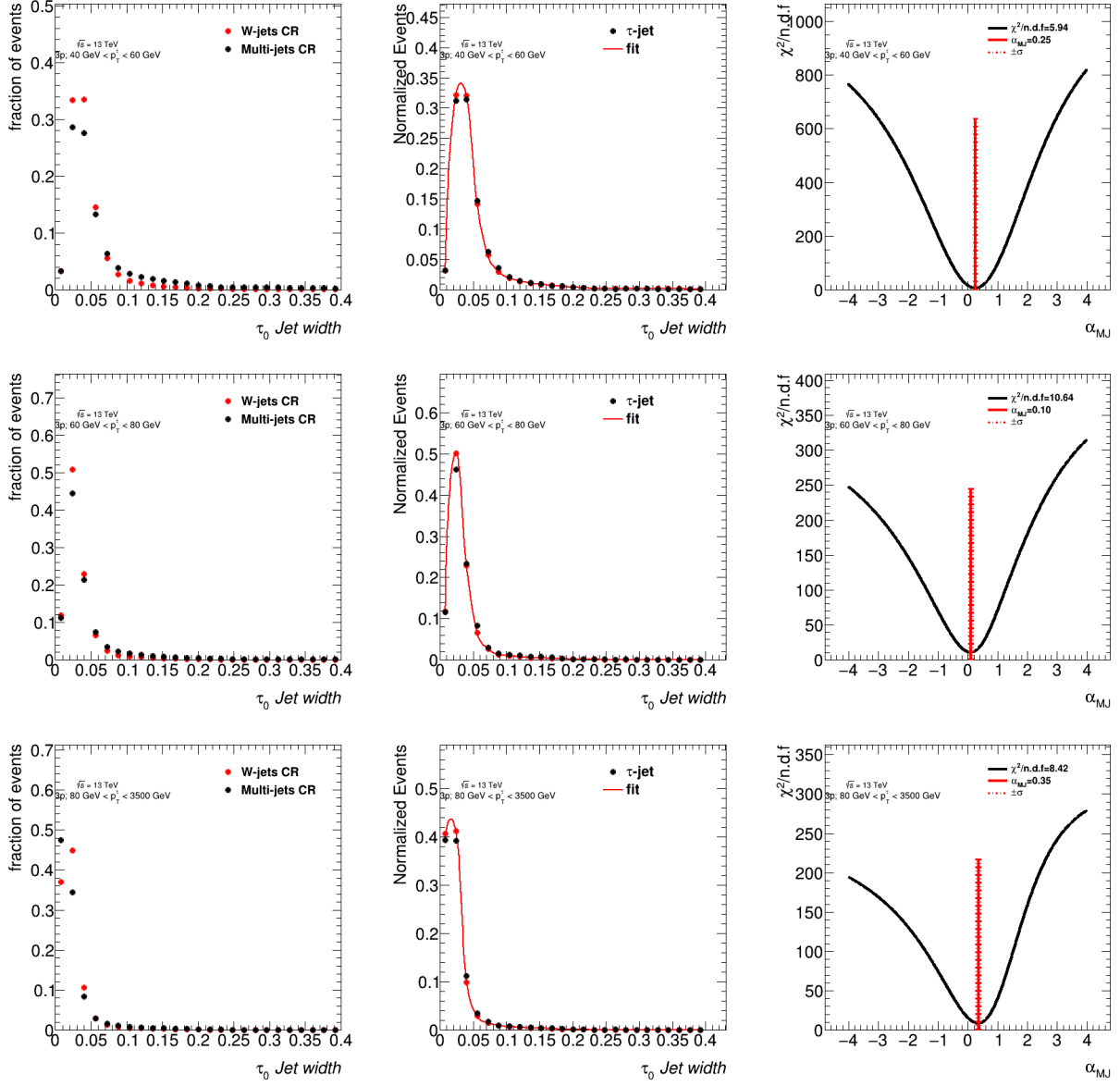


Figure B.5: Estimation of α_{MJ} in the $\tau_{\text{had-vis}} + \text{jets}$ signal region for 3-prong $\tau_{\text{had-vis}}$ candidates. Left: templates of discriminating variables for different $\tau_{\text{had-vis}}$ p_T and n-prong slices. Middle: shape of the discriminating variable obtained in the signal region and fitted shape using the templates measured in the control regions. Right: χ^2/ndf of the fit as a function of α_{MJ} , the error on α_{MJ} is defined by the band at $\chi^2_{\min}/\text{ndf} + \sqrt{\frac{2}{\text{ndf}}}$.

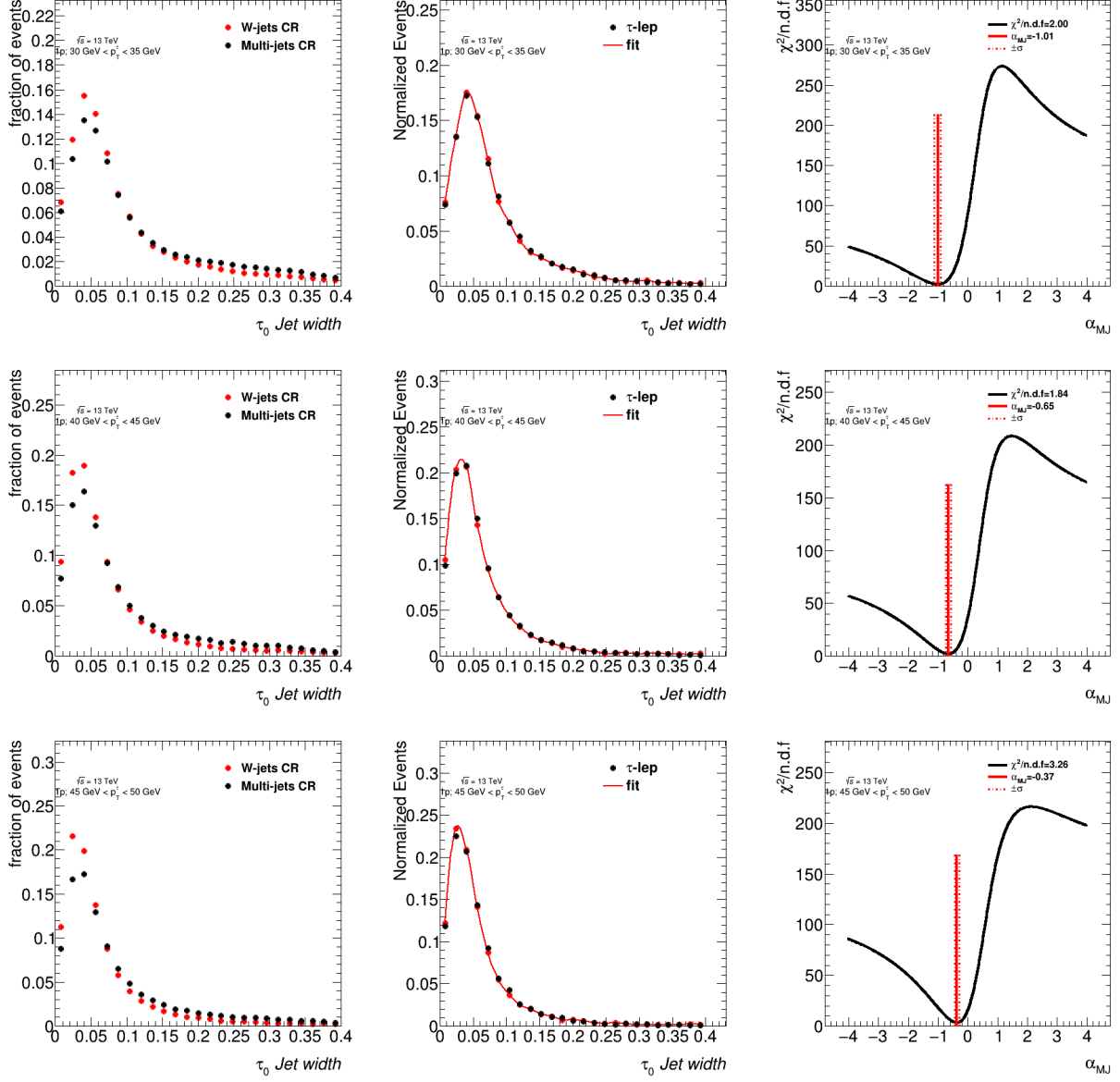


Figure B.6: Estimation of α_{MJ} in the $\tau_{\text{had-vis}} + \text{lepton}$ signal region for $p_T \leq 50 \text{ GeV}$ 1-prong $\tau_{\text{had-vis}}$ candidates. Left: templates of discriminating variables for different $\tau_{\text{had-vis}}$ p_T and n-prong slices. Middle: shape of the discriminating variable obtained in the signal region and fitted shape using the templates measured in the control regions. Right: χ^2/ndf of the fit as a function of α_{MJ} , the error on α_{MJ} is defined by the band at $\chi^2_{\min}/\text{ndf} + \sqrt{\frac{2}{\text{ndf}}}$.

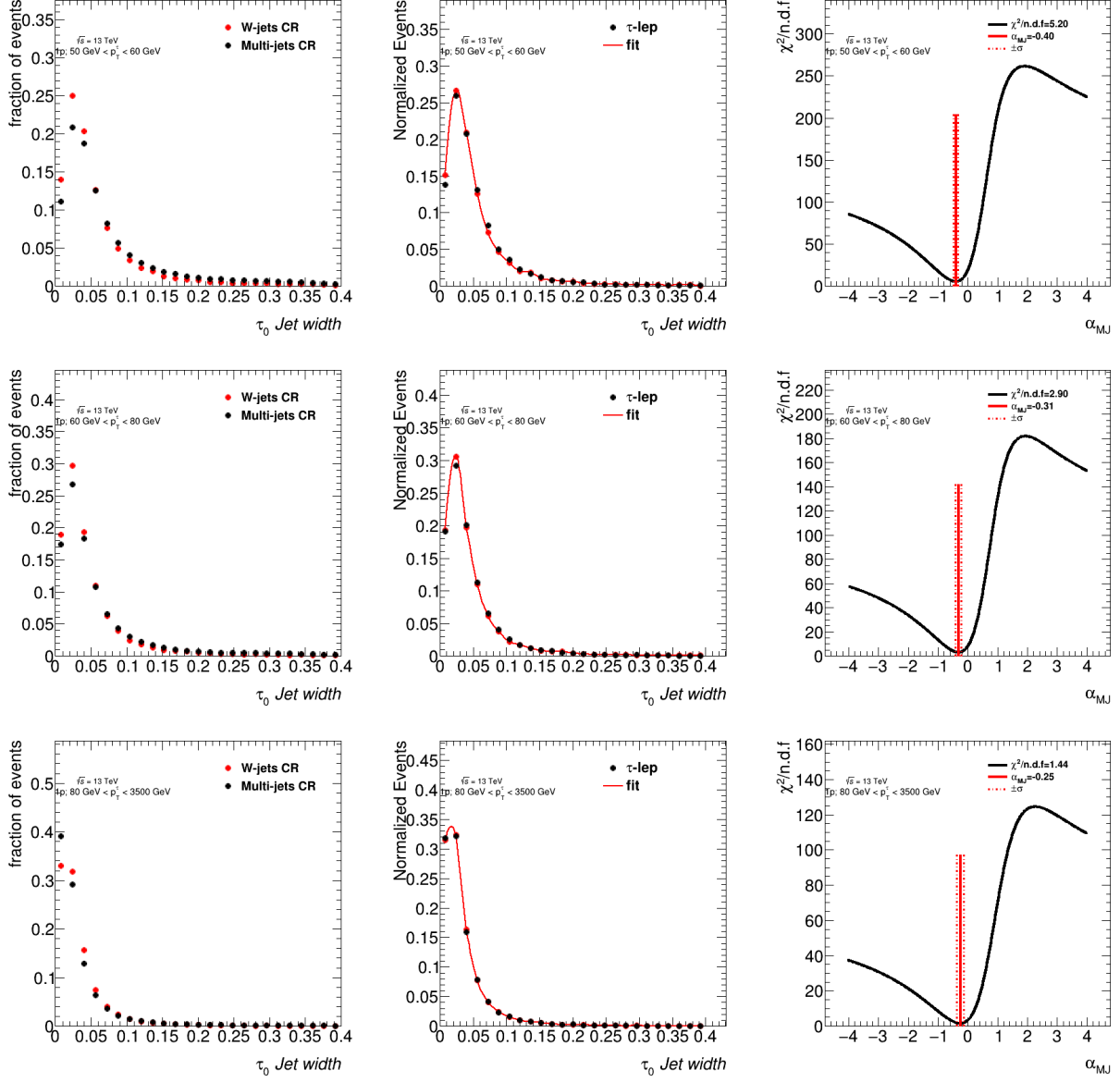


Figure B.7: Estimation of α_{MJ} in the $\tau_{had-vis} + \text{lepton}$ signal region for $p_T \geq 50 \text{ GeV}$ 1-prong $\tau_{had-vis}$ candidates. Left: templates of discriminating variables for different $\tau_{had-vis}$ p_T and n-prong slices. Middle: shape of the discriminating variable obtained in the signal region and fitted shape using the templates measured in the control regions. Right: χ^2/ndf of the fit as a function of α_{MJ} , the error on α_{MJ} is defined by the band at $\chi^2_{\min}/\text{ndf} + \sqrt{\frac{2}{\text{ndf}}}$.

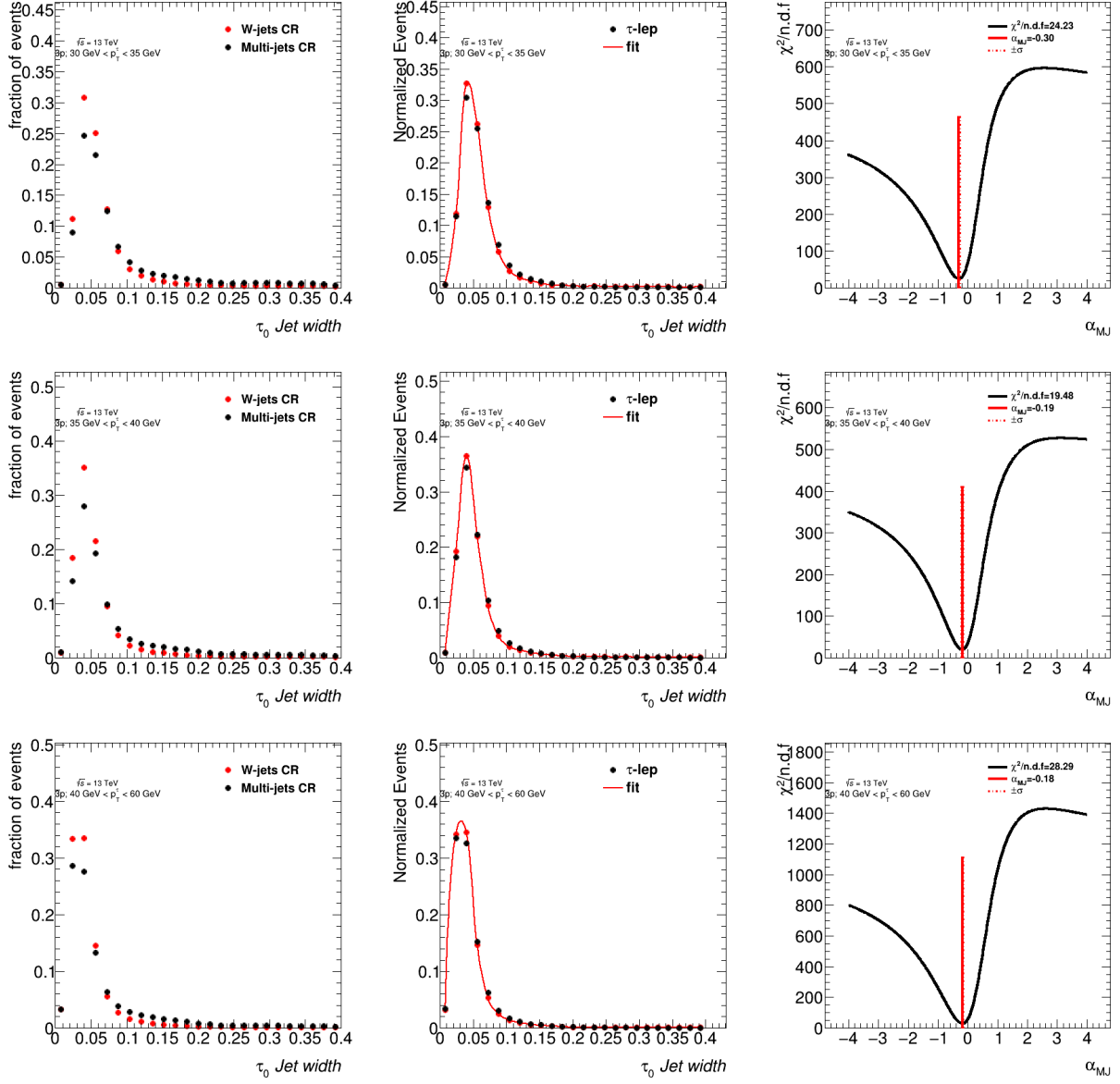


Figure B.8: Estimation of α_{MJ} in the $\tau_{\text{had-vis}} + \text{lepton}$ signal region for $p_T \leq 60 \text{ GeV}$ 3-prong $\tau_{\text{had-vis}}$ candidates. Left: templates of discriminating variables for different $\tau_{\text{had-vis}}$ p_T and n-prong slices. Middle: shape of the discriminating variable obtained in the signal region and fitted shape using the templates measured in the control regions. Right: χ^2/ndf of the fit as a function of α_{MJ} , the error on α_{MJ} is defined by the band at $\chi^2_{\min}/\text{ndf} + \sqrt{\frac{2}{\text{ndf}}}$.

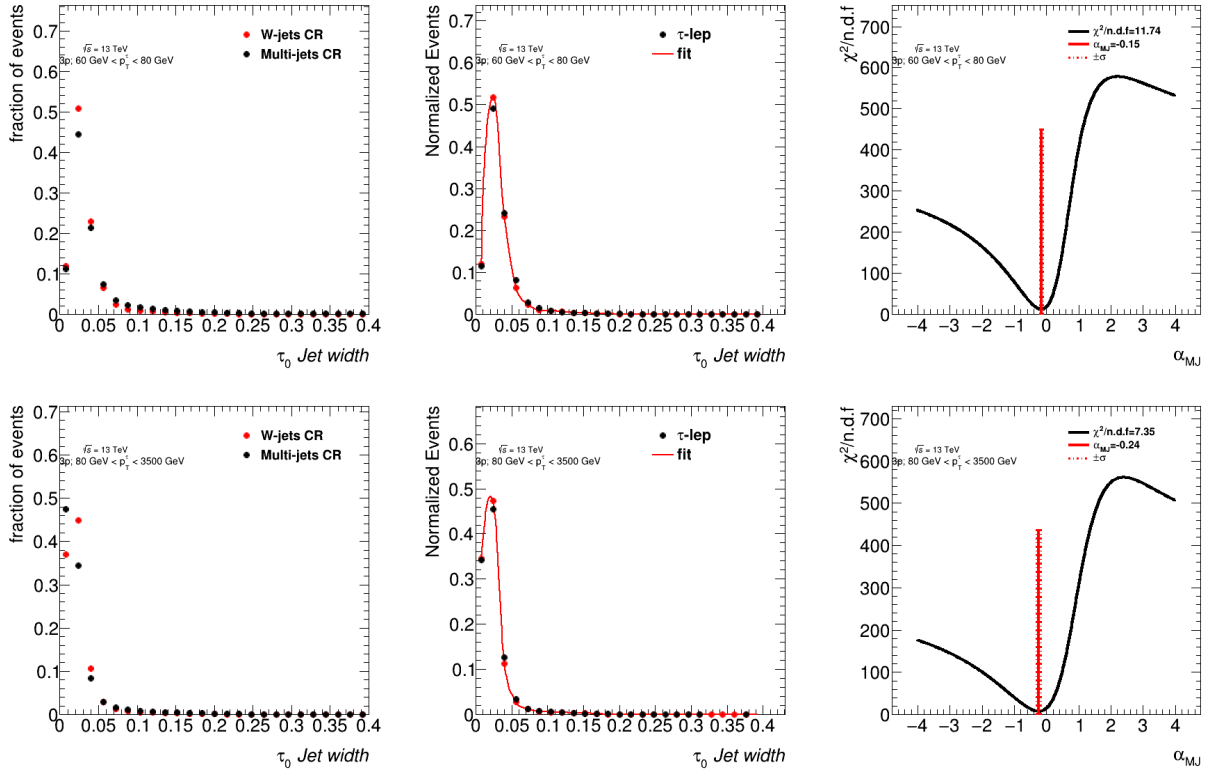


Figure B.9: Estimation of α_{MJ} in the $\tau_{\text{had-vis}} + \text{lepton}$ signal region for $p_T \geq 60 \text{ GeV}$ 3-prong $\tau_{\text{had-vis}}$ candidates. Left: templates of discriminating variables for different $\tau_{\text{had-vis}}$ p_T and n-prong slices. Middle: shape of the discriminating variable obtained in the signal region and fitted shape using the templates measured in the control regions. Right: χ^2/ndf of the fit as a function of α_{MJ} , the error on α_{MJ} is defined by the band at $\chi^2_{\min}/\text{ndf} + \sqrt{\frac{2}{\text{ndf}}}$.

APPENDIX C

ADDITIONAL VALIDATION PLOTS

C.1 $\tau + \text{jets}$ Background Validation Plots

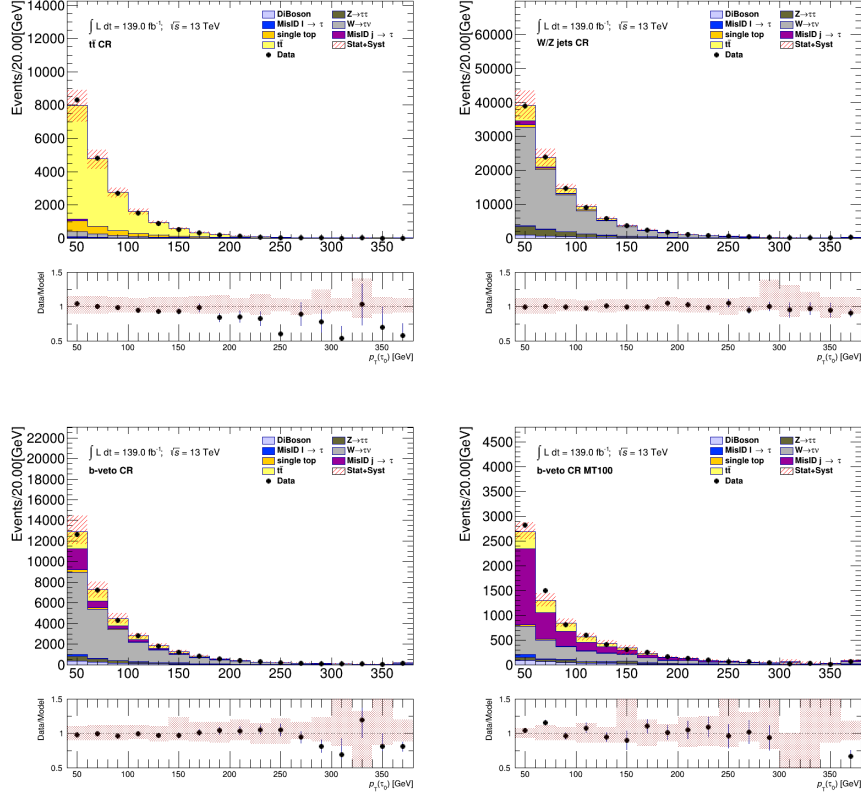


Figure C.1: Comparison between the predicted and the measured p_T^τ distributions in various control regions defined for the $\tau + \text{jets}$ channel. The uncertainty band includes both statistical and systematic uncertainties on the background prediction.

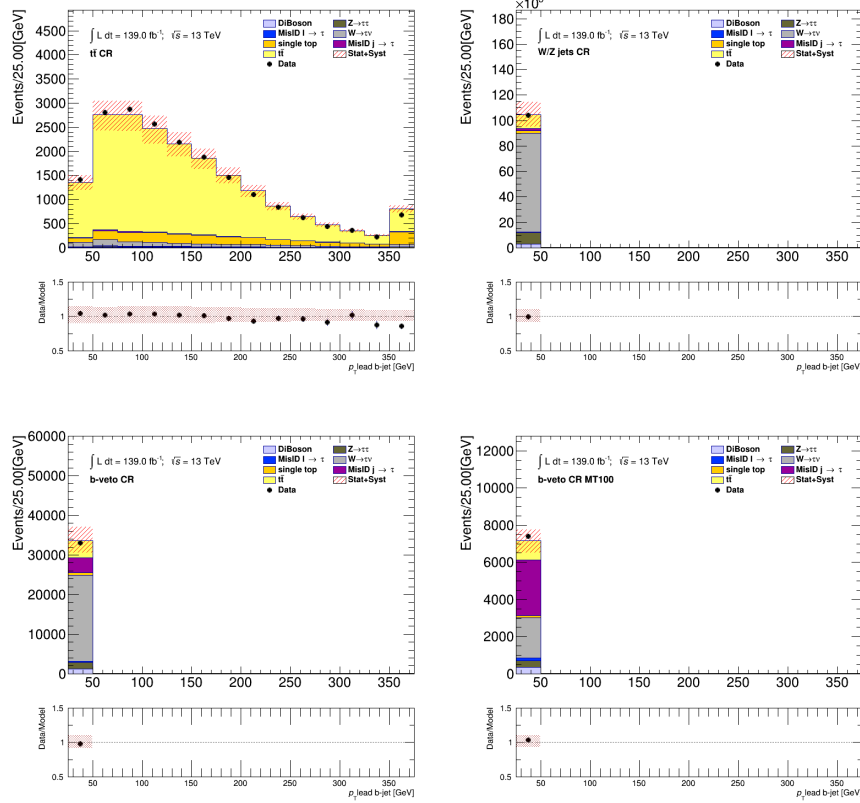


Figure C.2: Comparison between the predicted and the measured $p_T^{b\text{-jet}}$ distributions in various control regions defined for the $\tau+\text{jets}$ channel. The uncertainty band includes both statistical and systematic uncertainties on the background prediction.

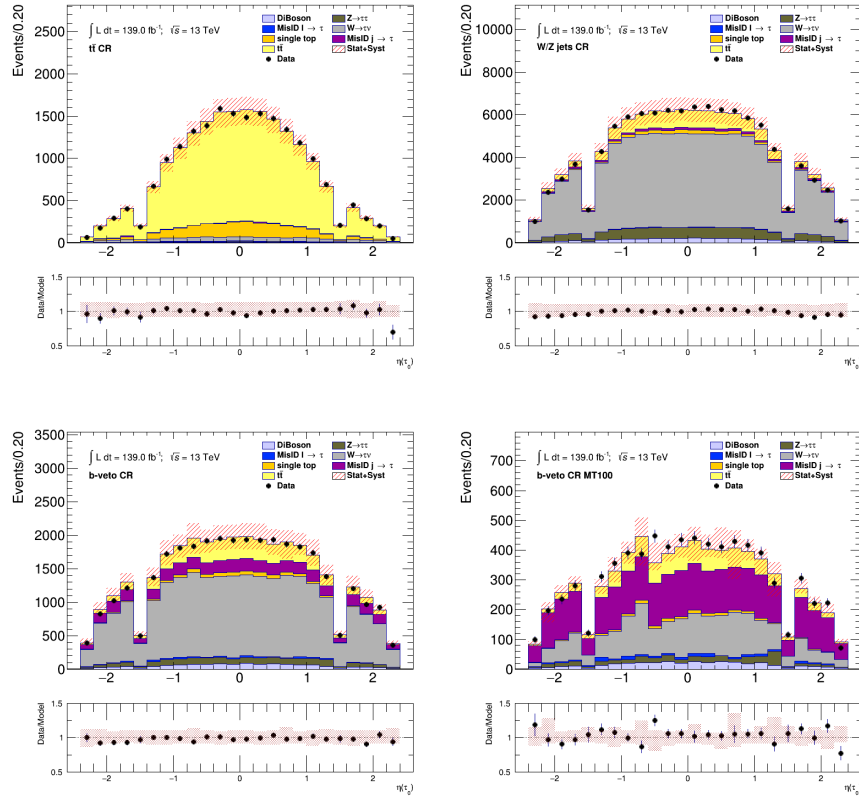


Figure C.3: Comparison between the predicted and the measured η^τ distributions in various control regions defined for the $\tau + \text{jets}$ channel. The uncertainty band includes both statistical and systematic uncertainties on the background prediction.

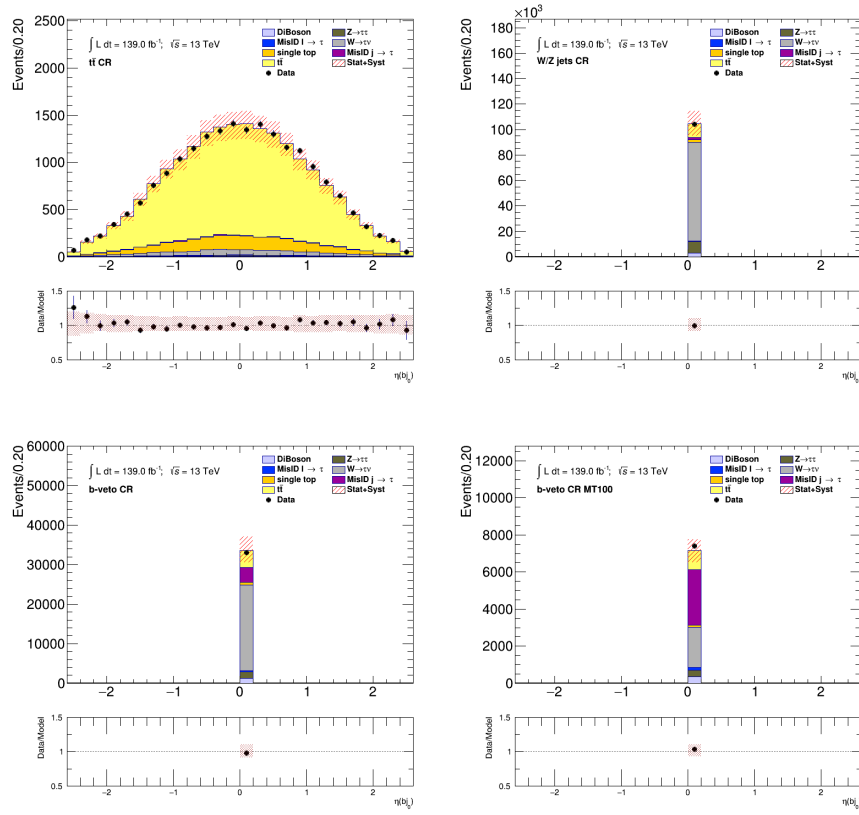


Figure C.4: Comparison between the predicted and the measured η^{b-jet} distributions in various control regions defined for the $\tau+jets$ channel. The uncertainty band includes both statistical and systematic uncertainties on the background prediction.

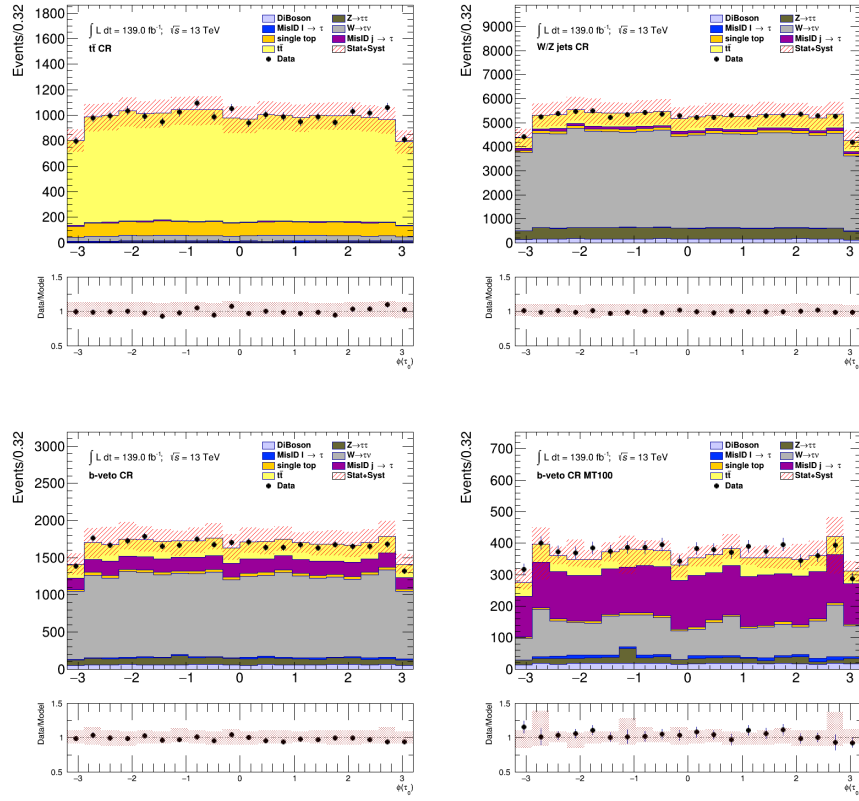


Figure C.5: Comparison between the predicted and the measured ϕ^τ distributions in various control regions defined for the $\tau + \text{jets}$ channel. The uncertainty band includes both statistical and systematic uncertainties on the background prediction.

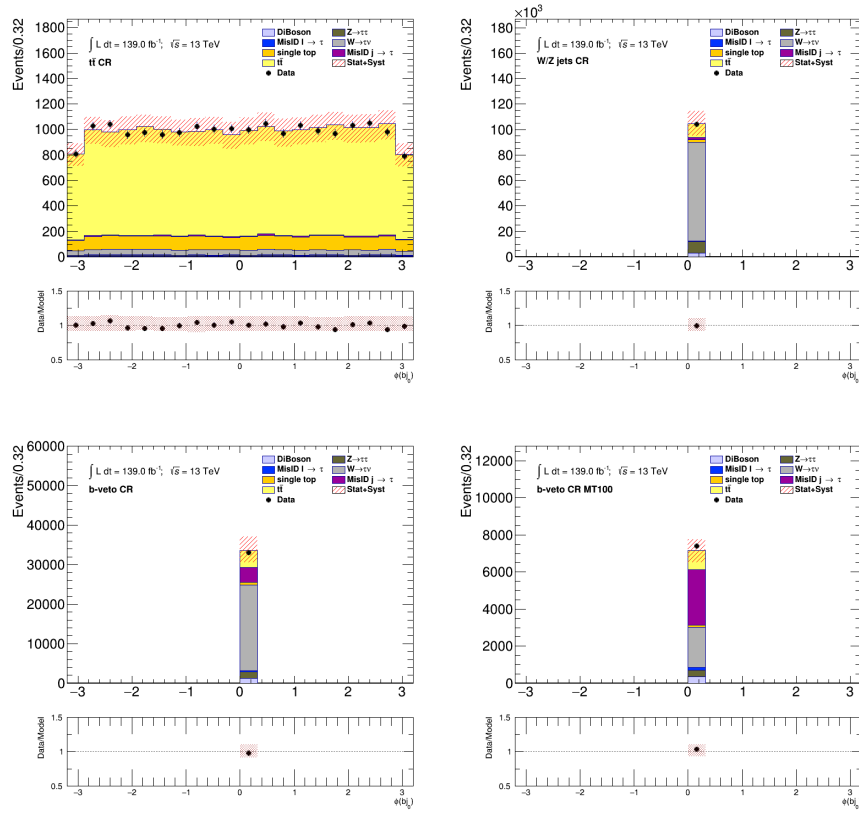


Figure C.6: Comparison between the predicted and the measured ϕ^{b-jet} distributions in various control regions defined for the $\tau+jets$ channel. The uncertainty band includes both statistical and systematic uncertainties on the background prediction.

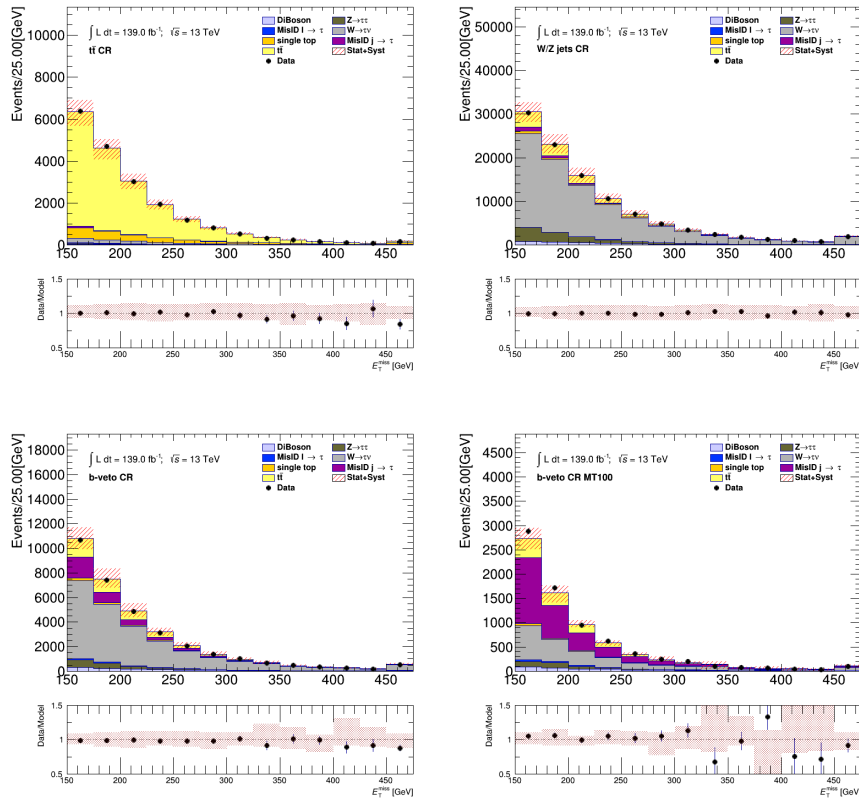


Figure C.7: Comparison between the predicted and the measured E_T^{miss} distributions in various control regions defined for the $\tau + \text{jets}$ channel. The uncertainty band includes both statistical and systematic uncertainties on the background prediction.

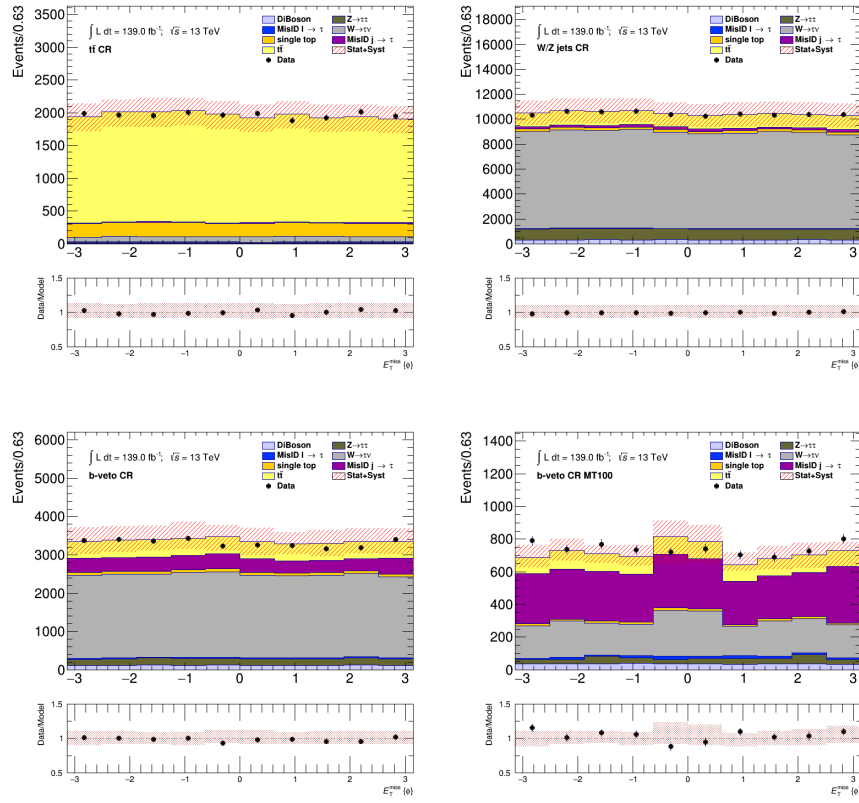


Figure C.8: Comparison between the predicted and the measured ϕ_T^{miss} distributions in various control regions defined for the $\tau+\text{jets}$ channel. The uncertainty band includes both statistical and systematic uncertainties on the background prediction.

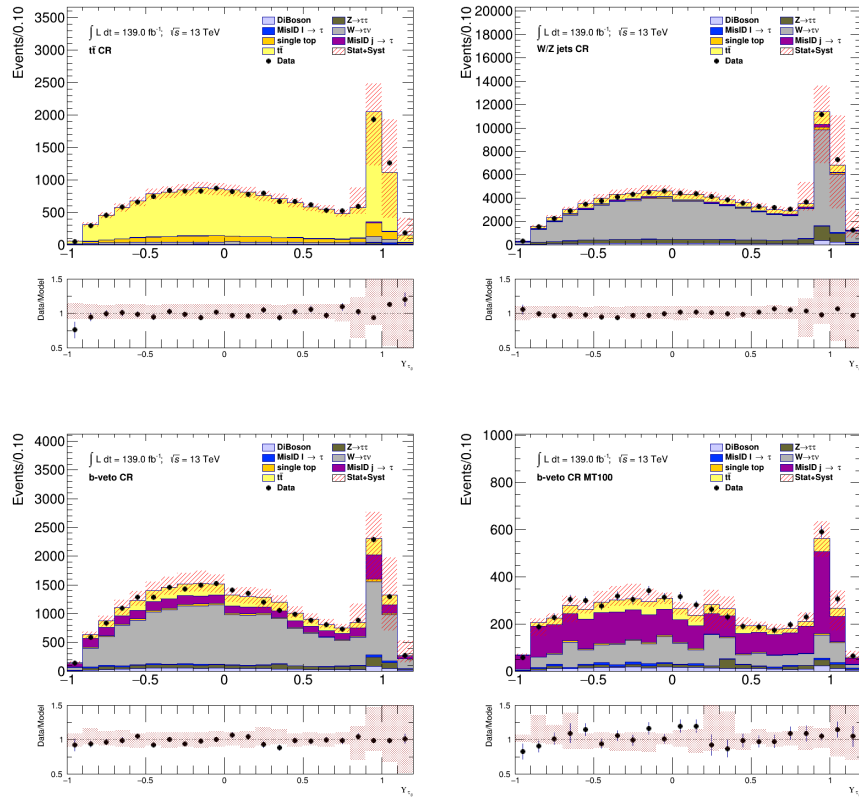


Figure C.9: Comparison between the predicted and the measured Υ_τ distributions in various control regions defined for the $\tau+\text{jets}$ channel. The uncertainty band includes both statistical and systematic uncertainties on the background prediction.

C.2 $\tau + \ell$ Background Validation Plots

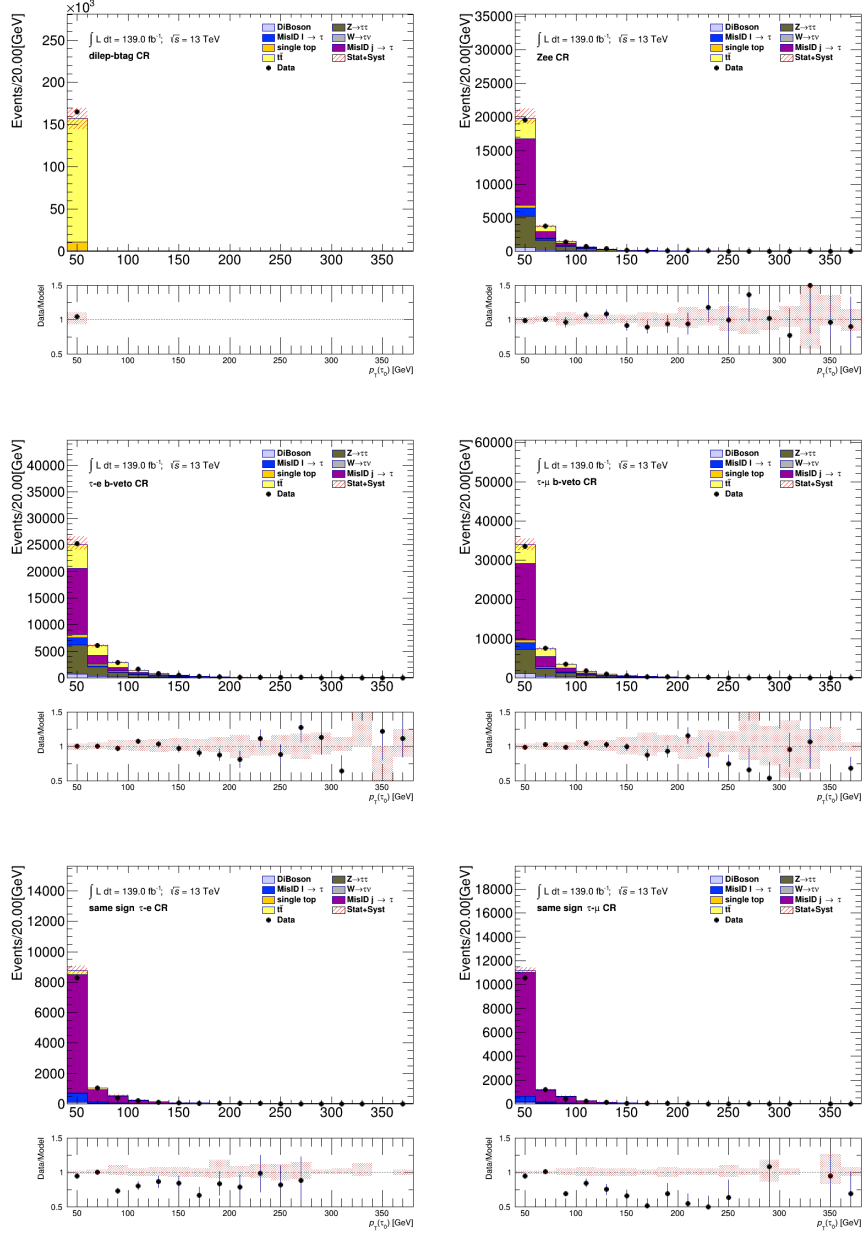


Figure C.10: Comparison between the predicted and the measured p_T^τ distributions in various control regions defined for the $\tau + \ell$ channel. The uncertainty band includes both statistical and systematic uncertainties on the background prediction.

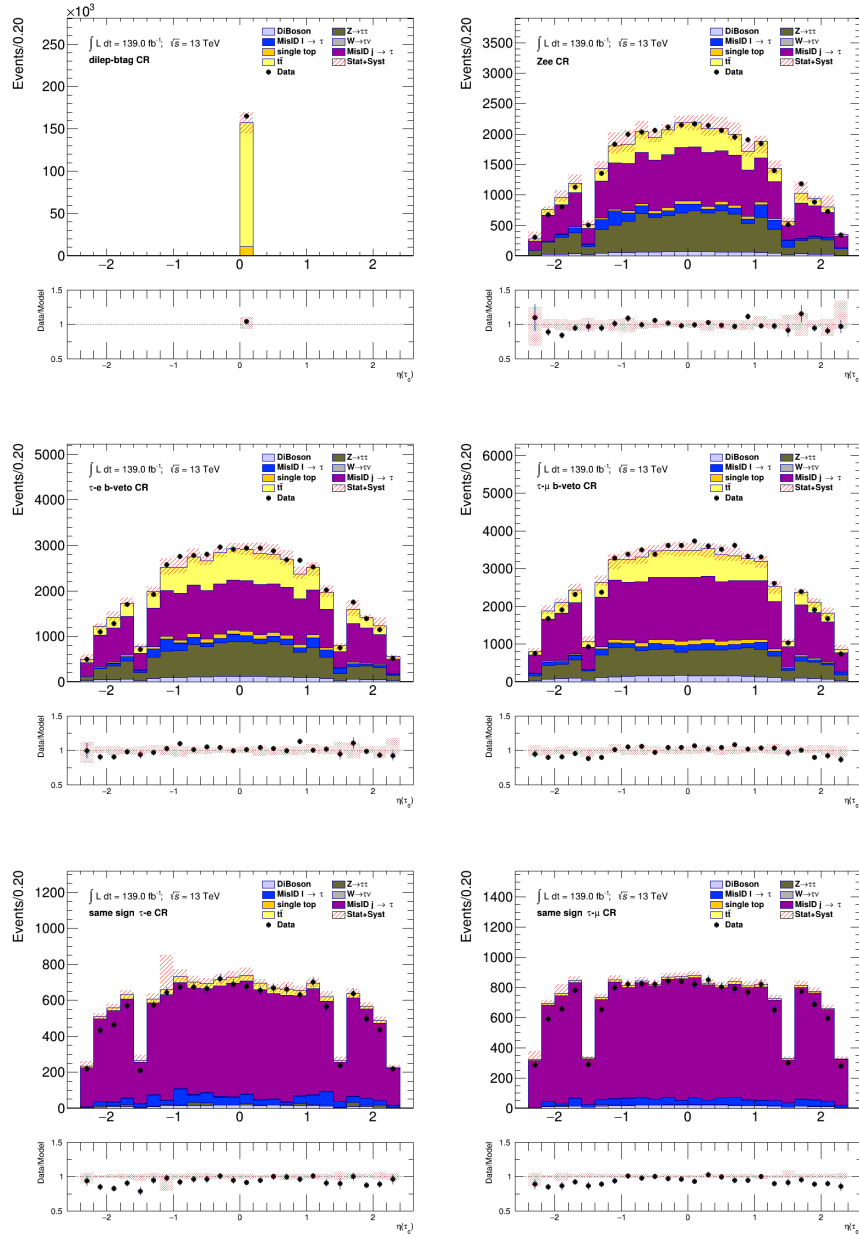


Figure C.11: Comparison between the predicted and the measured η^τ distributions in various control regions defined for the $\tau + \ell$ channel. The uncertainty band includes both statistical and systematic uncertainties on the background prediction.

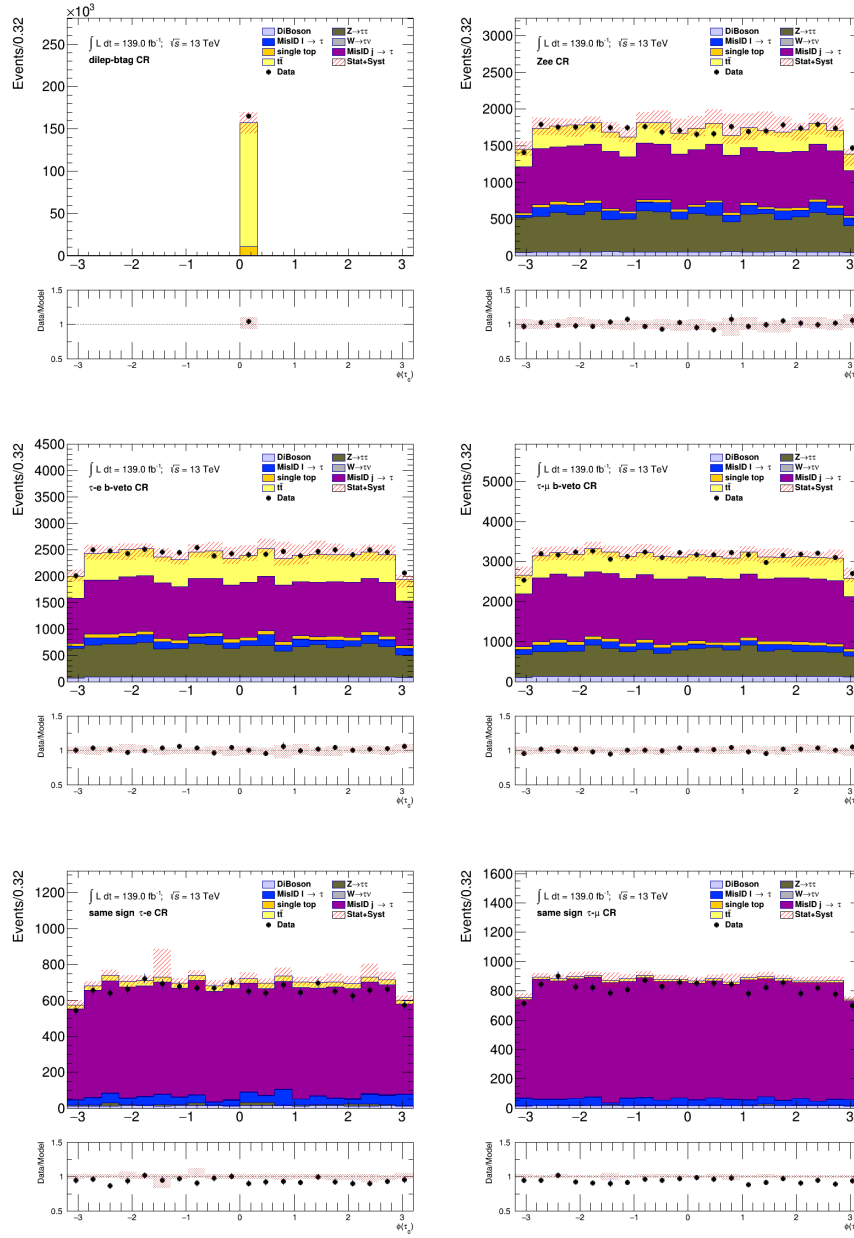


Figure C.12: Comparison between the predicted and the measured ϕ^τ distributions in various control regions defined for the $\tau + \ell$ channel. The uncertainty band includes both statistical and systematic uncertainties on the background prediction.

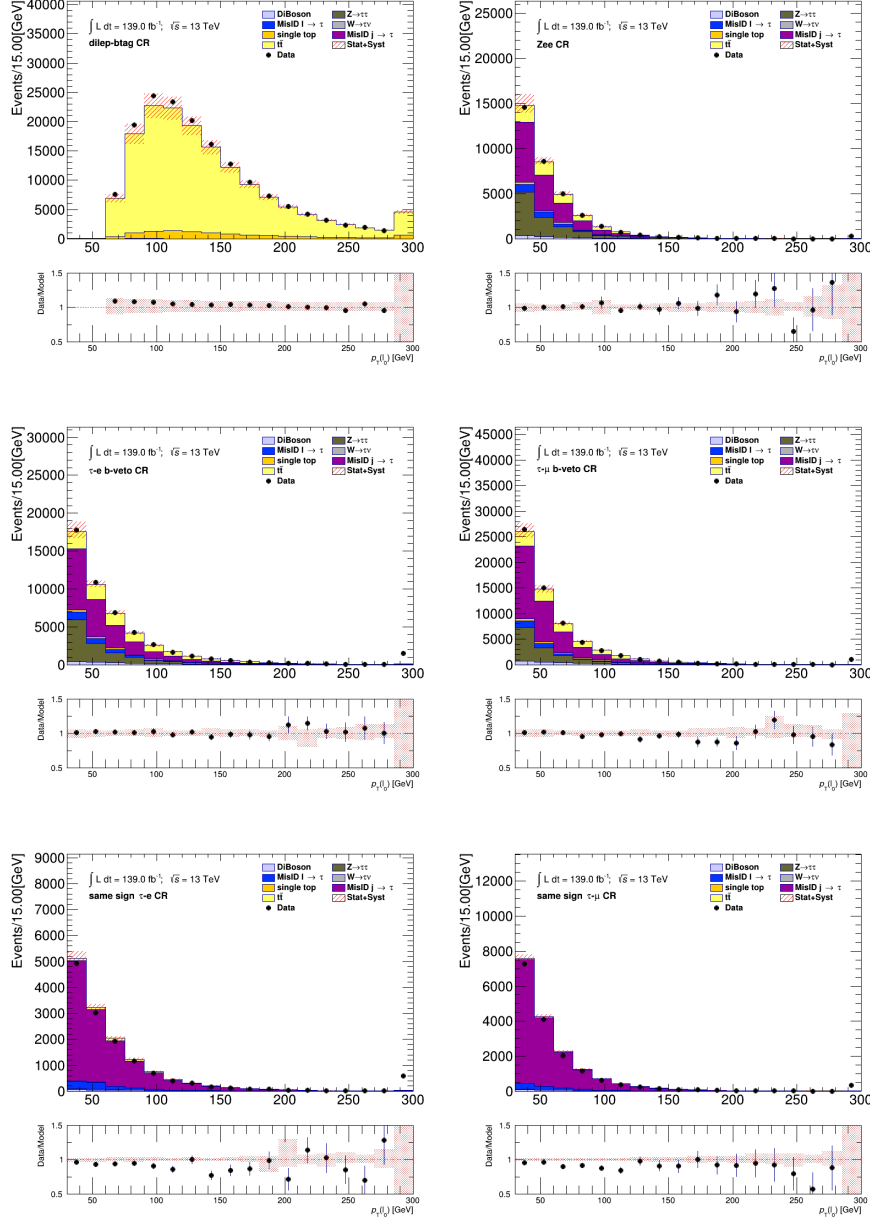


Figure C.13: Comparison between the predicted and the measured p_T^ℓ distributions in various control regions defined for the $\tau + \ell$ channel. The uncertainty band includes both statistical and systematic uncertainties on the background prediction.

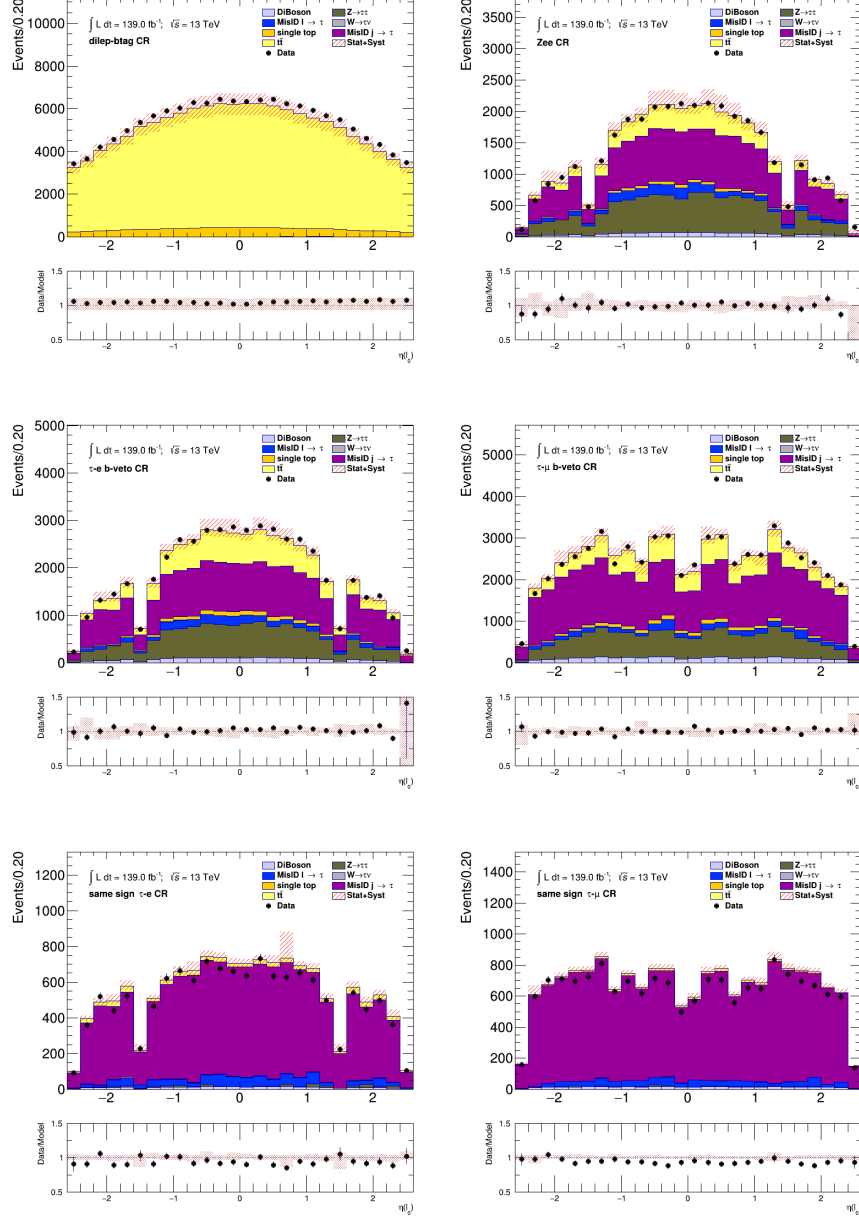


Figure C.14: Comparison between the predicted and the measured η^ℓ distributions in various control regions defined for the $\tau + \ell$ channel. The uncertainty band includes both statistical and systematic uncertainties on the background prediction.

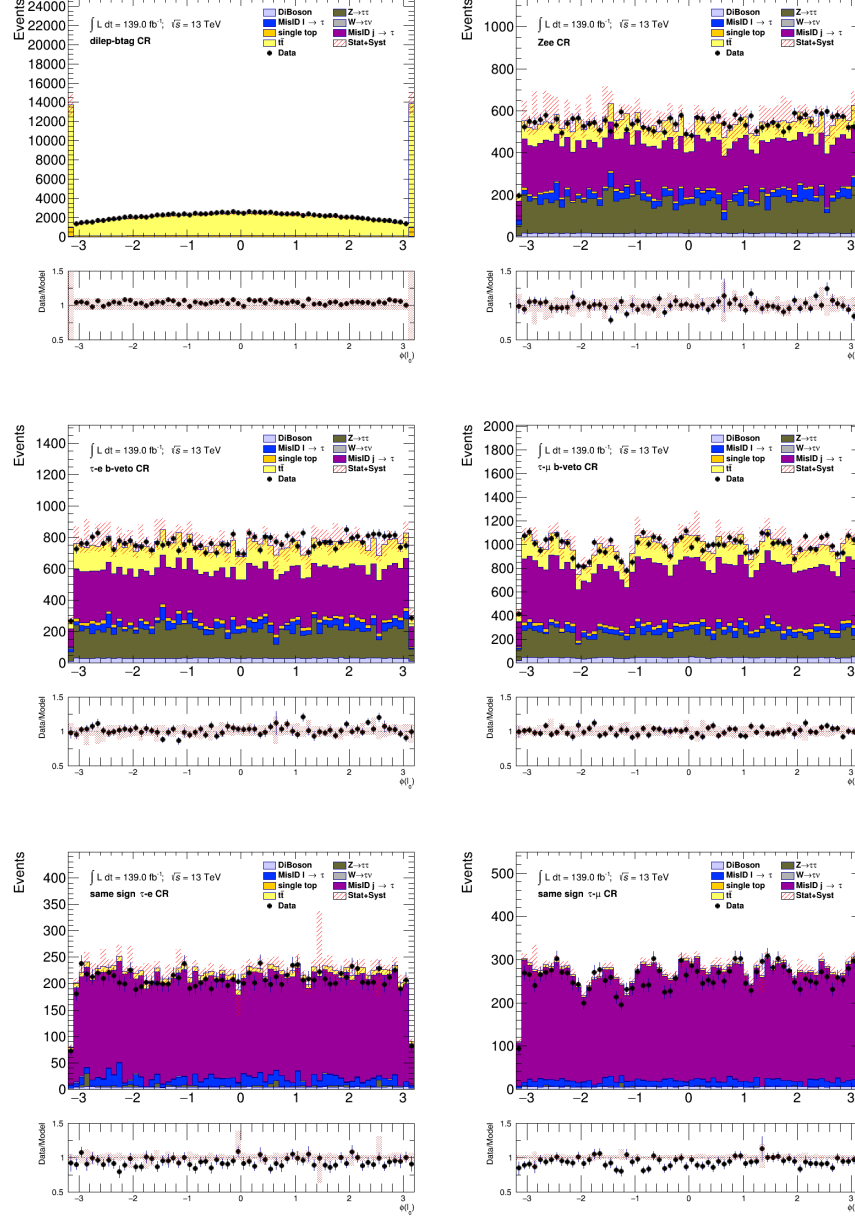


Figure C.15: Comparison between the predicted and the measured ϕ^ℓ distributions in various control regions defined for the $\tau + \ell$ channel. The uncertainty band includes both statistical and systematic uncertainties on the background prediction.

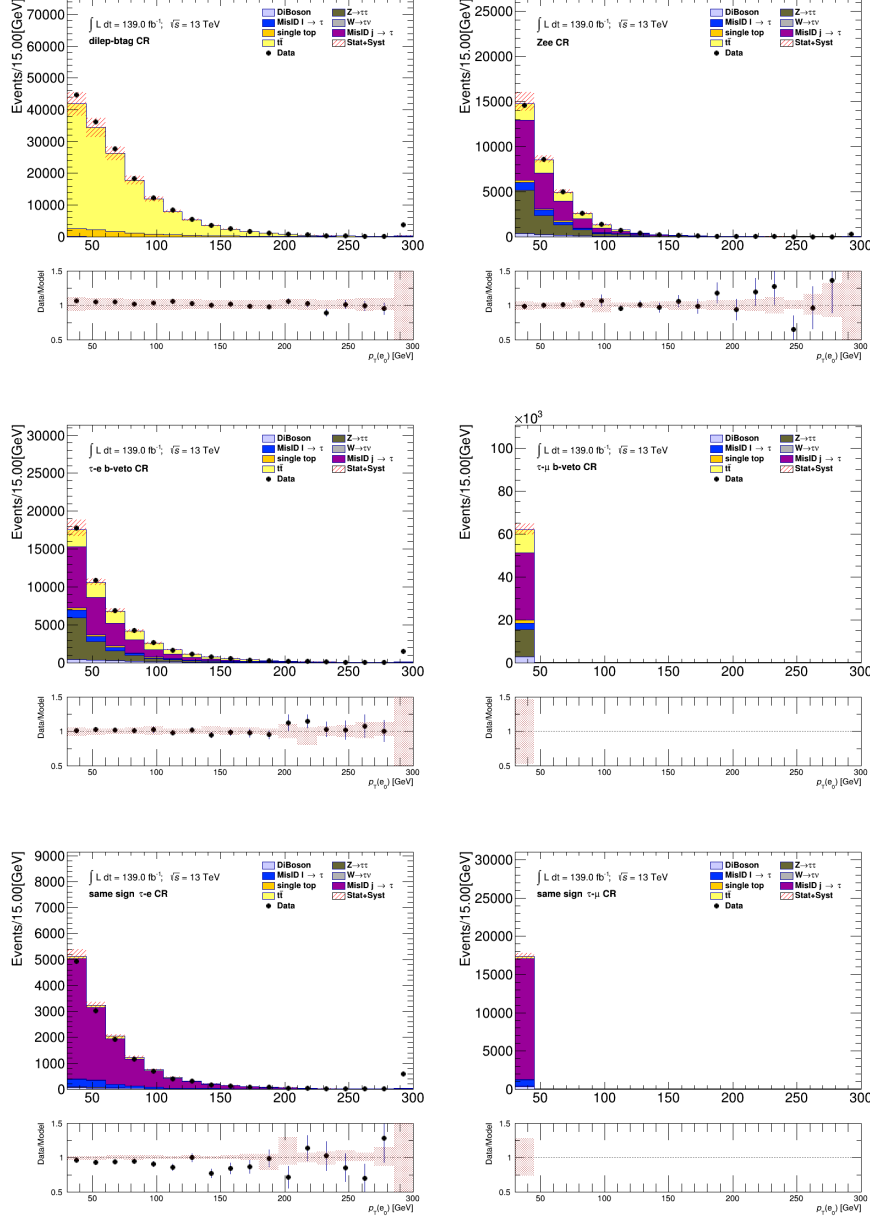


Figure C.16: Comparison between the predicted and the measured p_T^e distributions in various control regions defined for the $\tau + \ell$ channel. The uncertainty band includes both statistical and systematic uncertainties on the background prediction.

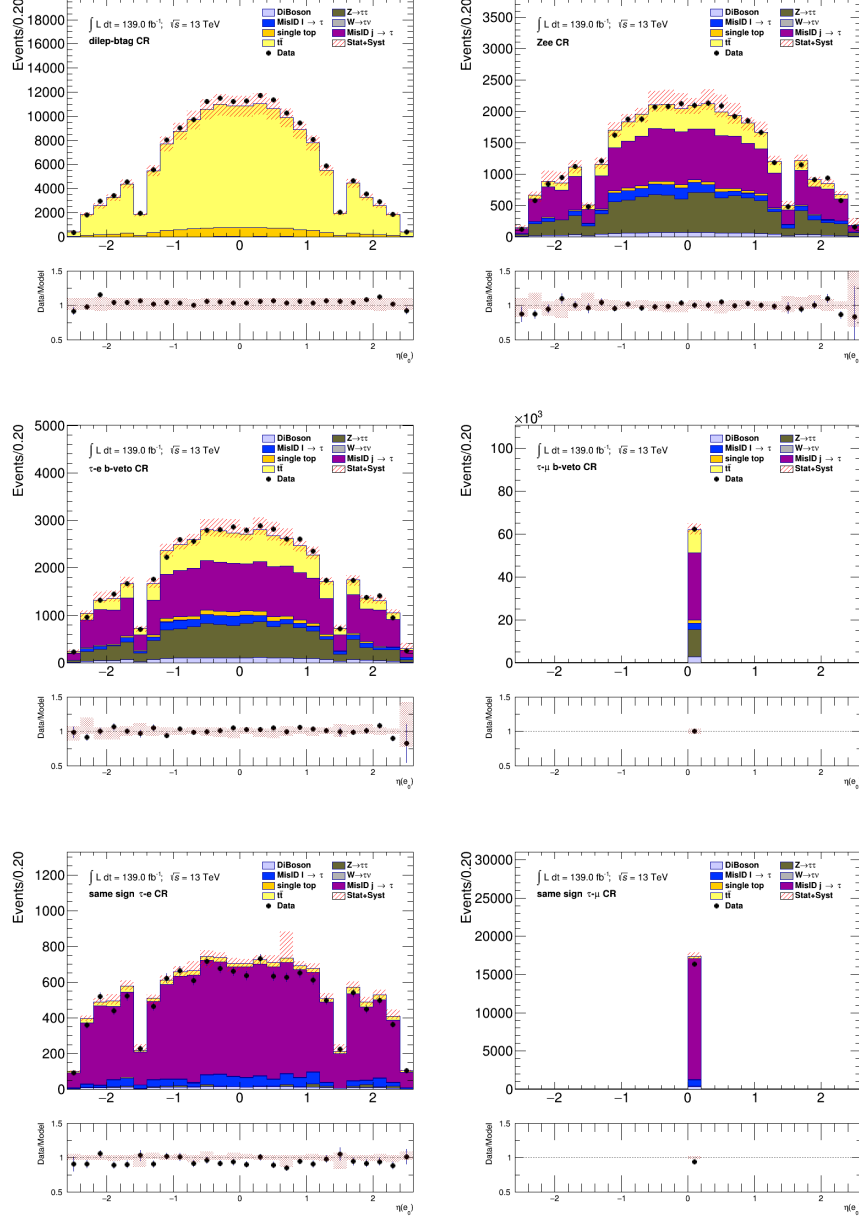


Figure C.17: Comparison between the predicted and the measured η^e distributions in various control regions defined for the $\tau + \ell$ channel. The uncertainty band includes both statistical and systematic uncertainties on the background prediction.

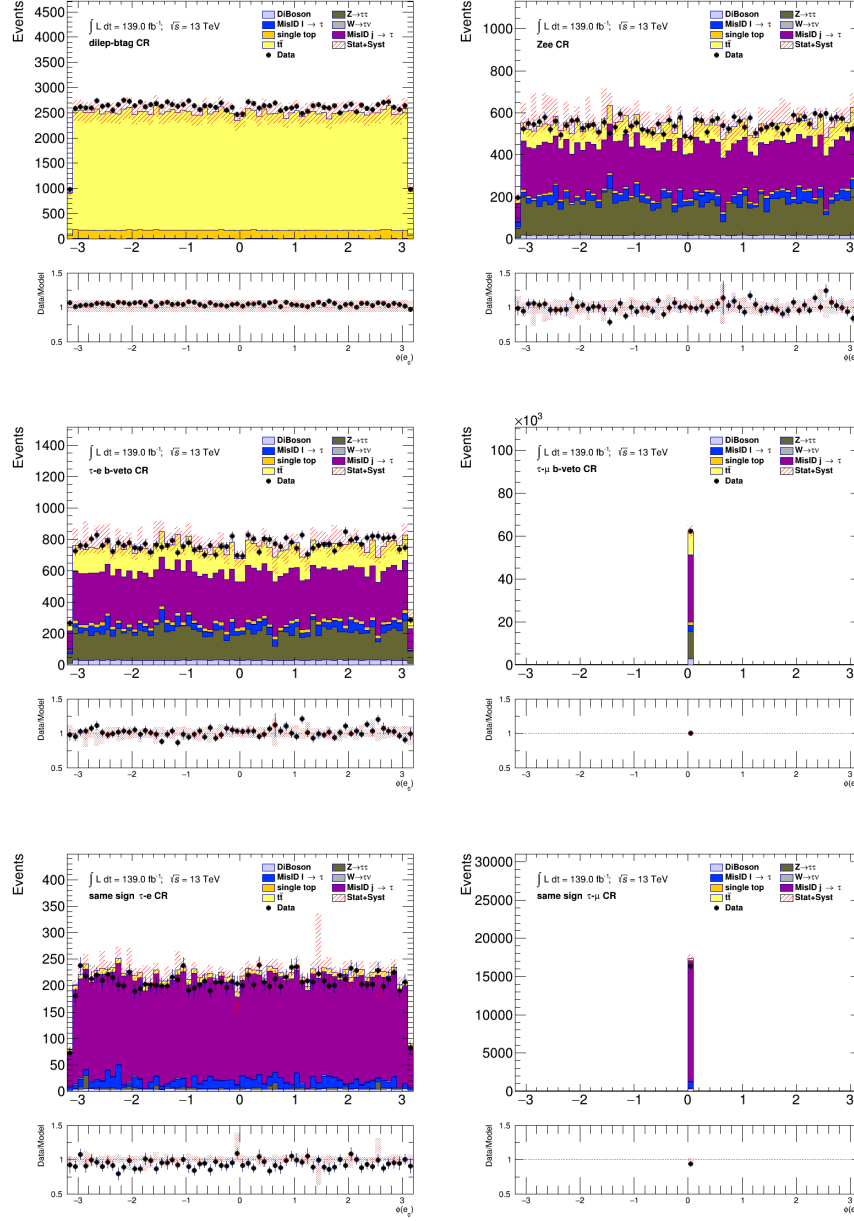


Figure C.18: Comparison between the predicted and the measured ϕ^e distributions in various control regions defined for the $\tau + \ell$ channel. The uncertainty band includes both statistical and systematic uncertainties on the background prediction.

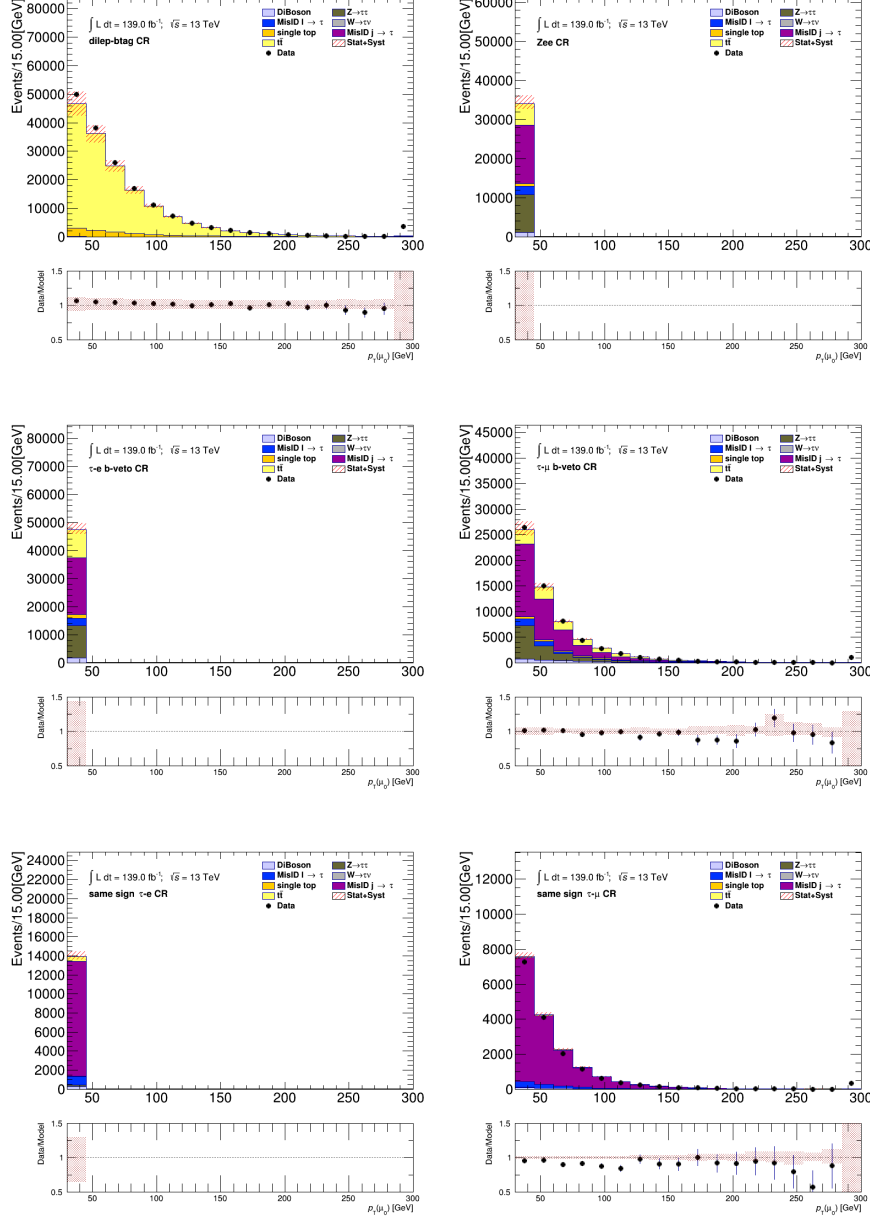


Figure C.19: Comparison between the predicted and the measured p_T^μ distributions in various control regions defined for the $\tau + \ell$ channel. The uncertainty band includes both statistical and systematic uncertainties on the background prediction.

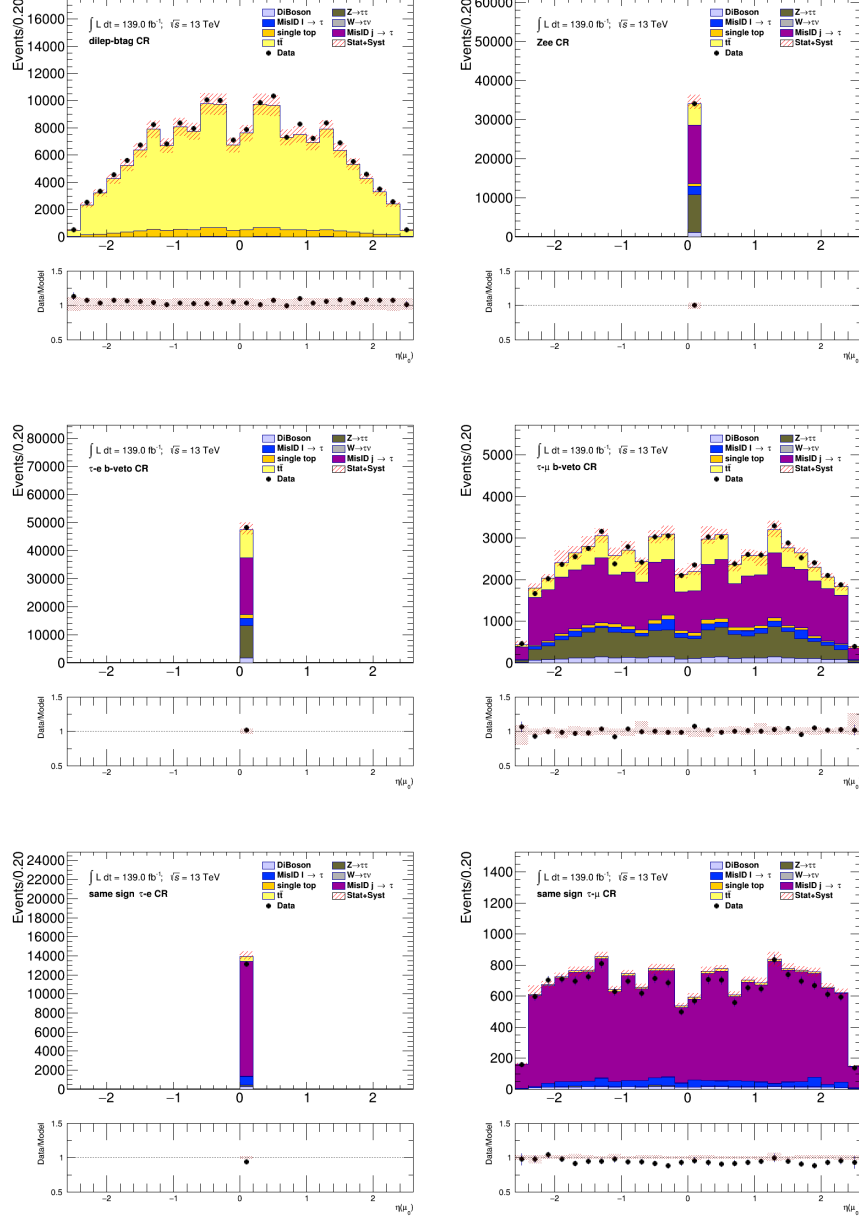


Figure C.20: Comparison between the predicted and the measured η^μ distributions in various control regions defined for the $\tau + \ell$ channel. The uncertainty band includes both statistical and systematic uncertainties on the background prediction.

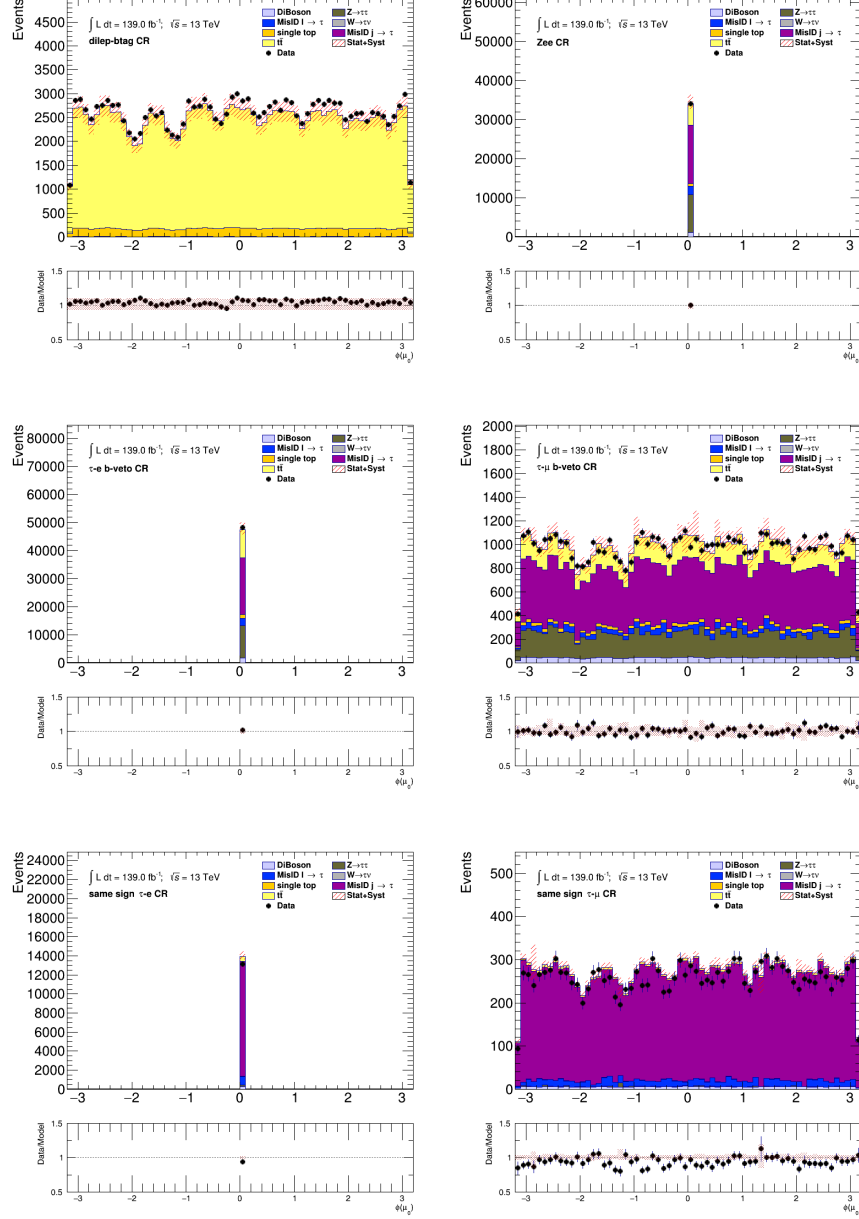


Figure C.21: Comparison between the predicted and the measured ϕ^μ distributions in various control regions defined for the $\tau + \ell$ channel. The uncertainty band includes both statistical and systematic uncertainties on the background prediction.

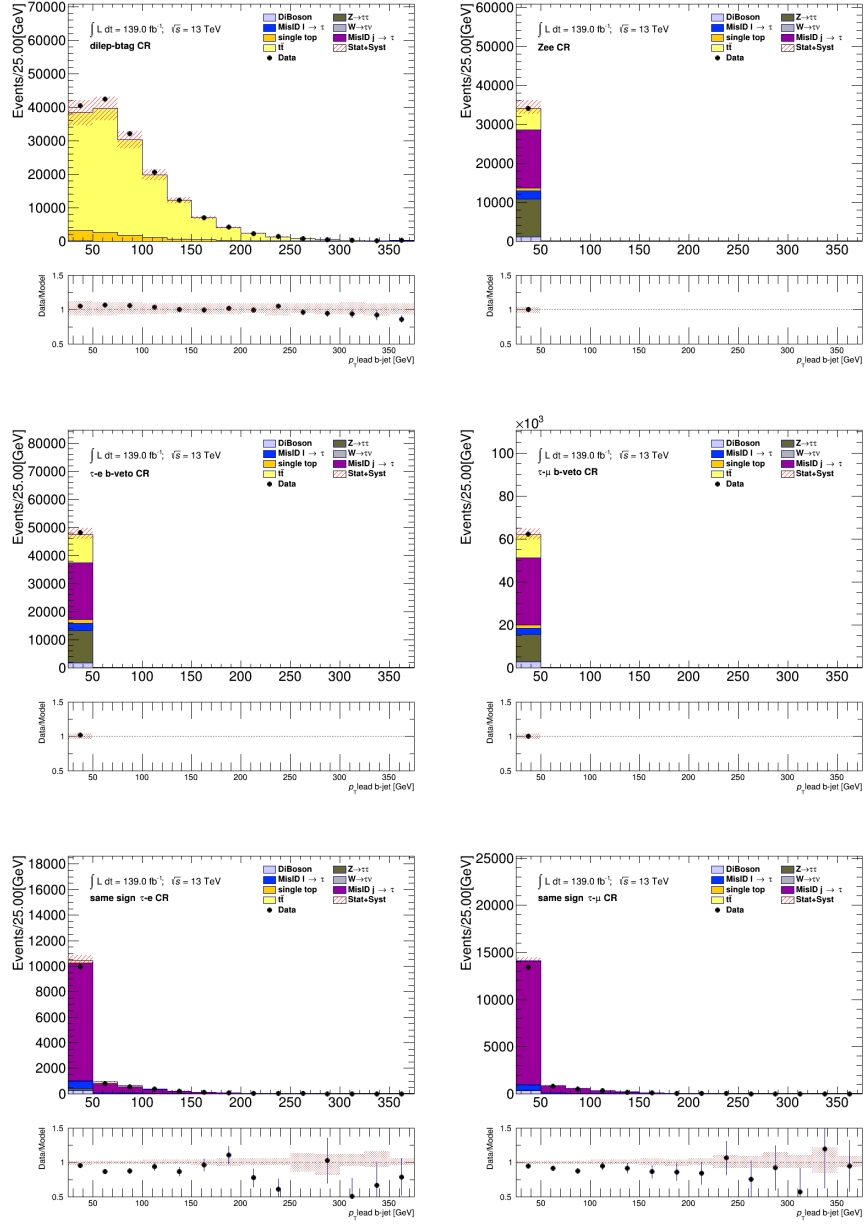


Figure C.22: Comparison between the predicted and the measured p_T^{b-jet} distributions in various control regions defined for the $\tau + \ell$ channel. The uncertainty band includes both statistical and systematic uncertainties on the background prediction.

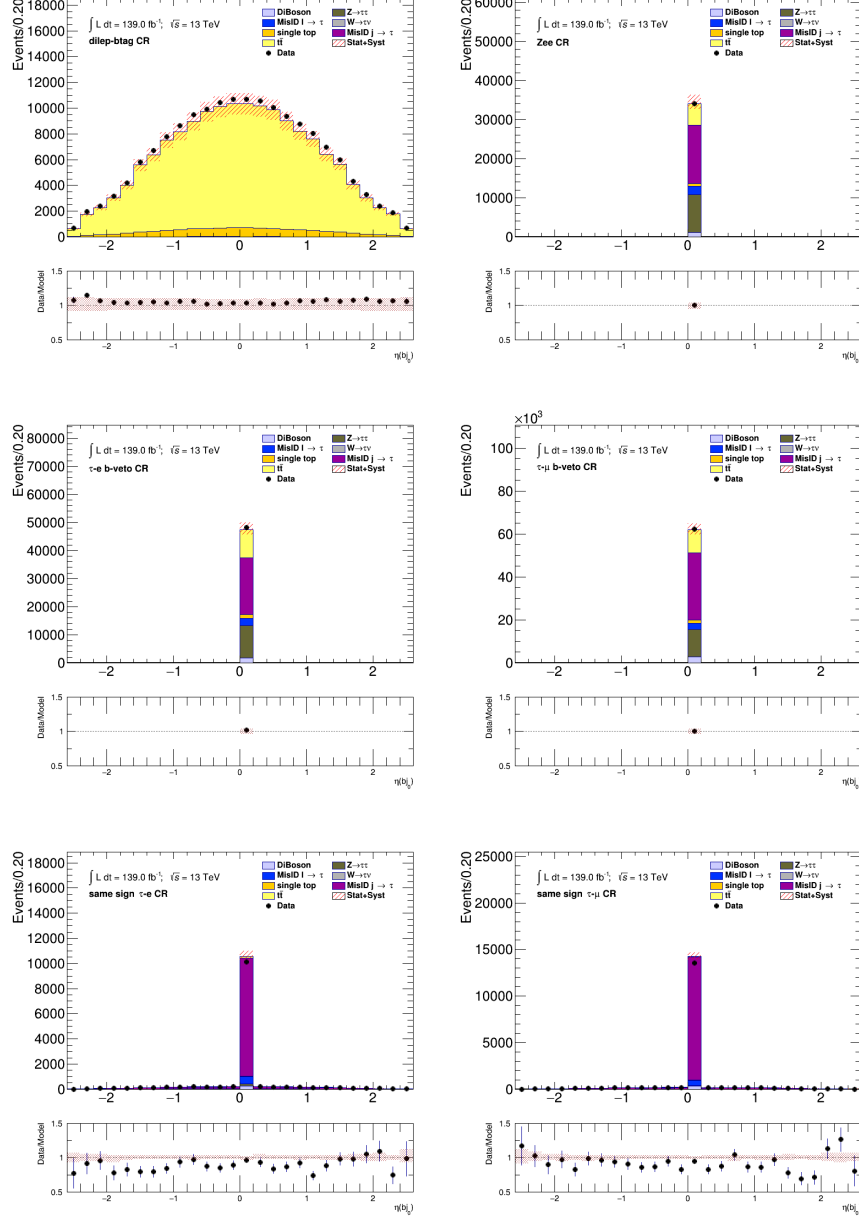


Figure C.23: Comparison between the predicted and the measured $\eta^{b\text{-jet}}$ distributions in various control regions defined for the $\tau + \ell$ channel. The uncertainty band includes both statistical and systematic uncertainties on the background prediction.

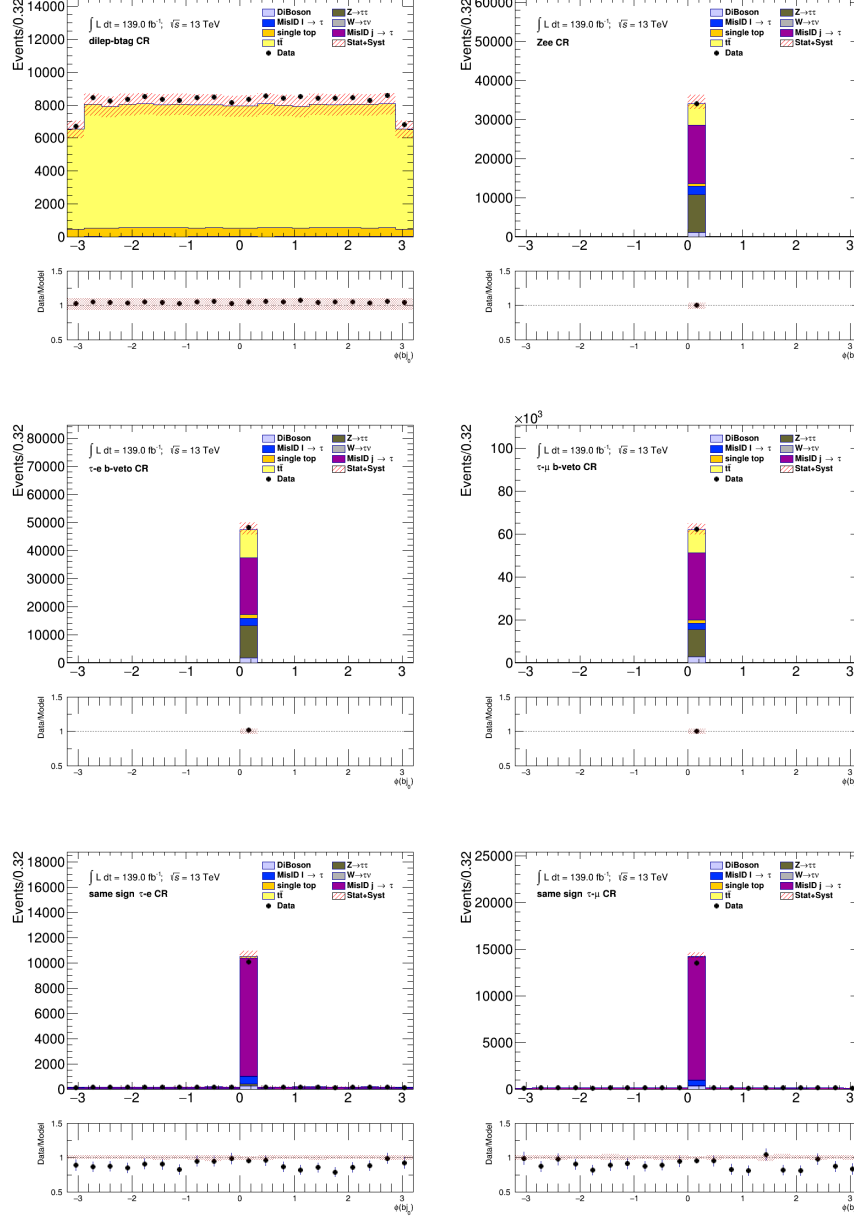


Figure C.24: Comparison between the predicted and the measured $\phi^{b\text{-jet}}$ distributions in various control regions defined for the $\tau + \ell$ channel. The uncertainty band includes both statistical and systematic uncertainties on the background prediction.

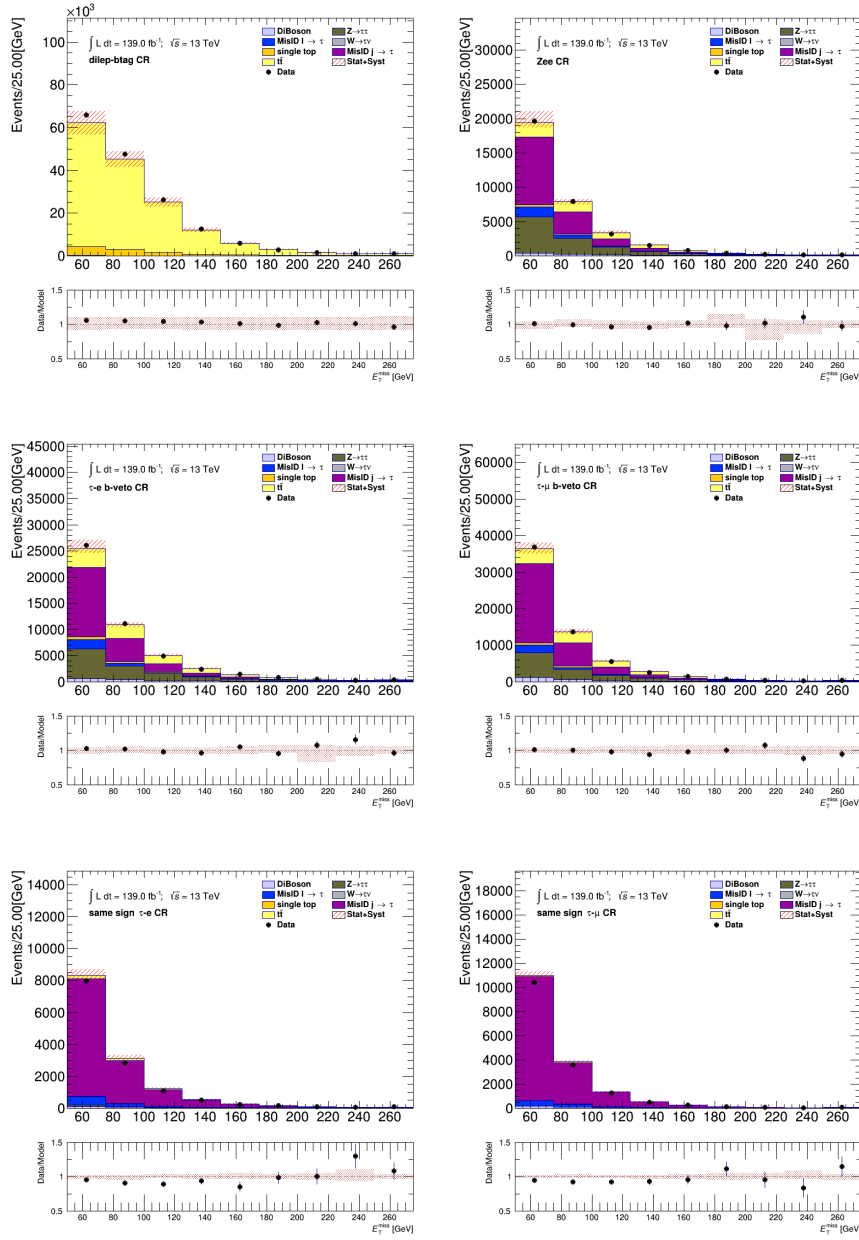


Figure C.25: Comparison between the predicted and the measured E_T^{miss} distributions in various control regions defined for the $\tau + \ell$ channel. The uncertainty band includes both statistical and systematic uncertainties on the background prediction.

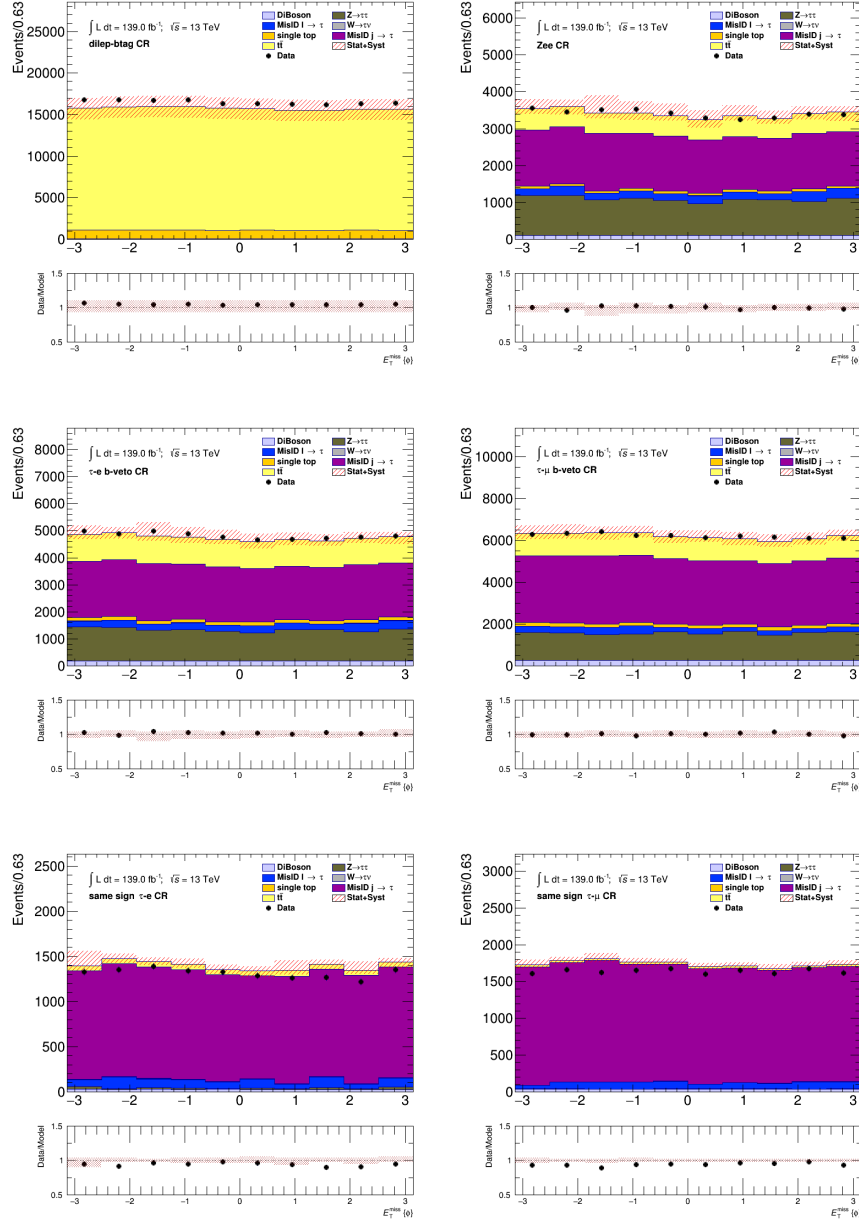


Figure C.26: Comparison between the predicted and the measured $\phi^{E_T^{\text{miss}}}$ distributions in various control regions defined for the $\tau + \ell$ channel. The uncertainty band includes both statistical and systematic uncertainties on the background prediction.

C.3 $\tau + \text{jets}$ Signal Region Plots

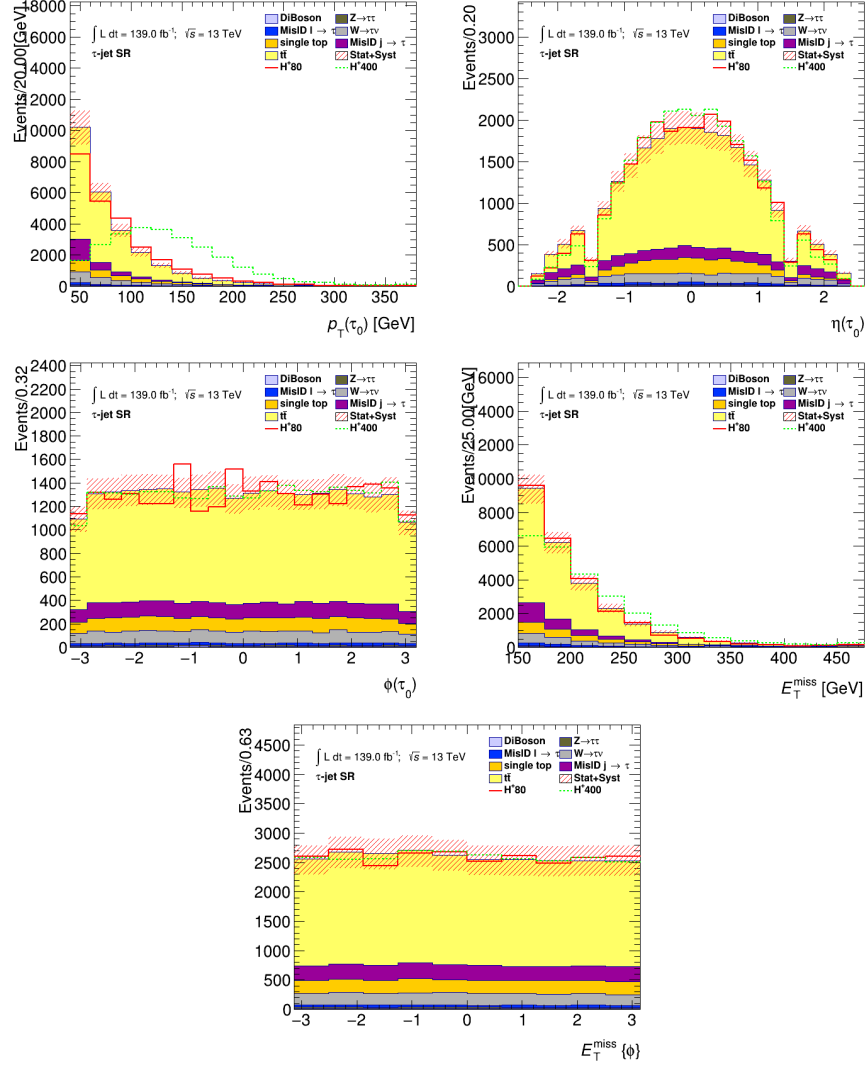


Figure C.27: PNN input variable distributions in $\tau + \text{jets}$ signal region. The uncertainty band includes both statistical and systematic uncertainties on the background prediction.

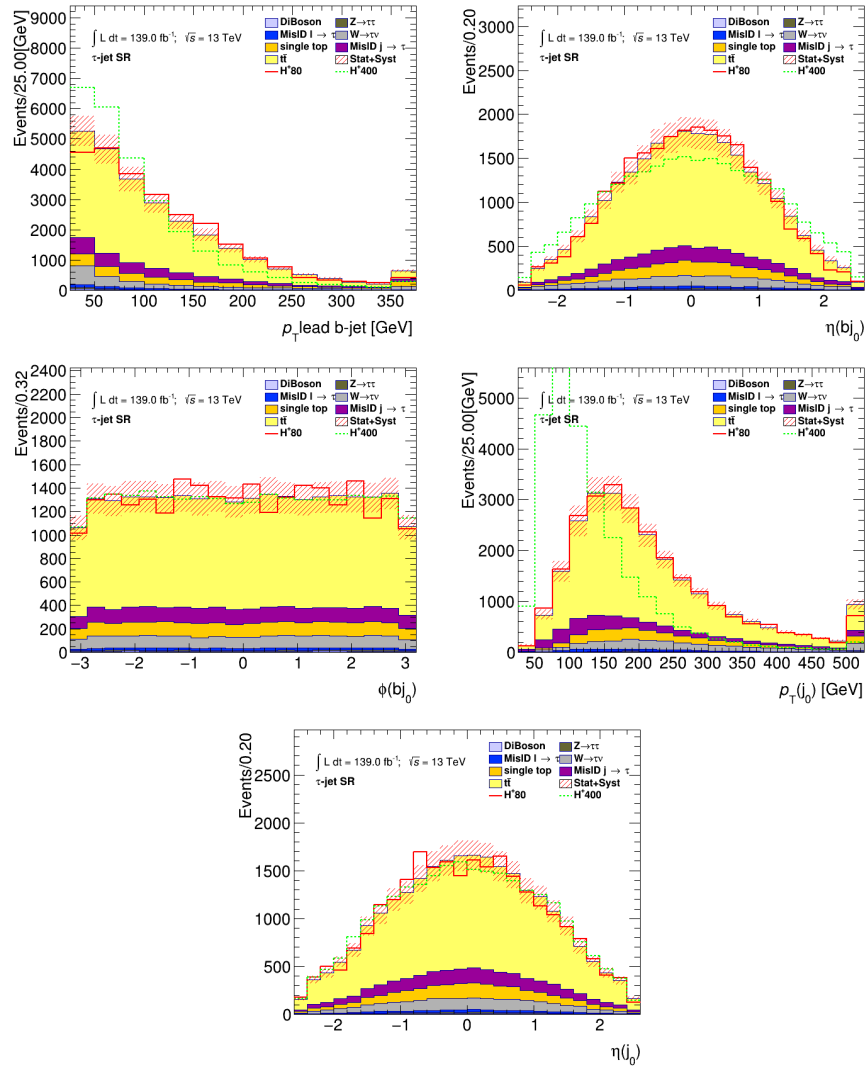


Figure C.28: PNN input variable distributions in $\tau + \text{jets}$ signal region. The uncertainty band includes both statistical and systematic uncertainties on the background prediction.

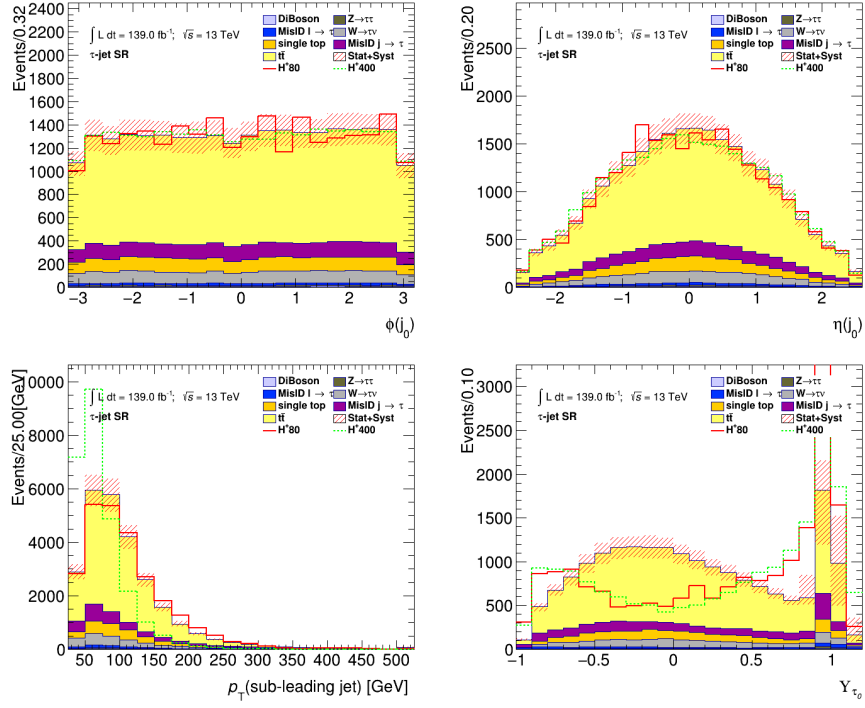


Figure C.29: PNN input variable distributions in $\tau + \text{jets}$ signal region. The uncertainty band includes both statistical and systematic uncertainties on the background prediction.

C.4 $\tau + \ell$ Signal Region Plots

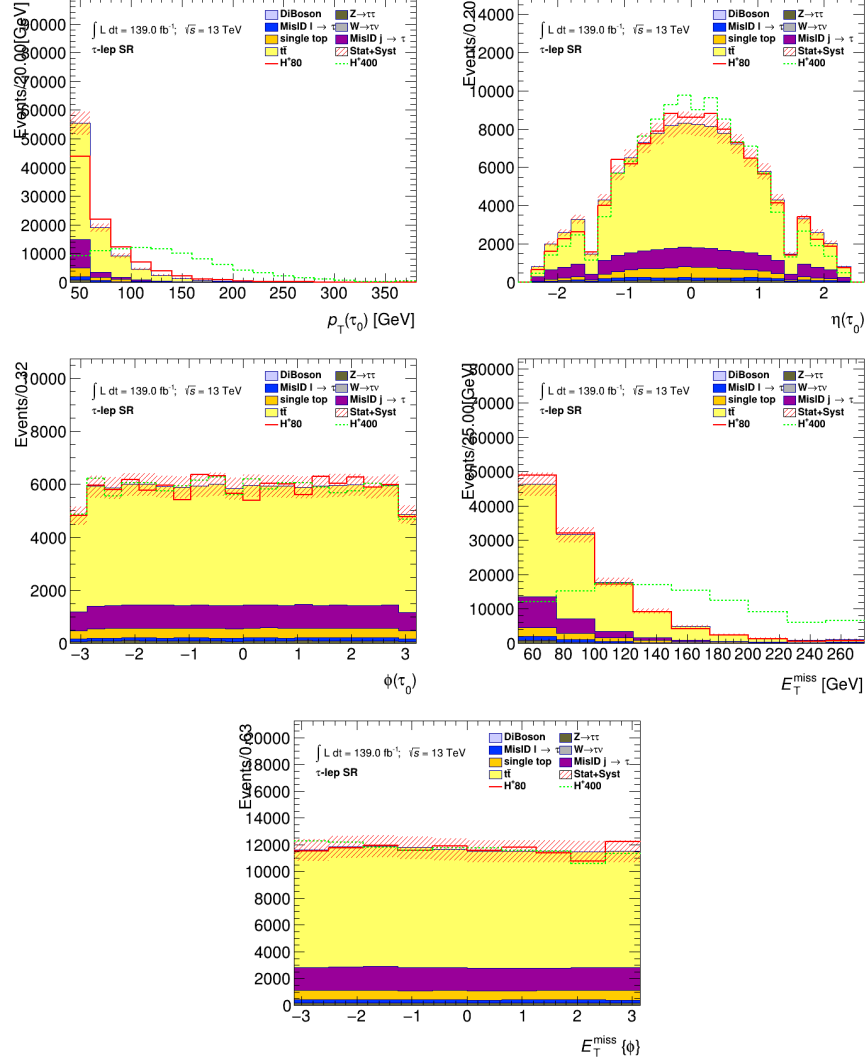


Figure C.30: PNN input variable distributions in $\tau + \ell$ signal region. The uncertainty band includes both statistical and systematic uncertainties on the background prediction.

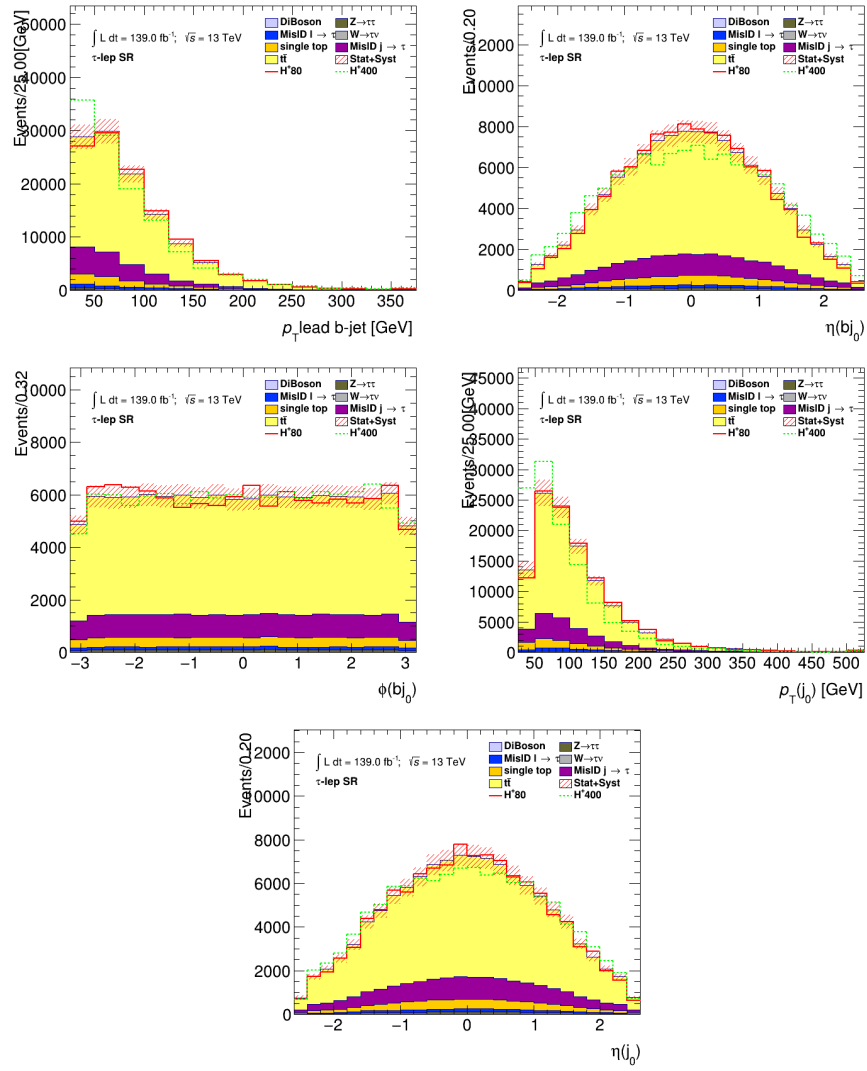


Figure C.31: PNN input variable distributions in $\tau + \ell$ signal region. The uncertainty band includes both statistical and systematic uncertainties on the background prediction.

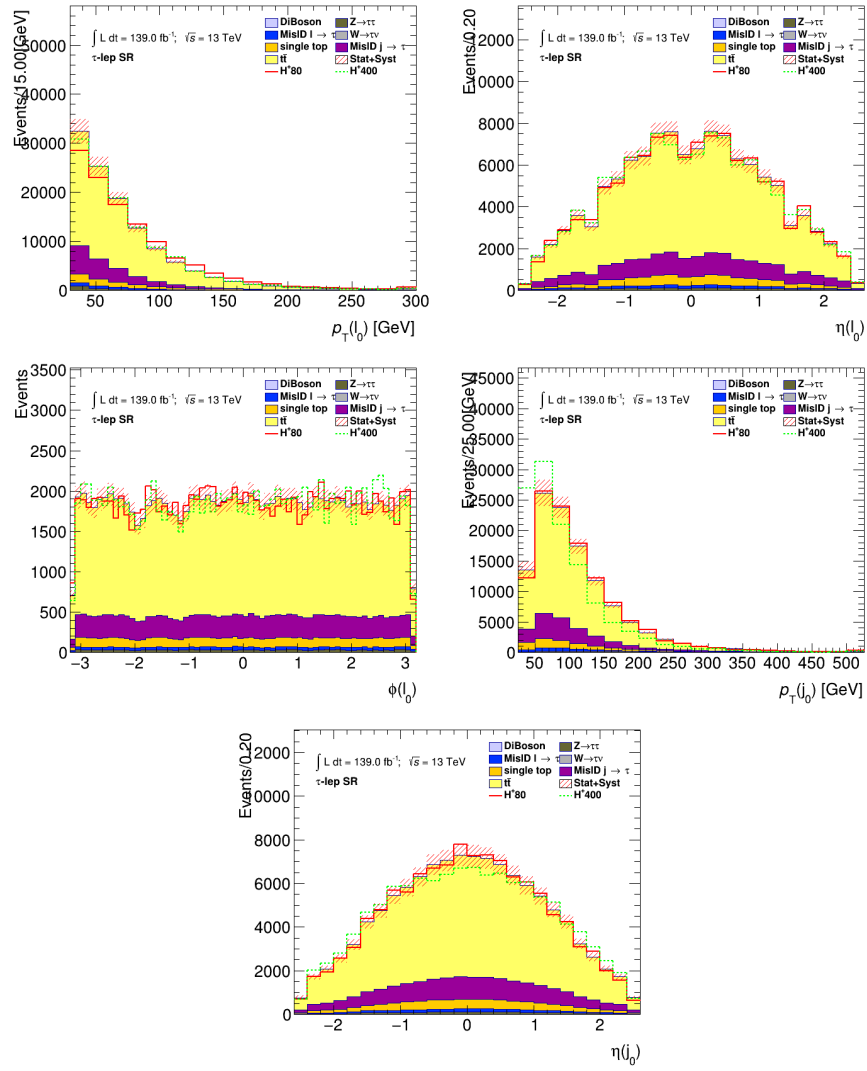


Figure C.32: PNN input variable distributions in $\tau + \ell$ signal region. The uncertainty band includes both statistical and systematic uncertainties on the background prediction.

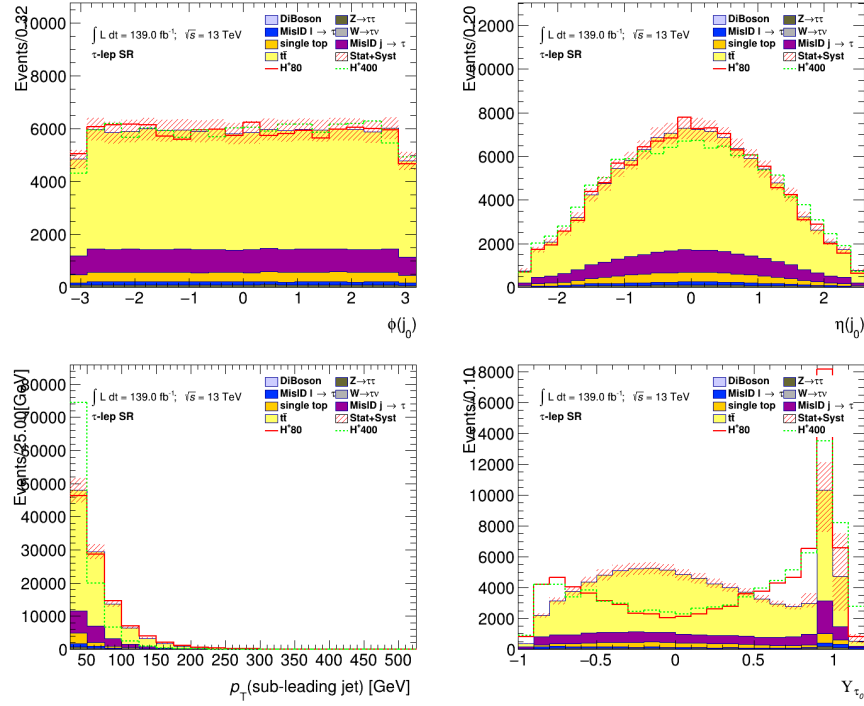


Figure C.33: PNN input variable distributions in $\tau + \ell$ signal region. The uncertainty band includes both statistical and systematic uncertainties on the background prediction.

APPENDIX D

ADDITIONAL PNN SCORE PLOTS

D.1 $\tau + \text{jets}$ PNN Scores

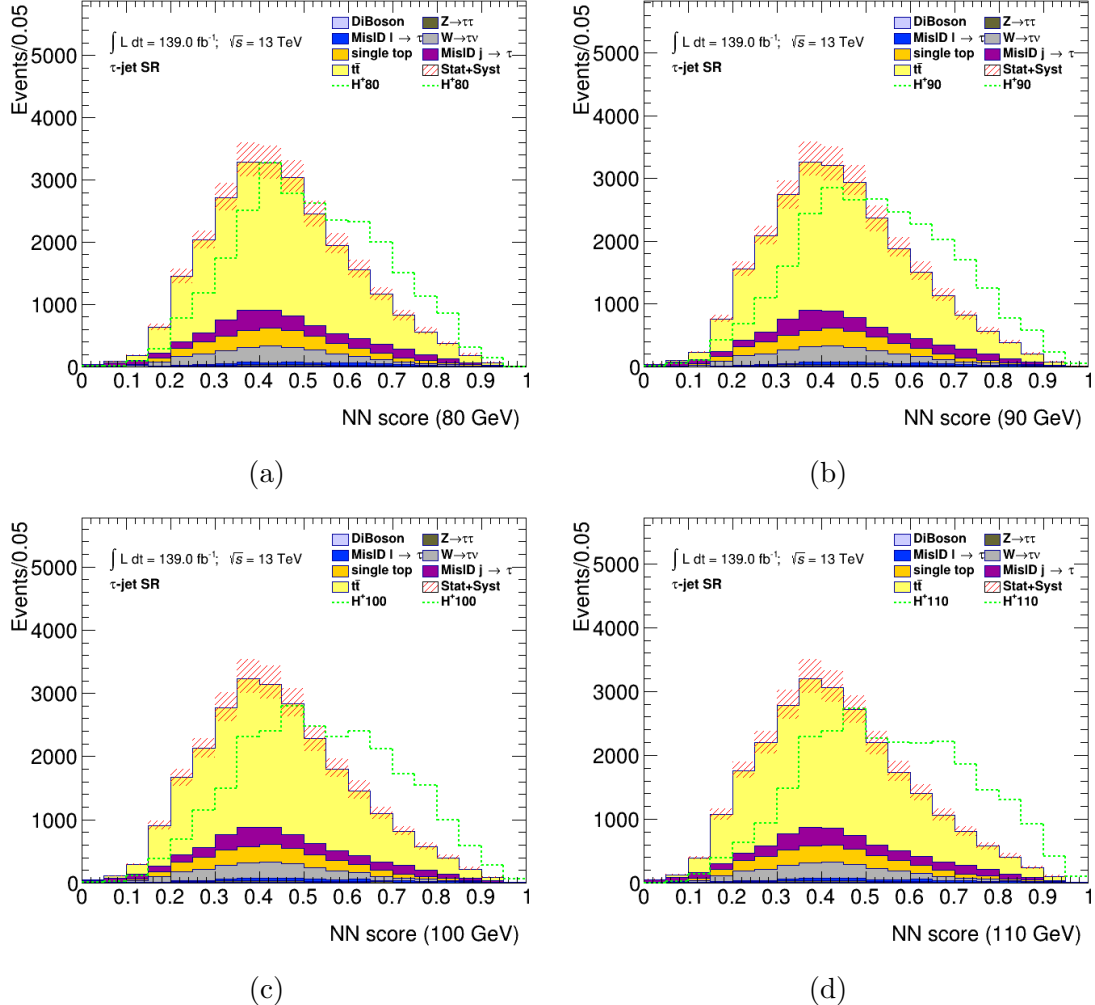


Figure D.1: PNN score distributions in the signal region of the τ +jets channel, for the chosen charged Higgs boson mass parameters. The uncertainty bands include all statistical and systematic uncertainties. The normalization of the signal (shown for illustration) corresponds to the integral of the background.

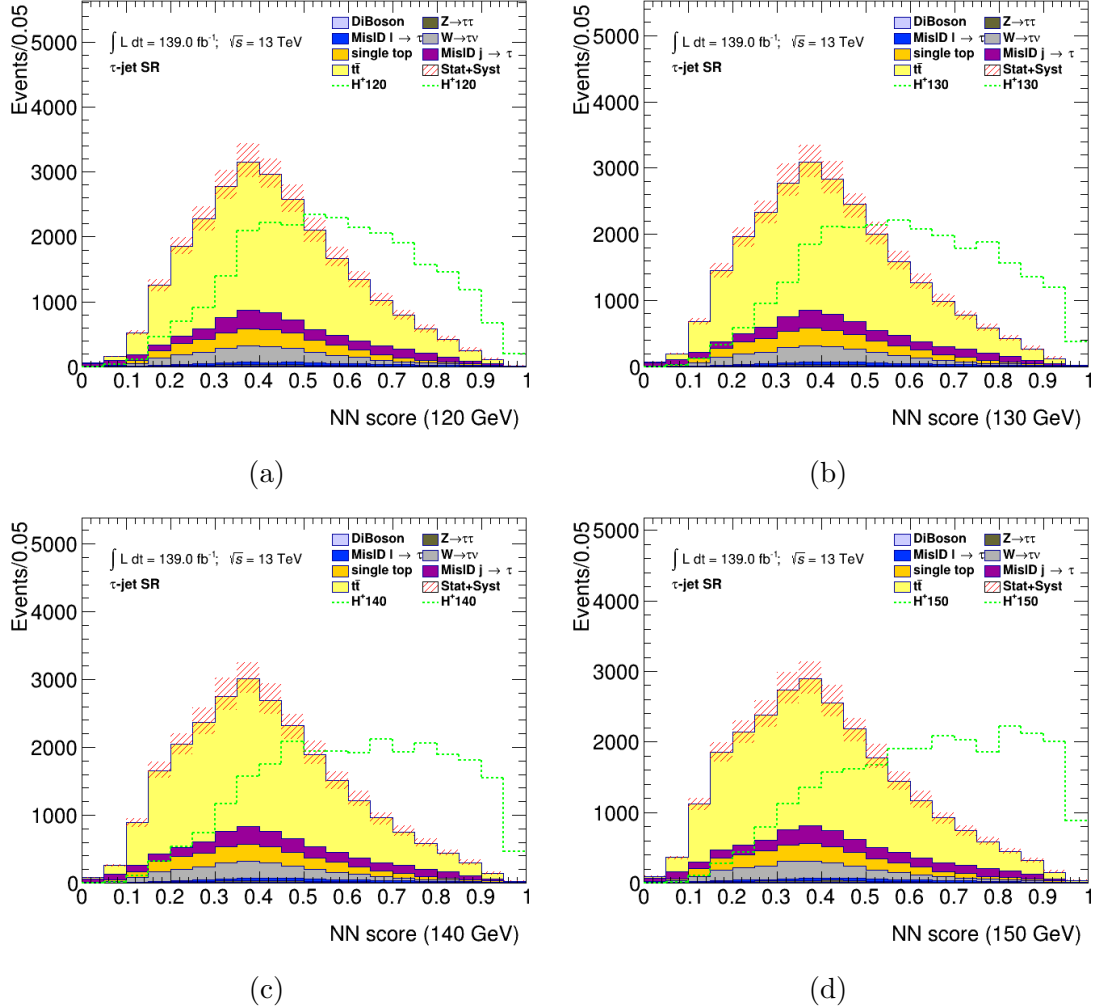


Figure D.2: PNN score distributions in the signal region of the $\tau + \text{jets}$ channel, for the chosen charged Higgs boson mass parameters. The uncertainty bands include all statistical and systematic uncertainties. The normalization of the signal (shown for illustration) corresponds to the integral of the background.

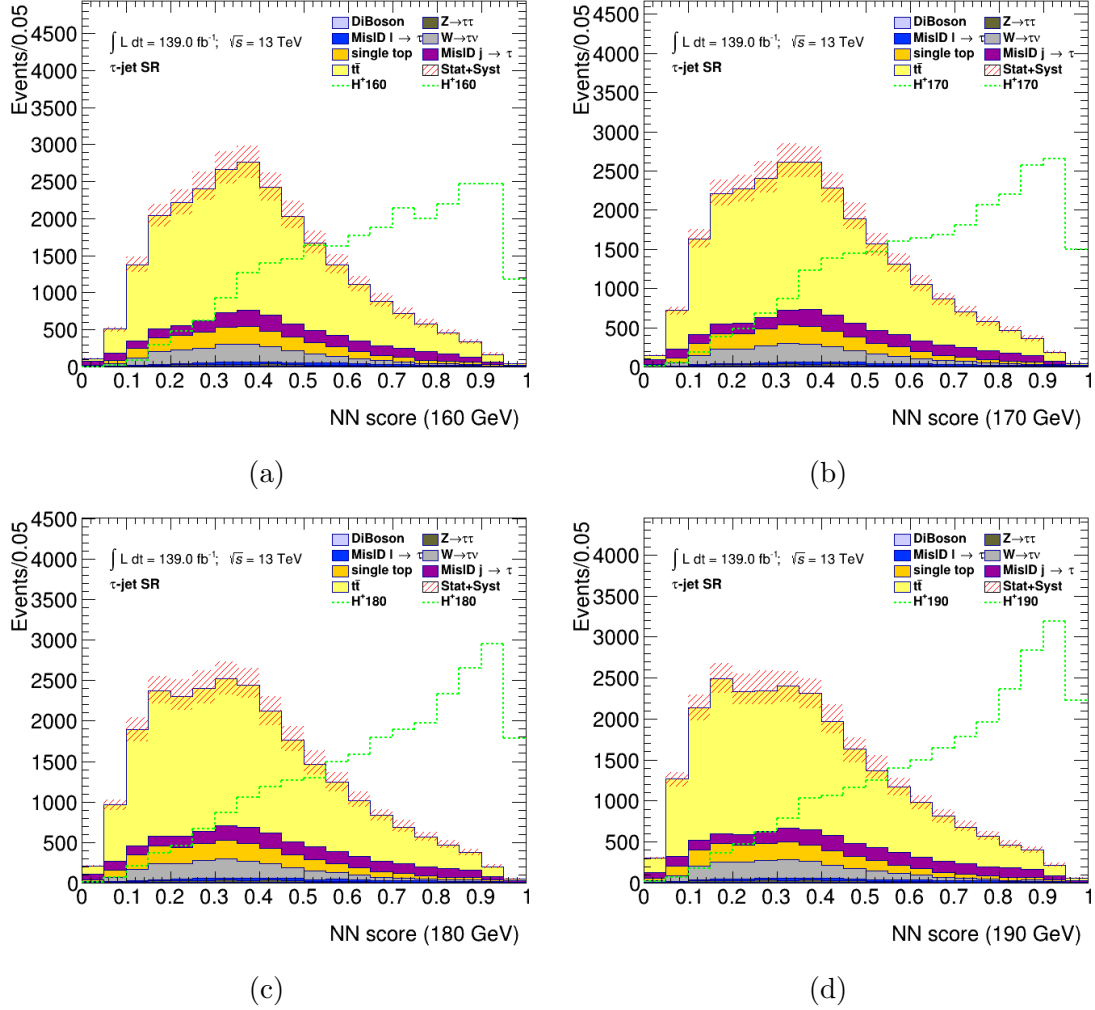


Figure D.3: PNN score distributions in the signal region of the $\tau+\text{jets}$ channel, for the chosen charged Higgs boson mass parameters. The uncertainty bands include all statistical and systematic uncertainties. The normalization of the signal (shown for illustration) corresponds to the integral of the background.

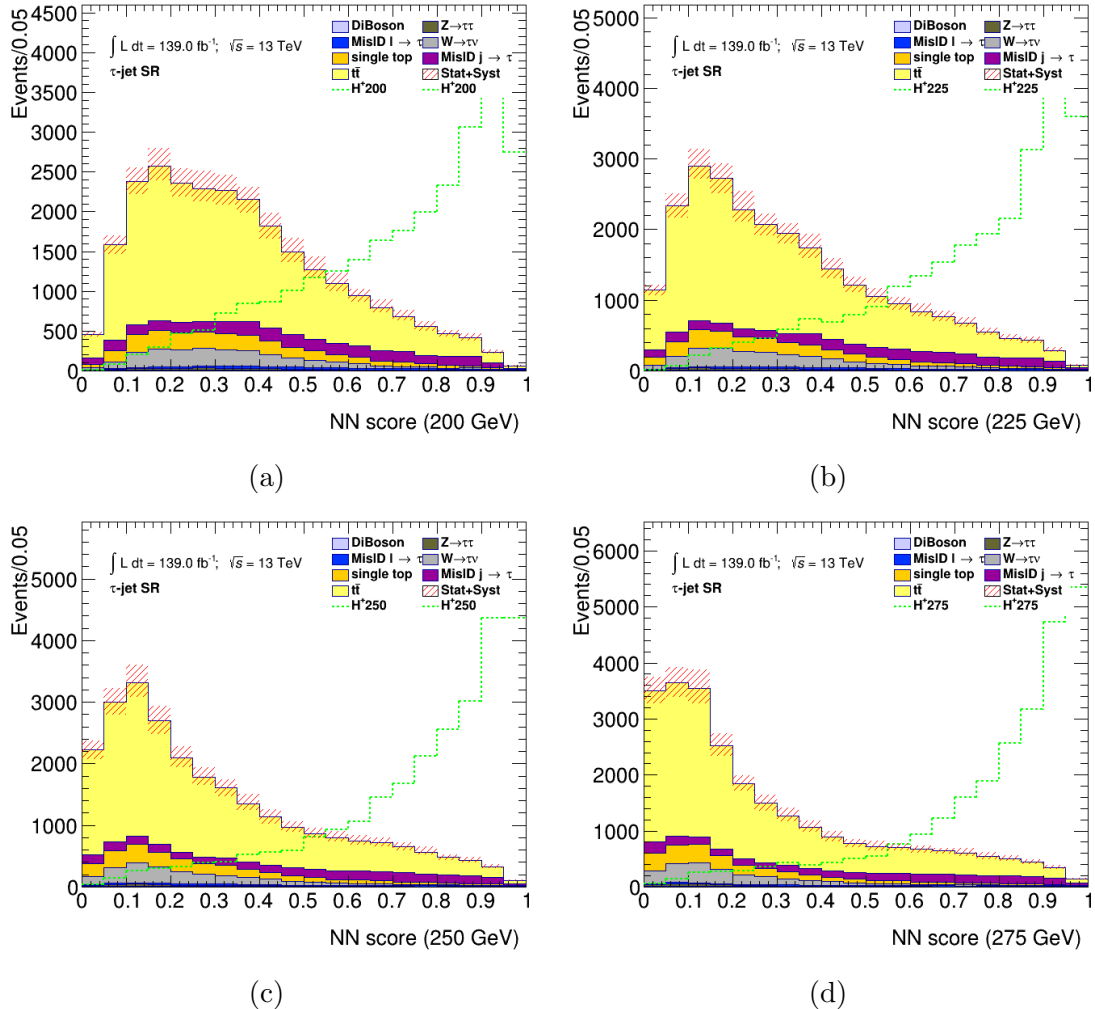


Figure D.4: PNN score distributions in the signal region of the τ +jets channel, for the chosen charged Higgs boson mass parameters. The uncertainty bands include all statistical and systematic uncertainties. The normalization of the signal (shown for illustration) corresponds to the integral of the background.

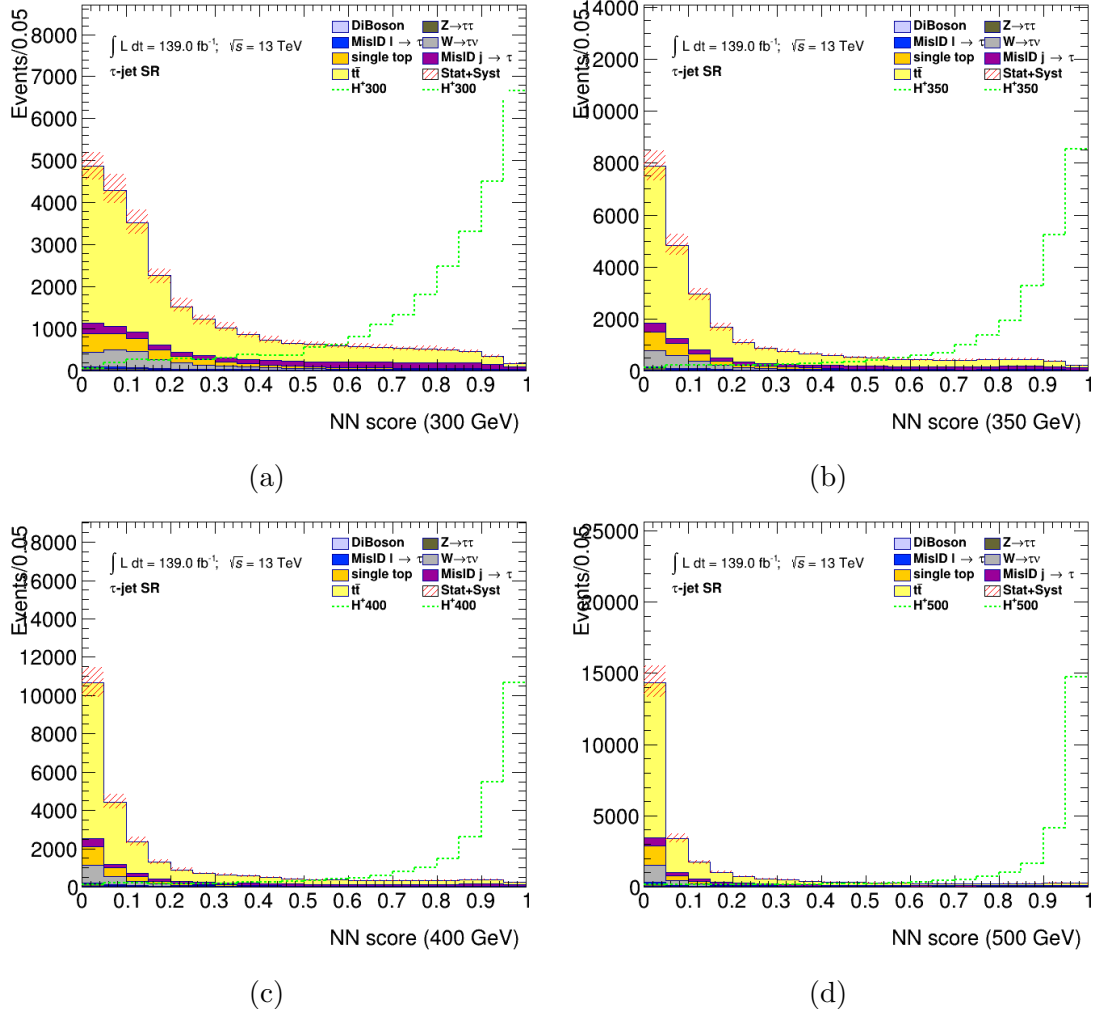


Figure D.5: PNN score distributions in the signal region of the τ +jets channel, for the chosen charged Higgs boson mass parameters. The uncertainty bands include all statistical and systematic uncertainties. The normalization of the signal (shown for illustration) corresponds to the integral of the background.

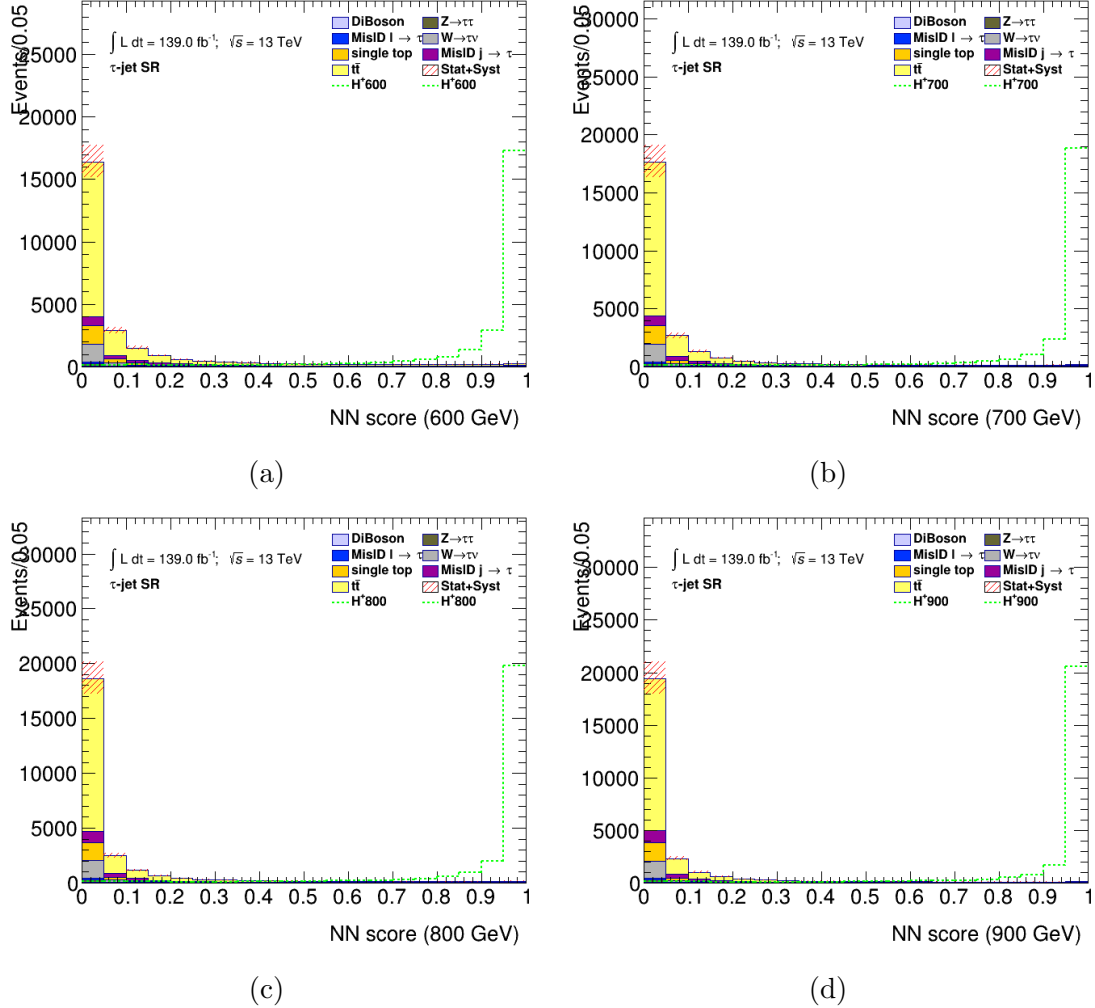


Figure D.6: PNN score distributions in the signal region of the τ +jets channel, for the chosen charged Higgs boson mass parameters. The uncertainty bands include all statistical and systematic uncertainties. The normalization of the signal (shown for illustration) corresponds to the integral of the background.

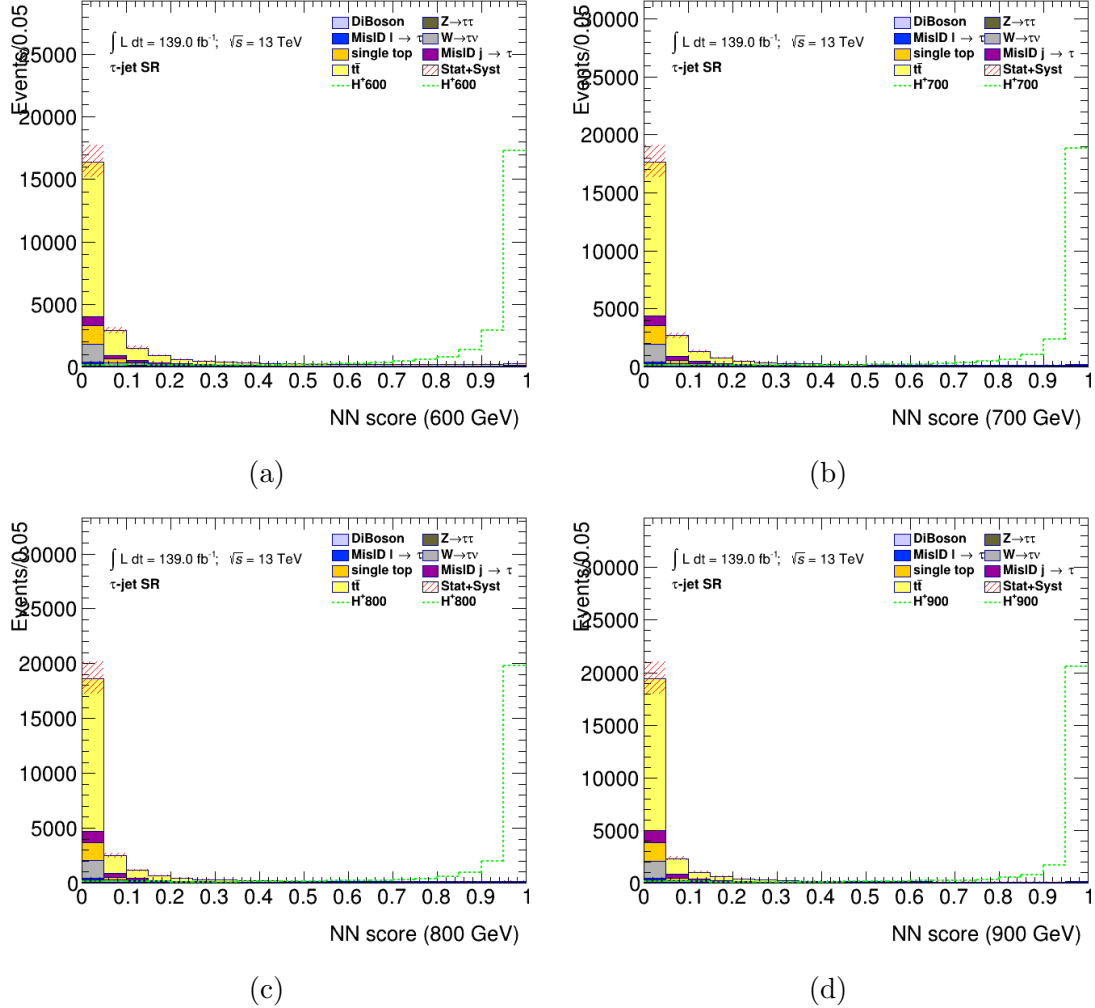


Figure D.7: PNN score distributions in the signal region of the $\tau+\text{jets}$ channel, for the chosen charged Higgs boson mass parameters. The uncertainty bands include all statistical and systematic uncertainties. The normalization of the signal (shown for illustration) corresponds to the integral of the background.

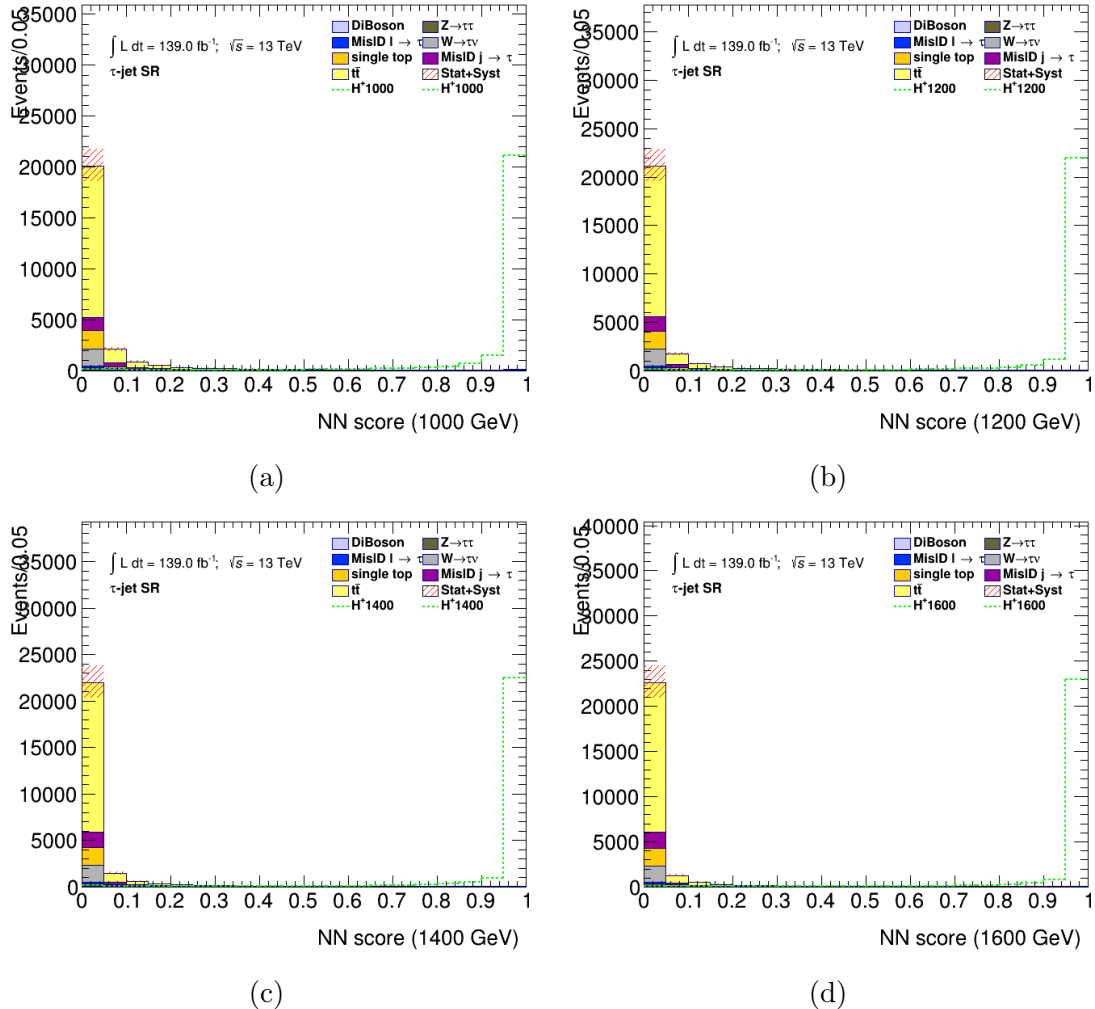


Figure D.8: PNN score distributions in the signal region of the $\tau+\text{jets}$ channel, for the chosen charged Higgs boson mass parameters. The uncertainty bands include all statistical and systematic uncertainties. The normalization of the signal (shown for illustration) corresponds to the integral of the background.

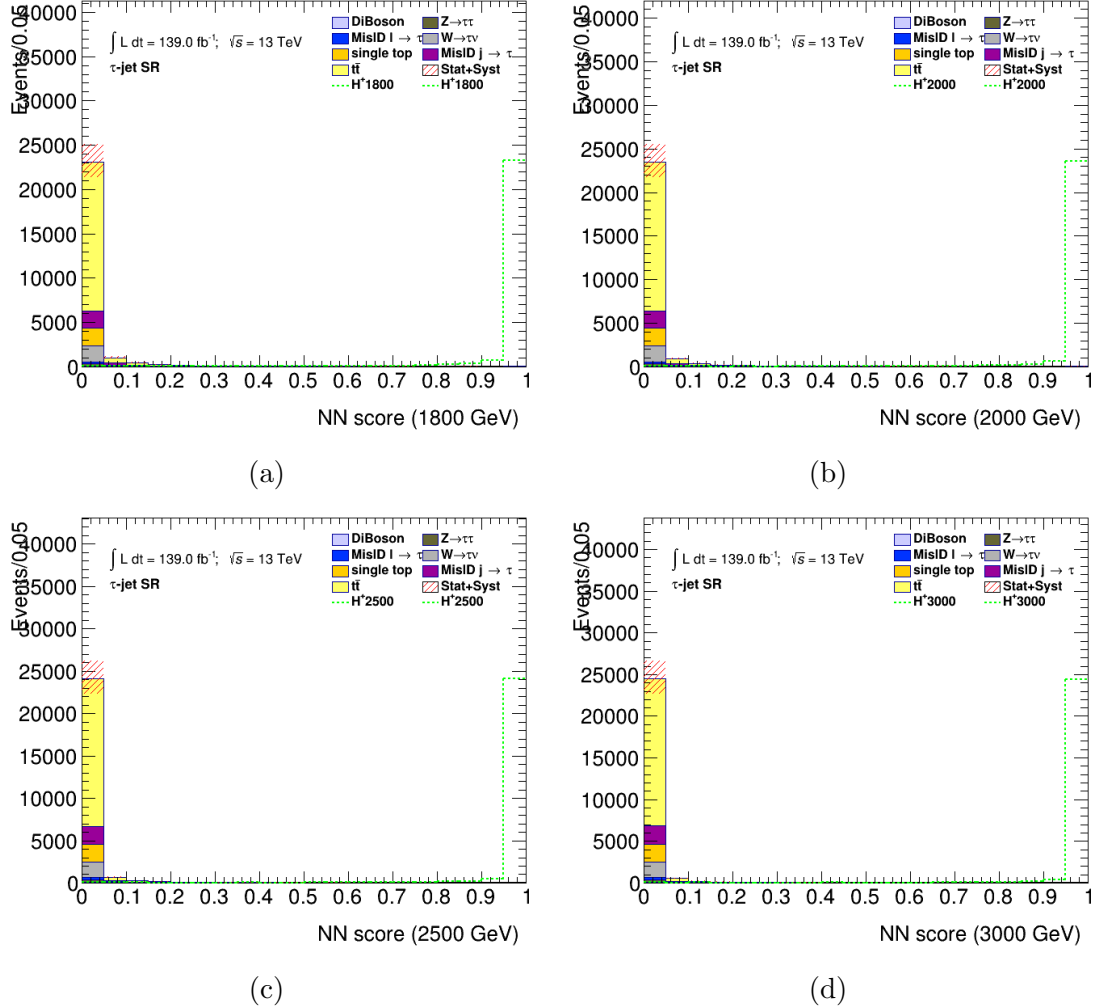


Figure D.9: PNN score distributions in the signal region of the τ +jets channel, for the chosen charged Higgs boson mass parameters. The uncertainty bands include all statistical and systematic uncertainties. The normalization of the signal (shown for illustration) corresponds to the integral of the background.

D.2 $\tau + \ell$ PNN Scores

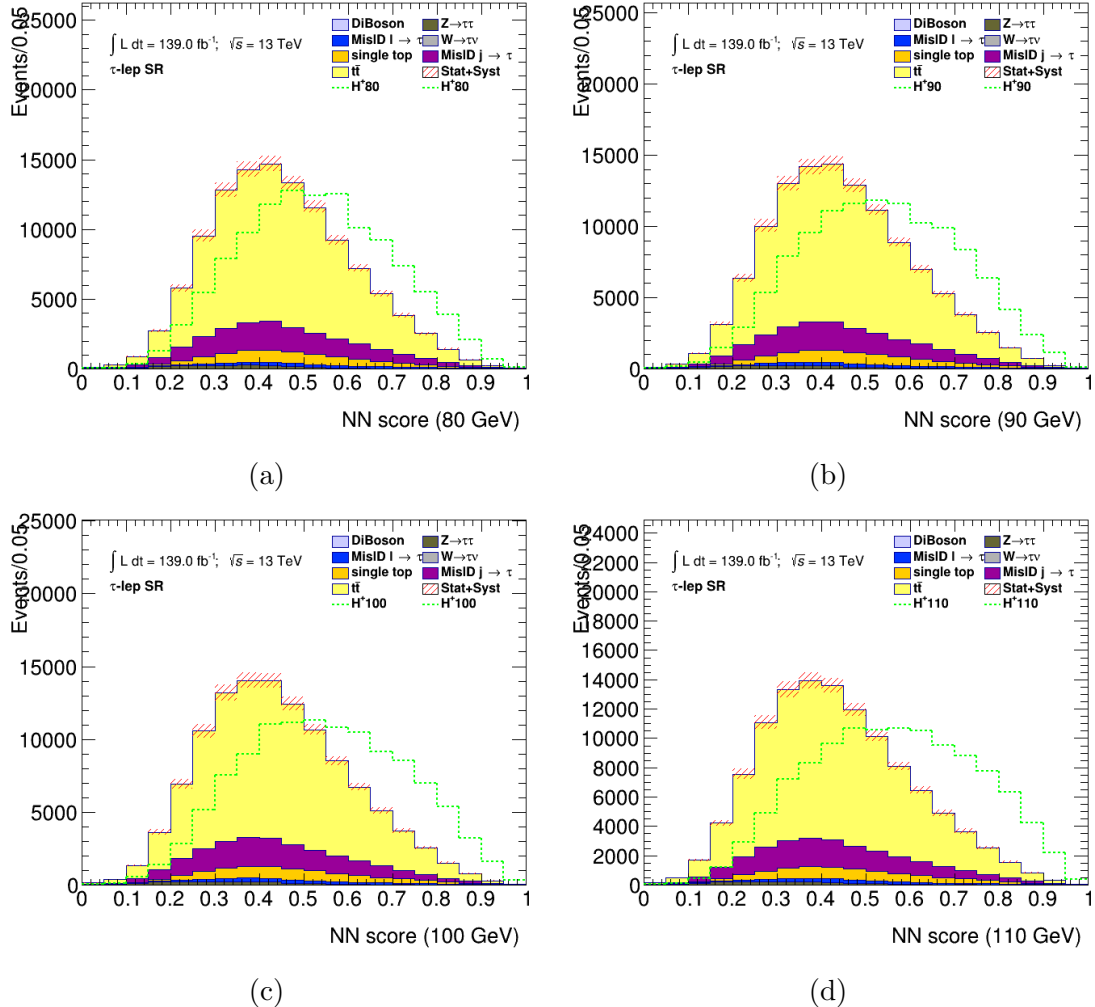


Figure D.10: PNN score distributions in the signal region of the $\tau + \ell$ channel, for the chosen charged Higgs boson mass parameters. The uncertainty bands include all statistical and systematic uncertainties. The normalization of the signal (shown for illustration) corresponds to the integral of the background.

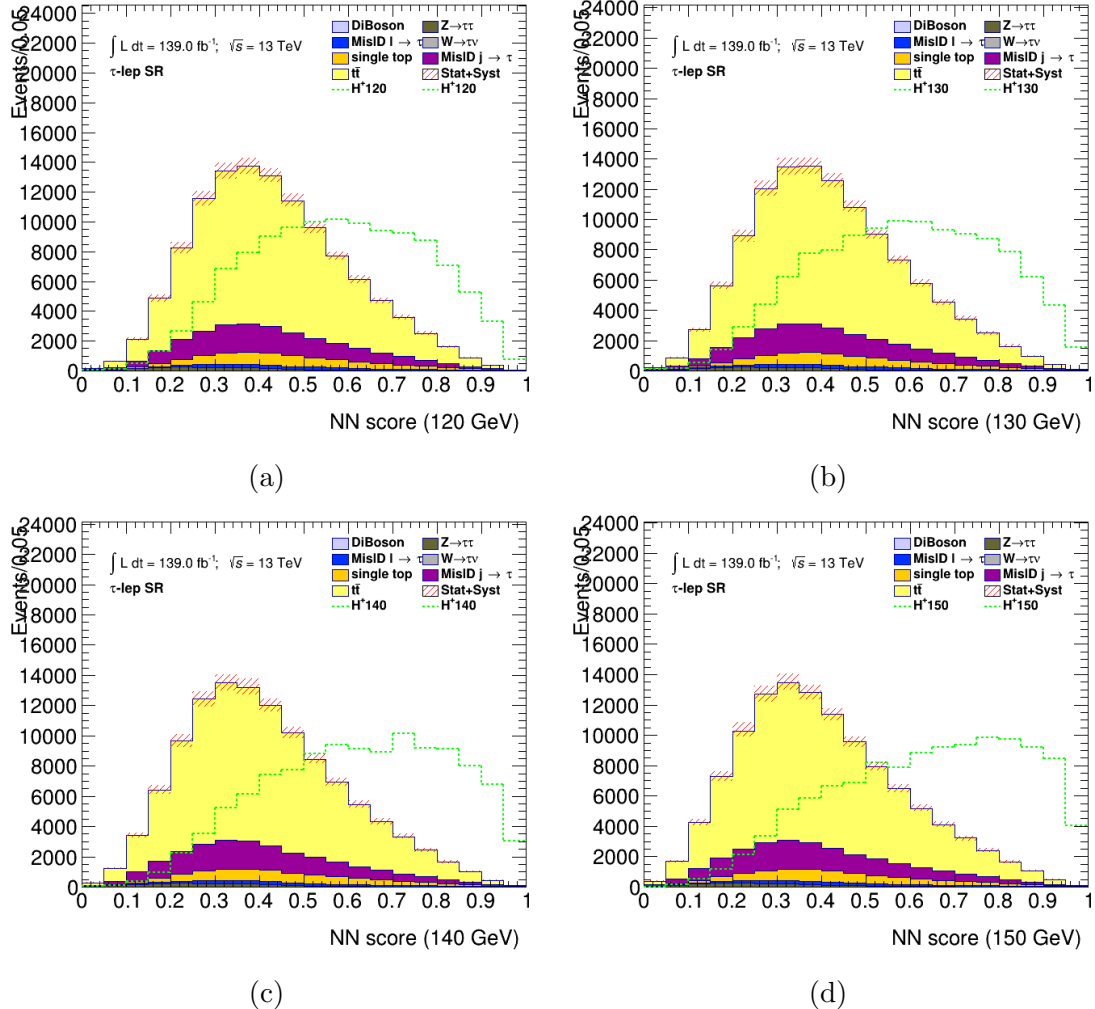


Figure D.11: PNN score distributions in the signal region of the $\tau + \ell$ channel, for the chosen charged Higgs boson mass parameters. The uncertainty bands include all statistical and systematic uncertainties. The normalization of the signal (shown for illustration) corresponds to the integral of the background.

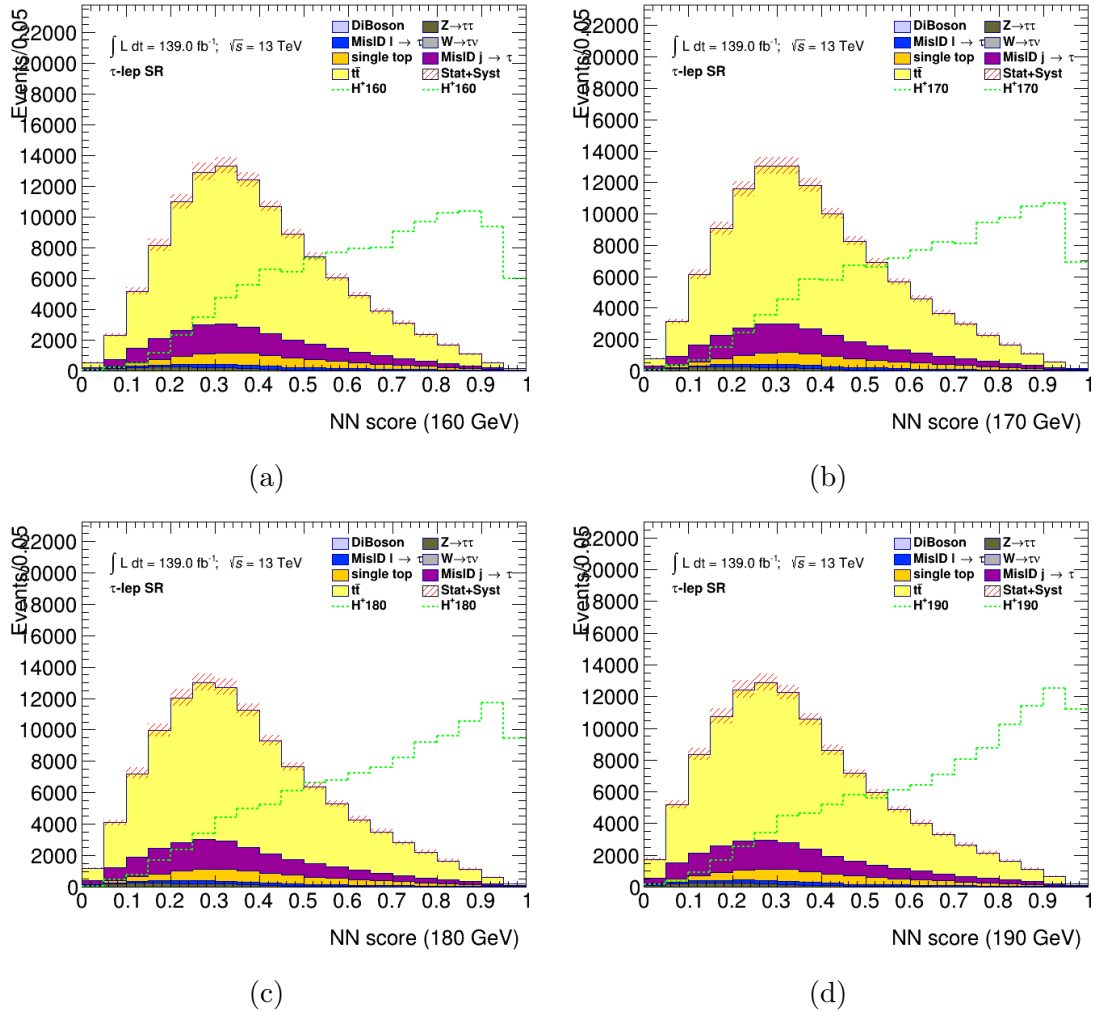


Figure D.12: PNN score distributions in the signal region of the $\tau + \ell$ channel, for the chosen charged Higgs boson mass parameters. The uncertainty bands include all statistical and systematic uncertainties. The normalization of the signal (shown for illustration) corresponds to the integral of the background.

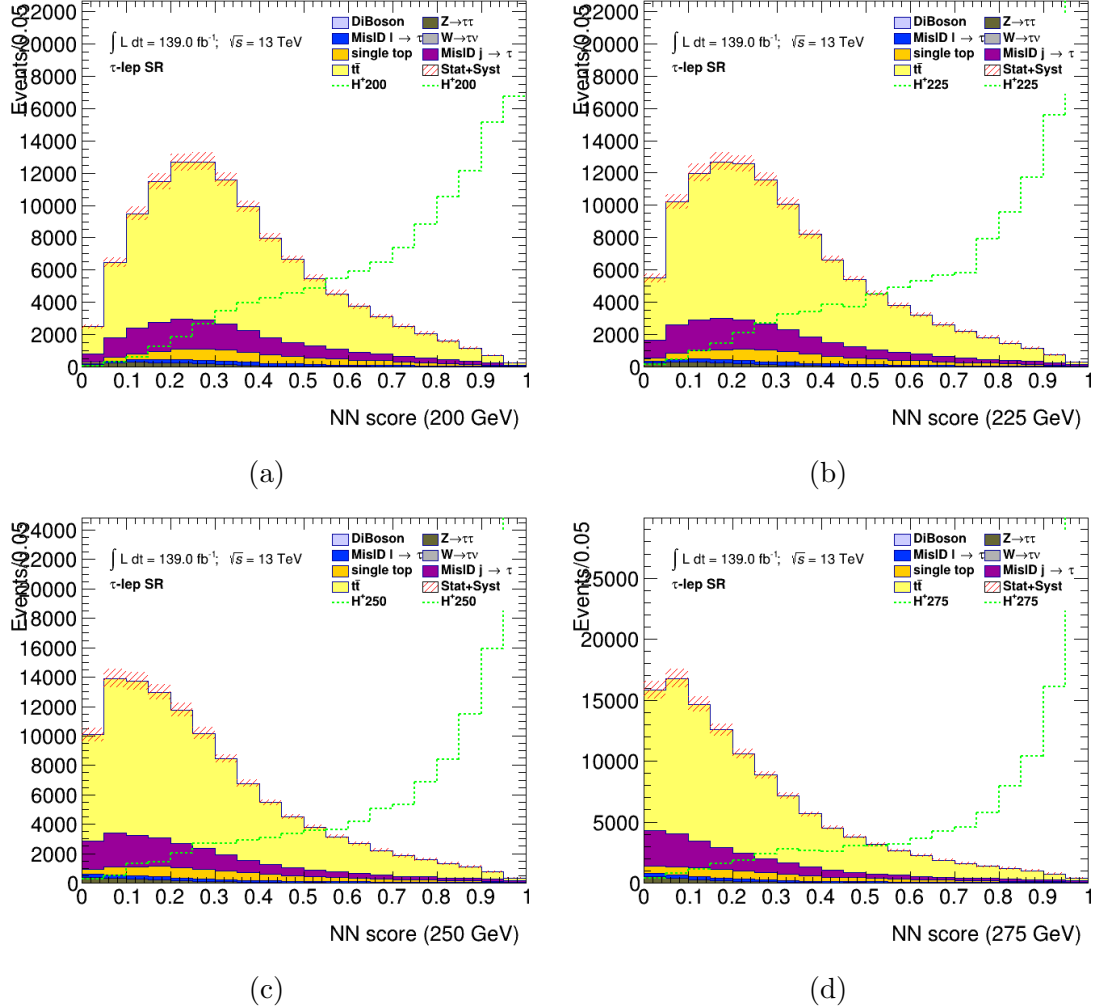


Figure D.13: PNN score distributions in the signal region of the $\tau + \ell$ channel, for the chosen charged Higgs boson mass parameters. The uncertainty bands include all statistical and systematic uncertainties. The normalization of the signal (shown for illustration) corresponds to the integral of the background.

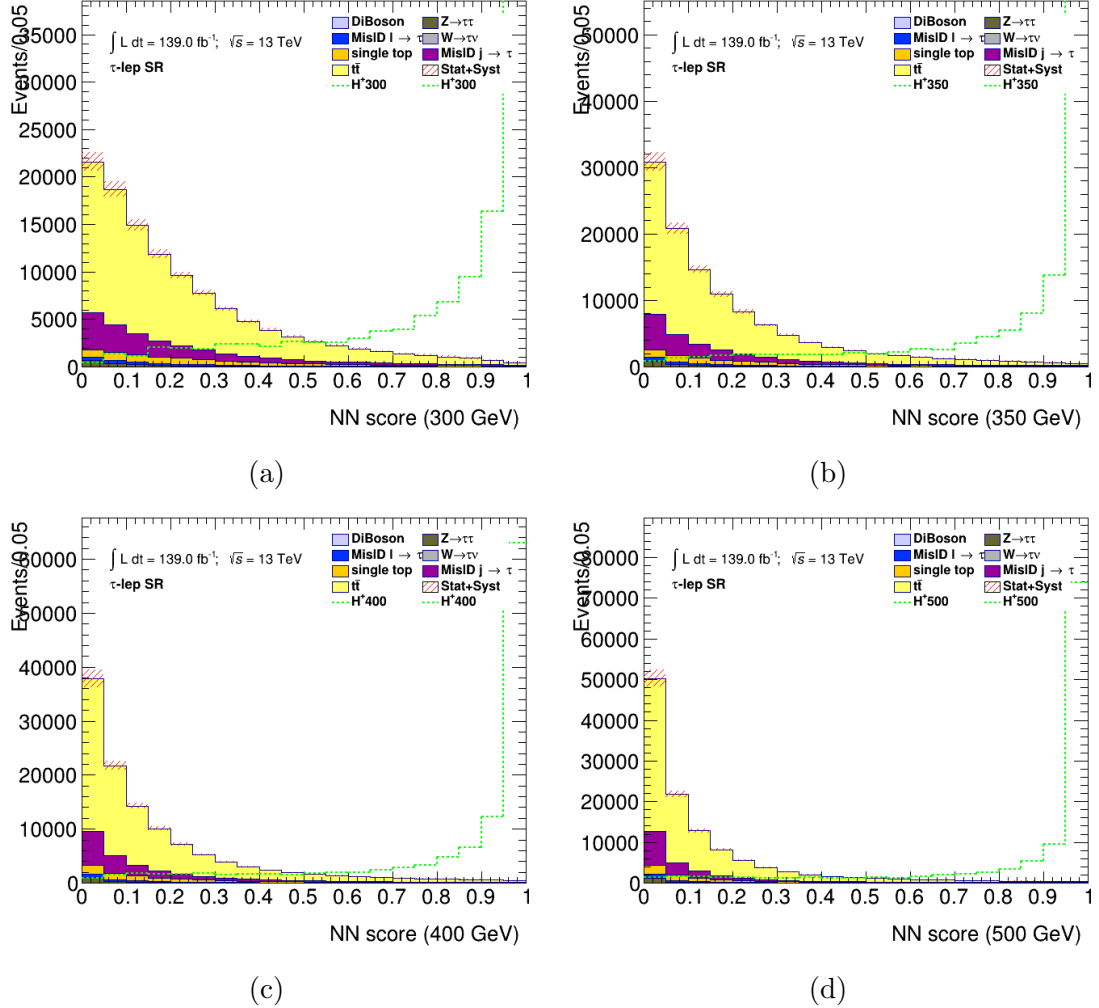


Figure D.14: PNN score distributions in the signal region of the $\tau + \ell$ channel, for the chosen charged Higgs boson mass parameters. The uncertainty bands include all statistical and systematic uncertainties. The normalization of the signal (shown for illustration) corresponds to the integral of the background.

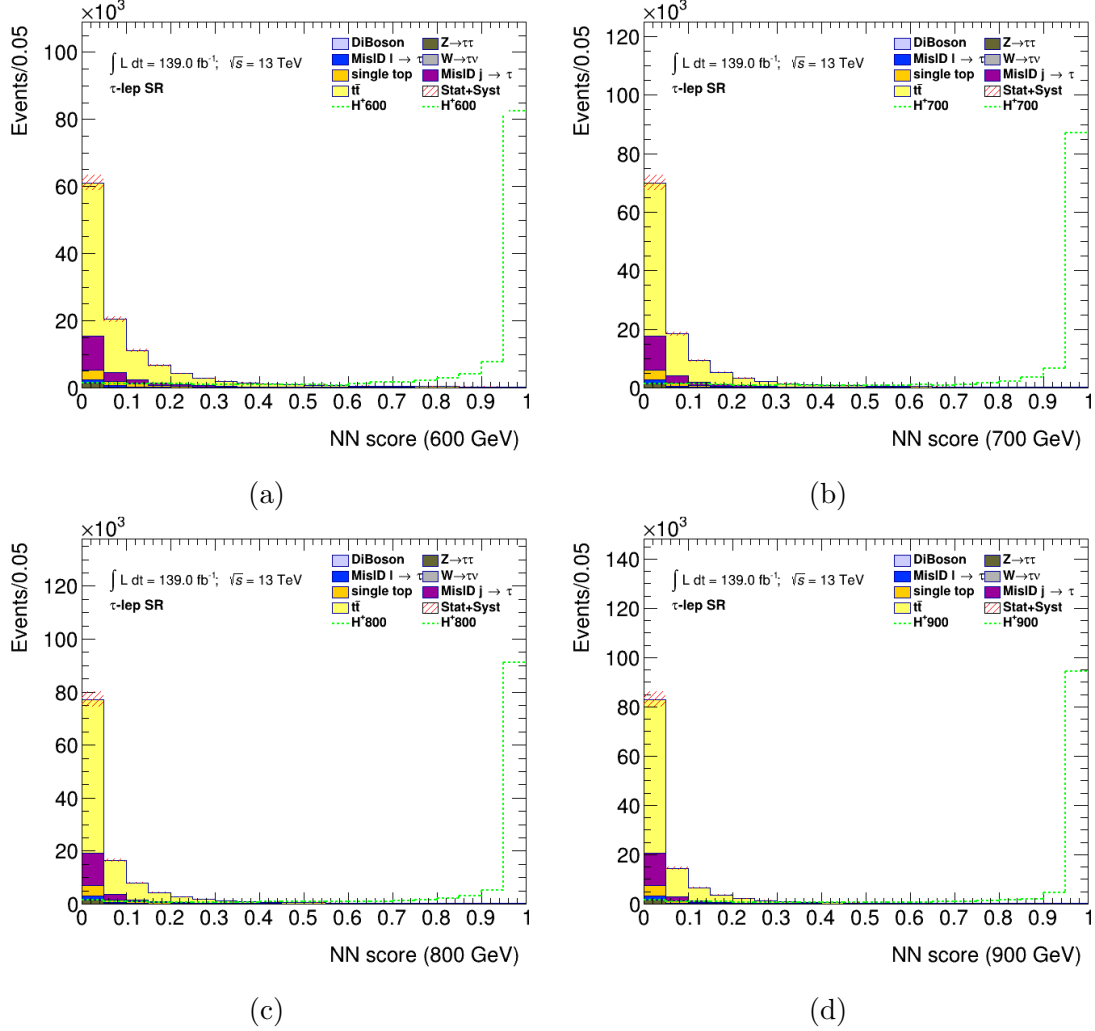


Figure D.15: PNN score distributions in the signal region of the $\tau + \ell$ channel, for the chosen charged Higgs boson mass parameters. The uncertainty bands include all statistical and systematic uncertainties. The normalization of the signal (shown for illustration) corresponds to the integral of the background.

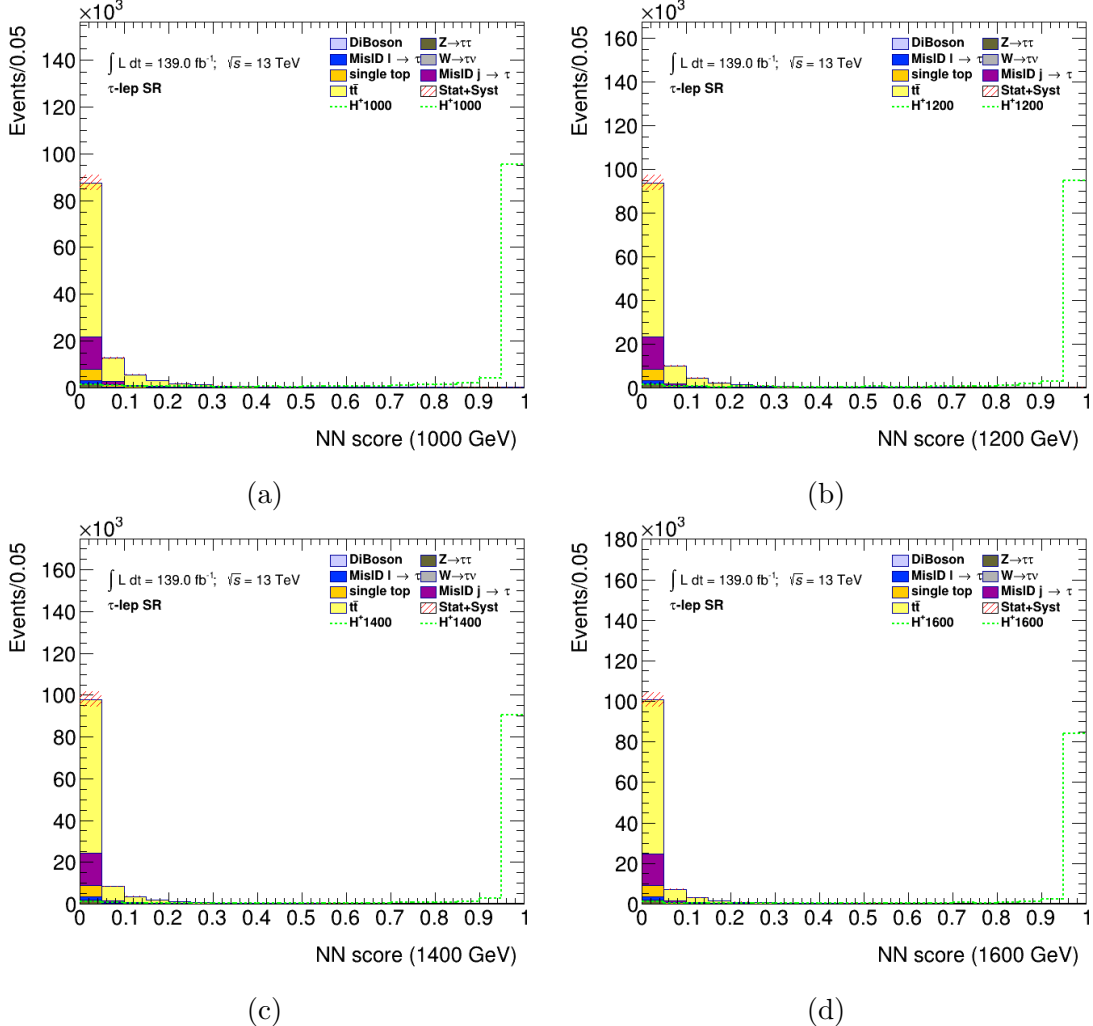


Figure D.16: PNN score distributions in the signal region of the $\tau + \ell$ channel, for the chosen charged Higgs boson mass parameters. The uncertainty bands include all statistical and systematic uncertainties. The normalization of the signal (shown for illustration) corresponds to the integral of the background.

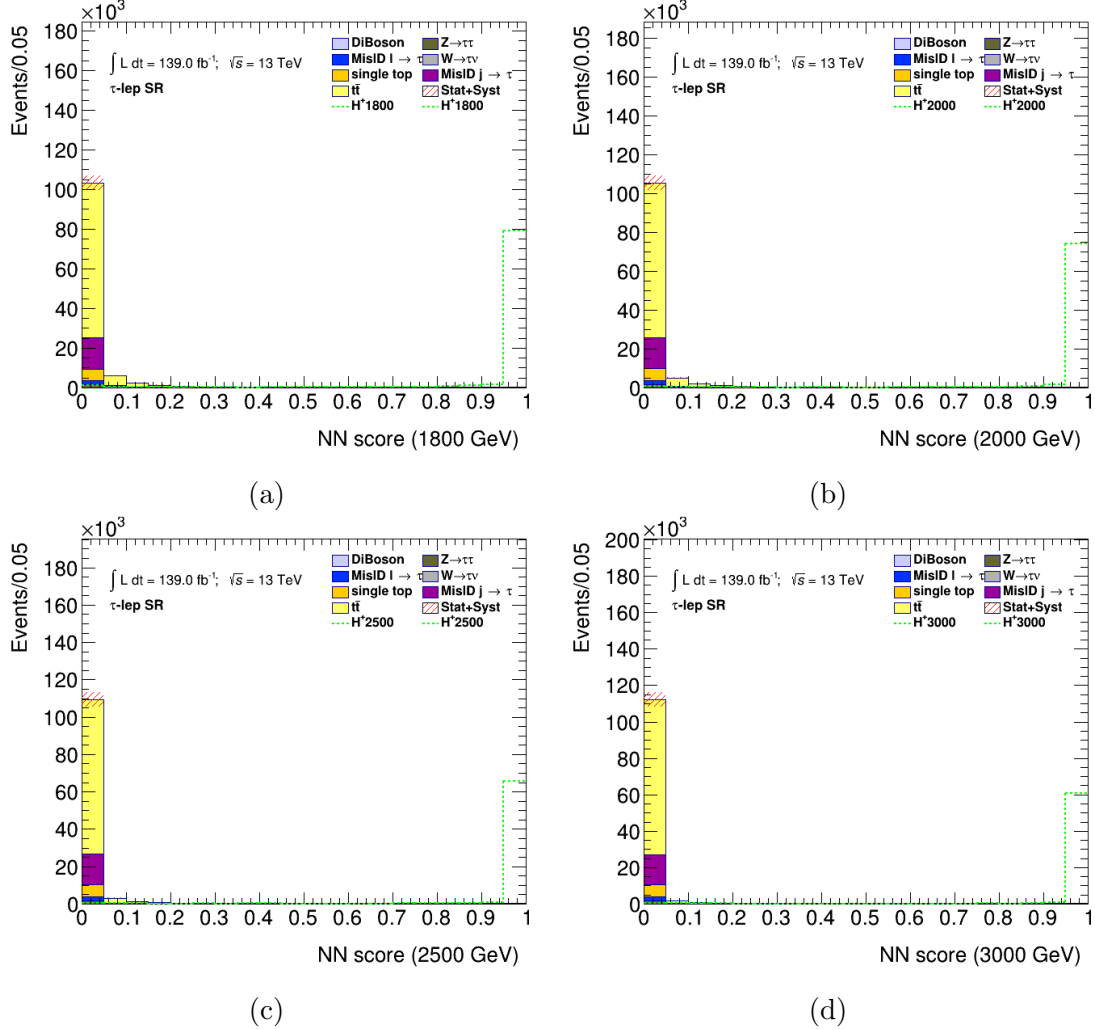


Figure D.17: PNN score distributions in the signal region of the $\tau + \ell$ channel, for the chosen charged Higgs boson mass parameters. The uncertainty bands include all statistical and systematic uncertainties. The normalization of the signal (shown for illustration) corresponds to the integral of the background.

D.3 $\tau + e$ PNN Scores

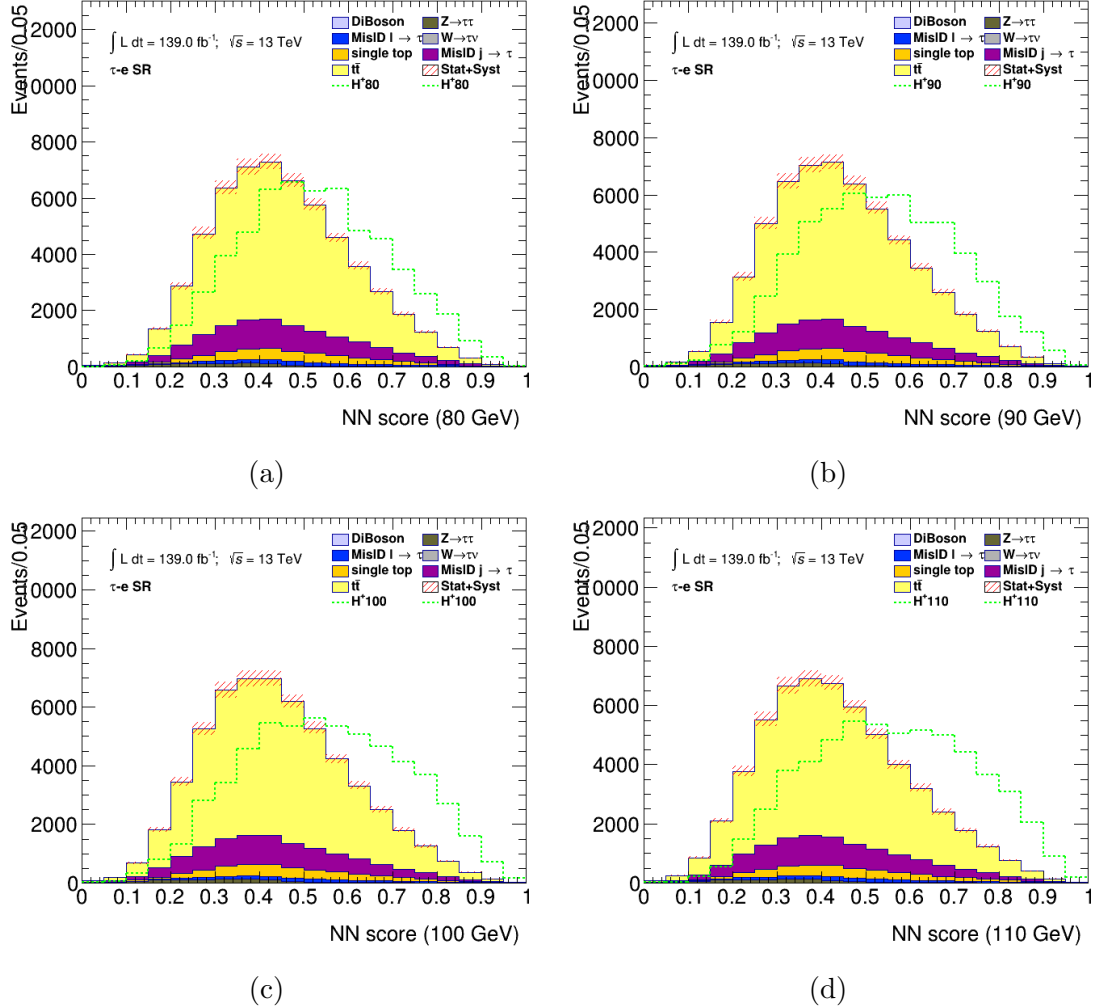


Figure D.18: PNN score distributions in the signal region of the $\tau+e$ channel, for the chosen charged Higgs boson mass parameters. The uncertainty bands include all statistical and systematic uncertainties. The normalization of the signal (shown for illustration) corresponds to the integral of the background.

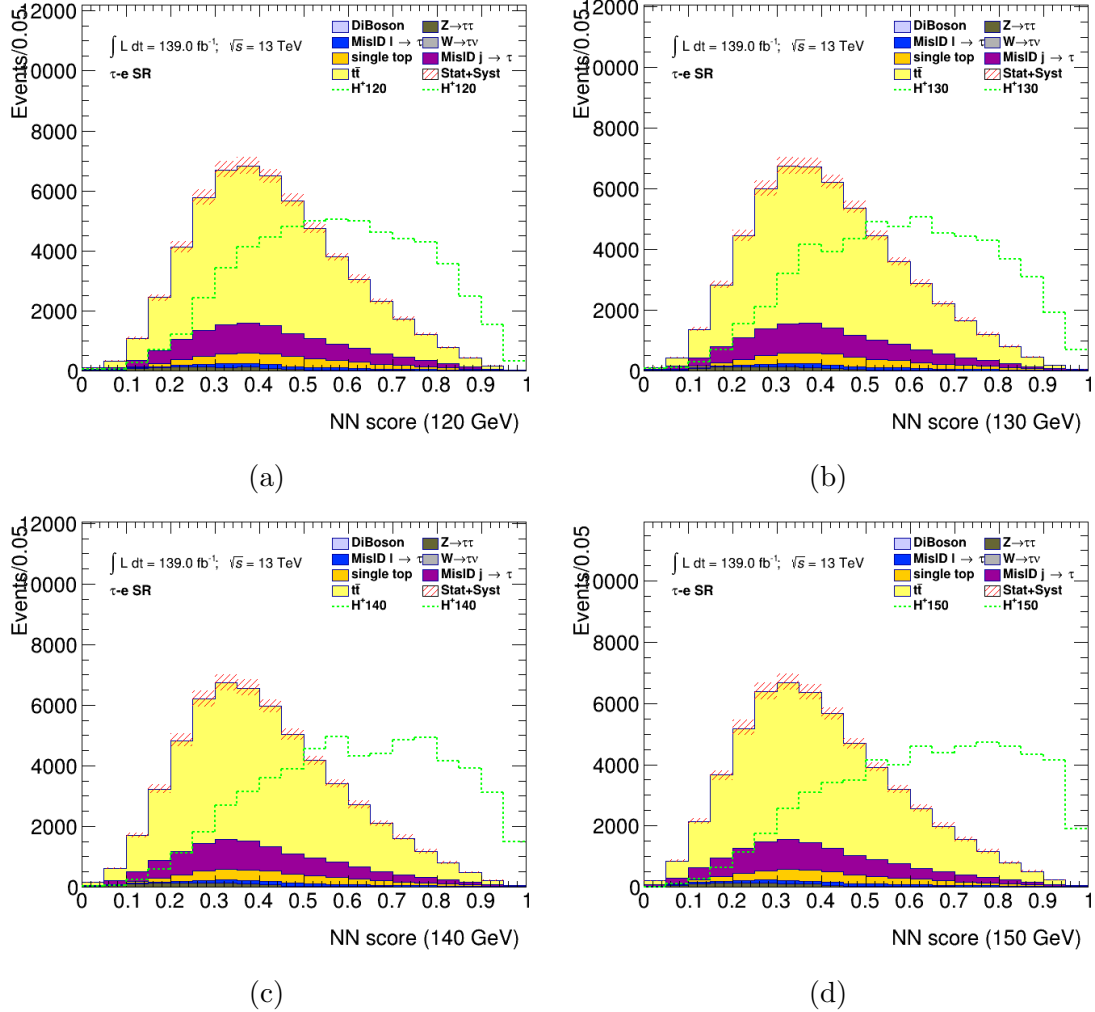


Figure D.19: PNN score distributions in the signal region of the $\tau + e$ channel, for the chosen charged Higgs boson mass parameters. The uncertainty bands include all statistical and systematic uncertainties. The normalization of the signal (shown for illustration) corresponds to the integral of the background.

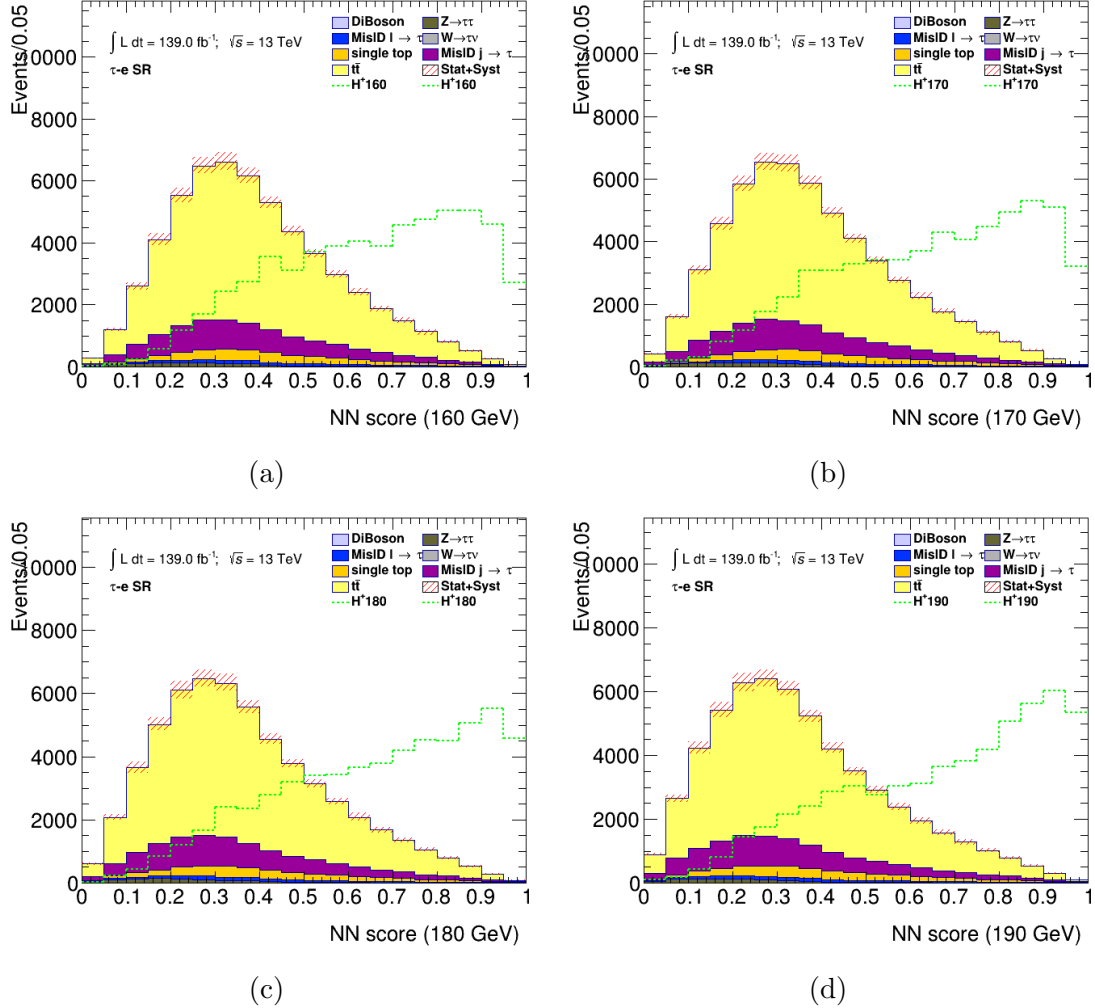


Figure D.20: PNN score distributions in the signal region of the $\tau+e$ channel, for the chosen charged Higgs boson mass parameters. The uncertainty bands include all statistical and systematic uncertainties. The normalization of the signal (shown for illustration) corresponds to the integral of the background.

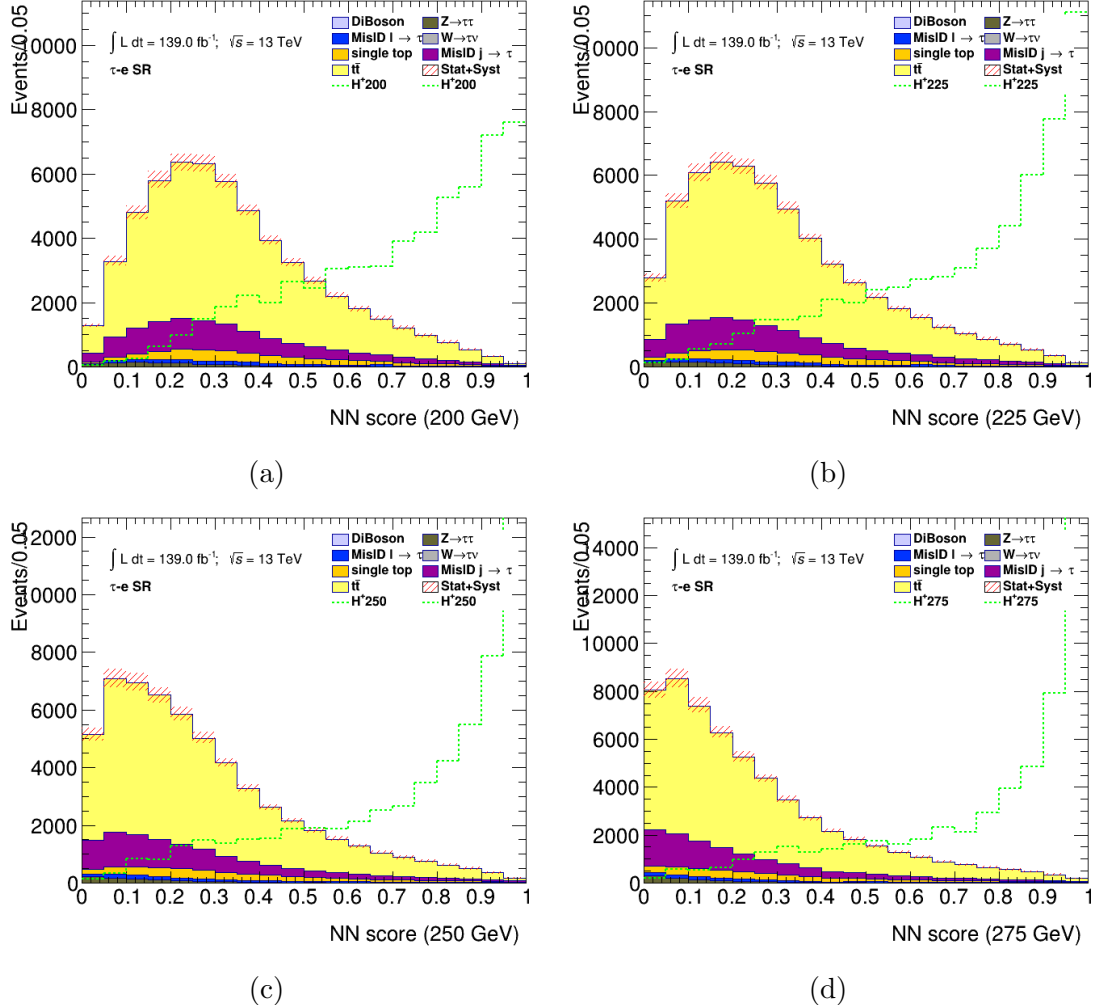


Figure D.21: PNN score distributions in the signal region of the $\tau+e$ channel, for the chosen charged Higgs boson mass parameters. The uncertainty bands include all statistical and systematic uncertainties. The normalization of the signal (shown for illustration) corresponds to the integral of the background.

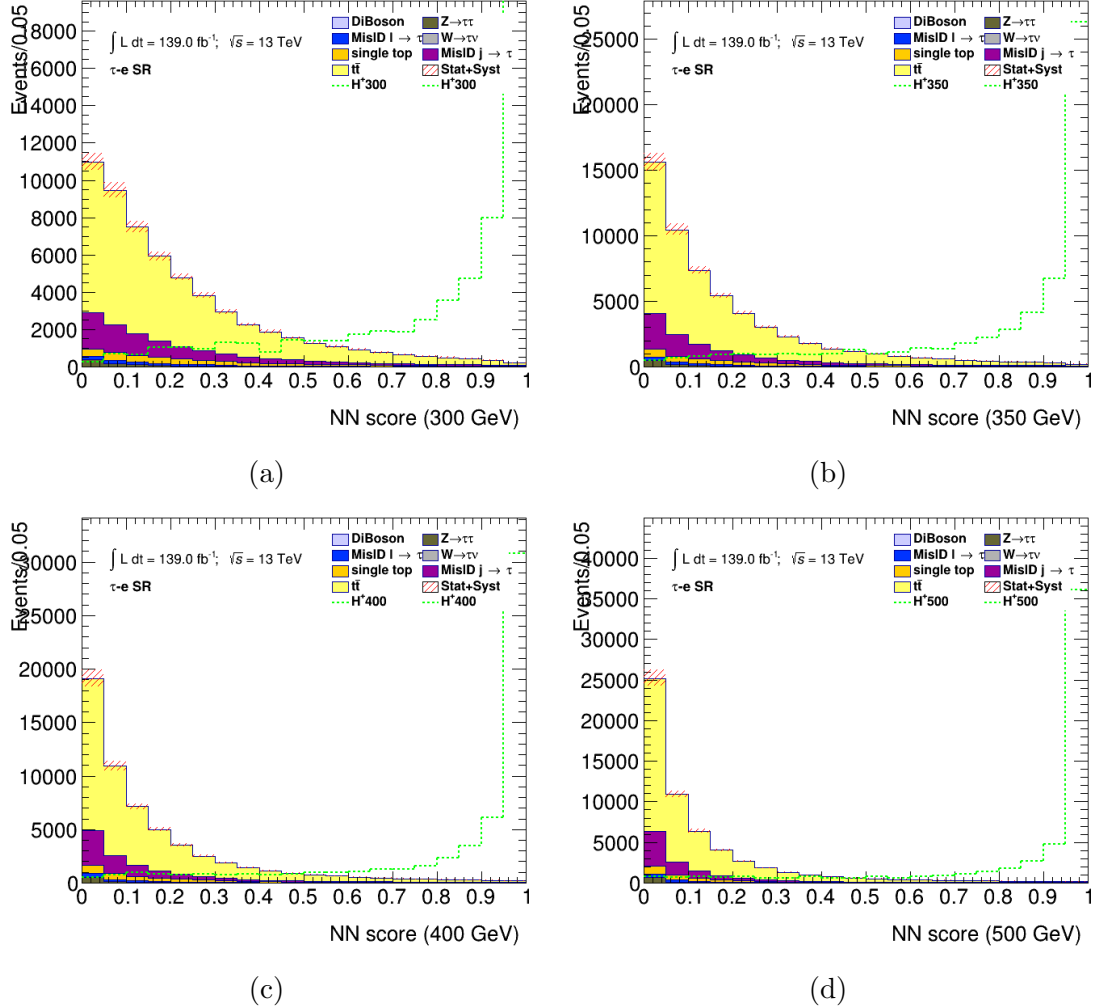


Figure D.22: PNN score distributions in the signal region of the $\tau+e$ channel, for the chosen charged Higgs boson mass parameters. The uncertainty bands include all statistical and systematic uncertainties. The normalization of the signal (shown for illustration) corresponds to the integral of the background.

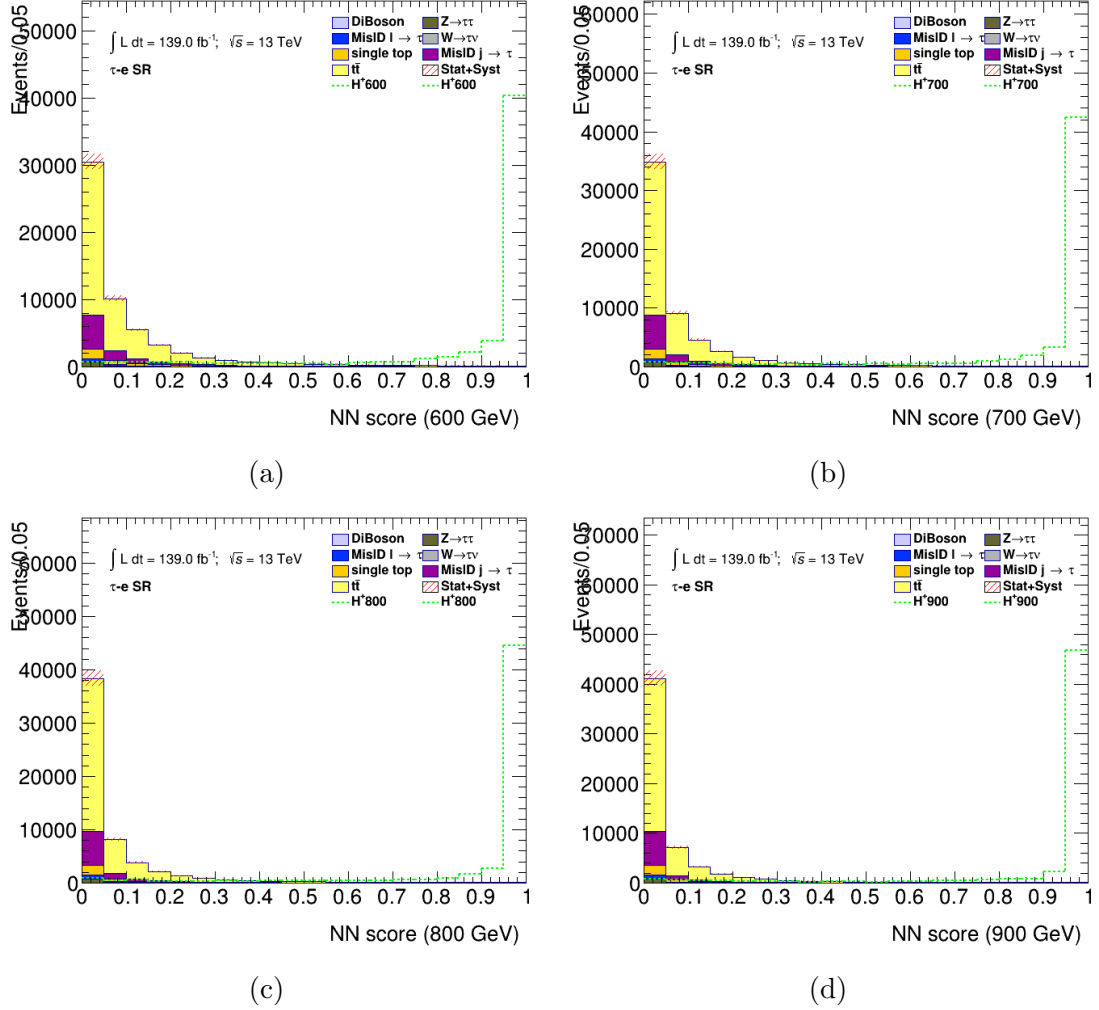


Figure D.23: PNN score distributions in the signal region of the $\tau+e$ channel, for the chosen charged Higgs boson mass parameters. The uncertainty bands include all statistical and systematic uncertainties. The normalization of the signal (shown for illustration) corresponds to the integral of the background.

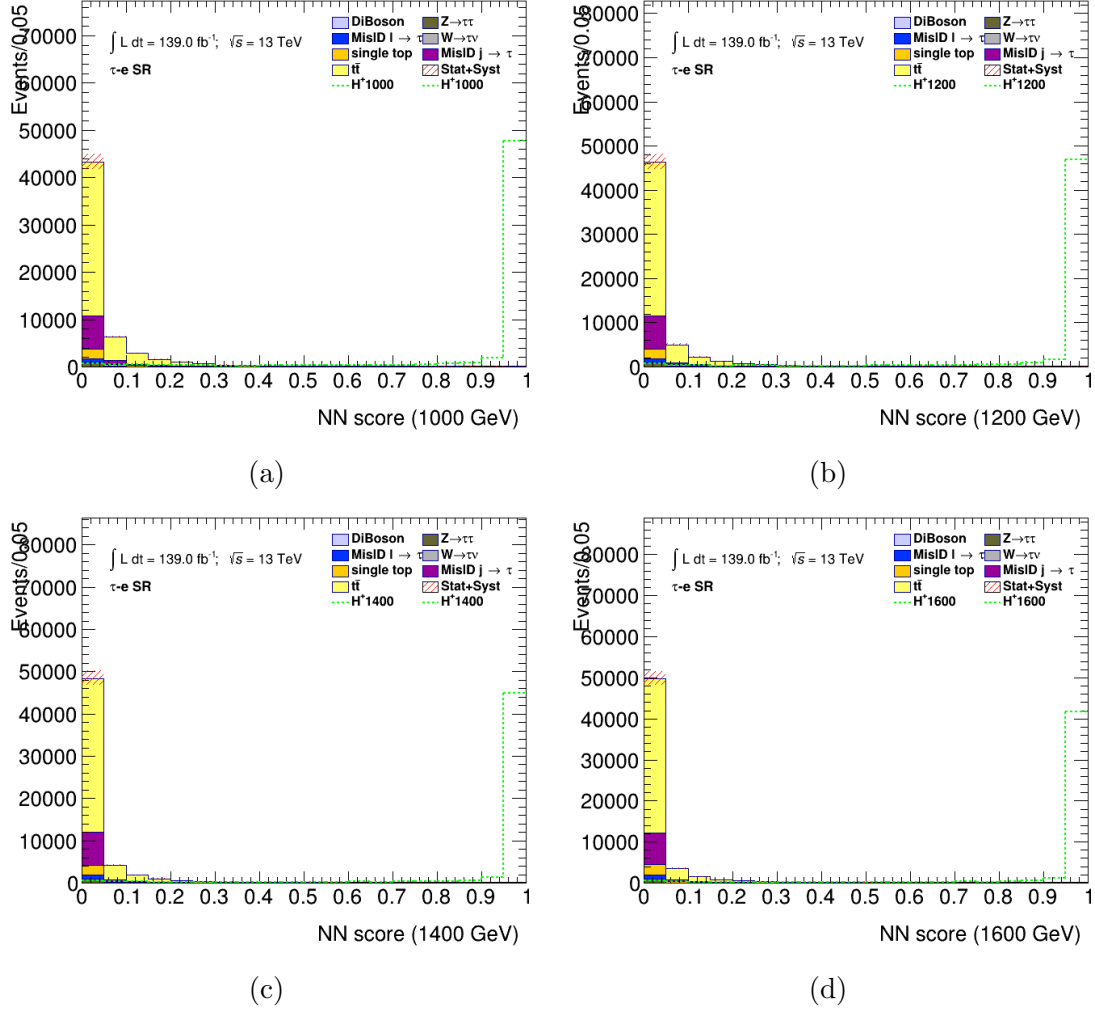


Figure D.24: PNN score distributions in the signal region of the $\tau+e$ channel, for the chosen charged Higgs boson mass parameters. The uncertainty bands include all statistical and systematic uncertainties. The normalization of the signal (shown for illustration) corresponds to the integral of the background.

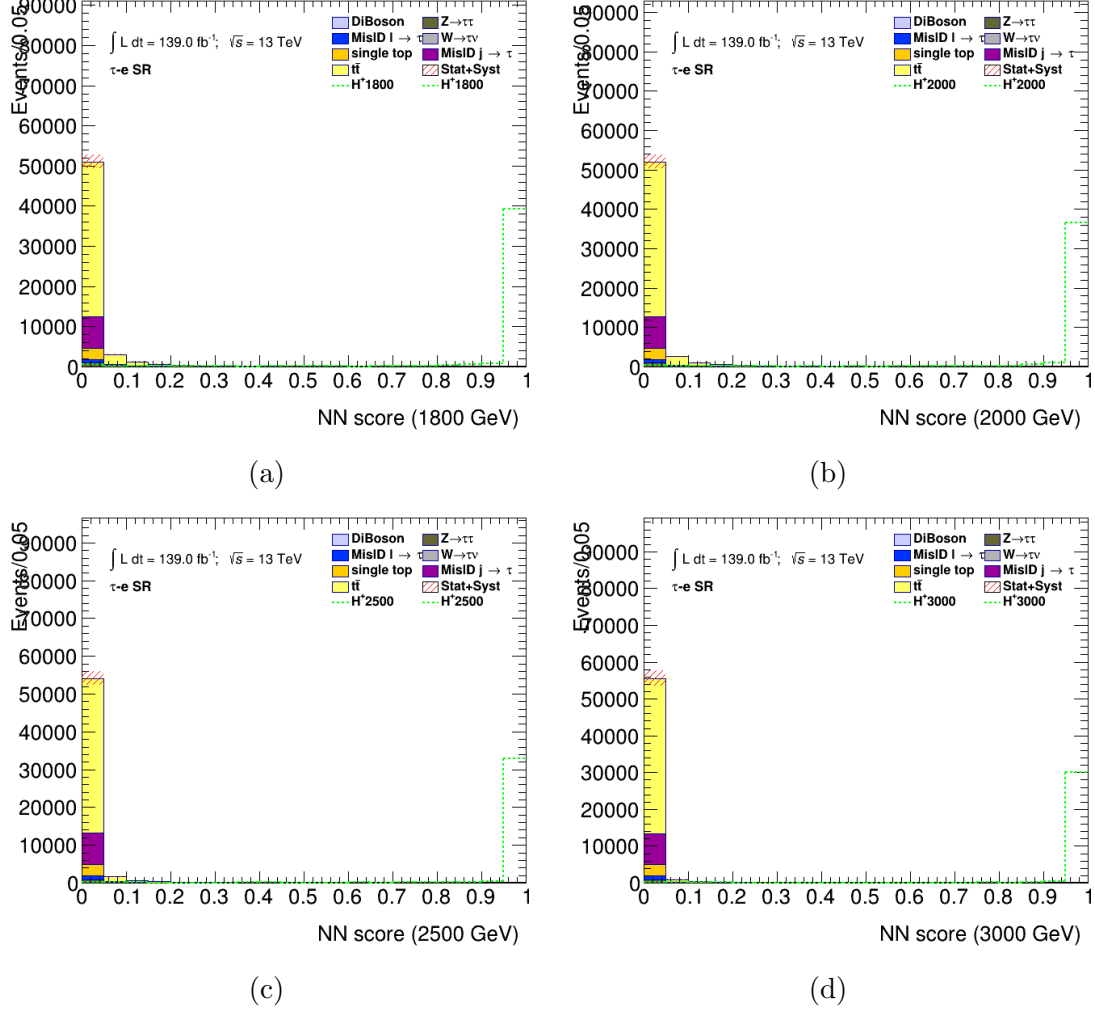


Figure D.25: PNN score distributions in the signal region of the $\tau + e$ channel, for the chosen charged Higgs boson mass parameters. The uncertainty bands include all statistical and systematic uncertainties. The normalization of the signal (shown for illustration) corresponds to the integral of the background.

D.4 $\tau + \mu$ PNN Scores

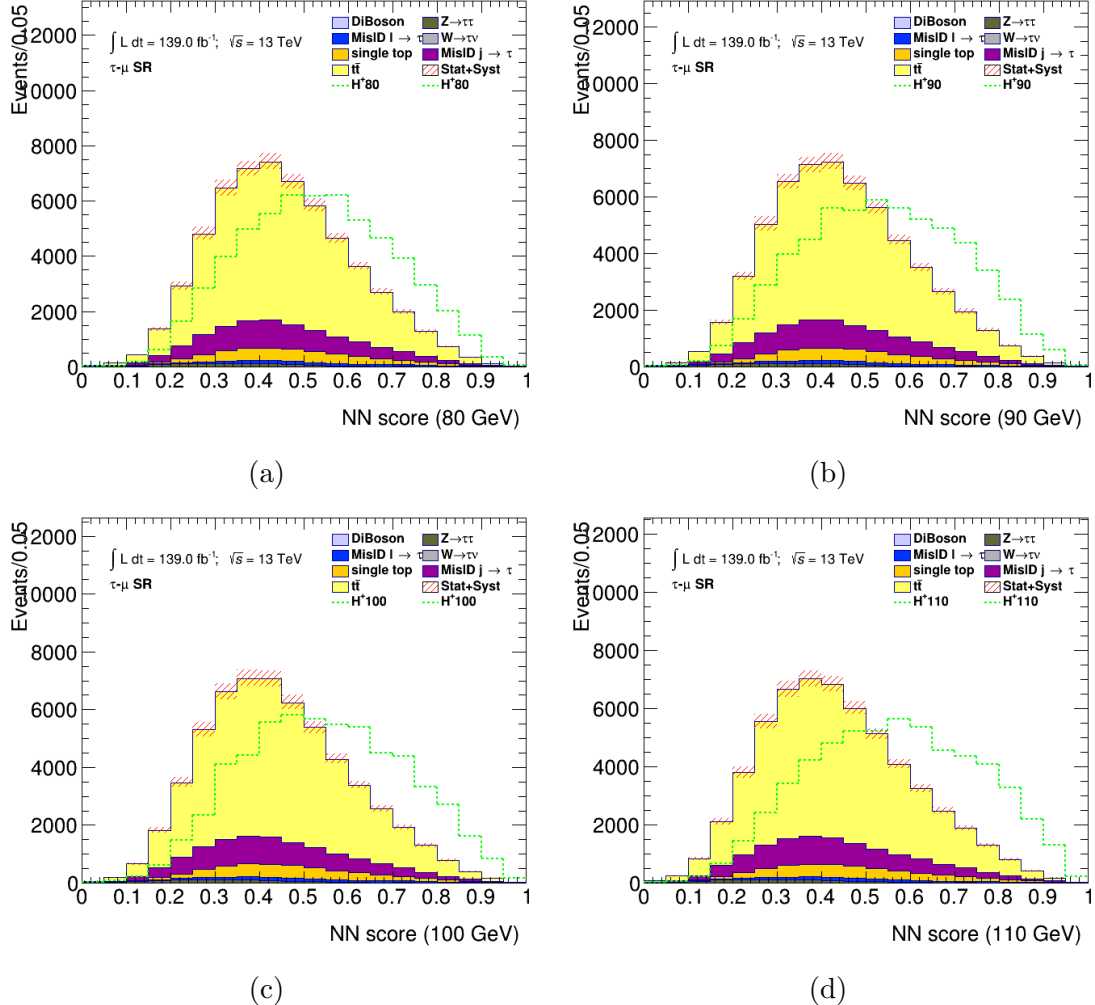


Figure D.26: PNN score distributions in the signal region of the $\tau + \mu$ channel, for the chosen charged Higgs boson mass parameters. The uncertainty bands include all statistical and systematic uncertainties. The normalization of the signal (shown for illustration) corresponds to the integral of the background.

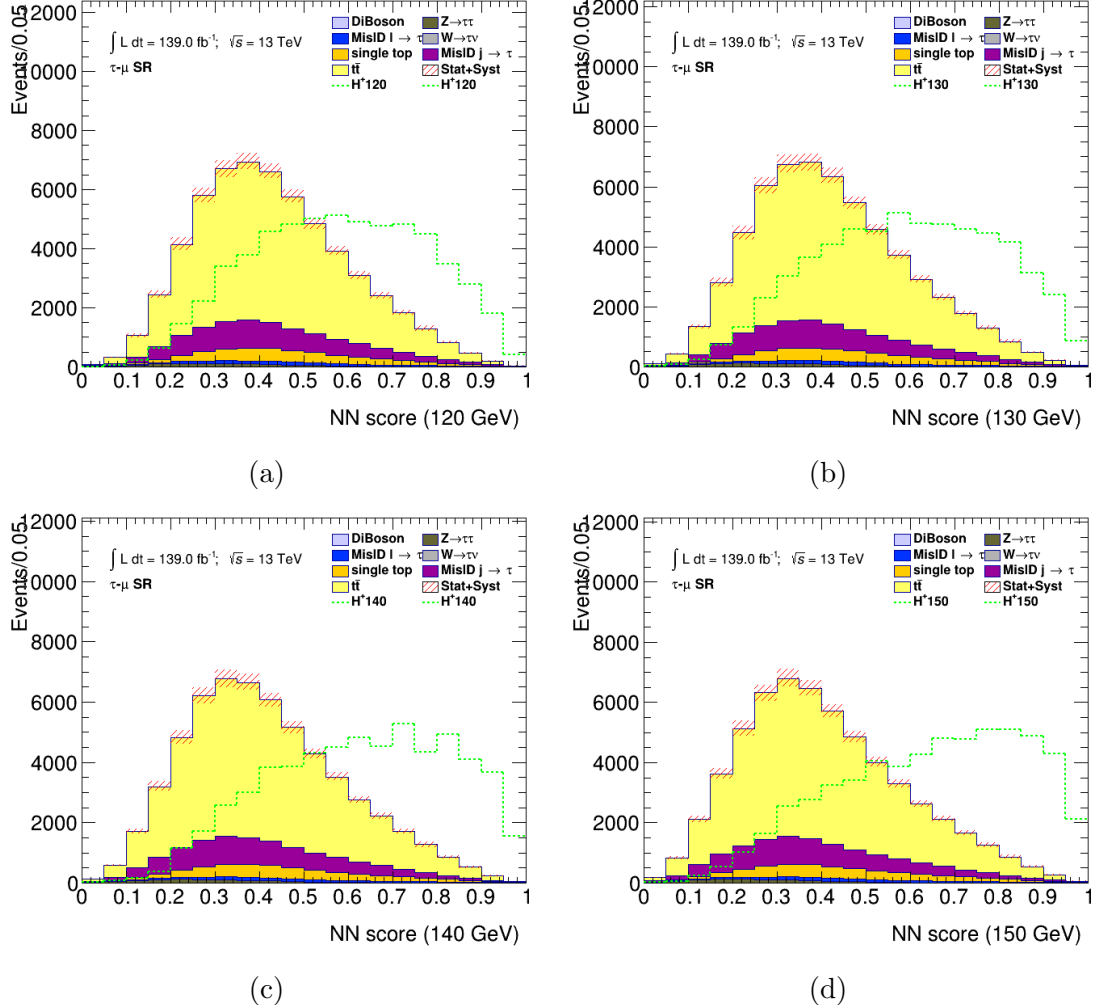


Figure D.27: PNN score distributions in the signal region of the $\tau+\mu$ channel, for the chosen charged Higgs boson mass parameters. The uncertainty bands include all statistical and systematic uncertainties. The normalization of the signal (shown for illustration) corresponds to the integral of the background.

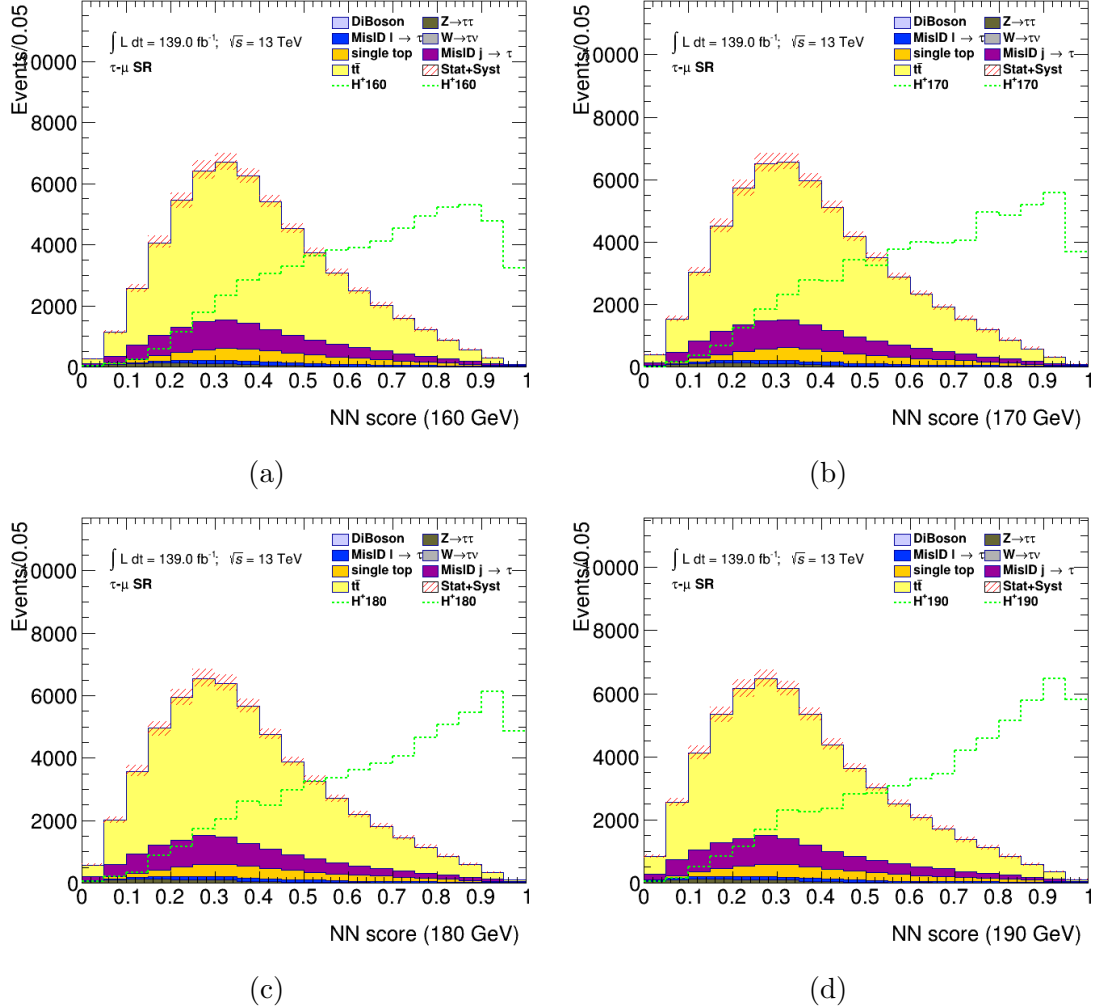


Figure D.28: PNN score distributions in the signal region of the $\tau+\mu$ channel, for the chosen charged Higgs boson mass parameters. The uncertainty bands include all statistical and systematic uncertainties. The normalization of the signal (shown for illustration) corresponds to the integral of the background.

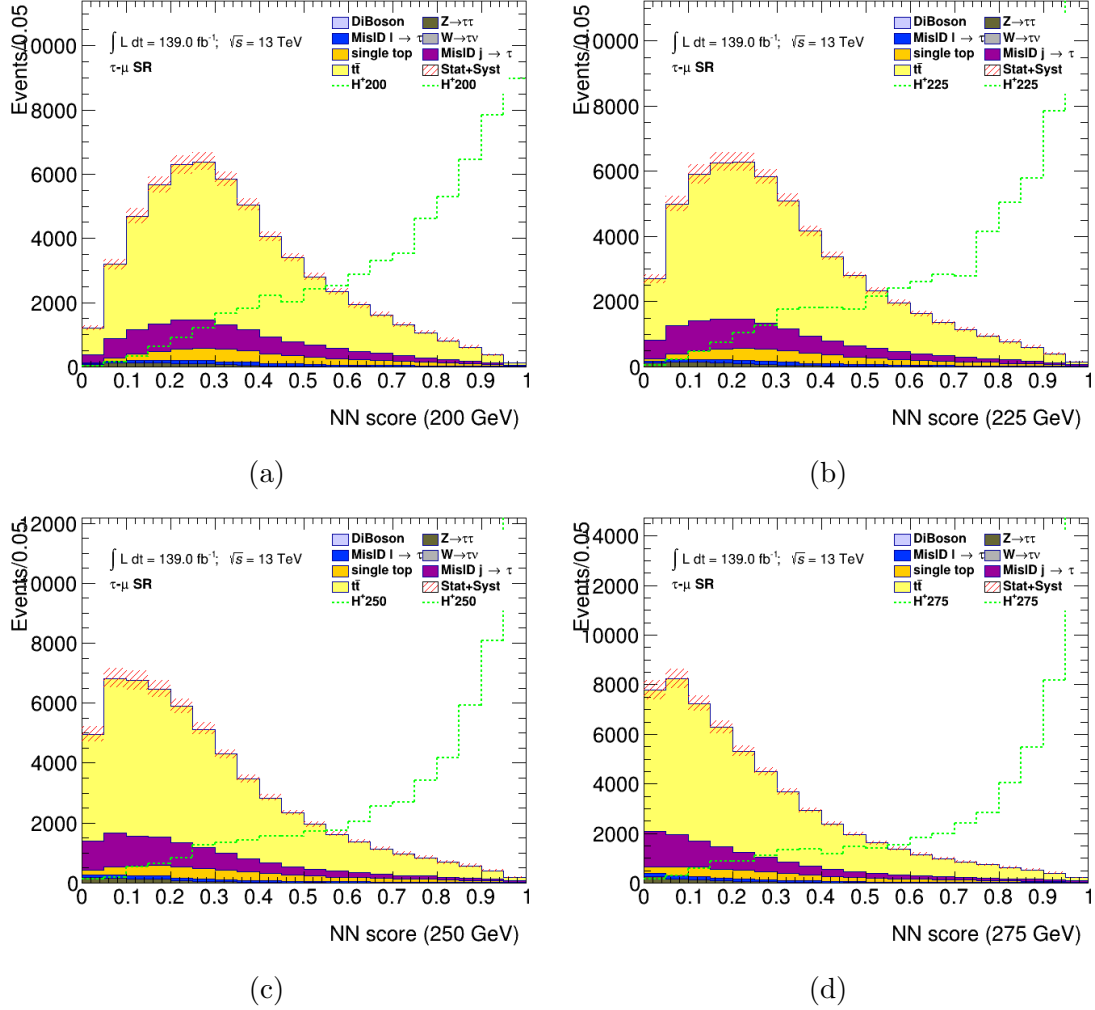


Figure D.29: PNN score distributions in the signal region of the $\tau+\mu$ channel, for the chosen charged Higgs boson mass parameters. The uncertainty bands include all statistical and systematic uncertainties. The normalization of the signal (shown for illustration) corresponds to the integral of the background.

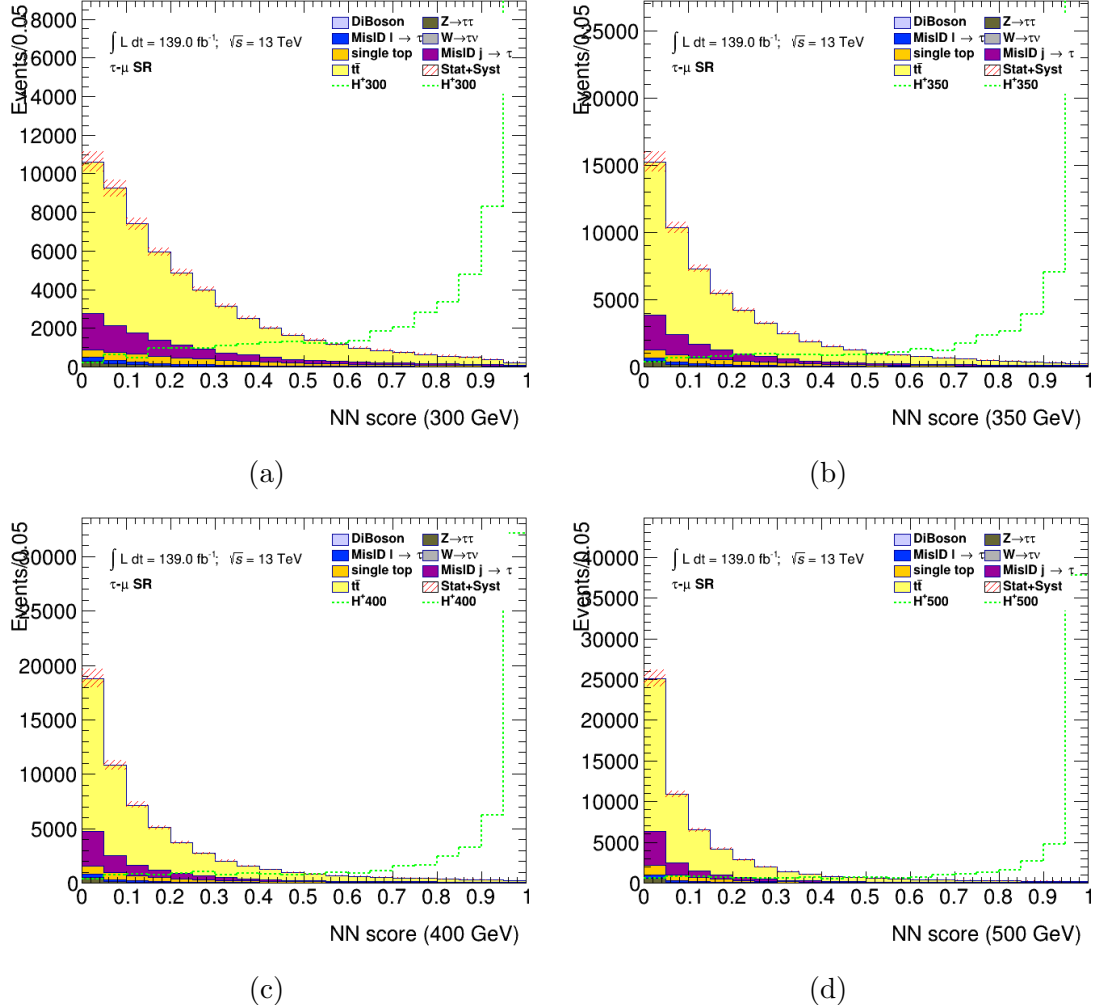


Figure D.30: PNN score distributions in the signal region of the $\tau + \mu$ channel, for the chosen charged Higgs boson mass parameters. The uncertainty bands include all statistical and systematic uncertainties. The normalization of the signal (shown for illustration) corresponds to the integral of the background.

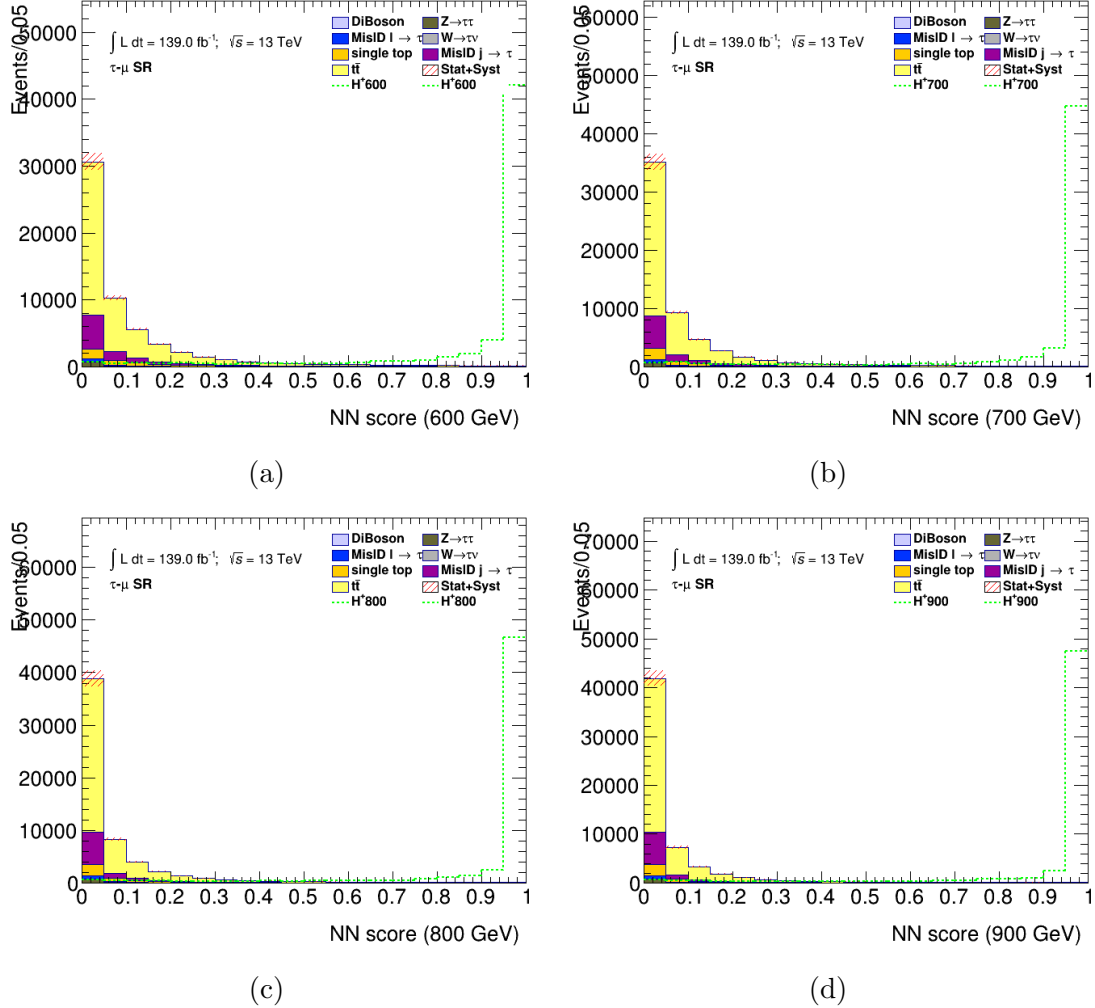


Figure D.31: PNN score distributions in the signal region of the $\tau + \mu$ channel, for the chosen charged Higgs boson mass parameters. The uncertainty bands include all statistical and systematic uncertainties. The normalization of the signal (shown for illustration) corresponds to the integral of the background.

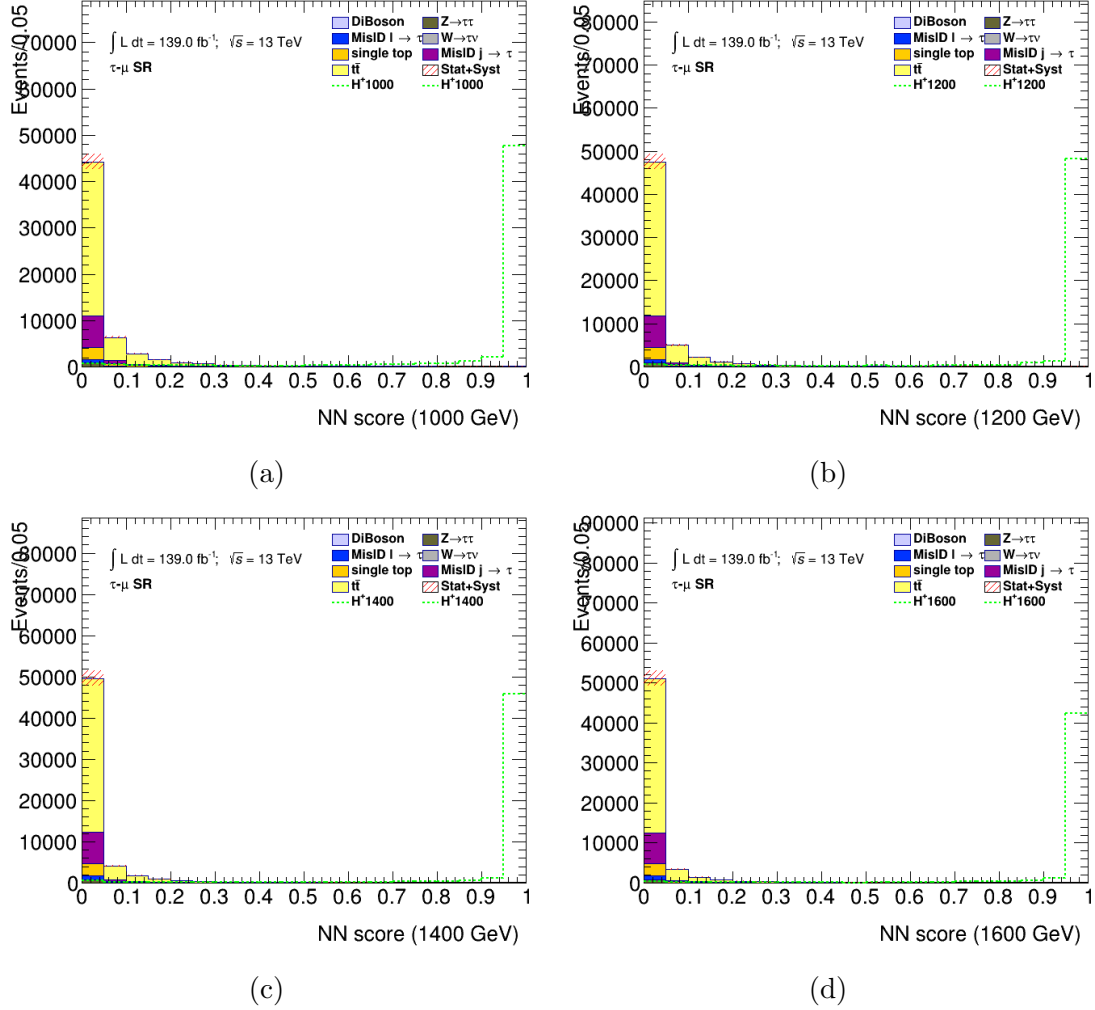


Figure D.32: PNN score distributions in the signal region of the $\tau+\mu$ channel, for the chosen charged Higgs boson mass parameters. The uncertainty bands include all statistical and systematic uncertainties. The normalization of the signal (shown for illustration) corresponds to the integral of the background.

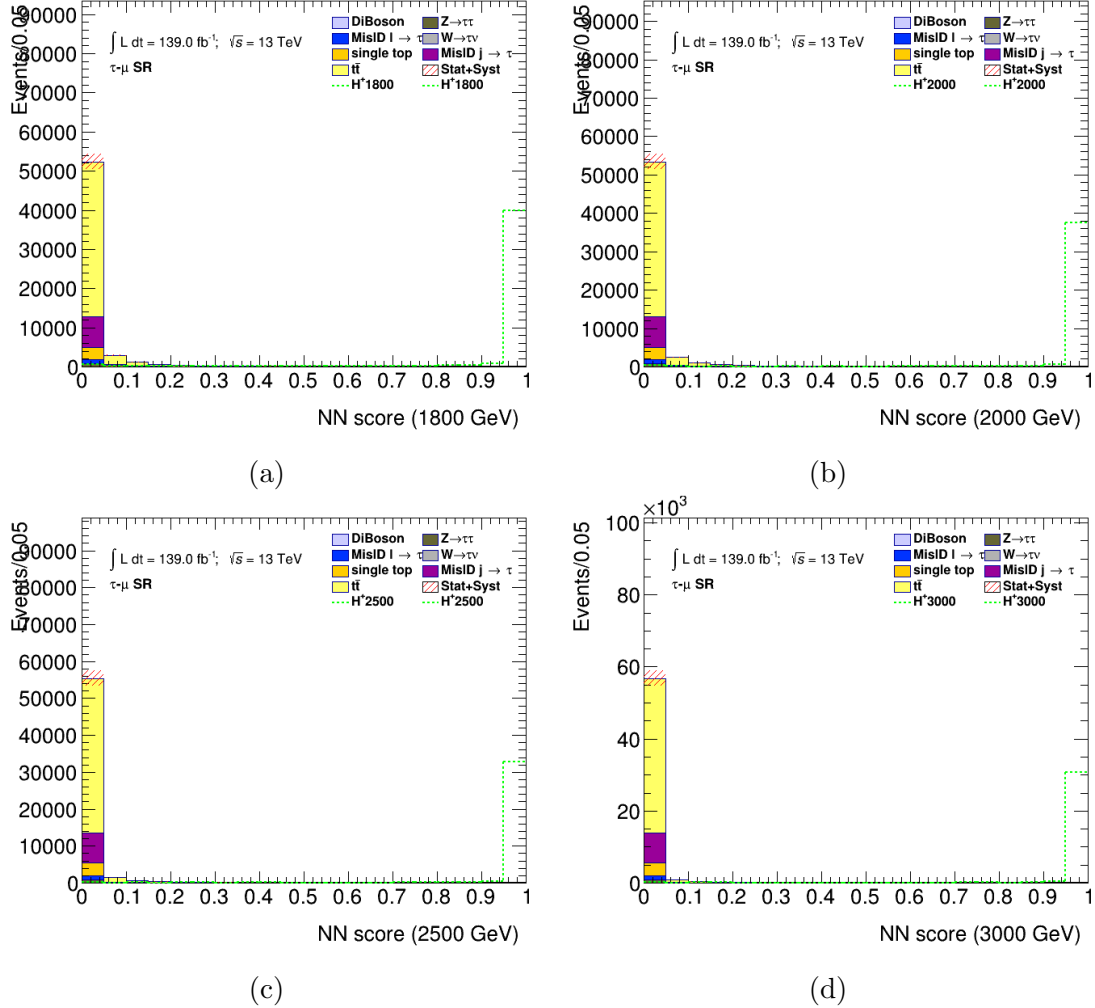


Figure D.33: PNN score distributions in the signal region of the $\tau + \mu$ channel, for the chosen charged Higgs boson mass parameters. The uncertainty bands include all statistical and systematic uncertainties. The normalization of the signal (shown for illustration) corresponds to the integral of the background.

ACRONYMS

2HDM 2-Higgs Doublet Model. ix, 3, 14, 108

ADC Analog to Digital Converter. 113

ATLAS A Toroidal LHC Apparatus. vi, ix, xiii, xiv, 1, 10, 14, 17, 23, 28, 29, 30, 31, 32, 33, 34, 38, 39, 42, 43, 44, 45, 46, 47, 48, 50, 51, 52, 61, 62, 108, 111

AUC Area Under the Curve. xi, xvi, 87, 89, 92, 93

BDT Boosted Decision Tree. xvi, 63, 83, 84

BSM Beyond the Standard Model. 1

CB Combined μ Identification Strategy. 52

CERN Conseil Européen pour la Recherche Nucléaire. 1, 10, 23

CIS Charge Injection System. 112

CMS Compact Muon Solenoid. 10, 14, 23, 30

CR Control Region. 63, 67, 74, 99, 119

CSC Cathode Strip Chamber. 43

CT Calorimeter-Tagged μ Identification Strategy. 53

DQ Data Quality. 111

DQM Data Quality Monitoring. 111

EM Electromagnetism. 5, 6, 7, 39, 40, 54, 112

EMB LAr Electromagnetic Main Barrel. xiv, 39, 40

EMEC LAr Electromagnetic End-Cap. 39, 40

FCAL LAr Forward Calorimeter. 39, 40

FF Fake Factor. xv, 74, 75

HEC LAr Hadronic End-Cap. 39

HLT High Level Trigger. 44

HPO Hyperparameter Optimization. xi, 87, 92

IBL Insertable B Layer. 35, 36

ID Inner Detector. 33, 34, 35, 36, 51, 52, 53, 54, 61

IO Inside-Out μ Identification Strategy. 53

IOV Interval of Validity. 112

IP Interaction Point. xiv, 31, 34, 35, 36, 41, 60

L1 Trigger Level-1 Trigger. 44

LAr Liquid Argon. 38, 39, 40, 204, 205

LB Luminosity Block. 111, 112

LHC Large Hadron Collider. ix, xiii, 1, 23, 24, 26, 29, 30, 31, 43, 111, 112

LL Leading-Logarithmic Order. 46

LO Leading Order. 46, 70

MC Monte Carlo. ix, 46, 47, 48, 50, 69, 71, 73, 76, 83, 85

MDT Monitored Drift Tube. 42, 43

ME Matrix Element. 46

MS Muon Spectrometer. 42, 43, 52, 53

MSSM Minimal Supersymmetric Standard Model. v, ix, xii, xiii, 3, 12, 13, 14, 15, 16, 17, 21, 87

MVA Multivariate Analysis Technique. 63

NLO Next-to-Leading Order. 46, 69

NN Neural Network. 83

PDF Parton Distribution Function. 46, 69, 70

PMT Photomultiplier Tube. 42, 112

PNN Parameterized Neural Network. 1, x, xvi, xvii, xxiv, xxv, xxvi, xxvii, xxviii, xxix, 63, 83, 84, 85, 86, 87, 88, 89, 99, 101, 102, 103, 104, 105, 106, 108, 165, 167, 168, 169, 170, 171, 172, 173, 174, 175, 177, 178, 179, 180, 181, 182, 183, 184, 186, 187, 188, 189, 190, 191, 192, 193, 195, 196, 197, 198, 199, 200, 201, 202

QCD Quantum Chromodynamics. 6, 7, 63, 74

QED Quantum Electrodynamics. 6

QFT Quantum Field Theory. 3, 5, 6, 7

RNN Recurrent Neural Network. 61, 74

RPC Resistive Plate Chamber. 42, 43

SCT Semiconductor Tracker. 34, 36, 51

SM Standard Model. ix, x, xvi, xvii, 1, 3, 4, 5, 6, 8, 9, 10, 11, 12, 13, 15, 22, 48, 61, 71, 101, 102, 103, 104, 105, 106, 108

SR Signal Region. xi, 63, 94, 95, 96, 99, 108, 119

ST Segmented-tagged μ Identification Strategy. 53

SUSY Supersymmetry. 3, 11, 12, 16

TDAQ Trigger and Data Acquisition. xiv, 30, 44, 45

TGC Thin Gap Chamber. 43

TileCal Tile Calorimeter. xiv, xviii, 41, 42, 111, 112, 113, 114, 115

TRT Transition Radiation Tracker. 35, 36, 37, 38, 51

VEV Vacuum Expectation Value. 8

WP Working Point. 53, 54, 55, 61

BIBLIOGRAPHY

- [1] D. Hemphill. *The behavior of the primordial universe*. Apr. 2020.
URL: https://www.physics.purdue.edu/about/prizes_awards/charlotte_ida_litman_tubis_award/2017_behavior_primordial_universe.html.
- [2] R. L. Workman et al. “Review of Particle Physics”. *PTEP* 2022 (2022), p. 083C01.
DOI: 10.1093/ptep/ptac097.
- [3] P. W. Higgs. “Broken Symmetries and the Masses of Gauge Bosons”.
Phys. Rev. Lett. 13 (16 Oct. 1964), pp. 508–509. DOI: 10.1103/PhysRevLett.13.508.
URL: <https://link.aps.org/doi/10.1103/PhysRevLett.13.508>.
- [4] F. Englert and R. Brout. “Broken Symmetry and the Mass of Gauge Vector Mesons”.
Phys. Rev. Lett. 13 (9 Aug. 1964), pp. 321–323. DOI: 10.1103/PhysRevLett.13.321.
URL: <https://link.aps.org/doi/10.1103/PhysRevLett.13.321>.
- [5] J. Ellis. “Higgs Physics” (Dec. 2013). 52 pages, 45 figures, Lectures presented at the ESHEP 2013 School of High-Energy Physics, to appear as part of the proceedings in a CERN Yellow Report, 117–168. 52 p. DOI: 10.5170/CERN-2015-004.117.
arXiv: 1312.5672. URL: <https://cds.cern.ch/record/1638469>.
- [6] ATLAS Collaboration. “Observation of a new particle in the search for the Standard Model Higgs boson with the ATLAS detector at the LHC”.
Physics Letters B 716.1 (2012), pp. 1–29.
- [7] CMS Collaboration. “Observation of a new boson at a mass of 125 GeV with the CMS experiment at the LHC”. *Physics Letters B* 716.1 (Sept. 2012), pp. 30–61.
DOI: 10.1016/j.physletb.2012.08.021.
URL: <https://doi.org/10.1016%2Fj.physletb.2012.08.021>.
- [8] G. Branco et al. “Theory and phenomenology of two-Higgs-doublet models”.
Physics Reports 516.1–2 (July 2012), pp. 1–102. ISSN: 0370-1573.

DOI: 10.1016/j.physrep.2012.02.002.

URL: <http://dx.doi.org/10.1016/j.physrep.2012.02.002>.

- [9] ATLAS Collaboration. *Summary plots for beyond Standard Model Higgs boson benchmarks for direct and indirect searches*. Tech. rep.
All figures including auxiliary figures are available at
<https://atlas.web.cern.ch/Atlas/GROUPS/PHYSICS/PUBNOTES/ATL-PHYS-PUB-2022-043>. Geneva: CERN, 2022. URL: <http://cds.cern.ch/record/2827098>.
- [10] ATLAS Collaboration. “Search for charged Higgs bosons decaying via $H^\pm \rightarrow \tau^\pm \nu_\tau$ in the $\tau + \text{jets}$ and $\tau + \text{lepton}$ final states with 36 fb^{-1} of pp collision data recorded at $\sqrt{s} = 13 \text{ TeV}$ with the ATLAS experiment”. *JHEP* 09 (2018), p. 139.
DOI: 10.1007/JHEP09(2018)139. arXiv: 1807.07915 [hep-ex].
- [11] C. T. Potter et al. *Handbook of LHC Higgs Cross Sections: 3. Higgs Properties: Report of the LHC Higgs Cross Section Working Group*. en. 2013.
DOI: 10.5170/CERN-2013-004. URL: <http://cds.cern.ch/record/1559921>.
- [12] M. Carena et al. “MSSM Higgs boson searches at the LHC: benchmark scenarios after the discovery of a Higgs-like particle”.
The European Physical Journal C 73.9 (Sept. 2013).
DOI: 10.1140/epjc/s10052-013-2552-1.
URL: <https://doi.org/10.1140%2Fepjc%2Fs10052-013-2552-1>.
- [13] A. Djouadi et al. “The post-Higgs MSSM scenario: habemus MSSM?”
The European Physical Journal C 73.12 (Nov. 2013).
DOI: 10.1140/epjc/s10052-013-2650-0.
URL: <https://doi.org/10.1140%2Fepjc%2Fs10052-013-2650-0>.
- [14] CMS Collaboration. “Search for charged Higgs bosons in the $H^\pm \rightarrow \tau^\pm \nu_\tau$ decay channel in proton-proton collisions at $\sqrt{s} = 13 \text{ TeV}$ ”.

Journal of High Energy Physics 2019.7 (July 2019). DOI: 10.1007/jhep07(2019)142.
 URL: <https://doi.org/10.1007%2Fjhep07%282019%29142>.

- [15] ATLAS Collaboration. “Search for charged Higgs bosons decaying into a top quark and a bottom quark at $\sqrt{s} = 13$ TeV with the ATLAS detector”.
Journal of High Energy Physics 2021.6 (2021), p. 145.
 DOI: 10.1007/JHEP06(2021)145.
 URL: [https://doi.org/10.1007/JHEP06\(2021\)145](https://doi.org/10.1007/JHEP06(2021)145).
- [16] L. R. Evans and P. Bryant. “LHC Machine”. *JINST* 3 (2008). This report is an abridged version of the LHC Design Report (CERN-2004-003), S08001. 164 p.
 DOI: 10.1088/1748-0221/3/08/S08001.
 URL: <https://cds.cern.ch/record/1129806>.
- [17] CERN. *Facts and figures about the LHC*.
 URL: <https://home.cern/resources/faqs/facts-and-figures-about-lhc>.
- [18] X. C. Vidal and R. C. Manzano. *Lorentz Force Taking a closer look at LHC*. URL:
https://www.lhc-closer.es/taking_a_closer_look_at_lhc/0.lorentz_force.
- [19] E. Lopienska. “The CERN accelerator complex, layout in 2022. Complexe des accélérateurs du CERN en janvier 2022” (Feb. 2022). General Photo.
 URL: <https://cds.cern.ch/record/2800984>.
- [20] ATLAS Collaboration. *Public atlas luminosity results for run-2 of the LHC*.
 URL: https://twiki.cern.ch/twiki/bin/view/AtlasPublic/LuminosityPublicResultsRun2#Integrated_and_Instantaneous_Lum.
- [21] ATLAS Collaboration.
Event displays from run 2 physics analyses not included in publications. URL: <https://twiki.cern.ch/twiki/bin/view/AtlasPublic/EventDisplayRun2Physics>.

- [22] ATLAS Collaboration. “The ATLAS Experiment at the CERN Large Hadron Collider”. *JINST* 3 (2008). Also published by CERN Geneva in 2010, S08003. 437 p. DOI: 10.1088/1748-0221/3/08/S08003. URL: <https://cds.cern.ch/record/1129811>.
- [23] ATLAS Collaboration. *Atlas schematics*. URL: <https://atlas.cern/Resources/Schematics>.
- [24] *Pseudorapidity*. Wikipedia, Feb. 2009. URL: <https://en.wikipedia.org/wiki/File:Pseudorapidity2.png>.
- [25] ATLAS Collaboration. *ATLAS central solenoid: Technical Design Report*. Technical design report. ATLAS. Electronic version not available. Geneva: CERN, 1997. DOI: 10.17181/CERN.ZZVJ.2JYE. URL: <https://cds.cern.ch/record/331067>.
- [26] ATLAS Collaboration. *ATLAS tile calorimeter: Technical Design Report*. Technical design report. ATLAS. Geneva: CERN, 1996. DOI: 10.17181/CERN.JRBJ.7028. URL: <https://cds.cern.ch/record/331062>.
- [27] J. P. Badiou et al. *ATLAS barrel toroid: Technical Design Report*. Technical design report. ATLAS. Electronic version not available. Geneva: CERN, 1997. DOI: 10.17181/CERN.RF2A.CP5T. URL: <https://cds.cern.ch/record/331065>.
- [28] ATLAS Collaboration. *ATLAS inner detector: Technical Design Report, 1*. Technical design report. ATLAS. Geneva: CERN, 1997. URL: <https://cds.cern.ch/record/331063>.

- [29] ATLAS Collaboration. “Performance of the ATLAS Inner Detector Track and Vertex Reconstruction in the High Pile-Up LHC Environment” (Mar. 2012). All figures including auxiliary figures are available at <https://atlas.web.cern.ch/Atlas/GROUPS/PHYSICS/CONFNOTES/ATLAS-CONF-2012-042>. URL: <https://cds.cern.ch/record/1435196>.
- [30] N. Wermes and G. Hallewel. *ATLAS pixel detector: Technical Design Report*. Technical design report. ATLAS. Geneva: CERN, 1998.
URL: <https://cds.cern.ch/record/381263>.
- [31] M. Capeans et al. “ATLAS Insertable B-Layer Technical Design Report” (Sept. 2010).
URL: <https://cds.cern.ch/record/1291633>.
- [32] ATLAS Collaboration. *ATLAS liquid-argon calorimeter: Technical Design Report*. Technical design report. ATLAS. Geneva: CERN, 1996.
DOI: 10.17181/CERN.FWRW.F00Q. URL: <https://cds.cern.ch/record/331061>.
- [33] ATLAS Collaboration.
“The ATLAS Experiment at the CERN Large Hadron Collider”.
Journal of Instrumentation 3.08 (Aug. 2008), S08003–S08003.
DOI: 10.1088/1748-0221/3/08/s08003.
URL: <https://doi.org/10.1088/1748-0221/3/08/s08003>.
- [34] ATLAS Collaboration. *ATLAS muon spectrometer: Technical Design Report*. Technical design report. ATLAS. Geneva: CERN, 1997.
URL: <https://cds.cern.ch/record/331068>.
- [35] ATLAS Collaboration. “Operation of the ATLAS trigger system in Run 2”.
Journal of Instrumentation 15.10 (Oct. 2020), P10004–P10004.
DOI: 10.1088/1748-0221/15/10/p10004.
URL: <https://doi.org/10.1088/1748-0221/15/10/p10004>.

- [36] ATLAS Collaboration. *ATLAS DAQ Approved Plots*. URL: <https://twiki.cern.ch/twiki/bin/view/AtlasPublic/ApprovedPlotsDAQ>.
- [37] C. Wanotayaroj. “Search for a Scalar Partner of the Top Quark in the Jets+MET Final State with the ATLAS detector”. Presented 25 Oct 2016. Nov. 2016. URL: <http://cds.cern.ch/record/2242196>.
- [38] C. Bierlich et al. *A comprehensive guide to the physics and usage of PYTHIA 8.3*. 2022. DOI: 10.48550/ARXIV.2203.11601. URL: <https://arxiv.org/abs/2203.11601>.
- [39] S. Alioli et al. “A general framework for implementing NLO calculations in shower Monte Carlo programs: the POWHEG BOX”. *Journal of High Energy Physics* 2010.6 (June 2010). DOI: 10.1007/jhep06(2010)043. URL: <https://doi.org/10.1007%2Fjhep06%282010%29043>.
- [40] S. Frixione, G. Ridolfi, and P. Nason. “A positive-weight next-to-leading-order Monte Carlo for heavy flavour hadroproduction”. *Journal of High Energy Physics* 2007.09 (Sept. 2007), pp. 126–126. DOI: 10.1088/1126-6708/2007/09/126. URL: <https://doi.org/10.1088%2F1126-6708%2F2007%2F09%2F126>.
- [41] T. Gleisberg et al. “Event generation with SHERPA 1.1”. *Journal of High Energy Physics* 2009.02 (Feb. 2009), pp. 007–007. DOI: 10.1088/1126-6708/2009/02/007. URL: <https://doi.org/10.1088%2F1126-6708%2F2009%2F02%2F007>.
- [42] J. Alwall et al. “The automated computation of tree-level and next-to-leading order differential cross sections, and their matching to parton shower simulations”. *Journal of High Energy Physics* 2014.7 (July 2014). DOI: 10.1007/jhep07(2014)079. URL: <https://doi.org/10.1007%2Fjhep07%282014%29079>.

- [43] S. Agostinelli et al. “Geant4 a simulation toolkit”. *Nuclear Instruments and Methods in Physics Research Section A: Accelerators, Spectrometers, Detectors and Associated Equipment* 506.3 (2003), pp. 250–303. ISSN: 0168-9002. DOI: [https://doi.org/10.1016/S0168-9002\(03\)01368-8](https://doi.org/10.1016/S0168-9002(03)01368-8). URL: <https://www.sciencedirect.com/science/article/pii/S0168900203013688>.
- [44] ATLAS Collaboration. “The ATLAS Simulation Infrastructure”. *The European Physical Journal C* 70.3 (Sept. 2010), pp. 823–874. DOI: 10.1140/epjc/s10052-010-1429-9. URL: <https://doi.org/10.1140%2Fepjc%2Fs10052-010-1429-9>.
- [45] ATLAS Collaboration. *Athena*. Version 22.0.1. Apr. 2019. DOI: 10.5281/zenodo.2641997. URL: <https://doi.org/10.5281/zenodo.2641997>.
- [46] Garelli, Nicoletta on behalf of the ATLAS Collaboration. “Performance of the ATLAS Detector in Run-2”. *EPJ Web Conf.* 164 (2017), p. 01021. DOI: 10.1051/epjconf/201716401021. URL: <https://doi.org/10.1051/epjconf/201716401021>.
- [47] ATLAS Collaboration. “Topological cell clustering in the ATLAS calorimeters and its performance in LHC Run 1”. *The European Physical Journal C* 77.7 (2017), p. 490. DOI: 10.1140/epjc/s10052-017-5004-5. URL: <https://doi.org/10.1140/epjc/s10052-017-5004-5>.
- [48] ATLAS Collaboration. “Muon reconstruction and identification efficiency in ATLAS using the full Run 2 pp collision data set at $\sqrt{s} = 13$ TeV”. *Eur. Phys. J. C* 81.7 (2021), p. 578. DOI: 10.1140/epjc/s10052-021-09233-2. arXiv: 2012.00578 [hep-ex].
- [49] ATLAS Collaboration. “Electron and photon performance measurements with the ATLAS detector using the 2015–2017 LHC proton-proton collision data”. *Eur. Phys. J. C* 81.7 (2021), p. 579. DOI: 10.1140/epjc/s10052-021-09234-1. arXiv: 2012.00579 [hep-ex].

- Journal of Instrumentation* 14.12 (Dec. 2019), P12006–P12006.
 DOI: 10.1088/1748-0221/14/12/p12006.
 URL: <https://doi.org/10.1088/1748-0221/14/12/p12006>.
- [50] ATLAS Collaboration.
 “Jet reconstruction and performance using particle flow with the ATLAS Detector”.
The European Physical Journal C 77.7 (2017), p. 466.
 DOI: 10.1140/epjc/s10052-017-5031-2.
 URL: <https://doi.org/10.1140/epjc/s10052-017-5031-2>.
- [51] M. Cacciari, G. P. Salam, and G. Soyez. “The anti- k_T jet clustering algorithm”.
Journal of High Energy Physics 2008.04 (Apr. 2008), pp. 063–063.
 DOI: 10.1088/1126-6708/2008/04/063.
 URL: <https://doi.org/10.48550/arXiv.0802.1189>.
- [52] M. Cacciari, G. P. Salam, and G. Soyez. “The catchment area of jets”.
Journal of High Energy Physics 2008.04 (Apr. 2008), pp. 005–005.
 DOI: 10.1088/1126-6708/2008/04/005.
 URL: <https://doi.org/10.1088/1126-6708/2008/04/005>.
- [53] ATLAS Collaboration. “Jet energy scale and resolution measured in proton–proton collisions at $\sqrt{s} = 13$ TeV with the ATLAS detector”.
The European Physical Journal C 81.8 (2021), p. 689.
 DOI: 10.1140/epjc/s10052-021-09402-3.
 URL: <https://doi.org/10.1140/epjc/s10052-021-09402-3>.
- [54] P. O. Hansson Adrian. “The ATLAS b -jet Trigger”
 (Nov. 2011). Comments: 4 pages, 6 figures, conference proceedings for PIC2011.
 arXiv: 1111.4190. URL: <https://cds.cern.ch/record/1397942>.

- [55] ATLAS Collaboration. “Optimisation and performance studies of the ATLAS b -tagging algorithms for the 2017-18 LHC run” (July 2017). All figures including auxiliary figures are available at <https://atlas.web.cern.ch/Atlas/GROUPS/PHYSICS/PUBNOTES/ATL-PHYS-PUB-2017-013>. URL: <http://cds.cern.ch/record/2273281>.
- [56] ATLAS Collaboration. “Expected performance of the ATLAS b -tagging algorithms in Run-2” (July 2015). All figures including auxiliary figures are available at <https://atlas.web.cern.ch/Atlas/GROUPS/PHYSICS/PUBNOTES/ATL-PHYS-PUB-2015-022>. URL: <https://cds.cern.ch/record/2037697>.
- [57] ATLAS Collaboration. “Identification and energy calibration of hadronically decaying tau leptons with the ATLAS experiment in pp collisions at $\sqrt{s = 8}$ TeV”. *The European Physical Journal C* 75.7 (2015), p. 303.
DOI: [10.1140/epjc/s10052-015-3500-z](https://doi.org/10.1140/epjc/s10052-015-3500-z).
URL: <https://doi.org/10.1140/epjc/s10052-015-3500-z>.
- [58] ATLAS Collaboration. “Identification of hadronic tau lepton decays using neural networks in the ATLAS experiment” (2019). All figures including auxiliary figures are available at <https://atlas.web.cern.ch/Atlas/GROUPS/PHYSICS/PUBNOTES/ATL-PHYS-PUB-2019-033>. URL: <https://cds.cern.ch/record/2688062>.
- [59] ATLAS Collaboration. “ E_T^{miss} performance in the ATLAS detector using 2015-2016 LHC p-p collisions” (June 2018). All figures including auxiliary figures are available at <https://atlas.web.cern.ch/Atlas/GROUPS/PHYSICS/CONFNOTES/ATLAS-CONF-2018-023>. URL: <https://cds.cern.ch/record/2625233>.

- [60] ATLAS Collaboration. “Muon reconstruction performance of the ATLAS detector in proton–proton collision data at $\sqrt{s} = 13$ TeV”. *The European Physical Journal C* 76.5 (2016), p. 292. DOI: 10.1140/epjc/s10052-016-4120-y. URL: <https://doi.org/10.1140/epjc/s10052-016-4120-y>.
- [61] ATLAS Collaboration. “Performance of the missing transverse momentum triggers for the ATLAS detector during Run-2 data taking”. *Journal of High Energy Physics* 2020.8 (Aug. 2020). DOI: 10.1007/jhep08(2020)080. URL: [https://link.springer.com/article/10.1007/JHEP08\(2020\)080](https://link.springer.com/article/10.1007/JHEP08(2020)080).
- [62] ATLAS Collaboration. “Performance of electron and photon triggers in ATLAS during LHC Run 2”. *The European Physical Journal C* 80.1 (Jan. 2020). DOI: 10.1140/epjc/s10052-019-7500-2.
- [63] ATLAS Collaboration. “Performance of the ATLAS muon triggers in Run 2”. *Journal of Instrumentation* 15.09 (Sept. 2020), P09015–P09015. DOI: 10.1088/1748-0221/15/09/p09015. URL: <https://iopscience.iop.org/article/10.1088/1748-0221/15/09/P09015>.
- [64] ATLAS Collaboration. “Luminosity determination in pp collisions at $\sqrt{s} = 13$ TeV using the ATLAS detector at the LHC” (June 2019). All figures including auxiliary figures are available at <https://atlas.web.cern.ch/Atlas/GROUPS/PHYSICS/CONFNOTES/ATLAS-CONF-2019-021>. URL: <http://cds.cern.ch/record/2677054>.
- [65] R. D. Ball et al. “Parton distributions for the LHC run II”. *Journal of High Energy Physics* 2015.4 (Apr. 2015). DOI: 10.1007/jhep04(2015)040. URL: <https://doi.org/10.1007%2Fjhep04%282015%29040>.

- [66] R. D. Ball et al. “Parton distributions with LHC data”.
Nuclear Physics B 867.2 (Feb. 2013), pp. 244–289.
 DOI: [10.1016/j.nuclphysb.2012.10.003](https://doi.org/10.1016/j.nuclphysb.2012.10.003).
 URL: <https://doi.org/10.1016%2Fj.nuclphysb.2012.10.003>.
- [67] ATLAS Collaboration. “A study of optimal parameter setting for MADGRAPH5_AMC@NLO + PYTHIA 8 matched setup” (Nov. 2015). All figures including auxiliary figures are available at <https://atlas.web.cern.ch/Atlas/GROUPS/PHYSICS/PUBNOTES/ATL-PHYS-PUB-2015-048>. URL: <https://cds.cern.ch/record/2103221>.
- [68] P. Baldi et al. “Parameterized neural networks for high-energy physics”.
The European Physical Journal C 76.5 (2016), p. 235.
 DOI: [10.1140/epjc/s10052-016-4099-4](https://doi.org/10.1140/epjc/s10052-016-4099-4).
 URL: <https://doi.org/10.1140/epjc/s10052-016-4099-4>.
- [69] Keras. URL: <https://keras.io/>.
- [70] Martín Abadi et al.
TensorFlow: Large-Scale Machine Learning on Heterogeneous Systems. Software available from tensorflow.org. 2015. URL: <https://www.tensorflow.org/>.
- [71] N. Srivastava et al.
 “Dropout: A Simple Way to Prevent Neural Networks from Overfitting”.
Journal of Machine Learning Research 15.56 (2014), pp. 1929–1958.
 URL: <http://jmlr.org/papers/v15/srivastava14a.html>.
- [72] B. Burghgrave. “Search for charged Higgs Bosons in the $\tau +$ lepton final state with 36.1 fb^{-1} of pp collision data recorded at $\sqrt{s} = 13 \text{ TeV}$ with the ATLAS experiment”. PhD thesis. Northern Illinois U., 2018.

- [73] ATLAS Collaboration. “Measurement of τ polarization in $W \rightarrow \tau\nu$ decays with the ATLAS detector in pp collisions at $\sqrt{s} = 7$ TeV”. *The European Physical Journal C* 72.7 (July 2012). DOI: 10.1140/epjc/s10052-012-2062-6. URL: <https://doi.org/10.1140%2Fepjc%2Fs10052-012-2062-6>.
- [74] ATLAS Collaboration. “Reconstruction, Energy Calibration, and Identification of Hadronically Decaying Tau Leptons in the ATLAS Experiment for Run-2 of the LHC” (2015). All figures including auxiliary figures are available at <https://atlas.web.cern.ch/Atlas/GROUPS/PHYSICS/PUBNOTES/ATL-PHYS-PUB-2015-045>. URL: <https://cds.cern.ch/record/2064383>.
- [75] ATLAS Collaboration. “Electron and photon energy calibration with the ATLAS detector using data collected in 2015 at $\sqrt{s} = 1$ TeV” (2016). All figures including auxiliary figures are available at <https://atlas.web.cern.ch/Atlas/GROUPS/PHYSICS/PUBNOTES/ATL-PHYS-PUB-2016-015>. URL: <https://cds.cern.ch/record/2203514>.
- [76] G. Cowan et al. “Asymptotic formulae for likelihood-based tests of new physics”. *The European Physical Journal C* 71.2 (Feb. 2011). DOI: 10.1140/epjc/s10052-011-1554-0. URL: <https://doi.org/10.1140%2Fepjc%2Fs10052-011-1554-0>.
- [77] A. L. Read. “Presentation of search results: Presentation of search results: the CL_s technique”. *Journal of Physics G: Nuclear and Particle Physics* 28.10 (Sept. 2002), pp. 2693–2704. DOI: 10.1088/0954-3899/28/10/313. URL: <https://doi.org/10.1088/0954-3899/28/10/313>.

- [78] ATLAS Tile Collaboration and Parrish, Elliot.
“Operation and Performance of the ATLAS Tile Calorimeter and its readiness for Run 3”
(2022). URL: <https://cds.cern.ch/record/2815951>.
- [79] ATLAS Collaboration.
“ATLAS data quality operations and performance for 2015–2018 data-taking”.
Journal of Instrumentation 15.04 (Apr. 2020), P04003–P04003.
DOI: 10.1088/1748-0221/15/04/p04003.
URL: <https://doi.org/10.1088/1748-0221/15/04/p04003>.